UNIVERSITY OF NOTTINGHAM

UNITED KINGDOM · CHINA · MALAYSIA

The Use of Passive Damping to Increase Sound Insulation in Buildings

by

Feng Yan, BEng.

Thesis submitted to the University of Nottingham

for the degree of Doctor of Philosophy

September 2015

To my parents

ABSTRACT

This thesis examined the potential sound insulation benefit by using damping material to absorb vibrational energy along its transmission path.

Statistical Energy Analysis (SEA) was used to evaluate the effect on system performance of adding damping globally, as well as its influence on individual transmission paths. Nine different theoretical models were studied using both bending only and three-wave SEA models to predict the system behaviour in different frequency regions. The results suggest that global damping treatment generally increases the sound insulation in buildings. Initial increases in the internal loss factor (a term used in SEA to describe material damping properties) were found to provide significant initial improvements in sound insulation and flanking paths as opposed to direct paths were found to benefit more from damping treatment. A simple approximation was proposed to predict the damping benefit of paths of specific order without the need to run a full SEA model.

In the presence of heavily damped structural element, where SEA is less likely to provide accurate prediction, a forward ray tracing algorithm was proposed as a supplement. It enables one to predict the energy transmission through a heavily damped component coupling two or more lightly damped components (or SEA subsystems). The energy distribution along the edges of the damped component was studied. The contribution from the direct field was found to dominate the incident energy and resulting transmission, especially in areas close to the source when damping is high.

Different passive damping treatment techniques were reviewed as well as the theoretical damping level that is achievable as a guidance for theoretical and experimental validation. Several damping measurement techniques were studied and experimental validation of the ray tracing code was undertaken.

Keywords: Damping, flanking transmission, sound insulation, SEA, ray tracing

ACKNOWLEGEMENTS

Whilst the past four years have been both fascinating and challenging, none of it would have been possible without continuous support and guidance from a group of wonderful people. I would like to take this chance to express my sincere gratitude to all of them.

I would like to thank Professor Robin Wilson for choosing to let me study for my PhD at the first place, which allows all the memorable experience begins. His kindness and patience as well as invaluable advice really support me through all those challenges. Many thanks to Dr. Peter Rutherford for his supervision and valuable advice. I would also thank the faculty of Engineering for providing scholarship to cover my tuition fee.

I would like to thank Dr. Yupeng Wu for providing excellent advice on my work at annual reviews. Many thanks to the technicians in the Lab, especially to Mr. David Oliver, for their great technical help. Special thanks to Miss. Lindsay Shepperson for administrative support.

I would like to thank my parents for their selfless love and continuous encouragement. I am too grateful to have them on my back through happiness and sadness.

Also many thanks to my good friends for giving immense help and support in all different aspects.

TABLE OF CONTENTS

LIST OF FIGURES

LIST OF TABLES

LIST OF SYMBOLS

B	Bending stiffness for a beam (Nm)
	Bending stiffness per unit width for a plate (Nm)
E	Young's modulus (N/m^2)
	Energy (J)
E_0	Reference energy (10^{-12}J)
F	Force (N)
G	Shear modulus (N/ m^2)
N	Mode count
S	Surface area (m^2)
T	Time (s)
V	Volume (m^3)
W	Power (W)
W_0	Reference power (10^{-12}W)
W_i	Power input to subsystem i (W)
W_{ij}	Power flow from subsystem i to j (W)
a	Acceleration (m/s^2)
b	Width of a beam (m)
c	Wave speed (m/s)
	Viscous damping coefficient (Ns/m)
c_0	Wave speed in air (m/s)
c_B	Bending wave speed (m/s)
f	Frequency (Hz)
f_c	Critical frequency (Hz)
Δf	Frequency bandwidth (Hz)
h	Hysteretic damping coefficient (N/m)
	Thickness (m)
i	$\sqrt{-1}$
k	Wavenumber (rad/m)
	Spring constant (N/m)
l	Dimension (m)
m	Mass (kg)
n	Modal density (modes/Hz)
t	Time (s)
u	Velocity (m/s)
v	Poisson's ratio
ρ	Density (kg/m^3)
ρ_s	Surface density (kg m^2)
π	3.14159…
ω	Angular frequency $= 2\pi f$ (rad/s)
θ	Start angle (degree)
θ_{ra}	Reflection angle (degree)
ε	Extensional strain
ζ	Damping ratio
η	Loss factor
η_i	Total loss factor of subsystem i

η_{id}	Internal loss factor of subsystem i
η_{ij}	Coupling loss factor from subsystem i to j
λ	Wavelength (m)
$\emptyset$	Shear strain
μ	Poisson's ratio
σ	Direct stress (N/m^2)
τ	Transmission coefficient
	Shear stress (N/m^2)

Other terms are used and defined locally.

ABBREVIATIONS

CLF	Coupling loss factor
ILF	Internal loss factor
SEA	Statistical energy analysis
TLF	Total loss factor

CHAPTER 1 INTRODUCTION

1.1 Sound transmission path

The indoor acoustic environment has been long recognized as having an important influence on people's lives. Concerns over noise control have been reflected in the Building Regulations, which specify the minimum performance criteria that need to be met by separating and adjoining walls and floors between new build and rehabilitated dwellings (The Building Regulations, 2010). Traditional sound insulation strategies focused on reducing transmission through the primary separating element, where the direct transmission was assumed to be dominant. However, as recognised in requirements such as those described in the Building Regulations, sound can also be transmitted through other structural elements giving rise to flanking transmission (Figure 1-1). Although the contribution of any individual flanking path is typically much less than direct path, the overall contribution of flanking transmission is believed to be more important than direct transmission (Craik, 2001). There exists a potential way to increase the indoor acoustic insulation by reducing the flanking transmission, which can potentially be achieved by applying passive damping treatments to the flanking elements.

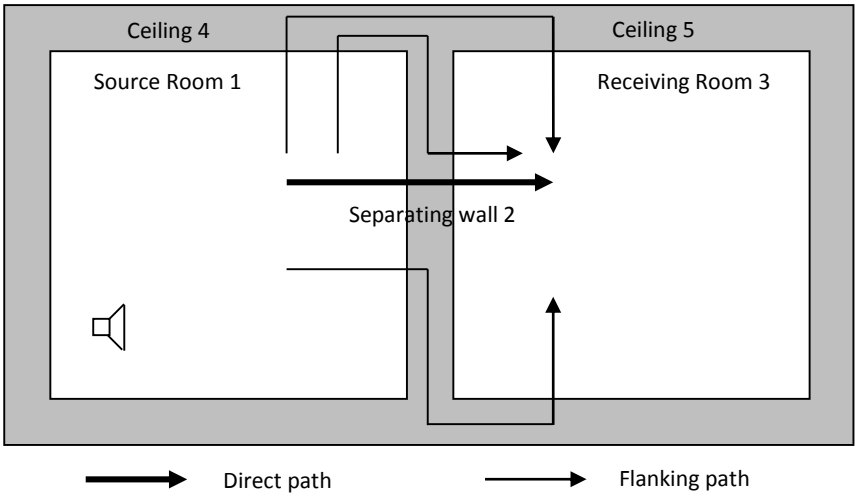

Figure 1-1 Illustration of direct path and flanking paths (Only some of the flanking paths have been shown)

1.2 General acoustic noise control techniques

There are four common techniques that can be used to increase sound insulation in buildings, namely mass, isolation, absorption and damping.

When the airborne noise transmission occurs across a solid wall, the wall acts like a sound barrier. The mass of the wall plays an important role in determining the effectiveness of blocking the noise. This is also known as the mass law, which suggests that each time the mass of the wall doubles the sound insulation will increase by approximately 6dB (Craik, 1996). The mass law implies that better sound insulation can be achieved by using materials with higher density. However, it is not very effective in minimizing the transmission of impact (structure-borne) noise such as footsteps.

Another noise control technique, i.e. isolation, is to trap the noise in the room and to prevent it from transmitting into sound sensitive spaces. This can be achieved by introducing sound deadening material (sound barriers) on the walls, floors and ceilings. Materials such as fibreglass serve this purpose. Another form of isolation is known as 'decoupling', which introduces flexible materials (rubber, spring, cork etc.) or physical breaks in the structures to decrease structure-borne transmission along its original path.

One may also use porous materials to absorb vibrational energy and to convert it as heat. The vibrational energy causes the air in the small cavities to vibrate. Energy conversion occurs due to friction and viscous force (Hopkins, 2012). This mechanism absorbs vibrational energy rather than noise being transmitted or reflected. Common absorption materials are melamine sponges and open cell rubber foams (Cox and D'antonio, 2009).

Noise can also be minimised by the use of damping treatment. Damping describes the ability of a system to dissipate vibrational energy into other forms of energy (normally heat). Passive damping treatments, such as free-layer damping, constrained-layer damping, tuned-mass dampers etc., have been used in areas of engineering and building practice to increase the damping of structure and in so

doing, reduce unwanted vibration. As vibration in structures is the primary means by which energy is transmitted from one location to another, any measures that serve to dissipate vibration along the transmission path is likely to increase sound insulation. As flanking paths are generally longer than the direct path between any two points in a structure, these are likely to be influenced most strongly by any global addition of damping.

1.3 Statistical Energy Analysis

Statistical Energy Analysis (SEA) was first developed in the 60's to allow complex structures to be modelled with relative ease. It divides a complex system into a number of subsystems, which can be loosely defined as components that exhibit their own modal response to excitation. Energy is assumed to be stored in each resonant mode of each subsystem and flows from subsystems with higher modal energy to subsystems with lower modal energy (these subsystems are normally physically connected). It is an analog of thermal conduction where the modal energy is an analog of temperature. SEA provides a framework to solve complex vibrational problems and has been proven effective when applied in building acoustics (Craik, 1996). In SEA simulation, damping is reflected through the internal loss factor (ILF), which is defined as the ratio of energy loss due to internal damping to the total energy in one radian cycle. The framework of SEA simulation provides the benefit of allowing damping treatment to be represented and investigated simply by changing the ILFs of individual or groups of subsystems or the entire system as a whole.

While it is possible to investigate the effect of damping by varying ILFs, there are limits to which this is feasible when using SEA. As the damping of a structural element is increased, the energy within it tends to become less and less evenly distributed. This then tends to violate one of the underlying assumptions behind the representation of this structural element as an SEA subsystem, i.e. that it exhibits modal behaviour and by implication energy is distributed uniformly within it. In light of this problem, an alternative prediction model needs to be developed as a supplement to normal SEA. Ray tracing techniques offer one approach to

explore the energy distribution and transmission within heavily damped subsystems by tracing the travel history of sound waves. In this approach, it is assumed that the sound field can be represented by a large number of discrete acoustic rays and its distribution within the structure that supports it may be described by their cumulative effect.

1.4 Research aim and objectives

This thesis aims to explore the potential benefit that applied damping can offer in improving sound insulation in complex/large building structures. The objectives were:

- To explore the influence of damping using conventional SEA modelling;
- To develop a new way (ray tracing code) to analyse heavily damped subsystems and compare the result with pure SEA modelling;
- To identify an effective method to measure the damping in heavily damped structure;
- To examine different damping treatment techniques and the corresponding achievable damping level;
- To undertake experimental work to validate a hybrid SEA/ray tracing approach to model systems with heavily damped element.

1.5 Thesis outline

The following chapters are constructed in such way that each aforementioned objective was achieved.

Chapter 2 describes three general damping mechanisms and some common damping models. In addition, different damping measurement techniques are introduced.

Chapter 3 reviews the origin, assumptions, advantages and limitations of Statistical Energy Analysis. A general procedure of conducting SEA modelling is also introduced.

Chapter 4 examines the effect of global damping treatment (damping applications on all structural elements) on nine different building designs for both bending only and three wave models. The damping effect on different orders of transmission path is also explored.

Chapter 5 proposes a ray tracing model to examine energy transmission through a heavily damped subsystem. It gives a detailed explanation of how the code is constructed. This ray tracing approach is then used to investigate the energy distribution at the edges of a damped plate.

Chapter 6 reviews four common passive damping treatments and their governing mechanisms. General rules of thumb for achieving high damping level are given and the values of achievable loss factor are briefly discussed.

Chapter 7 describes the experimental facilities and experimental techniques for loss factor measurement. Validation of ray tracing code is given to support the findings in Chapter 5.

Chapter 8 examines a one-room system to illustrate how one may use the ray tracing code to modify SEA modelling for damped systems. Comparison between the pure SEA and hybrid SEA/ray tracing modelling is given.

Chapter 9 contains a summary of the conclusions and offers some suggestions for future work.

CHAPTER 2 VIBRATION DAMPING

2.1 Introduction

This chapter explores the definition of damping, explaining what kind of damping mechanisms one may encounter in building acoustics, how to mathematically model them and measurement techniques commonly used to quantify damping.

2.2 What is damping?

Damping is normally accepted as the phenomenon where mechanical energy is dissipated in other forms of energy (usually internal thermal energy) in a dynamic system (Clarence and Silva, 2007). Knowledge of the level of damping is very important in analysing and testing a system. For most mechanical engineering cases, damping has a direct relation to the amplitude of vibration, which limits the maximum excitation the dynamic system can tolerate. In the acoustic point of view, damping defines the proportion of acoustic energy that can be converted to the form of heat. Ungar and Zapfe (2006) gave a good summary of the effect of increasing damping:

> *'(1) more rapid decay of unforced vibrations(2) faster decay of freely propagating structure-borne waves, (3) reduced amplitudes at resonances of structures subject to steady periodic or random excitation with attendant reductions in stresses and increases in fatigue life, (4) reduced response to sound and increased sound transmission loss (reduced sound transmission) above the coincidence frequency (at which the spatial distribution of the disturbing pressure matches that of the structural displacement), (5) reduced rate of buildup of vibrations at resonances, (6) reduced amplitudes of 'self-excited' vibrations, in which the vibrating structure accepts energy from an external source (e.g., wind) as the result of its vibratory motion.'*

2.3 Damping mechanisms

Three types of damping are normally inherent with vibrational systems, namely internal (material) damping, structural damping and acoustic damping.

2.3.1 Internal (material damping)

Internal (material) damping results from the energy dissipation associated with various microscopic and macroscopic processes. Quoting from Clarence and Silva (2007), microstructure defects, such as '*grain boundaries and impurities; thermoelastic effects caused by local temperature gradients resulting from nonuniform stresses, as in vibrating beams; eddy current effects in ferromagnetic materials; dislocation motion in metals; and chain motion in polymers*', can all contribute to internal damping. There exist a variety of models to represent the internal damping of different materials, however, no single model can satisfactorily characterise the properties of all materials (Clarence and Silva, 2007). Two commonly adopted models are viscoelastic damping and hysteretic damping. These will be explored in Section 2.4.

2.3.2 Structural damping

Structural damping is caused by the friction due to relative motion at joints, boundaries, supports and interfaces, etc. A generalized analytical model that describes structural damping is extremely difficult to develop due to the fact that the energy dissipation depends on the details of the particular system (Clarence and Silva, 2007). Nevertheless, one may use a Coulomb friction model to model energy dissipation caused by rubbing. For cases of impacting, the coefficient of restitution (the ratio of the relative speed after and before collision) of the two objects that are in contact is used to determine the energy dissipation as Clarence and Silva (2007) suggested.

2.3.3 Acoustic damping

Acoustic (radiation) damping relies on the presence of air (or other fluids) to dissipate energy in the structure. The local displacements of structural elements disturb the surrounding medium (in this thesis it is assumed to be air) and cause acoustic waves to radiate away from them. Part of the mechanical energy in the system is thus converted into acoustic energy. The main goal of indoor sound insulation is to minimise the acoustic waves radiated from the structural elements into noise sensitive areas. One way to reduce acoustic radiation is by minimising the

vibrational energy transmitted to the plate, which can be achieved by applying passive damping treatment. With less energy in a structure, even if the radiation efficiency stays the same, less noise will be generated.

2.4 Damping models

There are no generalised damping models that can satisfactorily describe all types of damping mechanisms. Instead, several different damping models have been developed to analyse specific damping mechanisms. In this section, viscous damping, viscoelastic damping, hysteretic damping, and interface damping models will be introduced.

2.4.1 Linear Viscous damping

Linear viscous damping model is one of the rudimentary models that has been introduced to understand the basic behaviour of a damped vibrational system. A single-degree-of-freedom (SDOF) linear spring-mass-damper system, with mass, m, spring constant, k, and a viscous damping coefficient, c, is taken as an example (Figure 2-1). The viscous damping force is assumed to be linear with velocity.

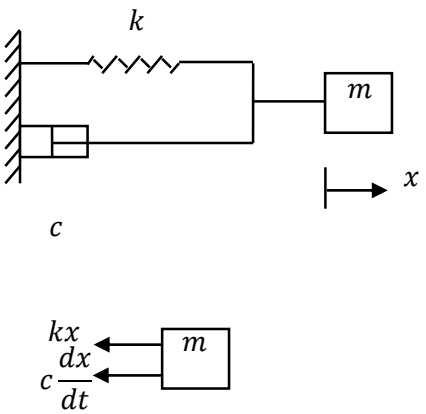

Figure 2-1 SDOF linear spring-mass-damper system

If this linear SDOF model is subjected to an external driving force $f(t)$, one obtains (Kinsler et al., 1999):

$$m\frac{d^2x}{dt^2} + c\frac{dx}{dt} + kx = f(t) \tag{2-1}$$

where the sum of inertia force md^2x/dt^2, the damping force cdx/dt and the stiffness force kx balance the external force $f(t)$.

If one introduces the following coefficients:

$$\omega_n = \sqrt{\frac{k}{m}} \tag{2-2}$$

$$\zeta = \frac{c}{2\sqrt{mk}} \tag{2-3}$$

where ω_n is the (undamped) natural frequency of the system and ζ (zeta) is the damping ratio, Equation 2-1 becomes:

$$\frac{d^2x}{dt^2} + 2\zeta\omega_n\frac{dx}{dt} + {\omega_n}^2x = \frac{f(t)}{m} \tag{2-4}$$

2.4.1.1 Free vibration

Consider the case where there is no external force (i.e. $f(t) = 0$), Equation 2-4 becomes (Kinsler et al., 1999):

$$\frac{d^2x}{dt^2} + 2\zeta\omega_n\frac{dx}{dt} + {\omega_n}^2x = 0 \tag{2-5}$$

One may solve this equation by assuming:

$$x = Ce^{st} \tag{2-6}$$

where C and s are both constants.

Substituting Equation 2-6 back into Equation 2-5, one obtains the characteristic equation to be:

$$s^2 + 2\zeta\omega_n s + {\omega_n}^2 = 0 \tag{2-7}$$

Therefore, one gets:

$$s = -\omega_n\left(\zeta \pm \sqrt{\zeta^2 - 1}\right) \tag{2-8}$$

2.4.1.1.1 Overdamped

When $\zeta > 1$, s has two different real solutions. The displacement has the form:

$$x(t) = e^{-\zeta\omega_n t}(C_1 e^{-\omega_n t\sqrt{\zeta^2-1}} + C_2 e^{\omega_n t\sqrt{\zeta^2-1}}) \tag{2-9}$$

This case is referred as *overdamped*. The mass is decaying exponentially without oscillation (see the case in Figure 2-2 when $\zeta = 1.5$).

2.4.1.1.2 Critically damped

When $\zeta = 1$, s has two identical real solutions. The displacement is in the form of:

$$x(t) = (C_1 + C_2)e^{-\omega_n t} \tag{2-10}$$

This case occurs when the system is *critically damped* and the critical damping coefficient is given by $c_c = 2\sqrt{mk}$. This is desirable in most engineering cases since it is the fastest way of damping the system to zero displacement without overshooting (see the case in Figure 2-2 when $= 1$).

2.4.1.1.3 Underdamped

When $\zeta < 1$, s has two complex solutions. The displacement has the form:

$$x(t) = e^{-\zeta\omega_n t}(A_1 e^{i\omega_n\sqrt{1-\zeta^2}t} + A_2 e^{-i\omega_n\sqrt{1-\zeta^2}t}) \tag{2-11}$$

This case is called *underdamped*. The system will decay exponentially with oscillation (see the case in Figure 2-2 when $= 0.5$).

2.4.1.1.4 Undamped

When $\zeta = 0$, the system is simply *undamped*, the mass undergoes sinusoidal oscillation (see the case in Figure 2-2when $= 0$).

2.1.4.1.5 System behaviour

The constants C_1, C_2 (A_1, A_2) in previous discussions can be found by applying initial condition such as:

$$x(0) = x_0 \tag{2-12}$$

and

$$\frac{dx(0)}{dt} = 0 \tag{2-13}$$

An example of the system behaviour of a linear SDOF system with these different damping coefficients is illustrated in Figure 2-2.

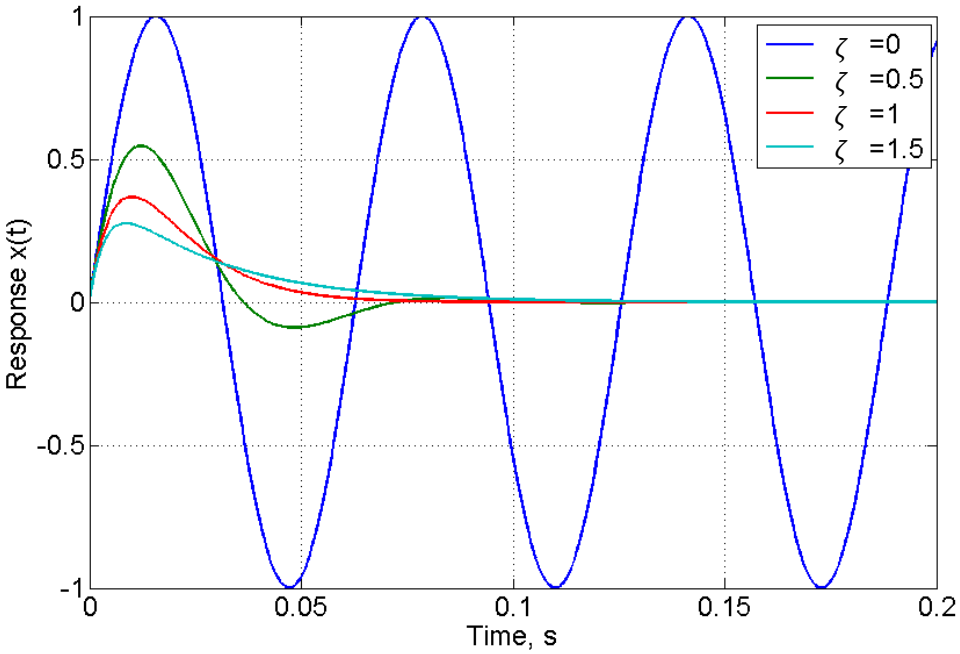

Figure 2-2 Response of a linear SDOF system with different damping coefficients (impulse excitation)

2.4.1.2 Harmonic excitation

When the system is subject to a harmonic excitation (i.e. $f(t) = F\sin\omega t$), Equation 2-1 becomes (Kinsler et al., 1999):

$$m\frac{d^2x}{dt^2} + c\frac{dx}{dt} + kx = F\sin\omega t \tag{2-14}$$

One may assume the solution has the form:

$$x(t) = A\cos\omega t + B\sin\omega t \tag{2-15}$$

Therefore, one has:

$$\frac{dx}{dt} = -A\omega\sin\omega t + B\omega\cos\omega t \tag{2-16}$$

$$\frac{d^2x}{dt^2} = -A\omega^2 \cos \omega t - B\omega^2 \sin \omega t \tag{2-17}$$

Substituting Equation 2-16 and 2-17 into Equation 2-14 and rearranging, one obtains:

$$(-mA\omega^2 + cB\omega + kA)\cos \omega t + (-mB\omega^2 - cA\omega + kB - F)\sin \omega t = 0 \tag{2-18}$$

This equation should be valid all points in time, thus one has:

$$-\mathrm{m}A\omega^2 + \mathrm{c}B\omega + kA = 0 \tag{2-19}$$

and

$$-mB\omega^2 - cA\omega + kB - F = 0 \tag{2-20}$$

Solving Equation 2-19 and 2-20 for A and B, one obtains:

$$A = \frac{-Fc\omega}{(c\omega)^2 + (m\omega^2 - k)^2} \tag{2-21}$$

$$B = \frac{-F(m\omega^2 - k)}{(c\omega)^2 + (m\omega^2 - k)^2} \tag{2-22}$$

Therefore, the steady state (where the excitation is assumed to be applied for an extremely long time and the transients are assumed to have died out) the solution is:

$$x(t) = \frac{F[-c\omega \cos \omega t + (k - m\omega^2)\sin \omega t]}{(c\omega)^2 + (m\omega^2 - k)^2} \tag{2-23}$$

One may also express this result in the form of (Jones, 2001):

$$x(t) = \frac{F \sin(\omega t - \varphi)}{\sqrt{(c\omega)^2 + (m\omega^2 - k)^2}} \tag{2-24}$$

$$\tan \varphi = \frac{c\omega}{k - m\omega^2} \tag{2-25}$$

where φ is the phase (or time) lag between the applied force and the resulting steady state response. One may immediately find that the maximum response

occurs when the excitation frequency ω equals $\sqrt{k/m}$, which is the resonant frequency for the undamped system.

2.4.1.3 Non-harmonic excitation

2.4.1.3.1 Impulsive excitation

Consider the case of impulsive excitation where $f(t) = F\delta(t)$. $\delta(t)$ is the Delta Function, which is usually used to simulate an impulse excitation (i.e. a discrete event which occurs in a very short time). A good approximation of this function is a rectangle of height $F/\delta t$ and width δt starting at $t = 0$ and ending at $t = \delta t$. The response of a SDOF system with impulsive excitation is (Jones, 2001):

$$x(t) = \frac{F}{m\omega_n\sqrt{1-\zeta^2}} \sin\left(\omega_n t\sqrt{1-\zeta^2}\right) e^{-\zeta\omega_n t} H(t) \tag{2-26}$$

where $H(t)$ is the Heaviside Step Function, equals to 1 when $t > 0$ and 0 when $t < 0$.

Some typical predicted impulse responses for several values of damping ratio ζ are shown in Figure 2-3. The effect of increasing the damping ratio is a reduction in the number of oscillations observed before the response approaches an infinitely small value, as well as decreasing the maximum amplitude of the same order oscillation. One may also observe that when the system is critically damped (i.e. $\zeta = 1$), the response takes the shortest time to vanish.

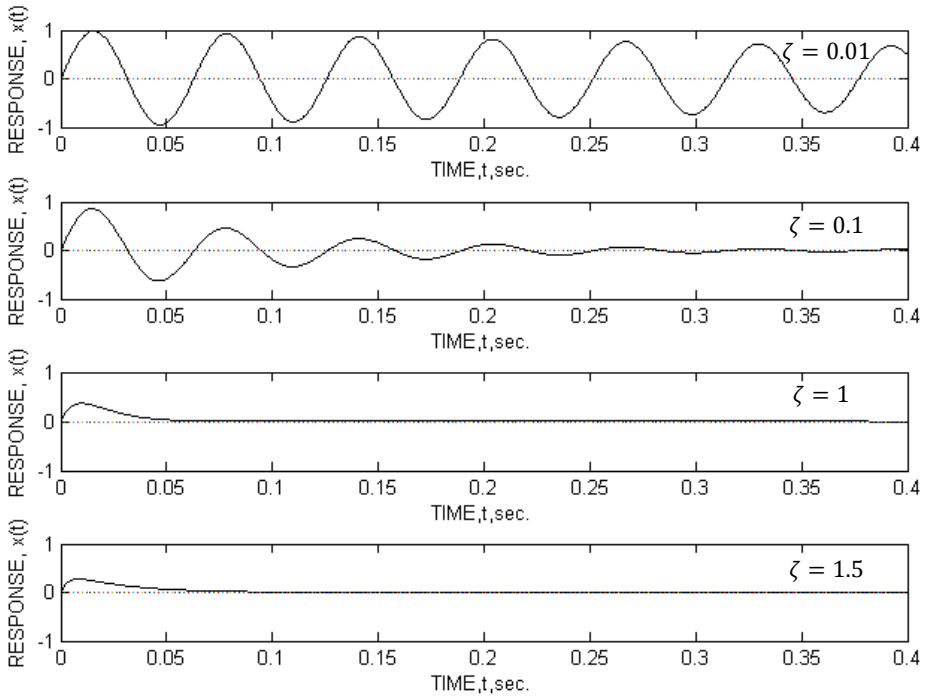

Figure 2-3 Typical responses to impulse excitation for $F = 1, m = 0.01, k = 3948, \omega_n = 100$ rad/sec

2.4.1.3.2 Step excitation

When the SDOF system illustrated in Figure 2-1 is subjected to a step excitation, where a steady force F is applied to the mass from $t = 0$, the displacement response can be given as (Jones, 2001):

$$x(t) = \frac{F}{k} - \frac{F}{k} e^{-\zeta \omega_n t} \left[\frac{\zeta}{\sqrt{1-\zeta^2}} \sin\left(\omega_n t \sqrt{1-\zeta^2}\right) + \cos\left(\omega_n t \sqrt{1-\zeta^2}\right) \right] \quad (2\text{-}27)$$

Typical step excitation responses for a SDOF system with different values of damping coefficients have been shown in Figure 2-4. Here F/k is normalized to be unity for a better illustration.

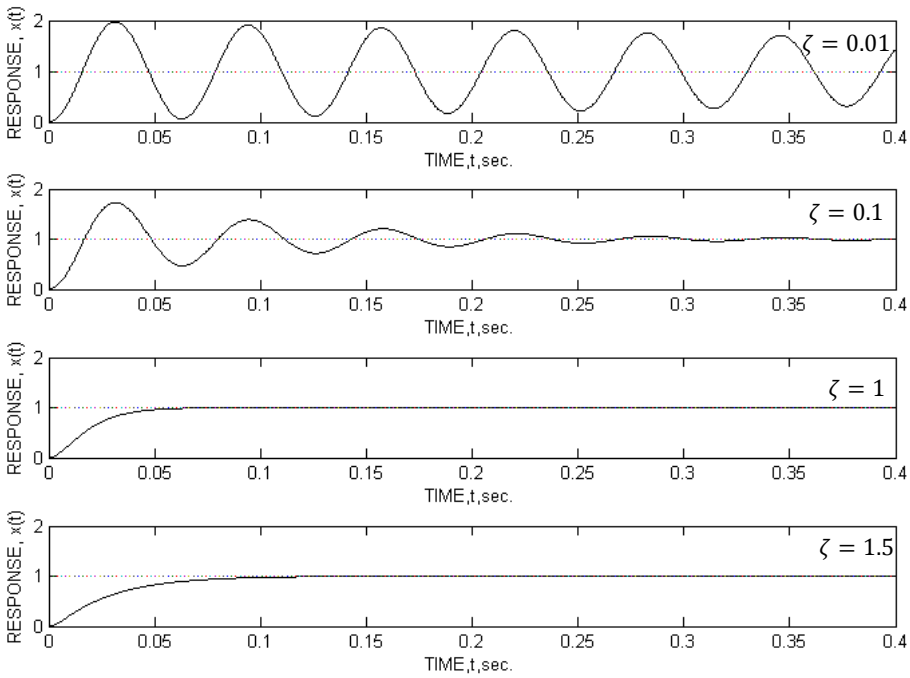

Figure 2-4 Typical responses to step excitation for $F/k = 1, m = 0.01, k = 3948, \omega_n = 100$ rad/sec ;

2.4.1.3.3 General time-dependent excitation

One may divide any time-dependent excitation into a succession of infinitesimally small impulsive excitations. Each such impulsive excitation is of magnitude $f(\tau)\Delta\tau$. The total response at any time can thus be obtained by summing all of the impulsive responses (Jones, 2001):

$$x(t) = \frac{1}{m\omega_n\sqrt{1-\zeta^2}}\int_0^t f(\tau)\sin\left[\omega_n(t-\tau)\sqrt{1-\zeta^2}\right]e^{[-\zeta\omega_n(t-\tau)]}H(t-\tau)d\tau \quad (2\text{-}28)$$

where $H(t-\tau)$ is the Heaviside Step Function, equals to 1 when $t > \tau$ and 0 when $t < \tau$.

2.4.2 Viscoelastic damping

2.4.2.1 What is viscoelasticity?

Ideal elastic materials exhibit deformation (strain) instantaneously when subjected to a dynamic load (stress). For an ideal viscous material, under the same condition, there exists a time lag ($\pi/2$) between the stress and strain. In reality, there do not exist pure elastic or pure viscous materials, instead, materials exhibit both viscous and elastic characteristics (Hosford, 2005). Most homogeneous isotropic polymeric materials exhibit significant viscoelastic behaviour when undergoing deformation (Jones, 2001). The viscoelastic behaviour of these materials is referred as viscoelasticity. The damping property of viscoelastic materials depends strongly upon the operation temperature, and to a lesser degree, on the excitation frequency, and is observed to be linear with respect to the vibration amplitude with the exception of extreme cases (Jones, 2001). Common viscoelastic materials are polymers, which are composed of long cross-linked and intertwined molecular chains, each containing thousands or even millions of atoms (examples of such kinds of material can be seen in Table 2-1).

2.4.2.2 Analytical models

The generation of internal force in viscoelastic materials results from the process of achieving new equilibrium positions when the molecules are subjected to an external force. Although the time to fully reach this new equilibrium state is theoretically infinite, the time needed to approach a close approximation is finite (Jones, 2001). This, in principle, gives one possible way to predict the behaviour of a specific viscoelastic material under external excitations if the molecular structure is fully understood. Analysis using such methods has been reported for applications of small molecules with enormous computational costs (Jones, 2001). However, it would be far too expensive and complex to apply such technique for large molecular structures such as polymers. For most engineering purposes, the analytical models are more commonly based upon experimental observations.

Table 2-1 List of some polymer types (Jones, 2001)

1.	Acrylic rubber
2.	Butadiene rubber (BR)
3.	Butyl rubber
4.	Chloroprene
5.	Chlorinated Polyethylenes
6.	Ethylene-Propylene-Diene
7.	Fluorocarbon rubber
8.	Fluorocarbon rubber
9.	Nitrile rubber
10.	Natural rubber
11.	Polyethylene
12.	Polystyrene
13.	Polyvinyl Chloride (PVC)
14.	Polymethyl Methacrylate (PMMA)
15.	Polybutadiene
16.	Polypropylene
17.	Polyisobutylene (PIB)
18.	Polyurethane
19.	Polyvinyl Acetate (PVA)
20.	Plolyisoprene
21.	Styrene-Butadiene (SBR)
22.	Silicone rubber
23.	Urethane rubber

2.4.2.3 Hysteresis loops

For a viscoelastic material, one important observation is that the resulting strain under harmonically varying stress is also harmonic (Jones, 2001). They share the same frequency but the strain has a time lag (phase difference) relative to the stress (see Figure 2-5 b). One may generate the hysteresis loop by plotting the stress (σ) and strain (ε) of the same point in a vibrating system. The ideal hysteresis

loop for viscoelastic materials is elliptical in shape and will retain its shape when the amplitude increases (see Figure 2-6). One typical hysteresis loop for mechanical damping is shown in Figure 2-7, which is not elliptical but is more preventive of the actual behaviour of a viscoelastic material. The area of a hysteresis loop gives the energy dissipation due to damping for a unit volume of material for each stress cycle. This is also defined as the unit-volume damping capacity, denoted by d, and can be given by

$$d = \oint \sigma d\varepsilon \tag{2-29}$$

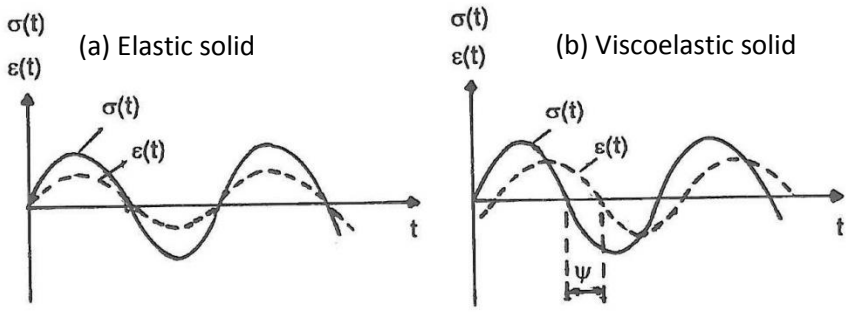

Figure 2-5 Harmonic excitation and response for (a) elastic solid, (b) viscoelastic solid (Jones, 2001)

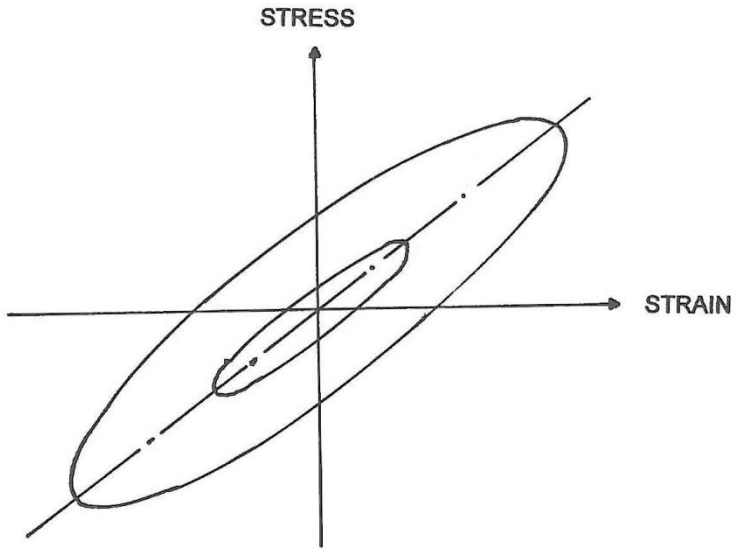

Figure 2-6 Ideal elliptical hysteresis loop (Jones, 2001)

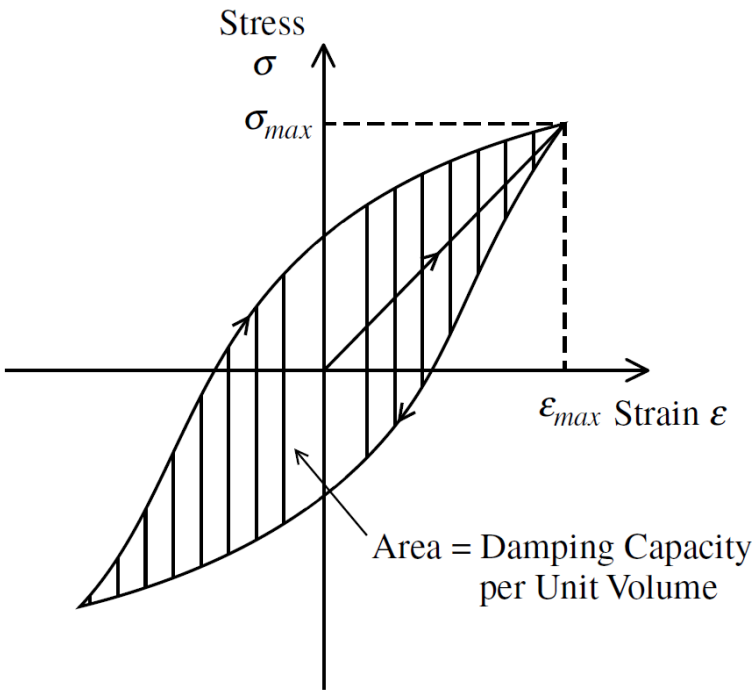

Figure 2-7 A typical hysteresis loop for mechanical damping (Clarence and Silva, 2007)

2.4.2.4 Viscoelastic models

2.4.2.4.1 Classic viscoelastic models

For an ideal elastic solid model, the stress and strain have a simple linear relationship:

$$\sigma = E\varepsilon \tag{2-30}$$

$$\tau = G\emptyset \tag{2-31}$$

where E is the Young's modulus, G is the shear modulus, σ and τ represent the direct stress and the shear stress, and ε and $\emptyset$ represent the extensional strain and shear strain respectively. For cases, where the shear and extensional modulus do not vary much with temperature and frequency, if the system is under harmonic excitation and the strain is within the limit (not very large), one has the relationship:

$$E = 2G(1 + v) \tag{2-32}$$

where v is Poisson's ratio.

For linear viscoelastic solid, there is no such simple relationship between stress and strain. Recalling the viscoelastic behaviour shown in Figure 2-5 b, one may represent the stress and strain in the form:

$$\sigma(t) = \sigma_{max} \sin(\omega t) \tag{2-33}$$

$$\varepsilon(t) = \varepsilon_{max} \sin(\omega t - \varphi) \tag{2-34}$$

If one takes the form:

$$\sigma(t) = \sigma_{max} \sin(\omega t) = \sigma_{max} \sin[(\omega t - \varphi) + \varphi] = \sigma_{max} \sin(\omega t - \varphi) \cos\varphi + \sigma_{max} \cos(\omega t - \varphi) \sin\varphi = \frac{\sigma_{max}}{\varepsilon_{max}} \cos\varphi \, \varepsilon(t) + \frac{\sigma_{max}}{\varepsilon_{max}\omega} \sin\varphi \frac{d\varepsilon(t)}{dt} \tag{2-35}$$

and write $E = (\sigma_{max}/\varepsilon_{max}) \cos\varphi$ and $\eta = \tan\varphi$, one has:

$$\sigma = E\varepsilon + \frac{E\eta}{\omega} \frac{d\varepsilon}{dt} \tag{2-36}$$

Similarly, one has:

$$\tau = G\emptyset + \frac{G\eta}{\omega} \frac{d\emptyset}{dt} \tag{2-37}$$

One needs to make sure ω is positive, otherwise the dissipative term (second term) in Equation 2-36 and 2-37 would not be subtracting energy during each cycle. This is commonly known as the Kelvin-Voigt model which is illustrated in Figure 2-8. It describes the relationship between the stress and stain under harmonic excitation for viscoelastic materials. More advanced analysis is needed to present non-harmonic behaviour.

If one defines the viscoelastic parameter E^* to be:

$$E^* = \frac{E\eta}{\omega} \tag{2-38}$$

and recalls Equation 2-29, the damping capacity for Kelvin-Voigt model per unit volume can be expressed as:

$$d_v = E^* \oint \frac{d\varepsilon}{dt} d\varepsilon\pi \tag{2-39}$$

One may express steady state strain under harmonic excitation to be:

$$\varepsilon = \varepsilon_{max} \cos \omega t \tag{2-40}$$

Substituting Equation 2-40 back into Equation 2-39, one gets:

$$d_v = \pi\omega E^* \varepsilon_{max}^2 \tag{2-41}$$

If one applies the initial condition, $\varepsilon = \varepsilon_{max}$ when $t = 0$ or when $d\varepsilon/dt = 0$, the stress from Equation 2-36 becomes $\sigma_{max} = E\varepsilon_{max}$. Therefore, one may get:

$$d_v = \frac{\pi\omega E^*}{E^2} \sigma_{max}^2 \tag{2-42}$$

where the damping capacity per volume is dependent on frequency of vibration.

There are another two classic viscoelastic models, namely the Maxwell model given by:

$$\sigma + k\frac{d\sigma}{dt} = \frac{E\eta}{\omega}\frac{d\varepsilon}{dt} \tag{2-43}$$

and the standard linear model given by:

$$\sigma + k\frac{d\sigma}{dt} = E\varepsilon + \frac{E\eta}{\omega}\frac{d\varepsilon}{dt} \tag{2-44}$$

These models are combinations of springs and viscous dampers (Figure 2-8) and one may find the standard model is a combination of Kelvin-Voigt and Maxwell model, which is hence the most accurate of the three. Clarence and Silva (2007) claimed that for most practical cases the Kelvin-Voigt model is sufficient. For modelling real viscoelastic behaviour, the accuracy can be greatly improved if one uses the multiple standard element model (Figure 2-8 d). Jones (2001) suggested that typically from four to ten elements is sufficient to give a reasonably accurate representation of viscoelastic behaviour.

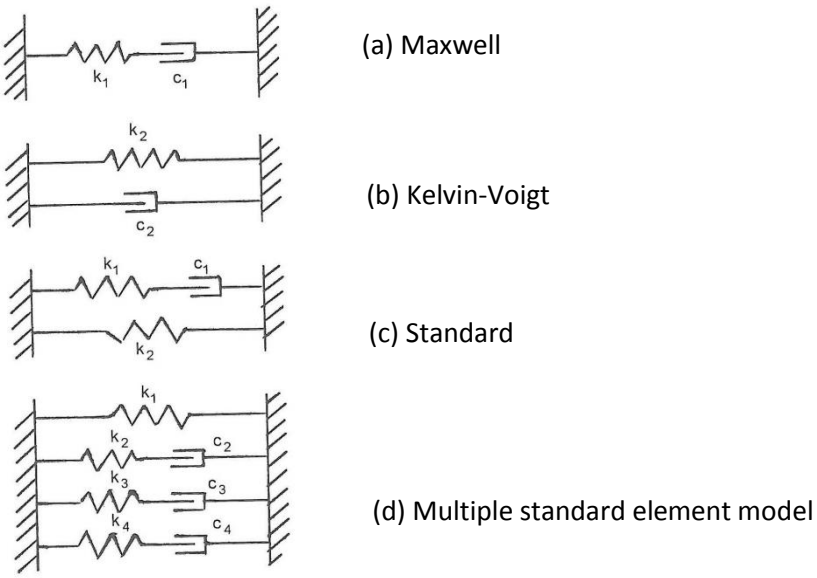

Figure 2-8 Classic models of viscoelastic material; (a) Maxwell, (b) Kelvin-Voigt, (c) Standard, (d) Multiple standard element model (Jones, 2001)

2.4.2.4.2 The complex modulus model

The Kelvin-Voigt model describes the relationship between the stress and strain under harmonic excitations with real number. There is another way of expressing the same relationship if one uses complex numbers to represent the sinusoid terms in the previous deviation. Recalling the Euler's formula:

$$e^{i\omega t} = \cos(\omega t) + i\sin(\omega t) \tag{2-45}$$

One may represent the strain by $\varepsilon(t) = \varepsilon_0 \exp(i\omega t)$, therefore $d\varepsilon/dt = i\omega\varepsilon_0 \exp(i\omega t) = i\omega\varepsilon$, and Equation 2-36 becomes:

$$\sigma = E\varepsilon + \frac{E\eta}{\omega} i\omega\varepsilon = E(1 + i\eta)\varepsilon \tag{2-46}$$

which is the complex modulus relationship for extensional deformation (one may derive a similar relationship for shear deformation).

One may obtain the effective stiffness by introducing the concept of a complex modulus model and substitute the effective stiffness back into the equation of motion (Equation 2-1) to get:

$$m\frac{d^2x}{dt^2} + k^*x = f(t) \tag{2-47}$$

where k^* is the effective stiffness and is a complex number.

The effective stiffness of the Maxwell model, where the spring and dashpot are connected in series (Figure 2-8 a), is obtained by:

$$k^* = k(1 + i\eta) = \frac{i\omega k_1 c_1}{k_1 + i\omega c_1} \tag{2-48}$$

where k_1 and c_1 are the spring constant and damping coefficient for the spring and the dashpot.

The effective stiffness of the Kevin-Voigt model, where the two elements are connected in parallel (Figure 2-8 b), is obtained by:

$$k^* = k(1 + i\eta) = k_2 + i\,\omega c_2 \tag{2-49}$$

The effective stiffness of the standard model (Zener model), which is a combination of the Maxwell and Kevin-Voigt model (Figure 2-8 c), is given by:

$$k^* = k(1 + i\eta) = \frac{i\omega k_1 c_1}{k_1 + i\omega c_1} + k_2 + i\omega c_2 \tag{2-50}$$

in which the term $i\omega c_2$ is normally made zero to avoid infinite stiffness at infinite frequency.

Similarly, the complex stiffness of the multiple standard element model (Figure 2-8 d) can be expressed as:

$$k^* = \sum_{j=1}^{j=n} k_j + \sum_{j=1}^{j=n} \frac{i\omega k_j c_j}{k_j + i\omega c_j} \tag{2-51}$$

The $i\omega c_j$ terms are eliminated for the same reason. One may separate Equation 2-51 into real and imaginary components as:

$$k^* = \left(\sum_{j=1}^{j=n} k_j + \sum_{j=1}^{j=n} \frac{\omega^2 k_j {c_j}^2}{{k_j}^2 + \omega^2 {c_j}^2}\right) + i\left(\sum_{j=1}^{j=n} \frac{\omega c_j {k_j}^2}{{k_j}^2 + \omega^2 {c_j}^2}\right) \tag{2-52}$$

Although the multiple standard element model gives better approximation of real viscoelastic behaviour, the mathematical complexity and the number of parameters that need to be determined is increased. One needs to take this into consideration when adopting such a model.

2.4.2.4.3 The fractional derivative model

There is an alternative model that has been recognised to be a great simplification in modelling viscoelastic behaviour (Jones, 2001), namely the fractional derivative model. This model is also known for its ability to model real dynamic behaviour (Pritz, 1996) and being causal (Bagley and Torvik, 1986; Torvik and Bagley, 1987; Gaul, Klein and Kemple, 1989).

Bagley and Torvik (1983) mentioned two important observations that form the basis of this model:

1). the fractional powers of time could be used to model stress relaxation

2). the stiffness and damping properties of viscoelastic materials were observed to be proportional to fractional powers of frequency.

Later, the fractional calculus were found to be attractive in modelling viscoelastic behaviour and proven to have advantages over linear viscoelastic models (where the derivatives are of integer order) (Bagley and Torvik, 1983). Reviews of the history and development of fractional derivative models have been presented by Bagley and Torvik (1983), Torvik and Bagley (1984), and Gaul et al. (1991).

The general form of the constitutive equation for the conventional viscoelastic models in the time domain can be given as (Bagley and Torvik, 1983):

$$\sigma(t) + b_1 \frac{d}{dt}\sigma(t) + b_2 \frac{d^2}{dt}\sigma(t) + \cdots + b_n \frac{d^n}{dt}\sigma(t) = a_0\varepsilon(t) + a_1 \frac{d}{dt}\varepsilon(t) + a_2 \frac{d^2}{dt}\varepsilon(t) + \cdots + a_m \frac{d^m}{dt}\varepsilon(t) \quad (2\text{-}53)$$

where b_1, b_2,…, b_n and a_0, a_1, a_2,…, a_m, are material constants. These constants can be determined using curve fitting method based on measured data. Due to the thermo-dynamic requirements, this equation is only physically meaningful if $m = n$ or $m = n + 1$ (Pritz, 1996).

The fractional derivative model replaced the integer order derivatives with fractional order and hence has the form:

$$\sigma(t) + b_1 \frac{d^{\beta_1}}{dt^{\beta_1}}\sigma(t) + b_2 \frac{d^{\beta_2}}{dt^{\beta_2}}\sigma(t) + \cdots + b_n \frac{d^{\beta_n}}{dt^{\beta_n}}\sigma(t) = a_0\varepsilon(t) + a_1 \frac{d^{\alpha_1}}{dt^{\alpha_1}}\varepsilon(t) + a_2 \frac{d^{\alpha_2}}{dt^{\alpha_2}}\varepsilon(t) + \cdots + a_m \frac{d^{\alpha_m}}{dt^{\alpha_m}}\varepsilon(t) \tag{2-54}$$

where $0 < \beta_1 < \beta_2 < \cdots \beta_m < 1$ and $0 < \alpha_1 < \alpha_2 < \cdots \alpha_m < 1$ are also material constants. The fractional derivative of αth order can be defined by the gamma function (Γ) as (Bagley and Torvik, 1983):

$$\frac{d^{\alpha}}{dt^{\alpha}}\varepsilon(t) = \frac{1}{\Gamma(1-\alpha)} \frac{d}{dt} \int_0^t \frac{\varepsilon(\tau)}{(t-\tau)^{\alpha}} d\tau \tag{2-55}$$

2.4.2.4.3.1 Four-parameter fractional derivative model

The typical behaviour of polymeric materials is that the loss factor exhibits a wide peak over a wide frequency range and the dynamic modulus grows with increasing frequency (Nashif, Jones and Henderson, 1985; Corsaro and Corsaro, 1990). Pritz (1996) proposed a four-parameter fractional model to simulate such material when only one peak of loss factor is observed. This model can be derived by assuming all the parameters in Equation 2-54 to be zero except a_0, a_1, b_1, α_1 and β_1, and making $\alpha_1 = \beta_1 = \alpha$, then one has:

$$\sigma(t) + b_1 \frac{d^{\alpha}}{dt^{\alpha}}\sigma(t) = a_0\varepsilon(t) + a_1 \frac{d^{\alpha}}{dt^{\alpha}}\varepsilon(t) \tag{2-56}$$

Analysis has been done by Prittz (1996) to show the physical meaning of those parameters:

$$b_1 = \tau^\alpha$$

$$a_0 = G_0$$

$$a_1 = G_\infty \tau^\alpha$$

where τ is the relaxation time, G_0 is the static modulus of elasticity (the dynamic modulus at zero frequency) and G_∞ is the high frequency limit value of the dynamic modulus. Substituting these back into Equation 2-56, one gets:

$$\sigma(t) + \tau^\alpha \frac{d^\alpha}{dt^\alpha}\sigma(t) = G_0\varepsilon(t) + G_\infty \tau^\alpha \frac{d^\alpha}{dt^\alpha}\varepsilon(t) \tag{2-57}$$

This equation is equivalent to the conventional Zener model (the standard model) when $\alpha = 1$. Therefore, it is also referred as fractional Zener model, or more specifically as the four-parameter fractional derivative Zener model (Pritz, 1996).

Recalling the definition of the complex modulus, one has:

$$\bar{G}(i\omega) = \frac{\bar{\sigma}(i\omega)}{\bar{\varepsilon}(i\omega)} = G_d(\omega) + jG_l(\omega) = G_d(\omega)[1 + i\eta(\omega)] \tag{2-58}$$

where $\bar{\sigma}(i\omega)$ and $\bar{\varepsilon}(i\omega)$ represent the Fourier transforms of the $\sigma(t)$ and $\varepsilon(t)$ functions respectively, G_d is the dynamic modulus of elasticity, G_l is the loss modulus and $\eta(\omega) = G_l(\omega)/G_d(\omega)$ is the loss factor.

By applying Fourier transform, the complex modulus of this model can be given as:

$$\bar{G}(i\omega) = \frac{G_0 + G_\infty(i\omega\tau)^\alpha}{1 + (i\omega\tau)^\alpha} \tag{2-59}$$

The components of the complex modulus are (Pritz, 1996):

$$G_d(\omega) = G_0 \frac{1 + (d+1)\cos(\alpha\pi/2)\omega_n^\alpha + d\omega_n^{2\alpha}}{1 + 2\cos(\alpha\pi/2)\omega_n^\alpha + \omega_n^{2\alpha}} \tag{2-60}$$

$$G_l(\omega) = G_0 \frac{(d-1)\sin(\alpha\pi/2)\omega_n^\alpha}{1 + 2\cos(\alpha\pi/2)\omega_n^\alpha + \omega_n^{2\alpha}} \tag{2-61}$$

$$\eta(\omega) = \frac{(d-1)\sin(\alpha\pi/2)\omega_n^{\alpha}}{1+(d+1)\cos(\alpha\pi/2)\omega_n^{\alpha}+d\omega_n^{2\alpha}} \tag{2-62}$$

where $d = G_\infty/G_0$ and $\omega_n = \omega\tau$ denotes the normalized frequency.

Further simplification can be given for cases where $d = G_\infty/G_0 \gg 1$ or $\omega_n \ll 1$ (Pritz, 2003).

A comparison of the dynamic modulus, loss modulus and loss factor predicted by this model is given in comparison to the conventional Zener model in Figure 2-9 where $\alpha = 0.7$ and $d = 1000$. It can be found that the dynamic modulus has a monotonic increase with increasing frequency and will reach its maximum at high frequency. Both the loss factor and the loss modulus have one peak which is symmetrical with respect to logarithmic frequency.

Experimental work has been undertaken and shows good agreement for a variety of materials especially for polymeric materials (Rogers, 1983; Bagley and Torvik, 1986; Pritz, 1996). However, the experimental data published from other authors show that the peak of the loss factor is not symmetric with respect to logarithmic frequency. It appears to be asymmetric and the loss factor tends to approach a limit value at very high frequency while the dynamic modulus has a weaker monotonic increase at these frequencies (Capps, 1983; Madigosky and Lee, 1993).

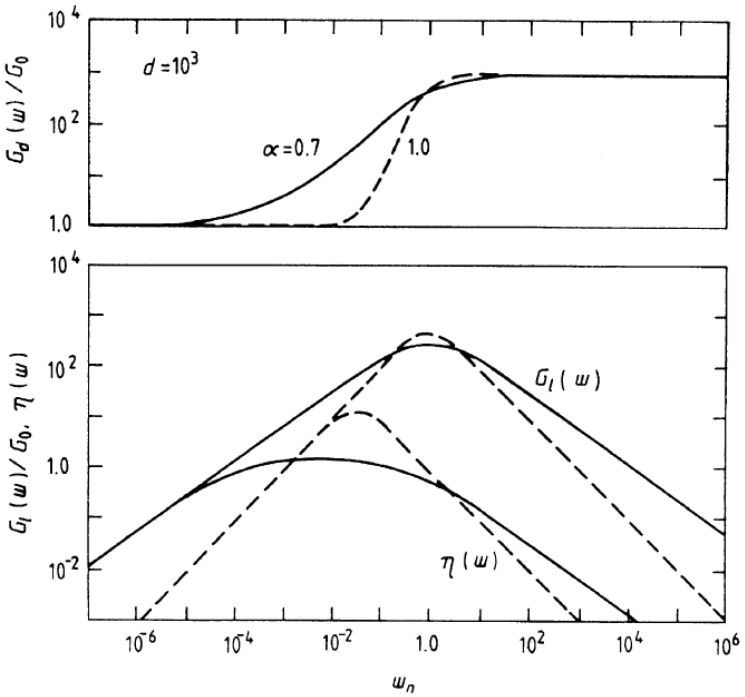

Figure 2-9 Frequency variations of the dynamic modulus, loss modulus and loss factor predicted by the four-parameter fractional Zener (—) model and the Conventional Zener model (- - - -), respectively. (Pritz, 2003)

2.4.2.4.3.2 Five-parameter fractional derivative model

In light of the observation of asymmetric behaviour of the loss peak, Pritz (2003) proposed a five-parameter fractional derivative model:

$$\sigma(t) + b_1 \frac{d^{\beta_1}}{dt^{\beta_2}}\sigma(t) = a_0\varepsilon(t) + a_1 \frac{d^{\alpha_1}}{dt^{\alpha_1}}\varepsilon(t) + a_2 \frac{d^{\alpha_2}}{dt^{\alpha_2}}\varepsilon(t) \qquad (2\text{-}63)$$

where $\alpha_2 > \alpha_1$. By assuming $\alpha_1 = \beta_1 = \beta$, the parameters can be represented as:

$$b_1 = \tau^{\beta}$$

$$a_0 = G_0$$

$$a_1 = G_1\tau^{\beta}$$

$$a_2 = G_2\tau^{\alpha}$$

where G_1 and G_2 have modulus dimension and $\alpha = \alpha_2$. The Equation 2-63 can be further simplified considering the fact that it must yield the four-parameter fractional Zener model if $\alpha = \beta$ (Pritz, 2003). This can be done by choosing:

$$G_1 = G_0$$

and

$$G_2 = G_\infty - G_0$$

The final five-parameter model can then be given as (Pritz, 2003):

$$\sigma(t) + \tau^\beta \frac{d^\beta}{dt^\beta}\sigma(t) = G_0\varepsilon(t) + G_0\tau^\beta \frac{d^\beta}{dt^\beta}\varepsilon(t) + (G_\infty - G_0)\tau^\alpha \frac{d^\alpha}{dt^\alpha}\varepsilon(t) \tag{2-64}$$

where it requires $\alpha > \beta$ for this model to be physical meaningful (to satisfy the thermodynamic requirements – the dissipated energy and the internal work must be positive)(Bagley and Torvik, 1986).

This model can be referred as the five-parameter fractional derivative Zener model. One may also derive the same expression by replacing the α terms in the denominator of Eqation 2-63 with β (Friedrish and Braun, 1992).

The complex modulus is given by (Pritz, 2003):

$$\bar{G}(i\omega) = G_0 + G_0(d-1)\frac{(i\omega\tau)^\alpha}{1 + (i\omega\tau)^\beta} \tag{2-65}$$

The components of the complex modulus are (Pritz, 2003):

$$G_d(\omega) = G_0 + G_0(d-1)\frac{\cos(\alpha\pi/2)\omega_n^\alpha + \cos[(\alpha-\beta)\pi/2)]\omega_n^{\alpha+\beta}}{1 + 2\cos(\beta\pi/2)\omega_n^\beta + \omega_n^{2\beta}} \tag{2-66}$$

$$G_l(\omega) = G_0(d-1)\frac{\sin(\alpha\pi/2)\omega_n^\alpha + \sin[(\alpha-\beta)\pi/2)]\omega_n^{\alpha+\beta}}{1 + 2\cos(\beta\pi/2)\omega_n^\beta + \omega_n^{2\beta}} \tag{2-67}$$

$$\eta(\omega) = \frac{(d-1)\{\sin(\alpha\pi/2)\omega_n^\alpha + \sin[(\alpha-\beta)\pi/2]\omega_n^{\alpha+\beta}\}}{1 + 2\cos(\beta\pi/2)\omega_n^\beta + \omega_n^{2\beta} + (d-1)\{\cos(\alpha\pi/2)\omega_n^\alpha + \cos[(\alpha-\beta)\pi/2)]\omega_n^{\alpha+\beta}\}} \tag{2-68}$$

Further simplification was given for cases where $d = G_\infty/G_0 \gg 1$ or $\omega_n \ll 1$ (Pritz, 2003).

A comparison between the behaviour of the five-parameter model and the four-parameter model has been given in Figure 2-10 with typical parameters of $\alpha = 0.7$; $\beta = 0.69, 0.65, 0.60$, and $d = 10^3$ (in the four-parameter case $\alpha = \beta = 0.7$). By analysing this result, Pritz (2003) had shown the physical meaning of the parameters in the five-parameter model as:

'*It is clear that α governs the low frequency increase of the loss modulus and the loss factor. The value of β, or more precisely the deviation of β from α, governs the asymmetry of the loss peak and the high-frequency behaviour of dynamic properties. Finally, the parameter G_∞ is related to the high-frequency value of the dynamic modulus, but here, in contrast to the four-parameter model, G_∞ is not the limit value of $G_d(\omega)$.*'

'*…G_∞ is a value of the dynamic modulus which occurs above the loss modulus peak at a frequency determined by the solution of equation as follows:*

$$\frac{G_d(\omega)}{G_\infty} = 1 = \frac{cos(\alpha\pi/2)\omega_n^\alpha + cos[(\alpha-\beta)\pi/2)]\omega_n^{\alpha+\beta}}{1 + 2\,cos(\beta\pi/2)\omega_n^\beta + \omega_n^{2\beta}} \tag{2-69}$$

Moreover, it has been found that the relaxation time τ in those two models has two different values (Friedrich and Braun, 1992).

Experimental results showed good agreement with the five-parameter model (Pritz, 2003). Arikoglu (2014) further developed the fractional derivative model by using genetic algorithms for parameter identification without shifting experiment data, which eliminated the possible error caused.

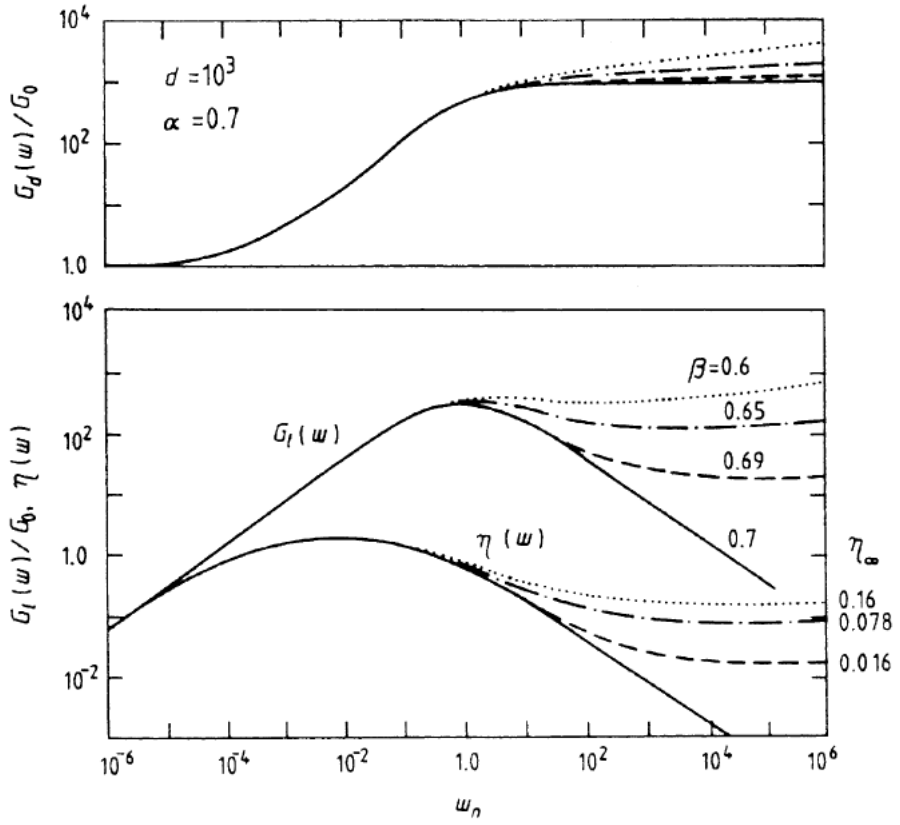

Figure 2-10 Frequency variations of dynamic modulus, loss modulus and loss factor predicted by the five-parameter fractional Zener model (- - - -, — · —, · · ·) and the four-parameter fractional Zener model (—), respectively (Pritz, 2003).

2.4.2.4.4 Effects of temperature, frequency and cyclic strain amplitude

The complex modulus properties, as well as loss factor of viscoelastic materials, are highly dependent on operation temperature and to a lesser degree on frequency. The non-linear behaviour depends on the amplitude of strain and varies for different materials from temperature to temperature (Jones, 2001).

The effects of temperature and frequency are shown in Figure 2-11 and Figure 2-12. When the temperature changes from low to high (or the frequency changes from high to low), the materials have three distinct states: i.e. the glassy state, the transition state and the rubbery state. It may be seen that the modulus G decreases as the temperature goes up (or frequency goes down). The loss factor has one peak at T_p (or at f_p). Another observation is that those two figures seem to be identical if either of them is shifted horizontally. This leads to the temperature-frequency

equivalence, i.e. the complex modulus values at any chosen temperature T_1 and frequency f_1 are the same to those with different temperature T_2 at different frequency f_2.(Jones, 2001).

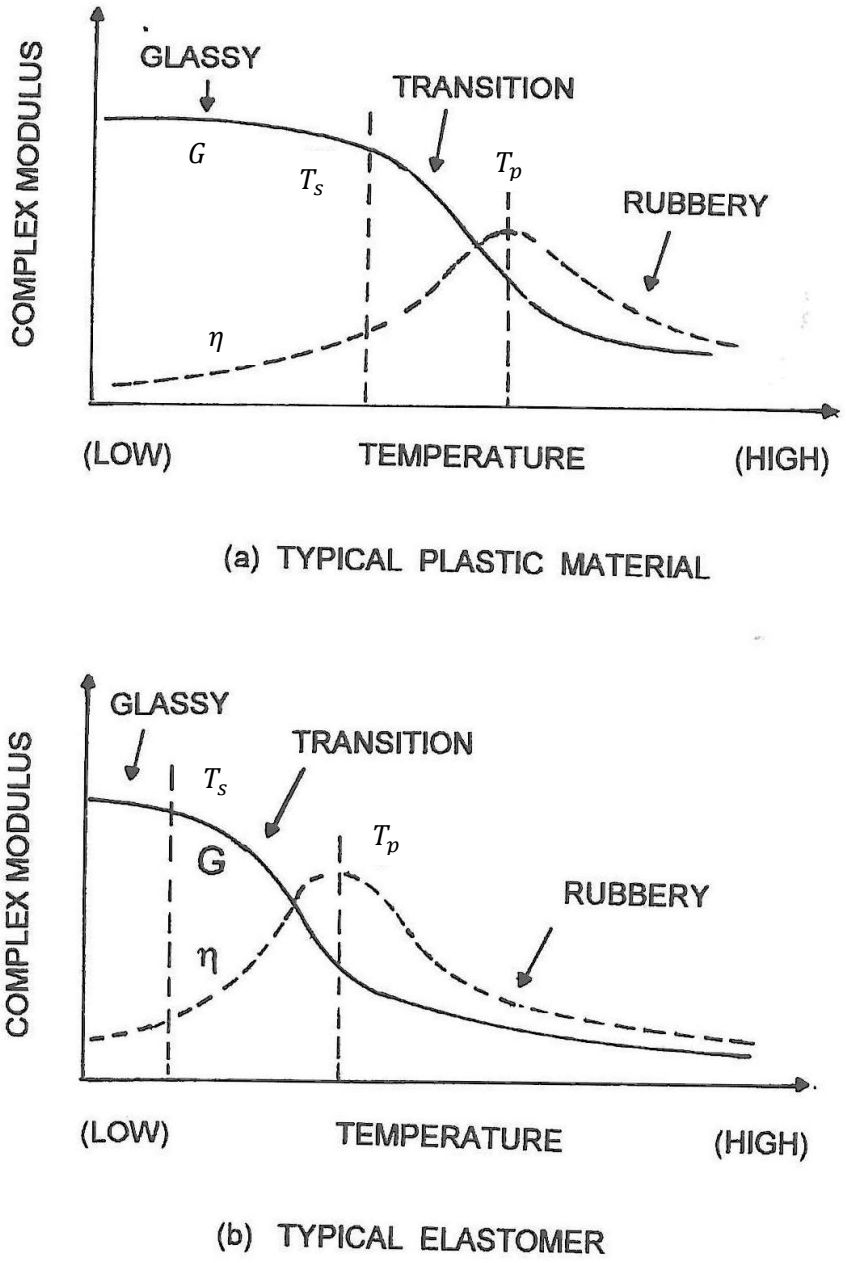

Figure 2-11 Effect of temperature on complex modulus behaviour; (a) typical plastic, (b) typical elastomer; where T_s is the transition temperature is and T_p is the peak loss factor temperature (Jones, 2001 P64)

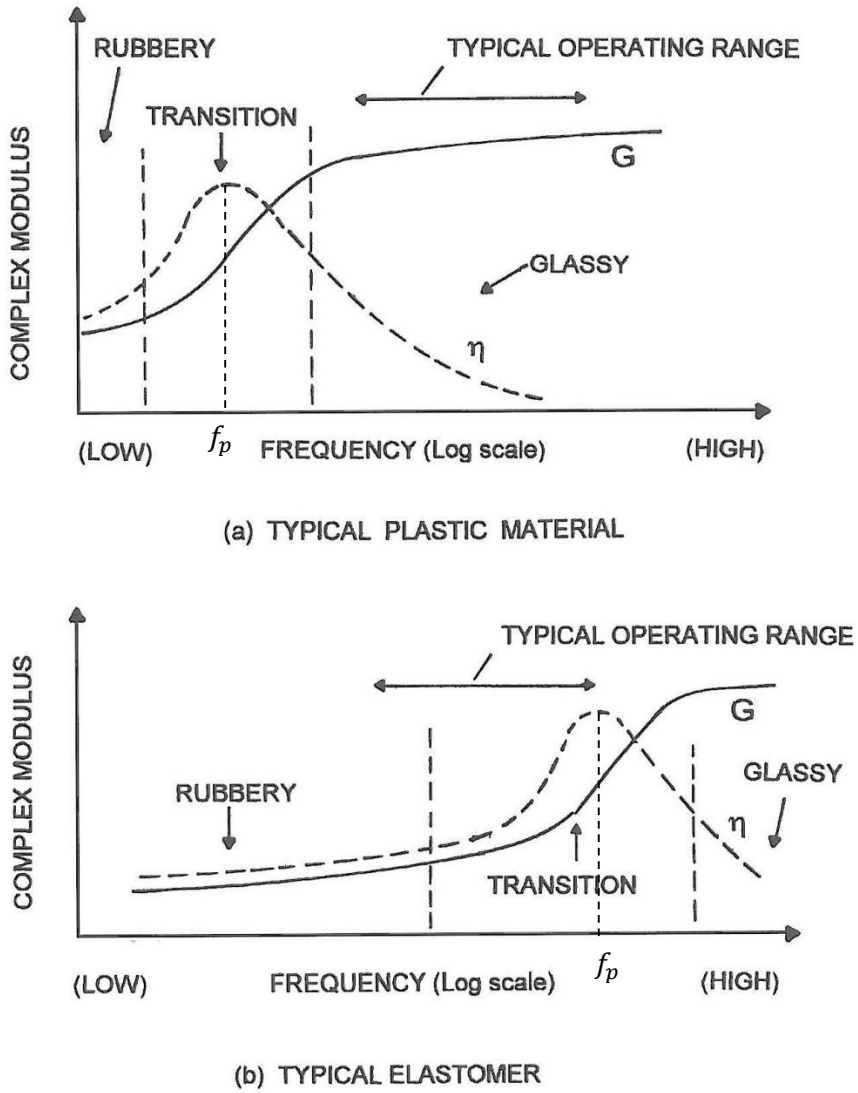

Figure 2-12 Effect of frequency on complex modulus behaviour; (a) typical plastic, (b) typical elastomer, where f_p is the peak loss factor frequency (Jones, 2001 P65)

The complex modulus properties are linear with respect to strain amplitude when the cyclic strain amplitudes are small (Jones, 2001). When the strain amplitude exceeds certain threshold, non-linear behaviour occurs. It is very difficult to apply non-linear model for general engineering purposes because the underlining theories are complicated and the number of tests required to quantify the non-linear behaviour are much larger than for linear models. It is thus generally suggested that linear complex modulus are used to simulate viscoelastic material properties in the manner that they are conservative to the nonlinear behaviour (Jones, 2001).

2.4.3 Hysteretic damping

In the damping models associated with viscous damping, the damping force depends on the frequency of vibration (Clarence and Silva, 2007) and hence the energy dissipation per cycle also depends on the frequency of oscillation (Nashif, Jones and Henderson, 1985). However, Theadorsen and Garrick (1940) have shown that there are cases where the damping capacity is frequency-independent (or varies rather slowly with frequency). Bishop and Johnson (1960) first addressed this type of damping as hysteretic damping. A more descriptive term of such damping model is given by Lazan (1968) as 'rate-independent linear damping'.

The general concept of hysteretic damping assumes that the damping force is proportional to the displacement and in phase with the velocity. Hence, the one dimensional differential equation can be written as:

$$m\frac{d^2x}{dt^2} + ihx + kx = f(t) \tag{2-70}$$

where h is the hysteretic damping coefficient.

2.4.3.1 Linear Hysteretic damping

Reid (1956) attempted a time-domain representation for linear hysteretic damping as:

$$f(t) = k\left\{1 + sgn\left[x(t)\frac{dx(t)}{dt}\right]\frac{\eta\pi}{2}\right\}x(t) \tag{2-71}$$

where k is a parameter with stiffness units, $sgn(x)$ is the Signum Function, $sgn(x) = 1$ for $x > 0$, $sgn(x) = -1$ for $x < 0$, and $sgn(x) = 0$ for $x = 0$, and η is the frequency-independent loss factor. This model gives a triangular hysteretic loop for harmonic excitation and the corresponding energy dissipation per cycle is linear with the square root of displacement and independent of the excitation frequency. However, Caughey and Vijayaraghavan (1970) have noted that this model is a non-linear model since it does not satisfy the superposition principle (Inaudi and Kelly, 1995).

Biot (1958) proposed another time-domain model as:

$$f[x(t)] = k\left\{x(t) - \frac{2\eta}{\pi}\int_{t_0}^{t} Ei[-\varepsilon(t-\tau)]\frac{dx(\tau)}{dt}d\tau\right\} \tag{2-72}$$

where ε is a small positive constant and $Ei(x) = \int_{-x}^{\infty}\frac{e^{-y}}{y}dy$ is the exponential integral. This model yields the energy loss per cycle under harmonic excitation to be (Caughey, 1962):

$$W_{cycle} = 2k\eta x^2 \tan^{-1}\left(\frac{\omega}{\varepsilon}\right) \tag{2-73}$$

which is frequency independent when $\omega/\varepsilon > 10$. Although this model is causal (the effect does not precede cause), the storage modulus of Boit's model is dependent of frequency (Inaudi and Kelly, 1995).

Inaudi and Kelly (1995) believed that, for linear-hysteretic damping model, the storage and loss modulus should be independent of frequency and hence has the form:

$$F(i\omega) = k[1 + i\eta sgn(\omega)]x(i\omega) \tag{2-74}$$

The energy dissipation per cycle under cyclic excitation is thus:

$$W_{cycle} = \pi k\eta x^2 \tag{2-75}$$

which is independent of the frequency of oscillation. However, this model also violates the principle of causality. In fact, in Inaudi and Kelly's (1995) paper, they mentioned that Kramers (1927) suggested, if the loss modulus is independent of frequency, the storage modulus must vary with frequency for the causal linear model. This violates the assumption that both the storage and loss modulus are frequency independent.

Inaudi and Kelly (1995) also claimed that two very commonly used expressions for linear hysteretic model need to be modified. The expression:

$$f(t) = k(1 + i\eta)x(t) \tag{2-76}$$

is not correct since it implies that the real-valued deformation history determines a complex-valued force. They suggested rewriting it in the form of Equation 2-74. Another expression:

$$f(t) = kx(t) + \frac{k\eta}{\omega}\frac{dx(t)}{dt} \tag{2-77}$$

is suggested to be written as

$$F(i\omega) = kx(i\omega) + \frac{k\eta}{|\omega|}\frac{dx(i\omega)}{dt} \tag{2-78}$$

which is equivalent to Equation 2-74.

In order to get the correct time-domain linear hysteretic damping model, the Hilbert transform is introduced by Inaudi and Kelly (1995). The expression is as:

$$f(t) = kx(t) + k\eta\hat{x}(t) \tag{2-79}$$

where $\hat{x}(t)$ is the Hilbert transform of $x(t)$ and is defined as

$$\hat{x}(t) = -\frac{1}{\pi}\int_{-\infty}^{\infty}\frac{x(\tau)}{t-\tau}d\tau \tag{2-80}$$

One may convert Equation 2-79 back into frequency domain as Equation 2-74.

To summarise the application of linear hysteretic damping model, the general limitation is the causality problem. This model has been mostly used in context of harmonic excitation (Inaudi and Kelly, 1995). For transient vibrations, the force may anticipate the deformation history which violates the physical principle that the effect cannot precede cause. For this reason, the applicability of hysteretic damping in general excitation has been questioned (Argyris and Mlejnek, 1991). Labonnote, Rønnquist and Malo (2013) derived a modified hysteretic damping model by defining complex elastic modulus and complex stiffness and experimentally validated this model to provide an efficient approach for material damping prediction to Timoshenko timber beams. Montalvão et al. (2013) presented detailed experimental setup for the measurement of the complex Young's modulus and the loss modulus of plates using a constant hysteretic damping model.

2.4.3.2 Non-linear Hysteretic damping

Structural systems may show non-linear behaviour under severe excitations, i.e. seismic excitation. A function of velocity and displacement is not sufficient to describe the restoring force in these cases. Since the restoring force depends on both the instantaneous deformation and the history of deformation, one may introduce a set of differential equations to represent the time dependent nature (Ismail, Ikhouane and Rodellar, 2009). The detailed modelling of this kind of damping based on physical laws is difficult. Instead, some so-called 'semi-physical' models are introduced combining the understanding of hysteresis and parameter identification.

One of the most popular models is the Bouc-Wen model, which was originally suggested by Bouc (1967) and further generalized by Wen (1976). This model requires only one auxiliary non-linear differential equation to model hysteretic behaviour and hence is computationally efficient (Song and Kiureghian, 2006).

The equations of Bouc-Wen model for a SDOF system is given by (Dobson, Noori, Hou, Dimentberg and Taber, 1997):

$$\frac{d^2x}{dt^2} + 2\zeta\omega_n \frac{dx}{dt} + \alpha{\omega_n}^2 x + (1-\alpha){\omega_n}^2 z = f(t) \tag{2-81}$$

$$\frac{dz}{dt} = A\frac{dx}{dt} - \beta\left|\frac{dx}{dt}\right||z|^{n-1} - \gamma\frac{dx}{dt}|z|^n \tag{2-82}$$

where $z(t)$ is the hysteretic restoring force, ζ is the damping parameter, ω_n is the natural frequency parameter; α is the ratio between post-yield and pre-yield stiffness; A, β, γ and n are parameters that related to the shape of the hysteresis loop. This formulation enables the model to be extended to many other hysteretic characterisation problems. One may find relevant reviews from papers written by Song and Kiureghian (2006) and Dobson et al. (1997)

2.4.4 Interface damping

In many practical applications, energy dissipation occurs at the interface of two sliding surfaces. Friction plays a major role in these situations. A simple illustration

of how the damping force changes as the relative velocity changes has been shown in Figure 2-13, where Region 1 describes Coulomb friction, Region 2 describes the 'Stribeck effect' and Region 3 describes Viscous friction.

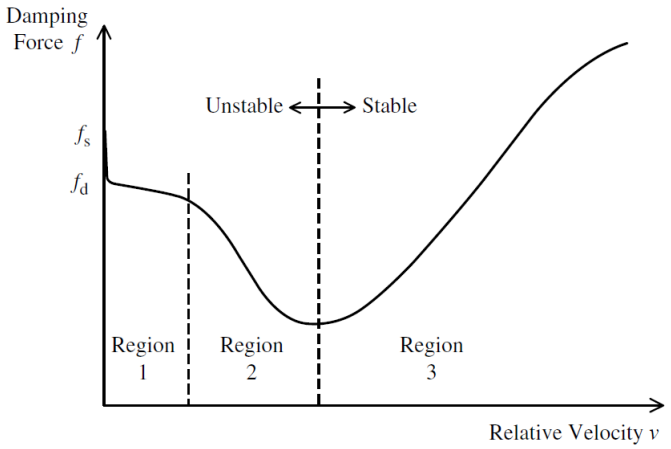

Figure 2-13 Illustration of interface damping (Clarence and Silva, 2007)

2.4.4.1 Coulomb friction

The coulomb friction model was derived by Coulomb in the 1700s and is widely used to describe the slipping-induced energy dissipation at structural joints. It is one of the major forms of structural damping and the degree of damping level depends on various factors including loading conditions, geometry of the moving parts, surface properties, material properties, type of connections, workmanship, level of determination, lubrication, magnitude of relative velocity, etc. (Clarence and Silva, 2007).

The damping force of Coulomb friction can be described in the form:

$$f = \mu F_n sgn(v) \tag{2-83}$$

where μ is the coefficient of sliding friction, F_n is the normal reaction force between the sliding surfaces, v is the relative velocity between the sliding surfaces. The Signum Function $sgn(v)$ is introduced here to represent that the friction force has an opposite direction of the relative velocity v (Figure 2-13, Region 1). One may

observe that the damping force of Coulomb friction does not have strong dependence on velocity.

2.4.4.2 Viscous friction

When there is lubricant between the surfaces, the friction force is mainly induced by the viscosity of the lubricant. This kind of friction is called viscous friction and the friction force has the relation (Reynolds, 1886):

$$f = F_v v \tag{2-84}$$

where the parameter $F_v = \mu A/y$, μ is the viscosity, A is the area of each surface and y is the length of separation. In viscous friction, the friction force is proportional to the relative velocity (Figure 2-13, Region 3). This only happens when the relative velocity exceeds certain level, i.e. the two surfaces are not in direct contact. When the relative velocity is low, the two surfaces have some kind of solid-to-solid contact and will exhibit Coulomb-type of friction. The proportion of solid-to-solid contact decreases as the velocity increases, meanwhile, the friction force also decreases. This phenomenon is termed as the Stribeck effect (Figure 2-13, Region 2).

2.4.4.3 Static friction

There are cases in which the connecting surfaces do not have relative motion, i.e. small value of driving force. Static friction is used to term this kind of phenomenon (Morin, 1833).

The friction force can be expressed as:

$$f = \begin{cases} f_e & if\ v = 0\ and\ |f_e| < f_s \\ f_s & if\ v = 0\ and\ |f_e| \geq f_s \end{cases} \tag{2-85}$$

The friction force equals the external (driving) force f_e until it exceeds the static friction force f_s (the minimum force required for the motion to begin). It then drops instantaneously to the value of dynamic friction force f_d (the minimum force needed to sustain the motion). This characteristic is usually known as ‘stiction’.

There may occur a so-called 'stick-slip' phenomena when the driving force drops below the dynamic friction force and then jumps above the static friction force, which is normally undesirable in practical cases (Clarence and Silva, 2007).

2.4.4.4 Other friction models

The three types of friction mentioned above are the most commonly used ones, there are however other types of models which are proposed for modelling more specific tasks. Since the main concern of this study is about internal damping, no further discussion will be given in the content. Good reviews of other friction models have been given by De Wit, Olsson, Åström and Lischinsky (1995), and Olsson, Åström, De Wit, Gäfvert and Lischinsky (1998).

2.4.5 General representation of damping in vibration analysis

2.4.5.1 General damping

It is difficult to incorporate microscopic details of damping in general vibration analysis. Simplified models are usually used to present various types of energy dissipation. Consider a system with n degrees of freedom. Vector $\boldsymbol{x}$ with n generalized coordinates, where x_i represents the independent motion of the object in direction i. For motions with small amplitude, spring elements can be assumed and hence the equation of motion can be given as (Clarence and Silva, 2007):

$$\boldsymbol{M\ddot{x}} + \boldsymbol{d} + \boldsymbol{Kx} = \boldsymbol{f}(\boldsymbol{t}) \tag{2-86}$$

where $\boldsymbol{M}$ is the mass matrix, $\boldsymbol{K}$ is the stiffness matrix. The vector $\boldsymbol{f}(\boldsymbol{t})$ represents the force in different directions. The damping force vector $\boldsymbol{d}(\boldsymbol{x}, \dot{\boldsymbol{x}})$ is normally a non-linear function of $\boldsymbol{x}$ and $\dot{\boldsymbol{x}}$. Different types of damping can be represented in the equation of motion. Their properties are determined by the nature of $\boldsymbol{d}(\boldsymbol{x}, \dot{\boldsymbol{x}})$ employed in the equation.

2.4.5.2 Hysteretic damping

For hysteretic damping, the damping force vector is usually represented in the form of $i\boldsymbol{Hx}$, where $\boldsymbol{H}$ is the hysteretic damping matrix. Therefore, the equation of motion becomes:

$$\boldsymbol{M\ddot{x}} + (i\boldsymbol{H} + \boldsymbol{K})\boldsymbol{x} = \boldsymbol{f}(\boldsymbol{t}) \tag{2-87}$$

The damping force described in this equation is proportional to the displacement and is $90°$ out of phase of the displacement. This model is mainly based on experimental observations and is suggested only to be used in the frequency domain with harmonic excitation (Liu and Gorman, 1995).

2.4.5.3 Equivalent Viscous damping

For the viscous damping model, the damping force vector can be written as $\boldsymbol{C\dot{x}}$, where $\boldsymbol{C}$ is the viscous damping matrix. The resulting equation of motion is :

$$\boldsymbol{M\ddot{x} + C\dot{x} + Kx = f(t)} \tag{2-88}$$

As discussed before, the linear viscous damping model can be handled with relatively simple mathematical analysis. It is therefore common to use equivalent viscous damping term to represent damping terms of other types. The equivalent viscous damping term is determined in such way that the resulting energy dissipation per cycle is equivalent to the original one. Hence, the motion of equation using equivalent viscous damping term can be expressed as:

$$\boldsymbol{M\ddot{x} + \widehat{C}\dot{x} + Kx = f(t)} \tag{2-89}$$

where $\widehat{\boldsymbol{C}}$ is the equivalent viscous damping matrix. Clarence and Silva (2007) have listed a few equivalent viscous damping terms of some common damping models in Table 2-2.

Table 2-2 Equivalent viscous damping term for common damping models used in dynamic analysis.

Damping type	**Equivalent viscous damping term**
Viscous	$\sum_j c_{ij}\,\dot{x}_j$
Hysteretic	$\sum_j \frac{1}{\omega} c_{ij}\,\dot{x}_j$
Structural	$\sum_j c_{ij}\,\lvert\dot{x}_j\rvert \mathrm{sgn}(\dot{x}_j)$
Structural Coulomb	$\sum_j c_{ij}\,\mathrm{sgn}(\dot{x}_j)$
Fluid	$\sum_j c_{ij}\,\lvert\dot{x}_j\rvert\dot{x}_j$

2.4.5.4 Rayleigh damping

In modal analysis of a dynamic system, the most commonly used model is the Rayleigh damping model, which can be seen as a special case of viscous damping. It was first introduced by Lord Rayleigh (1877) for the purpose of analysing linear dynamics of undamped systems (Adhikari and Phani, No date). The simplest damping matrix in the Rayleigh model consists of only two terms and can be expressed as:

$$\boldsymbol{C} = c_m \boldsymbol{M} + c_k \boldsymbol{K} \tag{2-90}$$

where c_m and c_k are pre-defined constants. It assumes the damping matrix is a linear combination of the mass and stiffness matrices and hence is also known as 'proportional damping model'. Clarence and Silva (2007) explained that the first term on the right of Equation 2-90 describes the inertial damping force, which is proportional to its momentum on each concentrated mass; the second term on the right describes the stiffness damping force which is '*proportional to the rate of change of the local deformation force at joints near the concentrated mass elements*'.

A more general approximation of the Rayleigh model for small levels of damping has been given by Caughey (1960):

$$\boldsymbol{C} = \boldsymbol{M} \sum_{k=0}^{p-1} \sigma_k \, (\boldsymbol{M^{-1}K})^k \tag{2-91}$$

This is equivalent to Equation 2-89 for special cases where $p = 1$.

The major benefit of Rayleigh damping is that the damping matrix of a structure with n degrees of freedom can be reduced to n of uncoupled equations (Chowdhury and Dasgupta, 2003). Additionally, since the mode shapes have not been altered, great simplification can be obtained in the process of finding the eigensolution or the calculated response (Liu and Gorman, 1995).

Extensions to this have been proposed by Liu and Gorman (1995), who introduced negative series and fractional indexed series to Caughey's formulation in

order to give more choices in selecting Rayleigh damping terms for practical use. Chowdhury and Dasgupta (2003) proposed a technique to compute Rayleigh damping coefficients (i.e. c_m and c_k) for large systems. The solutions are obtained by finding the best-fit values of c_m and c_k iteratively. Theoretical validation has been given to show that this technique can produce a more realistic representation of the structural behaviour under dynamic loading than using the presumptive damping ratio constant for all modes. Hall (2006) discussed the potential problems one may encounter under certain conditions, i.e. a non-linear analysis with softening non-linearity. A remedy to those problems has been proposed to avoid using unrealistically large damping forces calculated from Equation 2-90.

2.5 Damping measurement

There are various parameters (i.e. damping ratio, damping capacity, loss factor etc.) and damping models (viscous, viscoelastic, hysteretic, interface etc.) that can be used to describe damping. Before measuring the damping of a system, one needs to decide which parameter or model should be used to adequately describe the system characters. Knowledge of the theoretical basis and the application range of different damping measurement methods are thus important. Those methods can generally be divided into time-domain methods and frequency-domain methods.

2.5.1 Logarithmic Decrement Method

One of the most popular time-domain methods is the logarithmic decrement method. It comes from Load Rayleigh's observation that for the free vibration of a linear damped oscillator, '*the difference in the logarithms of successive extreme excursions is nearly constant, and is called the logarithmic decrement*' (Rayleigh, 1877). For a single-degree-of-freedom system with viscous damping, the time response of the displacement under impulse excitation is (Clarence and Silva, 2007):

$$x(t) = x_0 \exp(-\zeta \omega_n t) \sin \omega_d t \tag{2-92}$$

where ω_n and ω_d are the natural frequencies of the undamped and damped system respectively and they are related by the formula:

$$\omega_d = \sqrt{1-\zeta^2}\omega_n \tag{2-93}$$

The general impulsive response of a simple oscillator, described by Equation 2-92, is shown in Figure 2-14. The maximum displacement in ith cycle is defined as x_i.The logarithmic decrement (per cycle) is defined as:

$$\delta = \ln\left(\frac{x_i}{x_{i+1}}\right) = \frac{2\pi\zeta}{\sqrt{1-\zeta^2}} \tag{2-94}$$

The damping ratio can therefore be given as:

$$\zeta = \frac{1}{\sqrt{1+(2\pi/\delta)^2}} \tag{2-95}$$

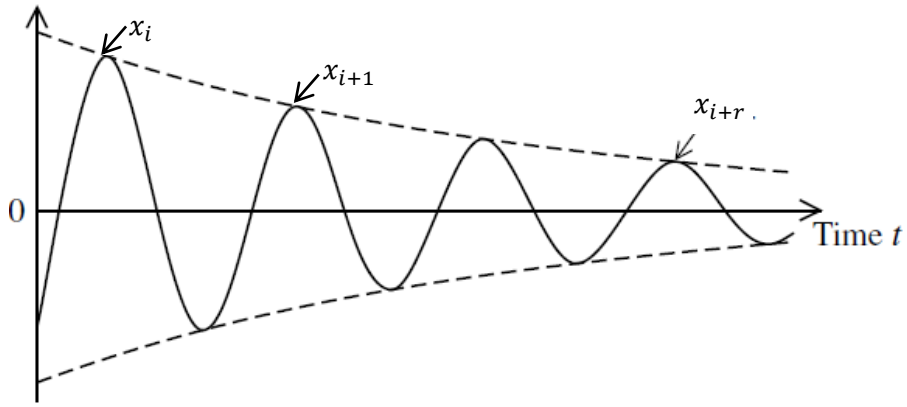

Figure 2-14 Impulsive response of a simple oscillator (Clarence and Silva, 2007)

For small damping, where $\omega_d \cong \omega_n$ holds (i.e. $\zeta < 0.1$), Equation 2-94 becomes:

$$\zeta = \frac{\delta}{2\pi} \tag{2-96}$$

The loss factor for low damping can be expressed as (Ungar and Zapfe, 2006):

$$\eta \cong 2\zeta = \frac{\delta}{\pi} \tag{2-97}$$

This method can be extended into multi-degree-of-freedom systems if the decay mainly occurs in one mode of vibration (Clarence and Silva, 2007). The

limitations associated with the implementation of the logarithmic decrement method are:

a) It normally requires at least two complete cycles for one to work out the logarithmic decrement. For heavily damped system (critically or overdamped), this method is not appropriate.

b) This method works well at low frequency when the system only possesses one mode. For higher frequency ranges, the decay takes place in multiple modes and therefore it is hard to distinguish the maximum placement in each cycle.

2.5.2 Reverberation Time Method

The most common method used to measure damping in building acoustics uses the reverberation time of the system (Craik, 1996), which is normally defined as the time it takes for the vibrational energy to decay by 60 dB when a steady excitation has been turned off. The reverberation time, T, has the relationship to the loss factor, η, as (Craik, 1996):

$$\eta = \frac{\ln(10^6)}{2\pi f T} = \frac{2.2}{fT} \tag{2-98}$$

This equation is valid for both structures and rooms. The reverberation time for some typical structures might be relatively short. This requires some specialised instrumentation with high precision (Craik, 1996). The excitation of a building structure with steady noise source is normally difficult; instead, one usually uses a transient excitation such as a hammer as the source.

2.5.3 Step – Response Method

When a single-degree-of-freedom viscously-damped system is subjected to a unit-step excitation, the time domain response can be expressed as (Clarence and Silva, 2007):

$$x_t = 1 - \frac{1}{\sqrt{1-\zeta^2}} \exp(-\zeta \omega_n t) \sin(\omega_d t + \emptyset) \tag{2-99}$$

where $\emptyset = \cos\zeta$. A typical step-response plot has been shown in Figure 2-15 (the response curve has to be normalized to unit steady-state value).

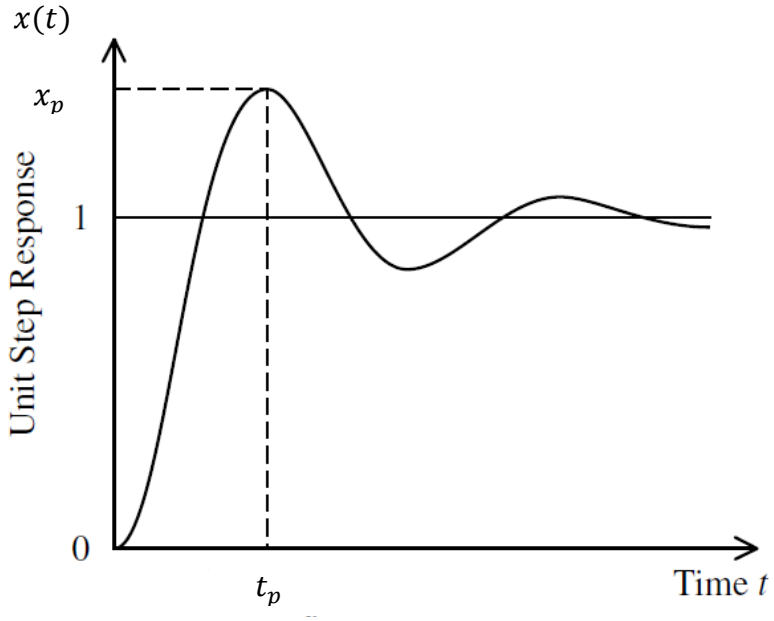

Figure 2-15 A typical unit-step response of a simple oscillator (Clarence and Silva, 2007)

The time when the first peak response x_p occurs can be given by:

$$t_p = \frac{\pi}{\omega_d} = \frac{\pi}{\sqrt{1-\zeta^2}\omega_n} \tag{2-100}$$

The corresponding first peak response is thus:

$$x_p = 1 + \exp(-\zeta\omega_n t_p) = 1 + \exp(\frac{-\pi\zeta}{\sqrt{1-\zeta^2}}) \tag{2-101}$$

The damping ratio can therefore be obtained through:

$$\zeta = \sqrt{1 - \left(\frac{\pi}{t_p\omega_n}\right)^2} \tag{2-102}$$

or

$$\zeta = \frac{1}{\sqrt{1 + \frac{1}{\left[\frac{\ln(x_p - 1)}{\pi}\right]^2}}} \tag{2-103}$$

The loss factor can be calculated through Equation 2-97 for small damping cases. This method can also be extended to multi-degree-of-freedom systems under modal excitations (Clarence and Silva, 2007).

2.5.4 Peak Amplitude Method

Another time-domain method is introduced here. Instead of using a unit-step excitation, harmonic excitation is applied (the response can be described by Equation 2-23, which is harmonic). The peak amplitude occurs at the frequency ω_r, which can be expressed as:

$$\omega_r = \omega_n\sqrt{1 - \zeta^2} \tag{2-104}$$

The peak response can be given as:

$$x_p = \frac{F}{2k\zeta\sqrt{1 - \zeta^2}} \tag{2-105}$$

The measureable amplification factor A is defined as the ratio of the peak response to the static response (F/k):

$$A = \frac{1}{2\zeta\sqrt{1 - \zeta^2}} \tag{2-106}$$

Therefore, the damping coefficient can be obtained by (Jones, 2001):

$$\zeta = 2\sqrt{\left[1 - \sqrt{1 - 1/A^2}\right]} \tag{2-107}$$

2.5.5 Magnification Factor Method

One frequency-domain method is introduced here. For a single-degree-of-freedom system with viscous damping, the magnitude of the frequency response function can be expressed as (Clarence and Silva, 2007):

$$|x(\omega)| = \frac{{\omega_n}^2}{[({\omega_n}^2 - \omega^2)^2 + 4\zeta^2 {\omega_n}^2 \omega^2]^{1/2}} \tag{2-108}$$

An illustration of the magnitude of frequency response function for simple oscillator has been shown in Figure 2-16. The frequency-response curve must be normalized so that the magnitude is unity at zero frequency. When the denominator reaches its minima, $|x(\omega)|$ has its maximum value. This happens at the resonant frequency ω_r, where:

$$\omega_r = \sqrt{1 - 2\zeta^2}\omega_n \tag{2-109}$$

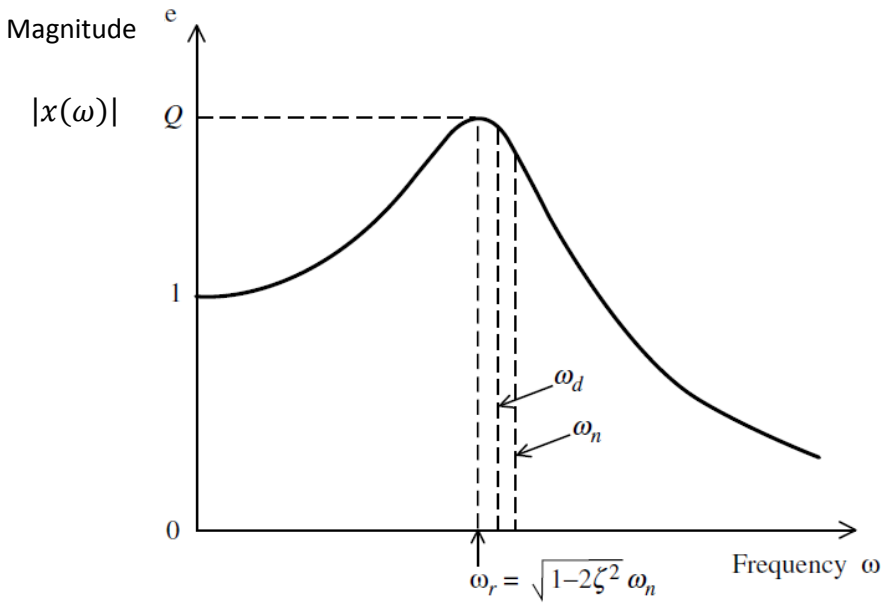

Figure 2-16 The magnitude of frequency response function for a simple oscillator (Clarence and Silva, 2007)

The magnitude of $|x(\omega)|$ at resonant frequency is defined as the amplification factor Q and has the form:

$$Q = \frac{1}{2\zeta\sqrt{1 - \zeta^2}} \tag{2-110}$$

For low damping cases (i.e. $\zeta < 0.1$), one has:

$$Q \cong \frac{1}{2\zeta} \tag{2-111}$$

Recall Equation 2-97, the loss factor can be expressed as:

$$\eta = 2\zeta = \frac{1}{Q} \tag{2-112}$$

This method can also be extended to multi-degree-of-freedom-system if the modal overlap is not to high (the intervals between the modal frequencies are not too small) and the system is lightly damped (Clarence and Silva, 2007).

2.5.6 Half-power Bandwidth Method

Another popular frequency-domain method is called the half-power bandwidth method. Considering the case where the frequency-response can be expressed as Equation 2-108, the peak value is given by Equation 2-111 for low damping. One may define the half-power bandwidth $\Delta\omega$ as the frequency range where the frequency-response magnitude is $1/\sqrt{2}$ times of the peak Q. Refer to Figure 2-17, the half-power bandwidth $\Delta\omega = \omega_2 - \omega_1$. By definition, ω_1 and ω_2 must satisfy the equation:

$$\frac{{\omega_n}^2}{[({\omega_n}^2 - \omega^2)^2 + 4\zeta^2{\omega_n}^2\omega^2]^{1/2}} = \frac{1}{\sqrt{2}}Q = \frac{1}{\sqrt{2}} \cdot \frac{1}{2\zeta\sqrt{1-\zeta^2}} \tag{2-113}$$

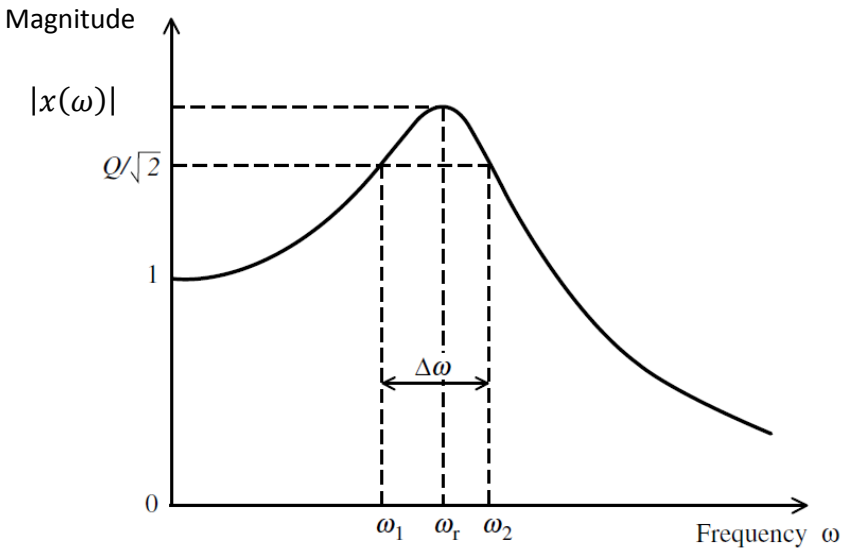

Figure 2-17 Illustration of the bandwidth method for a simple oscillator (Clarence and Silva, 2007)

For the case of low damping (i.e. $\zeta < 0.1$), one has $Q = 1/2\zeta$. Therefore, Equation 2-113 can be rearranged to:

$$\omega^4 - 2(1-2\zeta^2){\omega_n}^2\omega^2 + (1-8\zeta^2){\omega_n}^4 = 0 \tag{2-114}$$

Since ω_1 and ω_2 are the solutions, there must have:

$$(\omega^2 - {\omega_1}^2)(\omega^2 - {\omega_2}^2) = \omega^4 - 2(1-2\zeta^2){\omega_n}^2\omega^2 + (1-8\zeta^2){\omega_n}^4 = 0 \tag{2-115}$$

Therefore, one obtains:

$${\omega_1}^2 + {\omega_2}^2 = 2(1-2\zeta^2){\omega_n}^2 \tag{2-116}$$

and

$${\omega_1}^2{\omega_2}^2 = (1-8\zeta^2){\omega_n}^4 \tag{2-117}$$

So, the half-power bandwidth has the form:

$$\begin{aligned}\Delta\omega = |\omega_2 - \omega_1| &= \sqrt{(\omega_2 - \omega_1)^2} \\ &= \sqrt{2(1-2\zeta^2){\omega_n}^2 - 2\sqrt{(1-8\zeta^2)}{\omega_n}^2}\end{aligned} \tag{2-118}$$

When $\zeta < 0.1$, one has:

$$\sqrt{(1-8\zeta^2)} \cong 1 - 4\zeta^2 \tag{2-119}$$

Hence,

$$\Delta\omega \cong \sqrt{4\zeta^2{\omega_n}^2} = 2\zeta\omega_n \cong 2\zeta\omega_r \tag{2-120}$$

The damping ratio and loss factor can be estimated using the relation:

$$\eta = 2\zeta = \frac{\Delta\omega}{\omega_r} \tag{2-121}$$

For multi-degree-of-freedom systems, the modal loss factor can be obtained using:

$$\eta_i = 2\zeta_i = \frac{\Delta\omega_i}{\omega_{ri}} \tag{2-122}$$

where $\Delta\omega_i$ is the half-power bandwidth of ith mode and ω_{ri} is the resonant frequency of ith mode. One may notice that if the magnitude is plotted in dB, a factor of $1/\sqrt{2}$ means a 3dB drop. The definition of half-power bandwidth can also be expressed as the requency range where the magnitude of frequency-response function is 3dB lower than the peak.

The classsic form of half-power bandwidth method has been revisted by Wang (2010) and it is found to be sufficiently accurate for many practical cases where the damping ratio is less than 0.1. For cases where the damping ratio is higher, higher order corrections are suggested. Wang, Jin and Zhang (2012) examined the accuracy of the half-power bandwidth method in a two-degree-of-freedom linear system. It is found that this method might significantly overestimate the damping ratios of the two-degree-of-freedom system in some cases. Even for cases where the natural frequencies are spaced widely, the estimation error is still larger than that from a single-degree-of-freedom system. Therefore, this method should be used with caution when extended to multi-degree-of-freedom systems.

Papagiannopoulos and Hatzigeorgiou (2011) studied the half-power bandwidth method for both sigle and multi-degree-of-freedom systems that do not possess classical normal modes. A third order correction to the classical form is proposed to reduce the error. Similar research has been undertaken by Olmos and Roesset (2010), whose work includes a comparison of the half-power bandwidth method with approximate formulae and procedures used in practice.

2.6 Discussion and conclusion

This chapter sought to introduce the concept of damping, explaining how damping works, how it may be represented mathematically, and how it may be measured.

The linear viscous damping model is a very good starting model for one to understand the general behaviour of damping under different excitations. Based on

this model, different damping situations, i.e. overdamped, critically damped, underdamped and undamped, have been introduced. It is very helpful for understanding other damping models.

The viscoelastic damping model is probably the most relevant damping model that is related to the majority of passive damping treatments. Both free-layer and constrained-layer damping use viscoelastic materials to dissipate vibrational energy. The classic viscoelastic models are fundamental to understanding and representing viscoelastic behaviour. The idea of complex modulus provides a relatively simple way to describe damping mathematically and introduces loss factor into the equations. The concepts of both complex modulus and loss factor have been used throughout this thesis. The fractional derivative model is a good alternative in analysing viscoelastic damping. The four-parameter and five-parameter fractional derivative models are further implication of the classic viscoelastic damping model, i.e. the Zener model, and give the impression of how the value of loss factor may change with frequency. The effects of temperature and strain amplitude have also been discussed.

Hysteretic damping models describes some special cases where the loss factor is independent of frequency. The use of this model has been questioned due to the causality problem. This model is of less importance in this research and is only included here for completeness.

Coulomb friction damping is generally used to solve the problem of interface damping where two contact layers have relative motion. It is also of importance in analysing structural damping. As it may quantify losses that occur at the joints between components. The fundamental mechanism it seeks to quantify are also observed when granular materials are used to provide damping.

In analysing a damped system, an equivalent viscous damping model can be used to represent different kinds of common damping mechanisms. The equivalent viscous damping matrix is used so that the total energy loss per cycle does not

change. In addition, the Rayleigh damping model can be used to analysis the modal behaviour of a dynamic system.

Several common damping measurements have been reviewed. The main purpose is to understand the theory behind and to find a parameter that can be used to present damping level. Loss factor is chosen since it has a direct relation to these damping measurements and loss factor is also used in SEA to represent damping mechanisms. SEA is adopted as the main research framework in this study. The concept of SEA and its application will be introduced in the next chapter to show its applicability in solving acoustic transmission problems.

CHAPTER 3 DAMPING EFFECT MODELLING - STATISTICAL ENERGY ANALYSIS

3.1 Introduction of SEA modelling

3.1.1 Origin

Statistical Energy Analysis (referred as SEA) was first developed in the early 1960s to solve vibrational response problems of aerospace structures. Conventional deterministic methods were first adopted to resolve this kind of problem, but due to the constraint of computational speed, the size of the system and the analysable frequency range were limited (Fahy, 1994). The structural response of only a few lower modes could be computed while computation of those modal responses with higher natural frequencies were challenging. To quantify the scale of the challenge, it is was estimated that the number of natural frequencies of the Saturn launch vehicle in the frequency range 0 to 2000 Hz was in the order of 5,000,000 (Fahy, 1994). The desire to estimate the vibroacoustic response of such complex systems in the high frequency range motivated Lyon and his collaborators to develop SEA as an alternative to deterministic approaches (Lyon and Maidanik, 1962; Lyon and Eichler, 1964; Scharton and Lyon, 1968). Later on, SEA has been developed and extended to applications such as building acoustics and been proved to work well in this field (Craik, 1996).

As Fahy (1994) suggested, early studies of sound fields in rooms showed that it would neither by effective nor appropriate to apply deterministic methods to solve broad band vibrational response problems. Instead of estimating a complex system as a concomitant, SEA subdivides a system into several subsystems and expresses the subsystem parameters probabilistically. The time and space averaged vibrational energy of subsystems and vibratory input are used as alternatives to displacements and forces in classic acoustics. Research exploring power flow between oscillators (both single and multiple) and other idealized systems showed that the power flow between two subsystems is proportional to the difference in their modal energy (known as ‘coupling power proportionality’) (Fahy, 1994), which

serves as the firm theoretical foundation of SEA. Thus, the net power flow between two subsystems 1 and 2, $\overline{W}_{12}$, can be given as

$$\overline{W}_{12} = \left[\frac{E_1}{n_1} - \frac{E_2}{n_2}\right] \omega\beta \tag{3-1}$$

where E is the (time-averaged vibrational) energy of subsystem, n is the modal density (the number of modes that lie within 1 Hz or 1 radian band) and β is a measure of the coupling. In SEA, the coupling is reflected by a parameter called the coupling loss factor, CLF, which is defined as the fraction of energy transmitted in one radian cycle. There is a famous consistency relationship describing the relationship between the coupling in the two opposite directions, which can be expressed as

$$\beta = n_1\eta_{12} = n_2\eta_{21} \tag{3-2}$$

where η_{ij} is the CLF from subsystem i to subsystem j.

3.1.2 Limitations of deterministic methods

Although deterministic methods have been demonstrated to work well with simple systems, there exist difficulties to extend their use for analysing more complex models. With the increase in material and geometric model complexity and interested frequency range of interest, the computational cost of deterministic analysis will also increase. Fahy (1994) stated that it is generally impracticable to predict the comprehensive vibrational response of such complex structures at frequencies higher than a few hundred Hertz and gave a study of analysing the vibrational behaviour of a 2m length of aircraft fuselage at frequencies up to 225 Hz using 550,000 degrees of freedom in a finite element model as an example (Roozen, 1992).

With the rapidly development of computational technology, in principle, it is possible to extend deterministic analysis to higher and higher frequency ranges at the expense of higher computational cost. There is, however, a fundamental physical reason that limits their application. The physical and material properties of structures (in this paper, the main concern is buildings) are never known in great

detail. As frequencies increase, the prediction results from deterministic methods become more dependent on small changes in structural details. The results tend to be unreliable as relative modal phase response and the modal resonance frequencies are highly sensitive to the details of damping distribution and boundary conditions, especially for high order modes (Fahy, 1994). Moreover, there is increasing uncertainty as the distributions of the higher order modes begin to overlap (Fahy, 1994). One solution to solve this is to average the modal response over bands, where a statistical approach becomes an appropriate alternative.

3.1.3 Advantages of SEA

SEA uses energy as the primary variable instead of velocity, acceleration, force and pressure, and employs loss factor to represent the concepts of transmission and damping in classic acoustics. It can be seen as an analogy to thermal conduction, where the modal energy of different subsystems are like the temperatures of different bodies and the CLFs are like the conduction coefficients. Use of energy makes the transmission process much clearer and the calculation much simpler. Energy, as the key variable, describes the time-and-space averaged dynamic response of a subsystem, which can be easily converted back to common measures such as pressure and velocity. It enables SEA to incorporate simple classic theories, which are typically analytic and describe transmission between pairs of elements, to simplify the analysis of complex systems (Craik, 1996)

Another benefit of SEA is the concept of statistics. One cannot determine everything about a (building) structure and even structures built to the same design differ from each other. The structural details and material properties are influenced by the workmanship and fabrication processes as well as environmental variances and operational tolerances, such as temperature and static load. This means that even for identical structures, the frequency response of individual specimens will differ from each other. Figure 3-1 shows the standard deviation of ten measurements of airborne sound transmission through ten notionally identical concrete floors and ten measurements of structural transmission between ten notionally identical wall-to-floor systems. In each case, the standard deviation is

about 2 dB and is a bit higher at low frequencies. By introducing the concept of statistics, SEA can give the average response characteristics of a population of grossly similar systems, within which the individual members differ in an unpredictable manner. Therefore, the uncertainty in details can be represented by an assemble-average behaviour. However, this also means that SEA can never give an exact answer to a specific system as the deterministic methods purport to do. Instead, it provides a 'feel' of the averaged response of a population of similar systems and yields an estimated response expressed within a certain confidence interval.

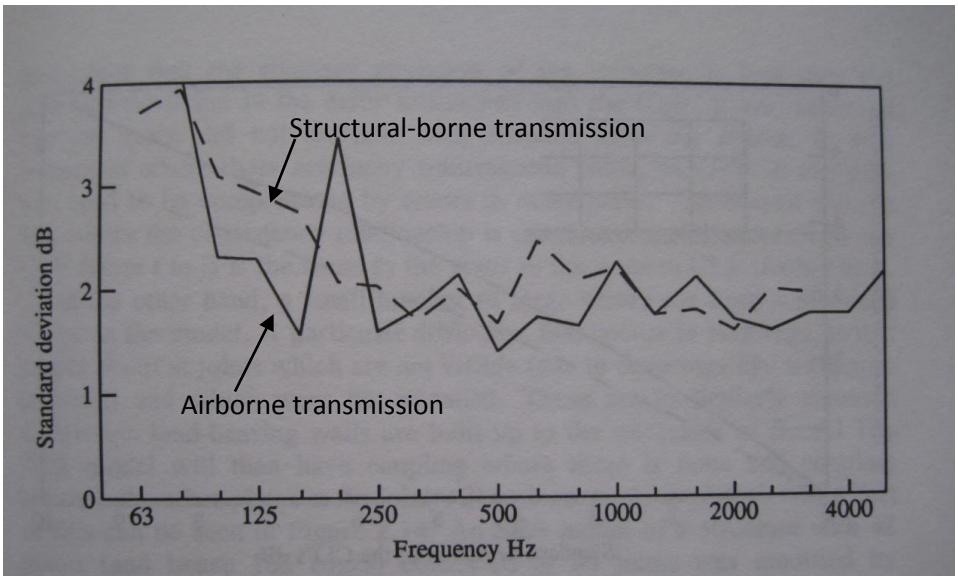

Figure 3-1 Standard deviation of ten measurements of airborne transmission through a concrete floor and ten measurements of structural transmission between a wall and a floor (Craik and Steel, 1989; Craik and Evans, 1989).

Moreover, SEA provides a framework rather than a specific method to solve vibroacoustic problems. Simple classical theory, as well as deterministic methods, can be utilized to determine CLFs. SEA has been shown to function well at high frequencies, where response is dictated by the collective behaviour of many modes. But certain considerations need to be given when applying it to low frequency regions, where individual modes may dominate response. Deterministic methods, such as the finite element method (FEM), can be applied to determine SEA coupling parameters to avoid the low frequency limitation of classic SEA. FEM has been

proved to give a good estimation of CLFs through physical (Simmons, 1991; Fredo, 1997) and numerical (Steel and Craik, 1994; Mace and Shorter, 2000) experiments. Experimental statistical energy analysis (ESEA) can also be conducted as an alternative to determine the CLFs, especially for irregular couplings. A review of such analysis has been done by Cimerman, Bharj and Borello (1997). Research studies that use different analysis methods to predict loss factors have been reported, such as the use of FEM, ESEA and Monte Carlo methods to predict the CLFs for coupled plates with low modal density and low modal overlap (Hopkins, 2002), the use of a hybrid method combining FEM and SEA to model mid-frequency system behaviour (Cotoni, Shorter and Langley, 2007).

SEA requires relatively few gross parameters compared with deterministic methods to predict performance. For any subsystem, apart from the dimensions, three key material properties are needed, namely, the density, elastic modulus (or Young's modulus) and Poisson's ratio. This also makes the computational overhead less costly.

3.1.4 SEA modelling

The basic idea behind SEA is to divide the building into subsystems (usually but not always to represent the physical elements such as walls, floors, ceilings etc. and the rooms they enclose) and assumes the energy only flows from one subsystem to neighbouring subsystems (there are exceptions, such as non-resonant transmission, which will be discussed later). To be more specific, a subsystem is an acoustic space or a structure that consists a group of similar resonant modes (Burroughs, Fischer and Kern, 1997). The proportion of energy transmitted from subsystem i to subsystem j in one radian cycle is called the coupling loss factor (CLF), denoted as η_{ij}. The proportion of energy that is dissipated as heat per radian cycle within subsystem i is called the internal loss factor (ILF), denoted as η_{id}. The sum of the CLFs and the ILF of subsystem i is called the total loss factor (TLF), denoted as η_i, which represents the proportion of the total energy leaving the subsystem per radian cycle

An illustration of a two room system is shown in Figure 3-2. A simple SEA model of part of this system comprising the two rooms, separating wall and two flanking walls is shown in Figure 3-3.

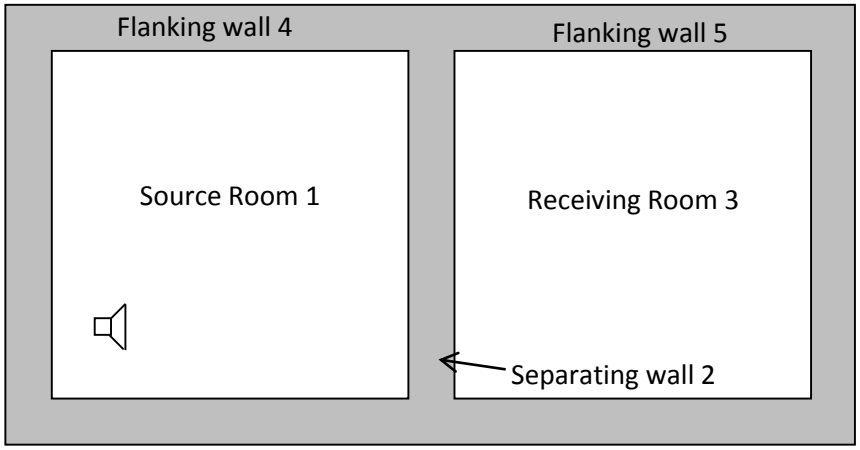

Figure 3-2 Illustration of a two room system

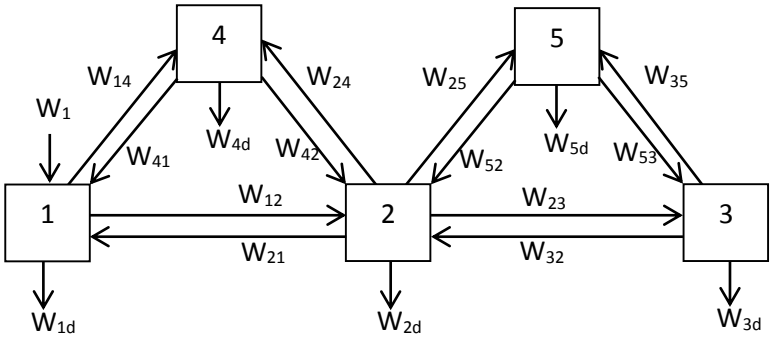

Figure 3-3 SEA model of the system shown in Figure 3-2

Here W_1 denotes energy input of the source room, W_{ij} denotes the energy flow from subsystem i to subsystem j and W_{id} denotes internal energy loss within subsystem i.

These parameters are related through:

$$W_{ij} = E_i \omega \eta_{ij} \tag{3-3}$$

$$W_{id} = E_i \omega \eta_{id} \tag{3-4}$$

where E_i denotes the energy of subsystem i and ω is the angular frequency related to frequency, f, through $\omega = 2\pi f$.

If the whole system is assumed to have attained a state of equilibrium, the energy balance equation for each subsystem, can be combined in matrix form to yield:

$$\begin{bmatrix} -\eta_1 & \eta_{21} & \eta_{31} & \cdots & \eta_{N1} \\ \eta_{12} & -\eta_2 & \eta_{32} & & \\ \eta_{13} & \eta_{23} & -\eta_3 & & \\ \vdots & & \ddots & & \\ \eta_{1N} & & & & -\eta_N \end{bmatrix} \begin{bmatrix} E_1 \\ E_2 \\ E_3 \\ \vdots \\ E_N \end{bmatrix} = \begin{bmatrix} -W_1/\omega \\ -W_2/\omega \\ -W_3/\omega \\ \vdots \\ -W_N/\omega \end{bmatrix} \tag{3-5}$$

All the TLFs and CLFs in the above matrix can be determined either theoretically or experimentally (Craik, 1996). If the external power inputs, W_i, are known, the energy distribution through the system can be determined.

3.2 Assumptions of SEA

In order to understand how to accommodate damping within SEA, it is reasonable to review the core assumptions and limitations of SEA first.

3.2.1 Diffuse fields

The heart of SEA prediction is to evaluate the CLFs between subsystems at their equilibrium states. There are two main approaches that can be used to predict the couplings, namely, the *modal* approach and (propagating) *wave* approach. The *modal* approach is an extension of the examination of energy exchange between two viscously damped, conservatively coupled oscillators under white noise excitation. It assumes that the response of a subsystem, its amplitude of vibration or pressure, is determined by the overall contribution of the different modes (resonances) it sustains. Put more simply, the vibrational energy is stored in modes and these modes dominate the response. In the *wave* approach, the vibrational fields of subsystems are represented by the superpositions of travelling waves. The CLFs are calculated from the consideration of reflection and transmission at subsystem boundaries.

In both cases, a diffuse field is assumed. From the modal approach point of view, the conditions that need to be satisfied are: (i) modes share the same amount of energy within the frequency band (energy equipartition), (ii) momenta and displacement of each mode are statistically independent and (iii) the displacements of different modes are statistically independent within the frequency band (Lyon, 1974). Weaver (2001) supplemented that energy equipartition is only valid for a time-averaged response, not for the response at any fixed time. This assumption also implies that the response of a system is directly proportional to the damping (Craik, 1996). Faller (see Lafont, Totaro and LeBot, 2014 p5) explained the definition of diffuseness from the geometrical acoustics point of view as comprising independent sound waves with the same strength arriving at a receiver from all directions. In other words, a sound field that is homogeneous and isotropic. There are definitions given by other authors in regards to their own perspectives (see Lafont et al., 2014; Fahy, 1985).

Generally speaking, a diffuse field can be achieved if homogenous and weakly coupled subsystems are excited by white noise. The 'rain-on-the-roof excitation' is commonly used as the excitation as it excites all modes of the structure at same level. It can simply be achieved by randomly hitting the structural subsystem with same level (keeping a safe distance away the boundaries).

3.2.2 Weak coupling

Weak coupling is generally assumed in SEA models. Using the simple two-subsystem system in Figure 3-4 as an example, the energy balance equation of subsystem 2 is given by:

$$E_1\omega\eta_{12} = E_2\omega\eta_{21} + E_2\omega\eta_{2\mathrm{d}} \tag{3-6}$$

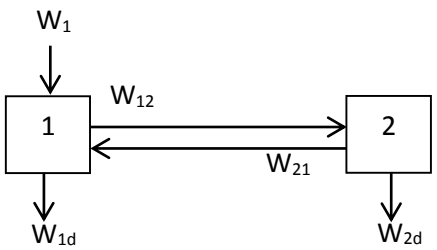

Figure 3-4 a two-subsystem SEA model

The energy ratio can thus be expressed as:

$$\frac{E_2}{E_1} = \frac{\eta_{12}}{\eta_{21} + \eta_{2d}} \tag{3-7}$$

As the coupling becomes large compared to the internal loss (material damping), the term η_{2d} can be ignored and the energy ratio becomes:

$$\frac{E_2}{E_1} = \frac{\eta_{12}}{\eta_{21}} \tag{3-8}$$

Recalling Equation 3-1 and 3-2, this gives the net power flow to be:

$$\overline{W}_{12} = E_1\eta_{12} - E_2\eta_{21} = 0 \tag{3-9}$$

There is thus no net power flow between two subsystems, indicating equipartition of modal energy between two subsystems (both subsystems share the same modal energy). This also means one may combine those two subsystems into one subsystem.

Mace (1994) gave a definition of weak coupling as occurring when the power flow via any individual coupling is small compared with the input power. It might be easier to understand if one expresses the definition in terms of loss factors. According to Smith's (1979) definition of strong coupling, the reverse gives one possible definition of weak coupling as:

$$\eta_{21} < \eta_{2d} \tag{3-10}$$

Instances where this relation is obeyed are not likely to be rare. Exceptions occur for simple structures such as the case where two undamped metal plates are coupled at a corner joint. In real buildings, each subsystem is connected to several other subsystems. These couplings need to be added with the subsystem's ILF as they also represent energy that leaves to the subsystem. This is the notion of the Total Loss Factor (TLF). As Craik (1996) suggested, a wall (or a floor) will approximately connected to ten other structural elements. Thus the effective

subsystem loss factor, its TLF, is at least ten times larger than the CLF between any single pair of subsystems, assuming all structural CLFs have roughly same value. Therefore, weak coupling is a reasonable assumption in practice for all but the simplest of systems.

3.3 Limitations of SEA

3.3.1 Mode count and modal overlap

Modes (resonances) occur when a wave travels around the subsystem and arrives back at its starting point with same direction and is in phase with itself so that cumulative interference happens. SEA presumes the response of a subsystem is only controlled by these modes. Since the frequency response of individual mode is controlled by damping, they are also referred as 'damping-controlled'. Knowledge of how many modes is present in a frequency band and to what extent the subsystem is damping-controlled is of interest if one wishes to understand the energy in a subsystem or its distribution within a system.

The number of modes in a band is known as the mode count and can be expressed as:

$$N = n(f)\Delta f \tag{3-11}$$

where $n(f)$ is the modal density in a band with the centre frequency of f and Δf is 0.23 times the centre frequency f for a 1/3 octave band and 0.707 times the centre frequency f for an octave band. Fahy and Mohammed (1992) suggested that, for plates, at least 5 modes need to be guaranteed to lie in the frequency band for the SEA modelling to work appropriately.

The extent to which a subsystem is damping controlled is referred as the modal overlap, M. A more specific definition can be given as the ratio of the modal bandwidth (either the half-power bandwidth or the effective bandwidth which is $\pi/2$ times higher) to the average frequency spacing between modes (Craik, 1996). This gives the modal overlap (using the half-power bandwidth) to be:

$$M = f\eta n \tag{3-12}$$

Both computational (Fahy and Mohammed, 1992; Davies and Wahab, 1981) and physical (Clarkson and Ranky, 1984) experiments on plates and beams indicated that the modal overlap factors (M) have to be equal or larger than 1 for the CLFs in SEA to be approximated using wave theory (Hopkins, 2002).

Hopkins (2002) suggested, the general conditions for SEA wave theory to be '*appropriate*' for plates are $M \geq 1$ and $N \geq 5$. However, Craik (1996) argued that for building structures, typically masonry walls, two modes are sufficient to give a modal overlap of 1 (see the predicted mode count and modal overlap for a $4m \times 2.5m \times 100mm$ wall in Figure 3-5). Therefore, one may propose that there should be a mode count of at least 2 for masonry type structures to work properly under an SEA framework.

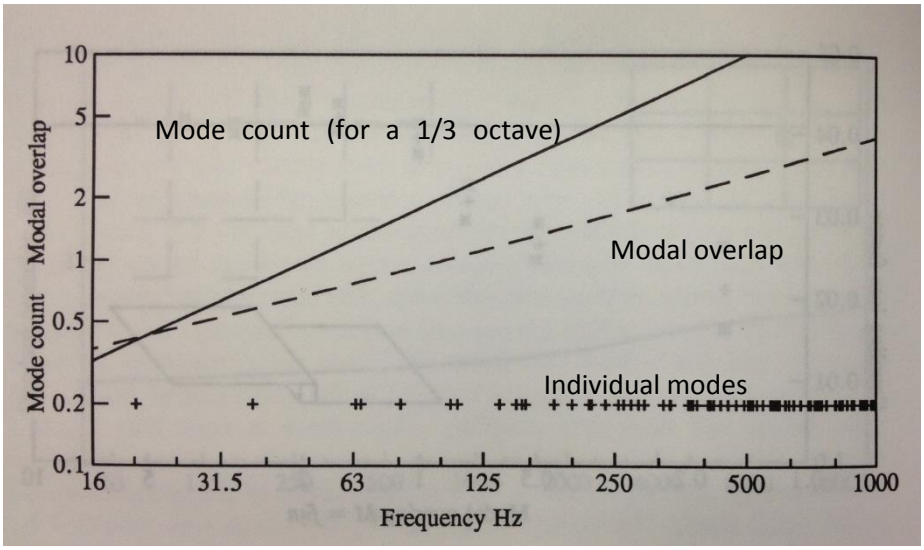

Figure 3-5 The predicted mode count and modal overlap of a $4 \times 2.5m \times 100mm$ wall with a longitudinal wavespeed of 2000 m/s and a total loss factor of $f^{-1/2} + 0.015$ (Craik, 1996)

3.3.2 Non-resonant transmission

Standard SEA modelling only concerns resonant transmission in which the system is damping-controlled. However, there are cases where the energy in subsystems is not proportional to the damping (see Figure 3-6).

When a source excites a subsystem (either a room or a wall), there exists a direct field which exists prior to the travelling wave undergoing any reflections.

Each time the distance is doubled, a direct sound field will decrease 6dB in room subsystems or 3dB in plate subsystems. The result of direct fields is to introduce a localized excitation in the subsystems (Craik, 1996), i.e. if a noise source is placed on the floor, the floor will be excited more than the walls or ceiling.

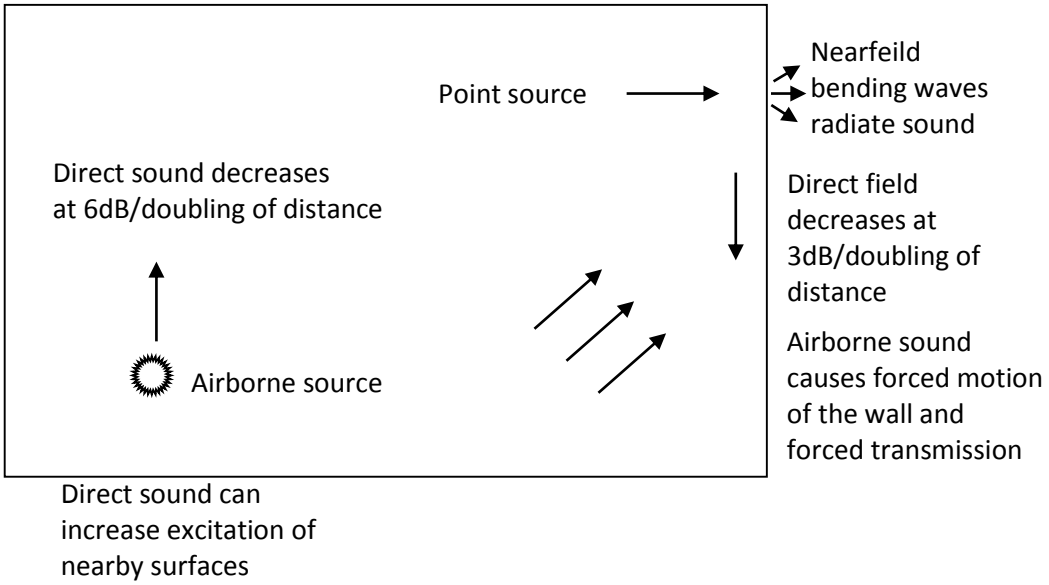

Figure 3-6 A room with an airborne source and a point source exciting a wall showing examples of non-resonant response and non-resonant transmission (after Craik, 1996)

If a plate (or a beam) is excited by a source, two types of bending waves are excited, namely travelling waves, which transfer the energy away from the source and lead to a direct and reverberant fields, and nearfield bending waves, which are controlled by the discontinuities and local disturbances. The nearfeild bending waves radiate sound below critical frequency (the frequency where the wavespeed of the plate and the air are the same) and are of importance when the damping is high as the plate will be poor radiator under these conditions (Craik, 1996).

When airborne source excites a plate subsystem, if the incident waves are below critical frequency, forced response occurs. This response is largely independent of the damping (an example is shown by Fahy, 1985) and is relatively important since the resonant modes of the plate are poor radiators below critical frequency. The non-resonant transmission coefficient of such motion is given by Leppington, Heron, Broadbent and Mead (1987) as:

$$\tau = \left[\frac{\rho_0 c_0}{\pi f \rho_s \left(1 - f^2/{f_c}^2\right)}\right]^2 \left\{\ln\left(\frac{2\pi f\sqrt{S}}{c_0}\right) + 0.160 + U\left(l_x, l_y\right) + \frac{1}{4\mu^6}\left[(2\mu^2 - 1)(\mu^2 + 1)^2 \ln(\mu^2 - 1) + (2\mu^2 + 1)(\mu^2 - 1)^2 \ln(\mu^2 + 1) - 4\mu^2 - 8\mu^2 \ln(\mu)\right]\right\} \quad (3\text{-}13)$$

where $U\left(l_x, l_y\right)$ is a function of shape and can be ignored for normal shaped structures (where $0.1 < l_x/l_y < 10$) and $\mu = (f_c/f)^{1/2}$. This can be used to derive a non-resonant CLF. Approximations to this equation are widely used when modelling building structures. For forced waves at normal incidence on an infinite plate, Beranek and Ver (1992) gave an approximation of the sound reduction index, R_0, as

$$R_0 = 10 \log\left[1 + \left(\frac{2\pi f \rho_s}{2\rho_0 c_0}\right)^2\right] \approx 20 \log\frac{2\pi f \rho_s}{2\rho_0 c_0} = 20 \log f\rho_s - 42 \quad (3\text{-}14)$$

These approximations need to be used with caution since they are widely misused as argued by Craik (1996).

Non-resonant transmission can usually be modelled by introducing either '*direct coupling between two resonant subsystems bypassing the physical element through which the sound is passing non-resonantly*' or '*additional noise sources*' as Craik (1996) suggested. It is particularly important to predict non-resonant transmission through systems that consist of light structural panels (Renji and Nair, 2001) or double walls (Craik, 2003). Recent study used a Statistical modal Energy distribution Analysis (SmEdA) as an alternative to model non-resonant transmission by the use of the dual modal formulation (Maxit, Ege and Totaro, 2014).

3.3.3 Non-conservative coupling

Classical SEA assumes that couplings between subsystems are conservative, which means there is no energy dissipation at the structural joints. This is, however, not always the case in real structures. Early study done by Gaul (1983) showed that on occasion there is an unavoidable energy dissipation at joints, which dissipate more energy than internal damping (material damping or structural damping). Fahy

and Yao (1987) analysed the power flow between two non-conservatively coupled oscillators and stated that the energy flows depend on both the time-averaged energy difference and the absolute time-averaged energy value of individual oscillator, and that the coupling damping plays an important part in controlling the energy of the directly driven subsystem if it is in the same order of structural damping. Sun, Lalor and Richards (1987) showed that the coupling damping increases the effective internal loss factors of subsystems and suggested a method to modify the SEA energy balance matrix to accommodate this effect. They also extended this analysis to two coupled continuous structures and argued that the effect of the coupling damping on the power flow in such systems is negligible. Chen and Soong (1991) showed that for non-conservatively coupled oscillators, the energy flow from the driven to the undriven oscillators may be increased by the coupling damping, especially when those two oscillators have different resonant frequencies. Beshara and Keane (1996) proposed to modify the main SEA energy balance equation by introducing the 'coupling damping loss factor', which represents the relation between the energy dissipated at the joints and the subsystem energy levels. Sheng, Wang and Sun, (1998) also recommended to include the coupling loss, however, they argued that the coupling damping is not only an additional item which increases the ILFs of subsystems, it also effects the CLFs. Baldanzini et al. (2003) proposed a hybrid numerical-experimental method to characterise non-conservative coupling and included the energy transmission loss within the couplings in SEA models.

3.3.4 Large subsystems

In standard SEA modelling, the energy in any given subsystem is assumed to be uniformly distributed. However, as the damping of subsystems get higher or as the wavelength of waves propagating within a structure goes shorter (the latter situation can be alternatively viewed as the structure growing large relative to the wavelength of the waves propagating across it), this hypothesis is increasingly violated. The attenuation with distance from a source can be so large that there comes a point where one building element cannot be modelled as a single

subsystem. It would be worthwhile to have an insight of the problems in large subsystems before discussing heavily damped subsystems.

Craik (1996) discussed the nonuniformity of a large brick wall and the space in long corridor. A $8.8m \times 4.7m \times 110mm$ external brick leaf of a cavity wall was subdivided into four parts. There were couplings at the wall ties that connected the external and internal partition and at the connection between the wall and the foundation. Attenuation between four parts was measured and the results are shown in Figure 3-7. These suggest the attenuation between different parts of the wall is between 1 and 3dB and suggest that modelling the wall as a single subsystem may not be appropriate. This runs counter to the conventional way of defining subsystems, i.e. there are no obvious boundaries or discontinuities. Similar situations happen in long corridors. One may treat the corridor as a one-dimensional system and subdivide it into n parts where n can be determined by controlling the attenuation between subsystems to be less than 5 dB as suggested by Craik (1996).

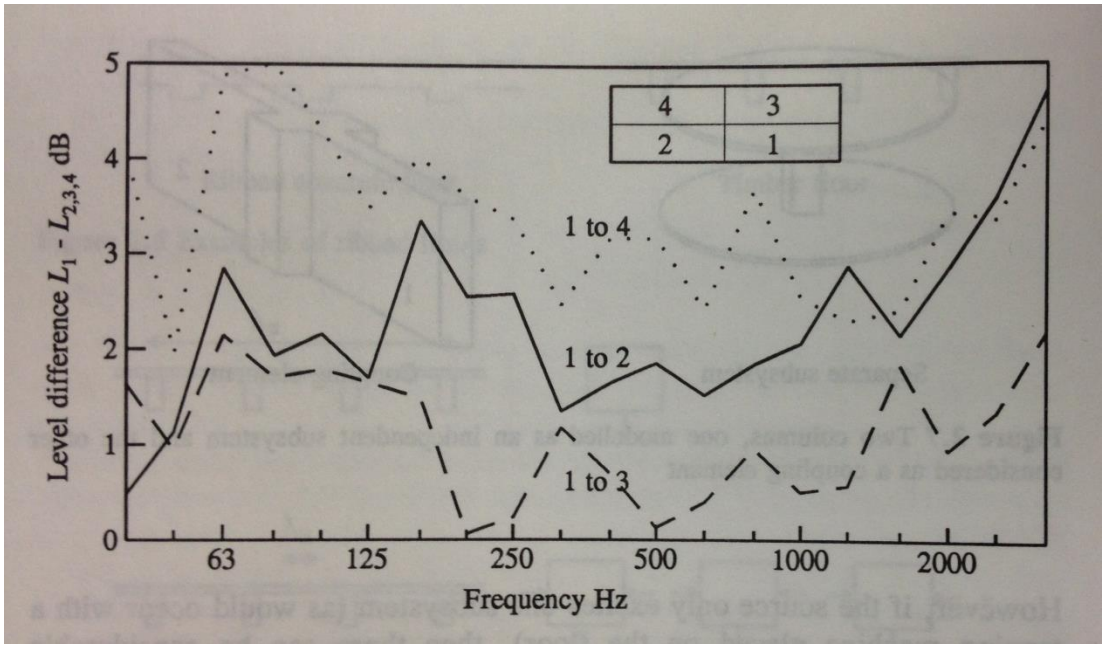

Figure 3-7 A 8.8m×4.7m×110mm brick wall was artificially subdivided into four parts and attenuation between the parts measured, a structural source excited part 1 (Courtesy of the Building Research Establishment)

3.3.5 Heavy damping

In terms of heavily damped subsystem, similar problems occur. There is little in the literature that deals directly with this kind of problem. One may utilize the technique used in analysing long corridor to subdivide one element into several subsystems. However, one may question what the general standard is. Can the attenuation go higher or lower than 5 dB?

Cremer, Heckl and Ungar (1988) gave an expression of the energy level attenuation per metre for a highly (but not extremely) damped beam as:

$$D^{'} = \frac{13.6\eta}{\lambda_B} \tag{3-15}$$

where $D^{'}$is the energy level difference per meter and λ_B is the bending wavelength at frequency f. Increasing the internal loss and decreasing the bending wavelength both result in more significant energy attenuation with distance. There comes a point (for line and point sources of excitation) where there will be significant attenuation across the structural element and it would be necessary to question whether it is truly a modal component anymore. A more sophisticated method is proposed in Chapter 5, which uses the technique of Ray Tracing to analyse the energy transmission across a subsystem even when it is not modal.

3.4 Discussion and conclusion

This chapter sought to introduce the concept of SEA modelling and the assumptions and limitations of it.

SEA is found to have advantages in modelling acoustic transmission within complex building structures. SEA framework can be used to explore the potential benefit of applying damping treatments to structural elements by simply change the ILFs of subsystems. This will be explored in Chapter 4.

Knowledge of the assumptions and limitations of SEA enables one to determine whether it is appropriate to use SEA modelling. One interesting finding is that the growth of internal loss and decrease of the wavelength (increase of the frequency) result in a more significant energy attenuation with distance. This is likely to happen

in subsystems with high internal damping or relatively large dimensions. There exists a penitential point where the attenuation becomes so significant that the energy is no longer evenly distributed within such subsystems (i.e. subsystems are no longer modal). SEA tends to fail in modelling such subsystems. An alternative approach using ray tracing technique is proposed to model these subsystems in Chapter 5.

CHAPTER 4 GLOBAL DAMPING

4.1 Introduction

This chapter aims to examine how acoustic transmission will be influenced by adding damping to structural elements in building. Different kinds of sound transmission paths will be introduced first. The concepts of path counts and path attenuation will be introduced to help understand sound transmission. Both bending-only and three-wave models will be presented to show the systematic damping effects on sound insulation.

4.2 Sound transmission path

In order to analyse the global damping effect, one needs to understand the various sound transmission paths it can support on a complete structure such as a building. Sound transmission in buildings occurs via two kinds of paths, namely the direct path and flanking paths as indicated in Figure 1-1. The direct path is usually the shortest path between the source and receiver while the flanking paths are longer and more numerous. The presence of flanking transmission has long been known. Craik (2001) used Statistical Energy Analysis (SEA) to explore the contribution of flanking transmission and indicated that the sound pressure level difference between the direct path and all paths (including direct path and flanking paths) of two neighbouring rooms could be over 10 dB in some theoretical cases. EN 12354 (ISO 15712-1) is commonly adopted to predict the airborne sound transmission between two adjacent rooms. This uses theoretical or measured flanking sound reduction indices to predict the contribution of flanking transmission. However, it has been shown that EN 12354 (ISO 15712-1) is equivalent to an SEA model that considers only first order flanking paths. As it does not include longer flanking transmission paths, it results in an overestimation of sound insulation (Galbrun, 2008). The term ‘long flanking path’ here does not necessarily mean that the source room and the receiving room are physically far apart or separated by numerous building elements. These paths can also be present between neighbouring rooms where transmission takes place back and forth on multiple occasions between flanking elements before emerging into the receiving room.

Several attempts have been made to analysis the transmission paths. Magrans (1993) systematized the concept of transmission paths, its classification and its numerical treatment under the framework of SEA modelling. Guasch and Aragones (2011) treated the problem of ranking dominant transmission paths as a variation of the so-called K shortest path problem in graph theory and proposed a modified method to find the dominant paths in an SEA model. Bussöw and Peterson (2007) proposed a sensitivity factor to present the sensitivity of the energy transmission to a certain coupling loss factor in a specific path. Craik (1996) also conducted theoretical analysis on paths of different order and examines the possible effect of increasing the path order. However, these studies did not examine the potential benefit of reducing the transmission contribution along these dominant paths.

Conventional sound insulation strategies tend to focus on separating walls and floors protecting noise sensitive spaces and seek to manipulate material properties and configurations to control the sound transmission via the direct path. There is, however, the potential to achieve improvements in sound insulation by applying damping to building elements as each time vibration is transmitted through a structural element, a proportion of the energy will be converted into heat. As a path gets longer, i.e. the number of transitions between elements increases, the effect grows larger. In other words, the benefit of applying internal damping is more effective in controlling individual long flanking paths than the direct path. The extent to which this strategy is effective, therefore, is dependent on the contribution the ensemble of flanking paths make relative to the direct path.

4.3 Proximal systems

This section seeks to present several practical-meaningful SEA models to simulate the effects of damping application in real buildings.

Nine different building designs were studied as shown in Figure 4-1. These designs are similar to those explored by Craik (2001) and the dimensions and material properties of the elements comprising the systems are given in Table 4-1. Damping benefit was studied by changing the value of all structural ILFs. Influence about the damping effect on paths with different length was also studied. These

models are representative of typical masonry constructions. Simple building fabric is used here for simplicity because its property is well examined. The hatched rooms are the source room and the receiving rooms. The relative positions of these two rooms have been kept constant and more structure has been added to each successive model to provide more routes for flanking paths.

The SEA models were built and analysed in the Parallel Programmable Calculator (PPC) written by Craik (2011). It is a general purpose software for acoustic and statistical energy analysis. A script was developed to create the models (see Appendix 1). By simply defining the numbers of rooms in three perpendicular directions and specifying the properties of the rooms and the structural elements, the script can easily create an SEA model within a few minutes. This saves a lot of time when creating new models with different properties.

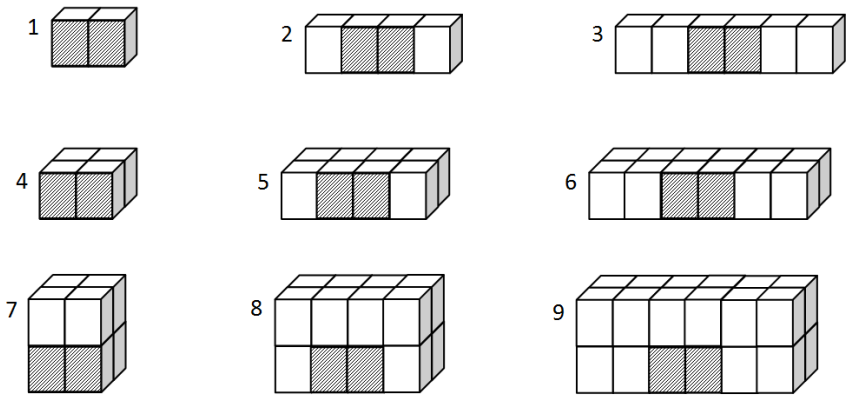

Figure 4-1 Nine different building designs ranging from a simple 2-room system to a 24-room system

Table 4-1 Dimensions and material properties used in numerical models

Element	Rooms	Common wall	Other walls	Floors
Dimensions (m)	3 x 4 x 2.5	3 x 2.5	3 or 4 x 2.5	3 x 4
Thickness (m)		0.2	0.1	0.15
Density (kg/m^3)		2000	2000	2300
Longitudinal wavespeed (m/s)		2000	2000	3400
Critical frequency (Hz)		162	324	127
Poisson's ratio		0.2	0.2	0.2
Initial internal loss factor		0.015	0.015	0.015
Reverberation time (s)	0.5			

4.4 Wave types

The focus of the analysis is on structural behaviour rather than transmission through air. It is important therefore to understand the different wave types structural elements can support. There are three types of vibrational waves, namely bending waves, transverse waves and longitudinal waves. The first type exhibits significant out of plane displacement. It can thus excite wave motion in any fluids that surround it and the resulting airborne noise is of great importance in building acoustics. The latter two are both in-plane waves (i.e. the particle motion occurs perpendicular to or in the same direction as wave propagation). As such they do not generally result in significant excitation of any surrounding fluids and so do not directly relate to noise generation (one might argue that transverse wave may also contribute to noise generation if the particle moves perpendicular to the plate surface). However, in-plane waves can excite bending waves at the junctions between structural elements and vice versa. In SEA, if in-plane waves are introduced in the transmission, normally two additional subsystems are generated for each structural element to represent the energy stored in each wave type and the transmission that takes place between each. This greatly increases the complexity of the system (Craik, 1996).

For normal size buildings with common material properties, the floors and walls can barely support many (in some cases any) in-plane modes at low frequency region (Craik, 2001). The mode count in each frequency band provides a means of quantifying this effect and can be calculated through:

$$N = n(f)\Delta f \tag{4-1}$$

where the modal density is:

$$n(f) = \frac{2\pi f S}{c^2}(inplane\ wave) \tag{4-2}$$

$$n(f) = \frac{\sqrt{3}S}{hc_L}(bending\ wave) \tag{4-3}$$

Here, c is the longitudinal or transverse wave speed depending on which type of waves is of interest.

If one considers a typical masonry type of construction (the dimension and material properties is the same as the floor in Table 4-1). The calculation shows that the mode count in each 1/3 octave band is larger than unity for bending wave above 125Hz (630Hz for transverse waves and 1000Hz for longitudinal waves). When the frequency band exceeds 2000Hz, all of the wave types have at least 5 modes in each frequency band, which satisfies the requirement for SEA to work properly as suggested by Fahy and Mohammed (1992), and Hopkins (2002). Therefore, it is reasonable to model a typical masonry building with bending-only model at low and mid frequencies (i.e. frequency below 1000Hz) and to use a three-wave model to give a good estimation at high frequencies (i.e. frequency above 2000Hz). A bending-only model will be examined first and followed by three-wave model to understand behaviour at high frequency.

4.5 Bending only model

A bending-only model will be used to examine the global damping effect in this section. Before discussing the damping effect on path attenuation, it is worth looking at how the number of paths may be quantified, how the attenuation of paths may be predicted and how this information in combination may be used to predict transmission.

4.5.1 Path counting

The number of paths of any given length involved in sound transmission between two subsystems is related to the complexity of the system. Knowing the number of paths of a given order can aid understanding of the contribution they, as an ensemble, make to flanking. There is an accumulative graphical method to count the number of paths of given order. Referring to Figure 1-1, the energy transmitted from subsystem 1 to subsystem 3 can follow Path 1-2-3, Path 1-4-2-3, Path 1-4-2-5-3, Path 1-4-2-4-2-3, etc. The number of paths that end in subsystem 3 having undergone 5 transmission steps between subsystems must equal the number of paths that end in subsystem 2 having undergone 4 transmission steps plus the

number of paths that end in subsystem 5 having undergone 4 transmission steps. Generally speaking, the number of paths that end in subsystem i must equal the sum of paths for all subsystems that are connected to it. This can be presented mathematically as (Craik, 1996):

$$N(m)_i = \sum_j N(m-1)_j \delta_{ji} \tag{4-4}$$

where $N(m)_i$ is the number of paths that pass through m subsystems and end in subsystem i and δ_{ji} is 1 if subsystem i and subsystem j are connected, otherwise it is 0. Using this method, it is possible to calculate the number of paths as a function of path length for each system with associated bounding structural elements as shown in Table 4-2 or graphically in Figure 4-2. Paths that involve the receiving room more than once, e.g. Path 1-2-3-2-3, are included in the results. It may be seen that the number of paths tends to grow in a logarithmic-like manner with increasing path order and a more complex system tends to have relatively larger number of paths than a simpler system as the path order grows.

Expressing the growth in number of paths in decibels for paths with maximum 8 subsystems (Table 4-3), those of low order may be seen to initially grow at around 10dB and then at 8dB thereafter for Design 1. For Design 9, the most complex design, the number of paths grows at an average rate of 9.6dB. Path growth has been expressed in dB (assuming a reference value of 1) here to assist in the discussion presented in Section 4.5.3, which explores its influence on power transmission.

Table 4-2 Number of paths between the source room and the receiving room (bending only)

	Subsystems in a path					
Design	3	4	5	6	7	8
1	1	12	86	560	3476	21088
2	1	12	86	592	4037	27476
3	1	12	86	592	4037	27508
4	1	12	90	672	4894	36032
5	1	12	90	704	5479	43852
6	1	12	90	704	5479	43884
7	1	12	94	784	6464	54968
8	1	12	94	816	7073	64220
9	1	12	94	816	7013	64252

Table 4-3 Growth in number of paths of nine different designs (dB)

	Subsystems in a path					
Design	3	4	5	6	7	8
1	10.8	8.6	8.1	7.9	7.8	
2	10.8	8.6	8.4	8.3	8.3	
3	10.8	8.6	8.4	8.3	8.3	
4	10.8	8.8	8.7	8.6	8.7	
5	10.8	8.8	8.9	8.9	9.0	
6	10.8	8.8	8.9	8.9	9.0	
7	10.8	8.9	9.2	9.2	9.3	
8	10.8	8.9	9.4	9.4	9.6	
9	10.8	8.9	9.4	9.3	9.6	

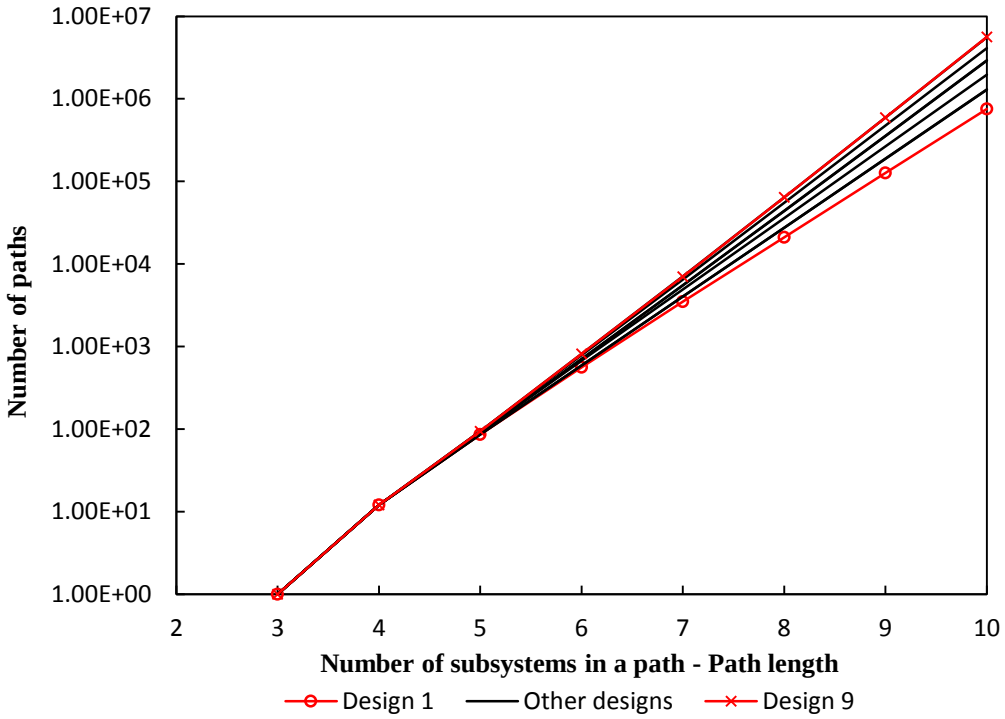

Figure 4-2 The number of paths against length of a path for nine different designs

4.5.2 Path attenuation

As sound energy progresses along a typical path, energy attenuation occurs. The energy attenuation for a typical path 1-2-3…m can be presented as (Craik, 1996):

$$D_{1-2-3-4\ldots m} = 10\log\frac{E_1}{E_m} = 10\log\frac{\eta_2\eta_3\eta_4\ldots\eta_m}{\eta_{12}\eta_{23}\eta_{34}\ldots\eta_{(m-1)m}} \tag{4-5}$$

Each time an added subsystem is involved in the path, the level difference will increase by:

$$\Delta = 10\log\frac{\eta_j}{\eta_{ij}} \tag{4-6}$$

Since the TLF of a subsystem is always larger than any single CLF, as path length grows, path strength diminishes. The TLF of a structural subsystem may be approximated by (Craik, 1996):

$$\eta_j = f^{-0.5} + \eta_{jd} \tag{4-7}$$

where f is frequency and η_{jd} represents the ILF. This expression assumes that structural subsystems are connected to around 10 similar structures, in which case the sum of the CLFs can be approximated by $f^{-0.5}$. For masonry structures, the ILF is relatively small and often taken to be 0.015, as Craik (1996) suggested. The sound insulation provided by a structure may thus be seen to be related directly to the structural damping and inversely to the strength of the structural coupling. If it is assumed that the internal damping of structural components may be increased without significantly affecting structural coupling (i.e. the ILF increases from η_{jd} to η'_{jd}, while leaving the coupling unaltered), in response, the TLF of the structural subsystem changes from η_T to η'_T. This description of path attenuation makes it possible to estimate the effects of adding damping without the need to build complex SEA model.

If one assumes that all structural CLFs in the system are the same, all structural subsystems have the same TLF and all the rooms have the same TLF, Equation 4-5 can be simplified to:

$$D_{1-2-3\ldots m} = 10\log\left(\left(\frac{\eta_T}{\eta_C}\right)^{m-a}\left(\frac{\eta_{Tr}}{\eta_C}\right)^{a-1}\right) \tag{4-8}$$

Here η_C is the CLF between two neighbouring structural subsystems and η_{Tr} is the TLF of a room, which is assumed to be the receiving subsystem in this path. In this expression, a is the number of times that rooms appear as subsystems in this path.

If one is looking at the path attenuation between two rooms, one may notice that in most cases the structural paths appear $\mathrm{m}-2$ times and a room always appears at the end of the path. There are exceptions such as the initial transmission from source room to structure and where transmission occurs on multiple occasions between the structure and the other room in the system. It is assumed, however, that these are few in number compared with the total (15% of total paths for Design 1 and 13% of total paths for Design 9 for paths up to 6 subsystems). The TLF of room will stay unchanged when we increase the structural ILFs. Equation 4-7

and Equation 4-8 may be used to estimate the change in the attenuation of any given structural path as a result of increasing ILF from η_{jd} to η'_{jd}, through:

$$\Delta D_{1-2-3\ldots m} = 10\log\left(\left(\frac{\eta_T{}'}{\eta_C}\right)^{m-a}\left(\frac{\eta_{Tr}}{\eta_C}\right)^{a-1}\right) - 10\log\left(\left(\frac{\eta_T}{\eta_C}\right)^{m-a}\left(\frac{\eta_{Tr}}{\eta_C}\right)^{a-1}\right) = 10\log\left(\frac{1+\eta_{id}{}'\sqrt{f}}{1+\eta_{id}\sqrt{f}}\right)^{m-a} \quad (4\text{-}9)$$

This equation, coupled with knowledge of the number of paths of any given length, offers a simple prediction of the improvement in performance for a specific path order without running a full SEA model. This will be explored in Section 4.5.4 and 4.6.

4.5.3 Damping effect on path attenuation

There are two mechanisms by which damping can influence the attenuation of transmission paths. The first is that predicted by Equation 4-6 and describes the effect observed when incrementing the order of a path. The second is that predicted by Equation 4-9 and describes the influence damping has on the chain of steps that make up a transmission path of given order. To help understand the likely change in path strength in response to changes in damping, behaviour will be explored for estimates of TLF made using Equation 4-7 with ILF equal to 0.015 and 0.120. The value of 0.015 is the common ILF for concrete structures (Craik, 1996) while the value of 0.120 is believed to be achievable since sand used as a granular damping layer can yield a loss factor of around 0.1 and the maximum loss factor for constrained-layer damping is of the order of 0.4 as suggested by Cremer, Heckl and Ungar (1988). The discussion about the theoretical ILF achievable using passive damping treatment is discussed in Chapter 6 and the practical value one can get in the lab is shown in Chapter 8. The predicted TLFs associated with these two values of ILF are shown in Figure 4-3. The data are extended down to low frequency and up to high frequency in order to illustrate behaviour at the extremes rather than to suggest the applicability of SEA in these regions.

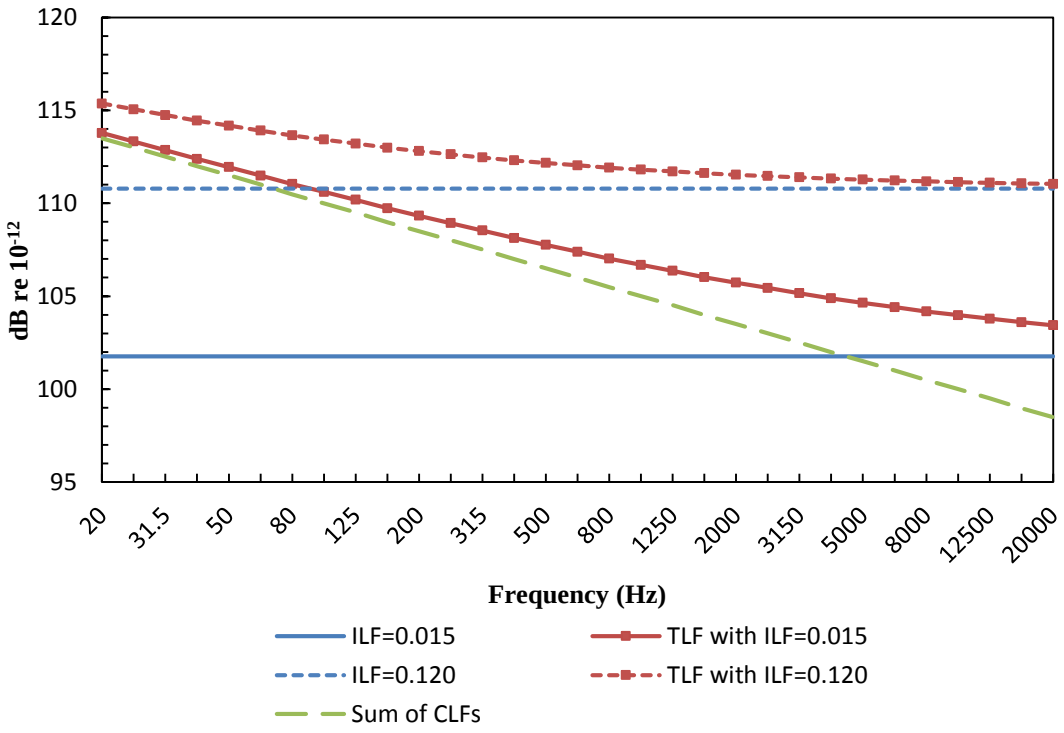

Figure 4-3 The predicted TLFs associated with ILF equal to 0.015 and 0.120

It may be seen that in structures where typical levels of internal damping are present, i.e. where the $\mathrm{ILF} = 0.015$, the CLFs are responsible for the majority of subsystem losses at low and mid frequencies. Given that Equation 4-7 assumes a subsystem is connected to around 10 neighbours, i.e. η_{ij} is approximately $0.1f^{-0.5}$, the increase in attenuation it predicts should be around 10dB for every increase in the order of a path in these frequency regions. In terms of the relative balance between growth in path numbers as path order increases, which initially grow at around 10dB as discussed in Section 5.1, and the reduction in path strength with increasing path length, this would suggest that for families of lower order paths at least, the contributions made by each would be similar, i.e. as path order increases, path numbers increase by around 10dB but path strength decreases by around 10 dB so there is little net change in transmission. For higher order paths, path numbers increase by less than 10 dB (as indicated in Figure 4-2) while path strength still decreases by around 10 dB so the overall contribution for higher order paths becomes increasingly insignificant as path order grows.

If the ILF is increased to the point where it dominates the TLF, Equation 4-6 predicts attenuation increases in excess of 10 dB and for the case where the ILF = 0.120, this can be seen in Figure 4-3 to occur across the entire frequency range. Given the sensitivity of longer paths to TLF and the fact that path numbers will be unaffected by changes to damping, it might be expected that as ILF increases, flanking paths become increasingly attenuated and transmission would increasingly be dominated by the direct path.

For the case where the behaviour of a family of paths of a given order is of interest, Equation 4-9 suggests that at frequencies where internal losses dominate, there will be an increase of 3 dB in level difference each time ILF is doubled. At lower frequencies, where coupling losses dominate, increases in level difference will be observed but by less than 3dB.

4.5.4 Results and discussion

This section uses nine different systems (Figure 4-1) to explore the influence of damping on flanking transmission. The source room is assumed to have constant noise input. Prediction of the energy level distribution within each system has been made by solving the energy balance equations for several values of structural internal loss factor. The TLF of each subsystem is determined by adding its CLFs and ILF.

The effect of increasing ILF on airborne level difference is first explored for the two room system (Figure 4-1 Design 1). Figure 4-4 indicates that adding damping to building elements can lead to reasonable improvements in sound insulation

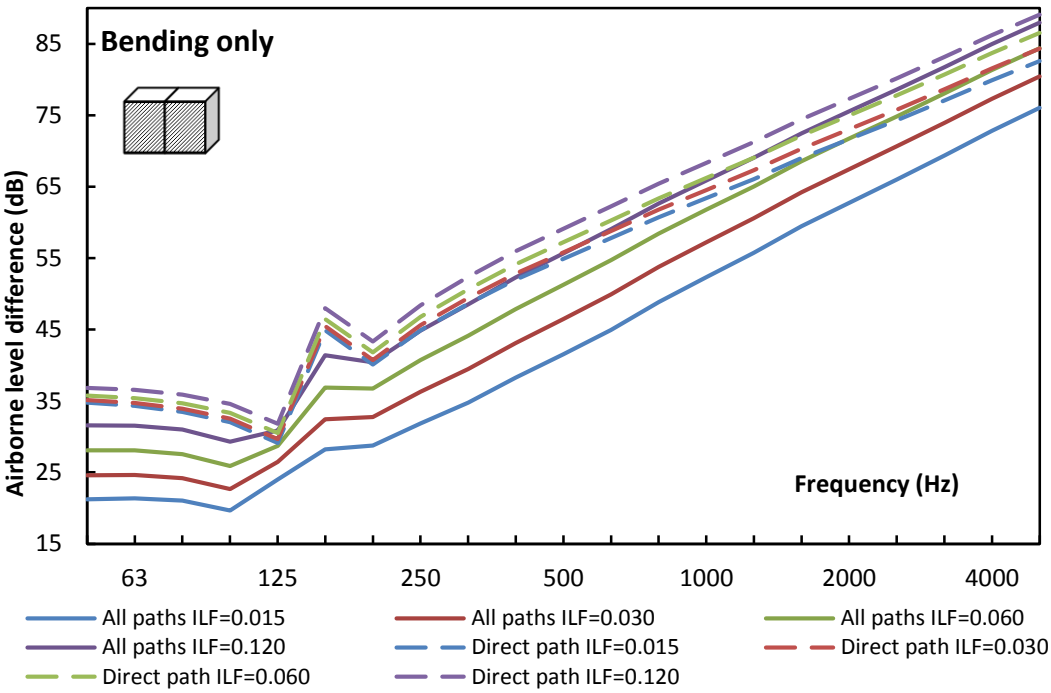

Figure 4-4 Airborne level difference between the source and receiving room with different structural ILFs – Design 1 (Bending only)

An increase in sound insulation of around 15dB can be achieved by increasing the ILFs from 0.015 to 0.120. As the transmission of the flanking paths starts to grow weaker than the direct path with continued addition of damping, the strategy would begin to exhibit diminishing returns, i.e. transmission would be controlled by the direct path. It can be seen that initial applications of damping yield greater improvements in performance than subsequent ones. As the damping level gets higher, although the transmission through direct path decreases, its relative significance increases because other flanking paths are more sensitive to changes in damping.

Figure 4-5 illustrates the benefit of increasing ILF from 0.015 to 0.120 for all nine designs. It can be seen that a more complex design has slightly better sound insulation than a simpler one and the benefit of applying damping is slightly more significant for simpler designs. This is because for the large model there is more structure for sound to travel into and be attenuated before arriving in the receiving room. The attenuation of longer paths increases, leaving transmission via shorter

paths to assume increasing dominance. These in effect are the paths that occur via subsystems close to the source and receiving rooms and as a consequence the behaviour of the large model begins to mirror that of the smaller ones.

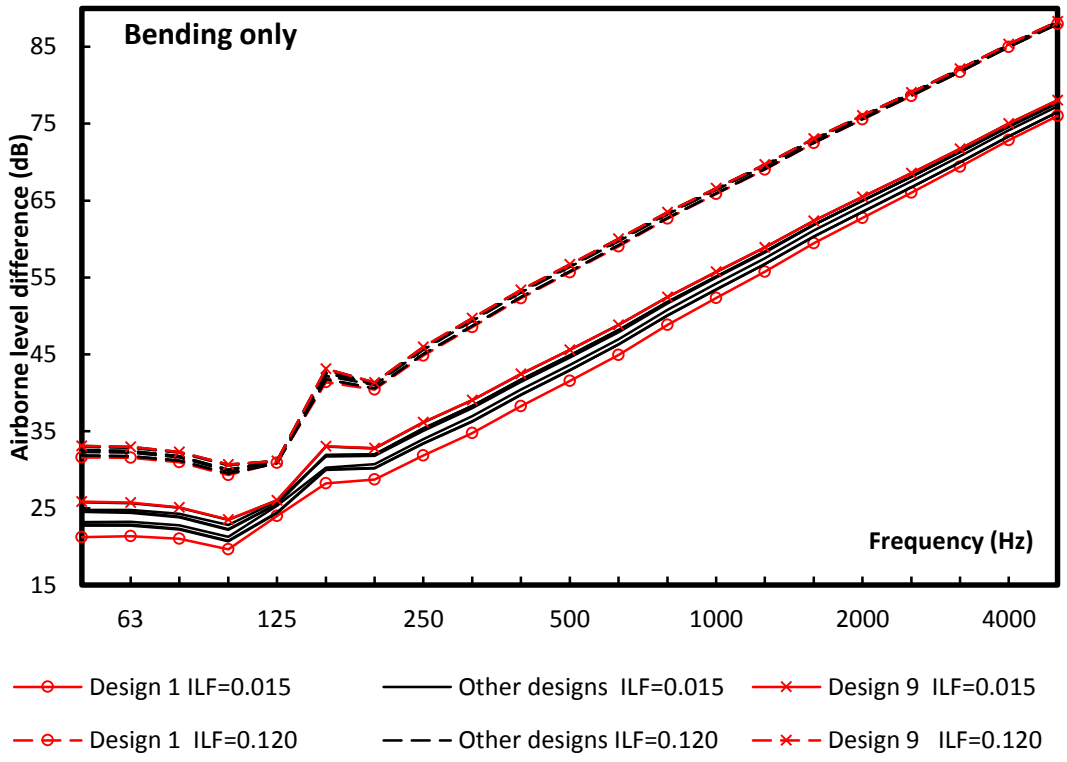

Figure 4-5 Airborne level difference between the source and receiving room with different structural ILFs – Nine different designs (Bending only)

The behaviour illustrated in Figure 4-4 can be better understood by exploring the sensitivity of paths of different length to damping as presented in Figure 4-6 and Figure 4-7. In these figures the direct path occurs via the separating wall and is of 3 (resonant) subsystems in length; 1st order paths are taken as the shortest flanking paths between the two rooms (and involve 4 subsystems in this case), 2nd order flanking paths involve 5 subsystems, etc. The non-resonant path between the two rooms has been included so that its contribution relative to the resonant transmission may be seen. For the case of low internal damping when all ILFs equal 0.015, as shown in Figure 4-6, it can be seen that the contribution of the direct path is comparable to the combined transmission from each family of low order flanking paths.

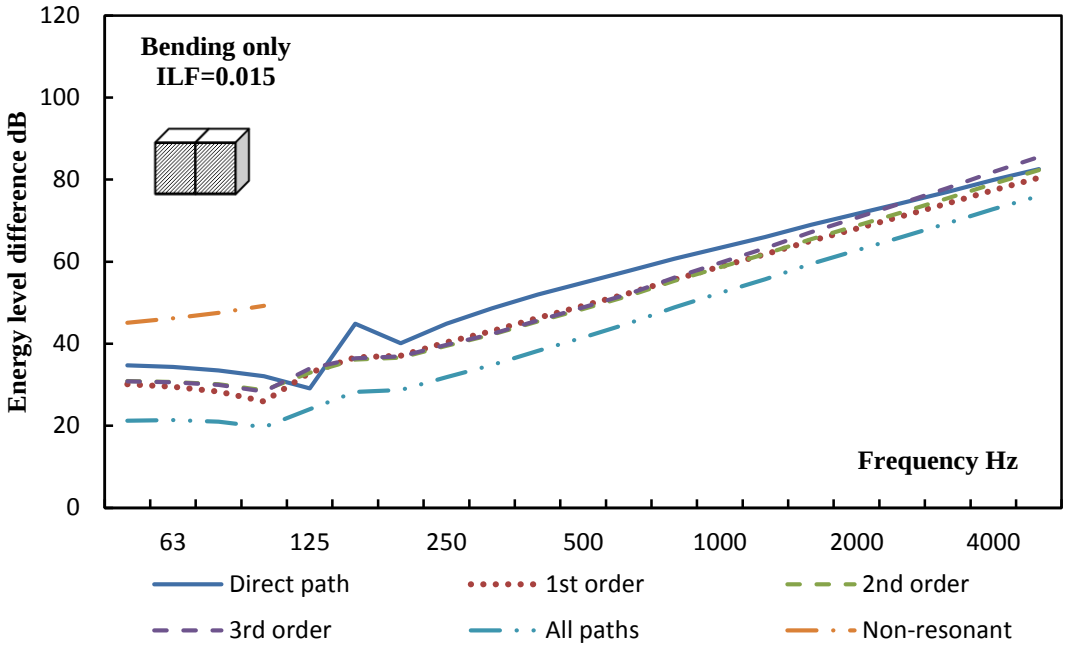

Figure 4-6 Contribution of path orders with all ILFs equal 0.015 – Design 1(Bending only)

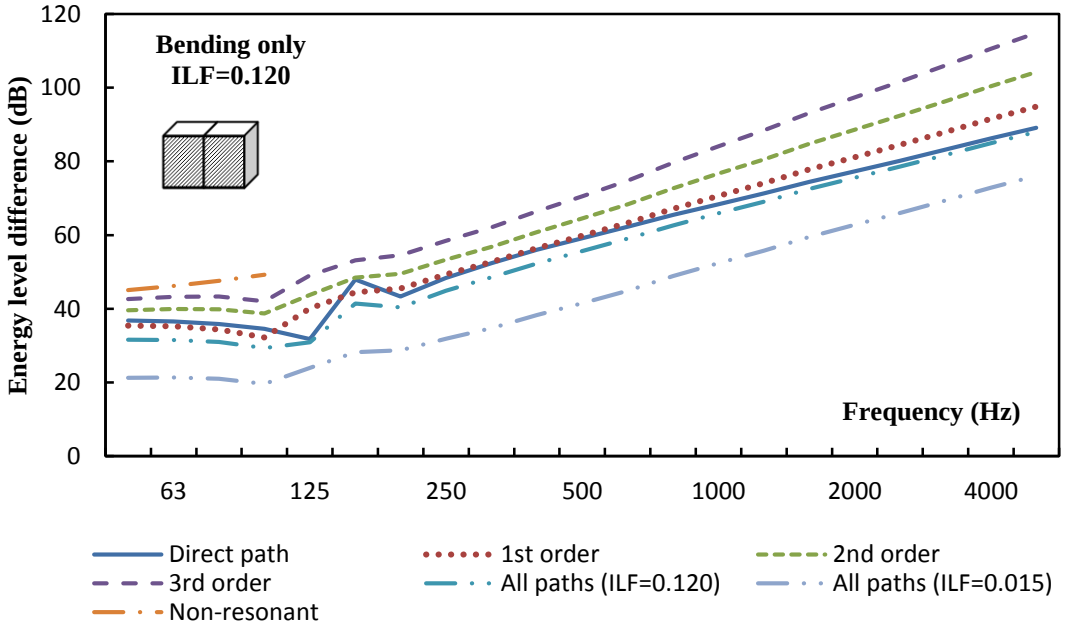

Figure 4-7 Contribution of path orders with all ILFs equal 0.120 – Design 1 (Bending only)

This suggests that for a system with low internal damping, the direct and low order flanking paths, exhibit a combination of path attenuation and growth in path numbers that yields very similar level differences. There is therefore no single path or path order that dictates transmission. When the internal damping is increased, as illustrated in Figure 4-7, the increased attenuation of progressively higher order flanking paths combined with the fact that the number of paths remains unaltered yields the situation where flanking paths are heavily attenuated and the direct path increasingly dictates overall transmission. As shown in Figure 4-6 and Figure 4-7, non-resonant transmission does not have a significant influence on the findings for the structure assumed in this example.

The differences in the contribution made to transmission by paths of different order as a result of increasing structural ILFs from 0.015 to 0.12 are shown in Figure 4-8. This gives a clearer picture of the effect that increasing damping has and the extent to which higher order paths are affected. This statement depends on all materials having similar material properties as varying 'contributions' will occur if the pathway subsystems' material properties are different. The predicted curves are obtained from a combination of Equation 4-5 and Equation 4-9 and suggest this approach offers a reasonable approximation of the benefit that may be gained by applying damping. In arriving at these flanking path results, Equation 4-9 has been modified to reflect the fact that in Design 1, structural subsystems are connected to 6 rather than the 10 structures assumed in its derivation. Furthermore, due to the fact that in the majority of paths rooms occur only as the start and end subsystem, 2 is chosen as the value of a.

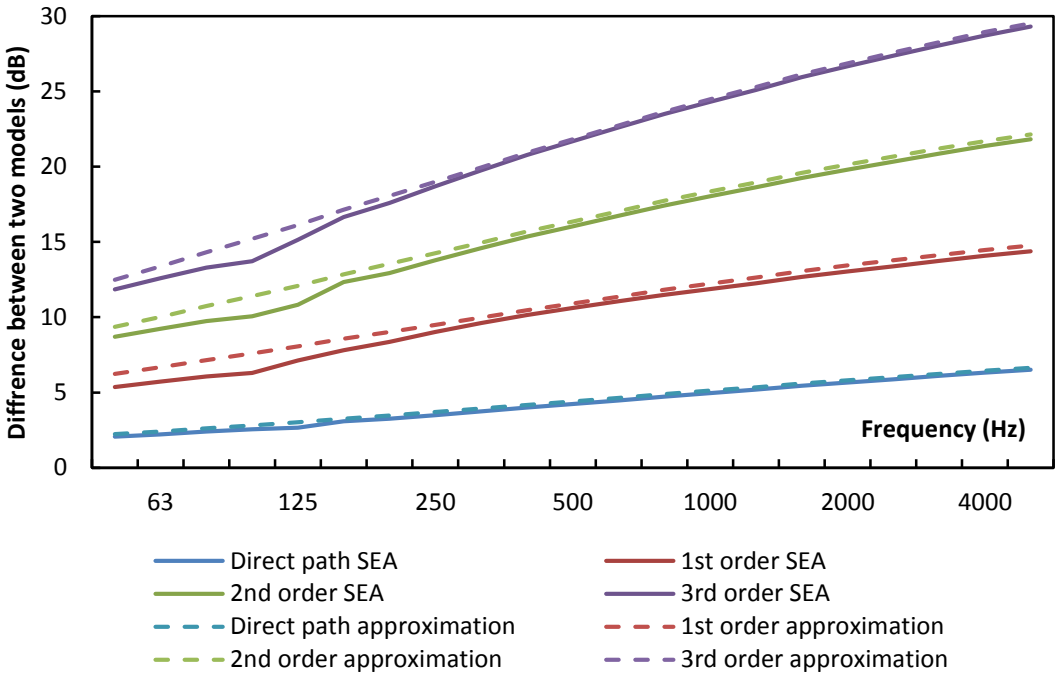

Figure 4-8 Predicted difference in attenuation of path orders for the system where all ILFs equal 0.015 and where all ILFs equal 0.120 – Design 1 (Bending only)

Similar analyses are done for the other eight designs and the general conclusions are the same. As the complexity of the model increases, each structural subsystem is more likely to be connected to 10 structures. Generally speaking, a building that is more complex than Design 7 can be treated as such a model and Equation 4-9 remains unaltered for them.

In understanding the global behaviour illustrated in Figure 4-4, it may be inferred that two mechanisms are at play. The first involves the rapid growth in attenuation of flanking paths resulting from their increased sensitivity to the TLFs of subsystems involved in the chain of transmission as suggested by Equation 4-6 and illustrated in Figure 4-8. The result, illustrated in Figure 4-7, is that the direct path begins to assume an increasingly dominant role in dictating performance. These initial rapid rates of growth in flanking attenuation yield significant improvements in level difference being observed.

The second mechanism reflects improved attenuation observed in the direct path as a result of increases to its internal damping. This becomes visible once the

direct path begins to dominate performance, at which point successive doublings of internal loss factor yield approximately 3dB improvements in insulation. These are observed initially at high frequency but the effect spreads to lower frequencies as internal losses begin to dominate across more of the spectrum.

One thing to be noticed here is that the above discussions are based on bending only models, which represents the system behaviour at low frequency region where there are few or no in-plane modes. The results illustrated at high frequency (frequency above 2000Hz) are for illustrative purpose only and do not account for the influence that the in-plane modes that would be supported by the structure would have.

4.6 Three wave model

Three wave models have also been examined here to represent the real system behaviour at high frequency region where all three wave types coexist. The general findings are the same as those for bending only models. By increasing the ILF from 0.015 to 0.120, a global sound insulation increases about 12dB for Design 1 and about 9dB for Design 9 (see Figure 4-9). As the bending waves that are excited by in-plane waves have been included in three wave models, more energy has been dissipated as heat. Therefore, the results predicted by three wave models generally have larger energy level difference, i.e. better sound insulation. The differences between the results from three wave models and bending only models become more significant as the ILF gets higher or the system gets more complicated (see Figure 4-9). EN 12354 is highly restricted in its use where there are complicated transmission paths. This is because some CLFs used in EN12354 are from a menu of existing in-situ measurements which can also be highly influenced by the boundary conditions of the test construction.

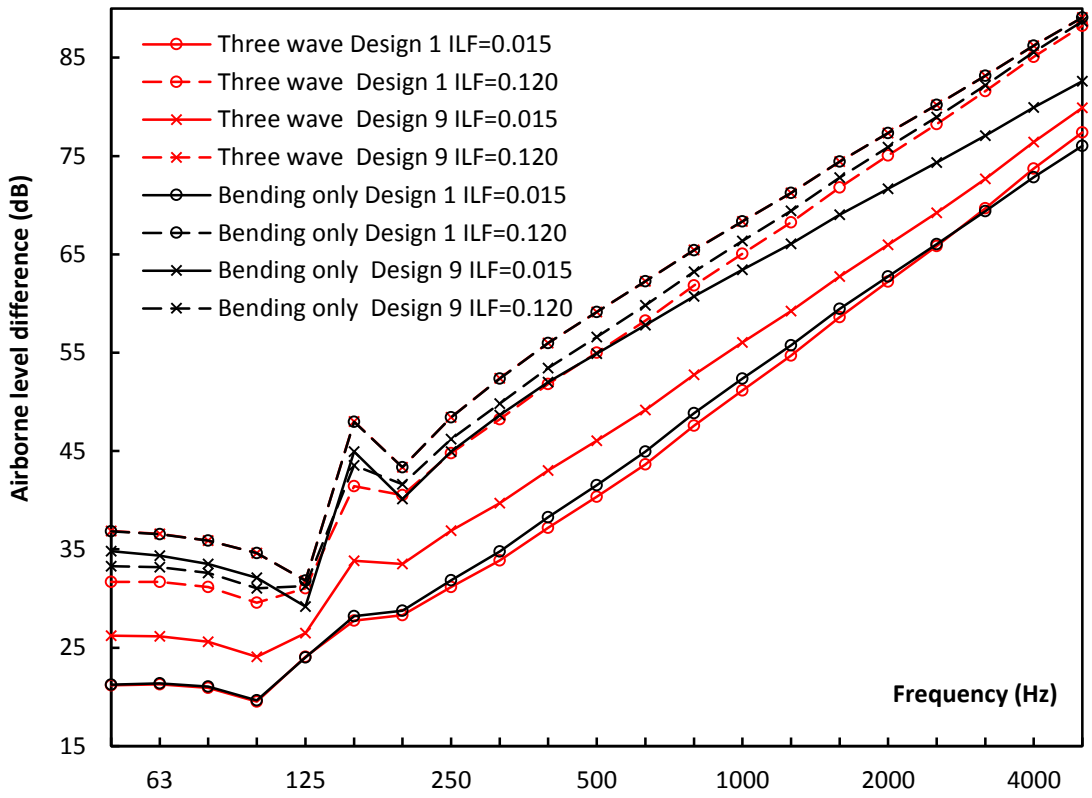

Figure 4-9 Airborne level difference between the source and receiving room with different structural ILFs – Three wave models & Bending only models

For bending only model, adding more subsystems results in increased insolation between rooms because energy is dissipated elsewhere in the system rather than completing its journey to the receiving room. Using a three wave model also has the effect of adding more subsystems (two in-plane subsystems are generated for each subsystem), but for each same design, the prediction from three wave model generally has lower airborne level difference (worse sound insulation). This is because in bending only model, adding subsystems results in longer transmission paths with subsystems in a series-like arrangement and more energy dissipation occurring along the path. In three-wave model, the additional subsystems assume a parallel-like arrangement with the result that the number of paths for any given order increase, which is likely to increase the energy transmission. For Design 9 with ILF=0.120, however, three wave model has a better sound insulation then bending only model. As the ILF grows higher, attenuation along flanking paths becomes dominant, which overrules the effect of more transmission paths.

The damping effects on different order paths have also been analysed. The general behaviours are the same as that modelled with bending only model (Figure 4-10, Figure 4-11, Figure 4-12 and Figure 4-13). In systems with low damping, flanking paths play an important role as the direct path. When the internal damping has been increased, energy attenuation along longer paths increases, which results in a growing dominance of the direct path in transmission.

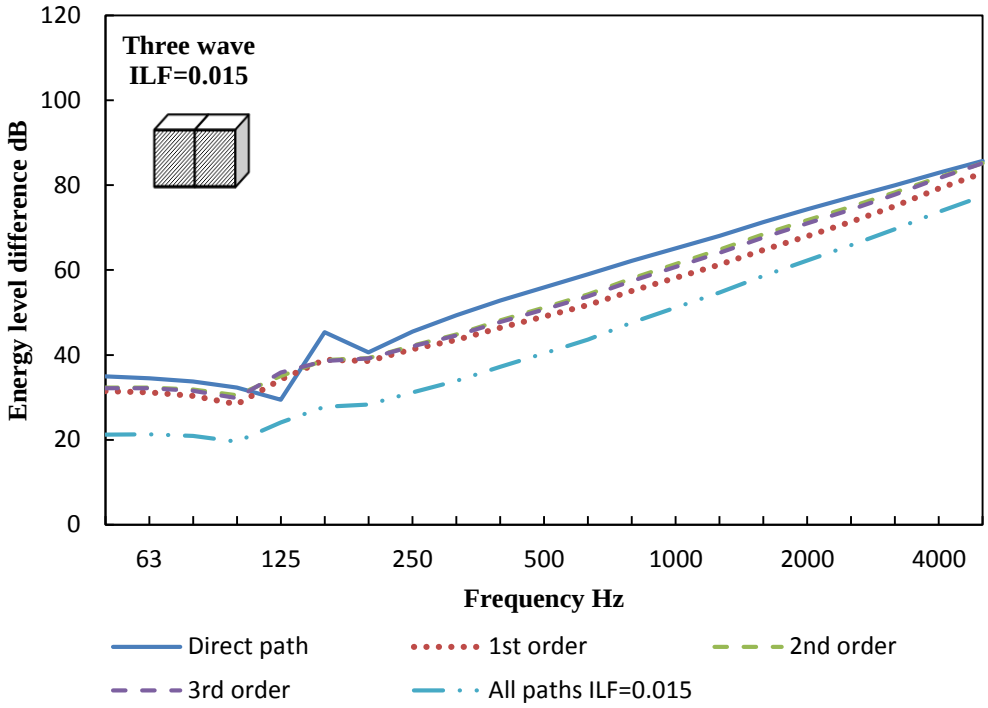

Figure 4-10 Contribution of path orders with all ILFs equal 0.015 – Design 1 (Three wave)

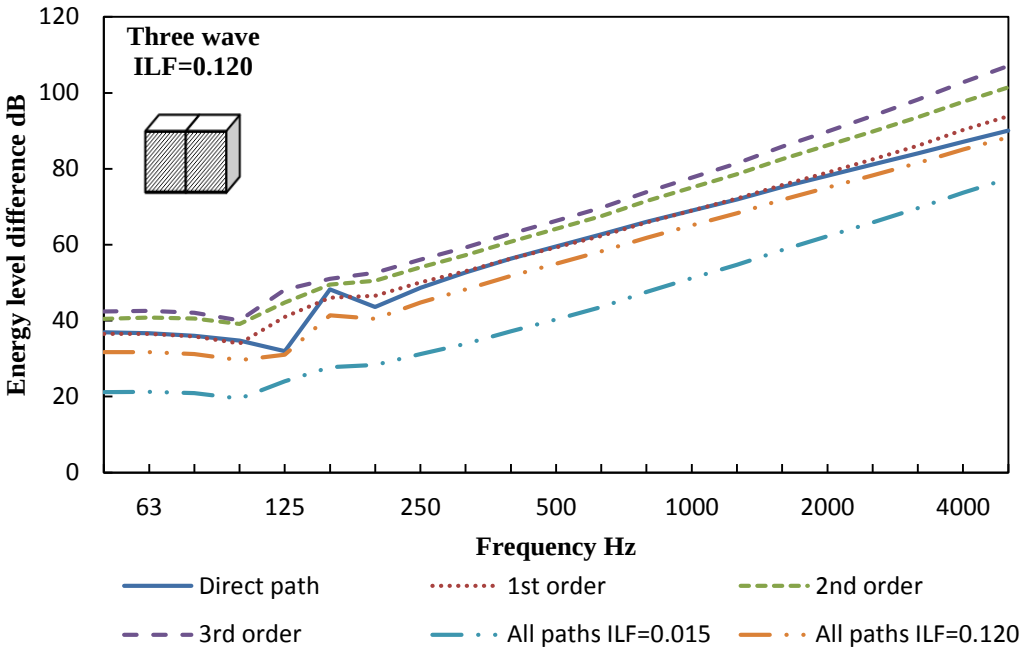

Figure 4-11 Contribution of path orders with all ILFs equal 0.120 – Design 1 (Three wave)

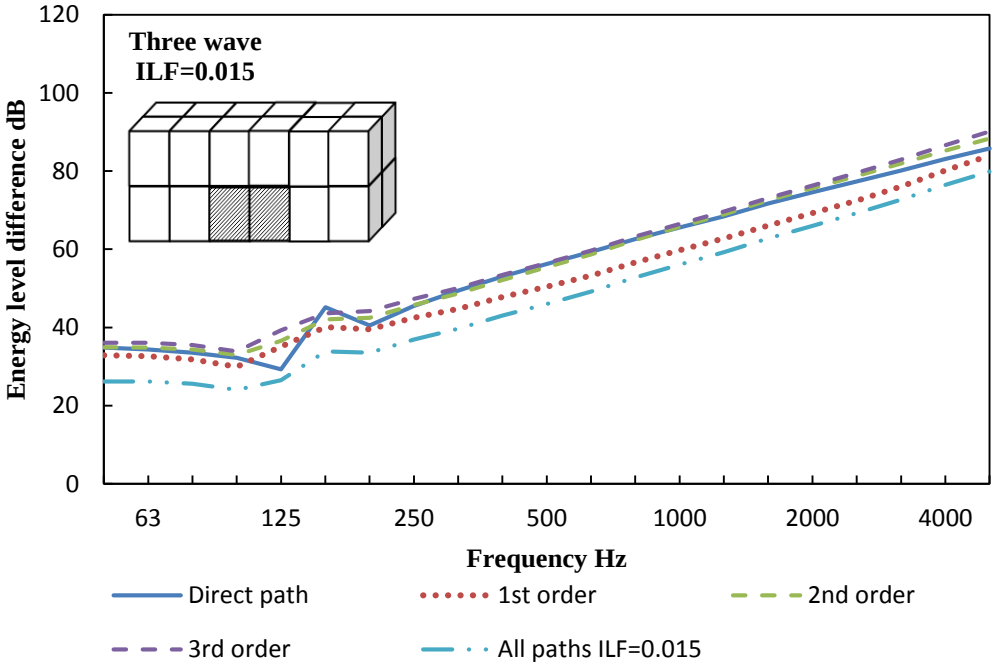

Figure 4-12 Contribution of path orders with all ILFs equal 0.015 – Design 9 (Three wave)

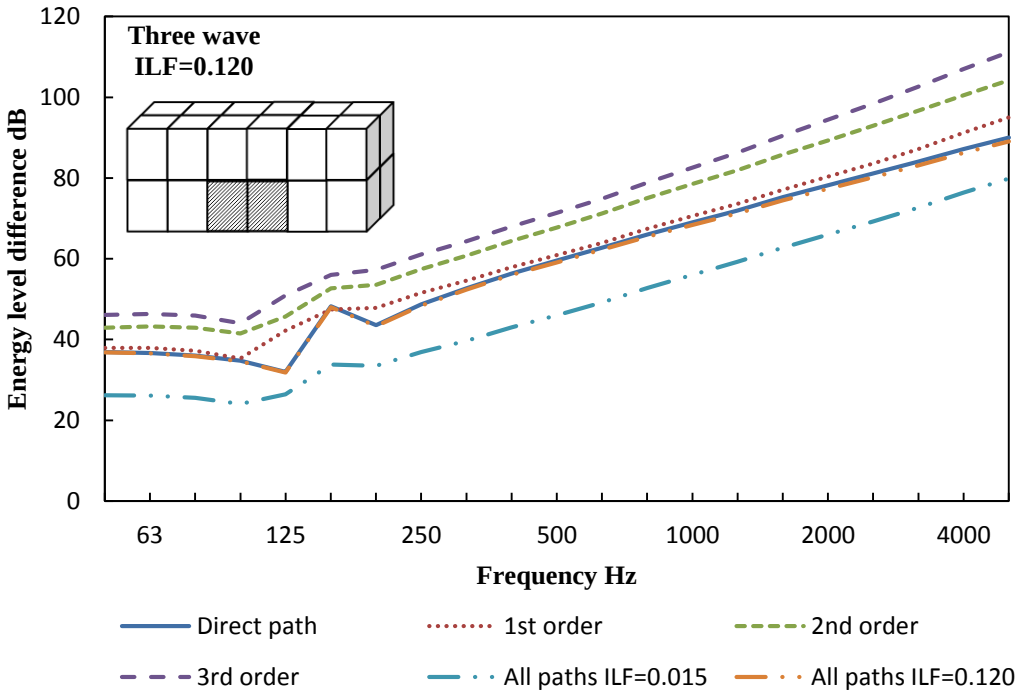

Figure 4-13 Contribution of path orders with all ILFs equal 0.120 – Design 9 (Three wave)

The proposed Equation 4-9 can still be used to give a simple prediction of the improvement in performance for a specific path order. However, modifications have to be made to reflect the average number of couplings each structural subsystem is increased (Figure 4-14 and Figure 4-15). There exist significant difference between the prediction and the result from simulation at frequencies below 2000Hz where the system examined is less likely to support in-plane waves. The prediction is more likely to agree with the result from simulation at high frequencies because the models examined have all three types of waves at the higher frequency bands.

The discussions from the three wave model are more representative of behaviour at the high frequency range. The results from the low frequency region are for illustrative purposes only. More realistic results can be obtained by using bending only model in low frequency region (frequency below 1000Hz) and three wave model in high frequency region (above 2000Hz) in this case.

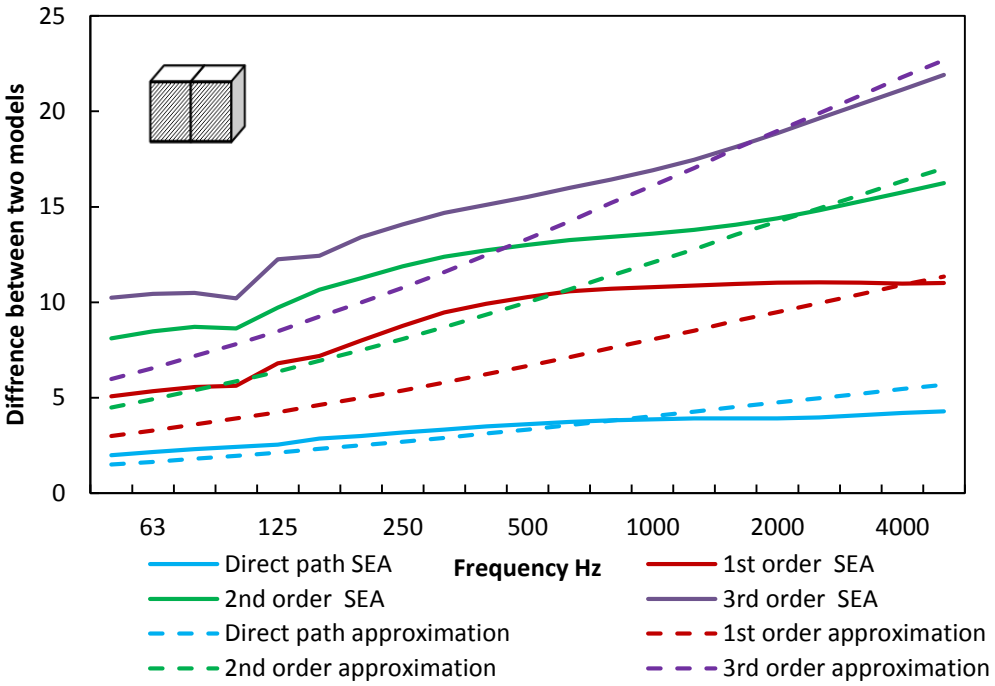

Figure 4-14 Predicted difference in attenuation of path orders for the system where all ILFs equal 0.015 and where all ILFs equal 0.120 – Design 1 (Three wave)

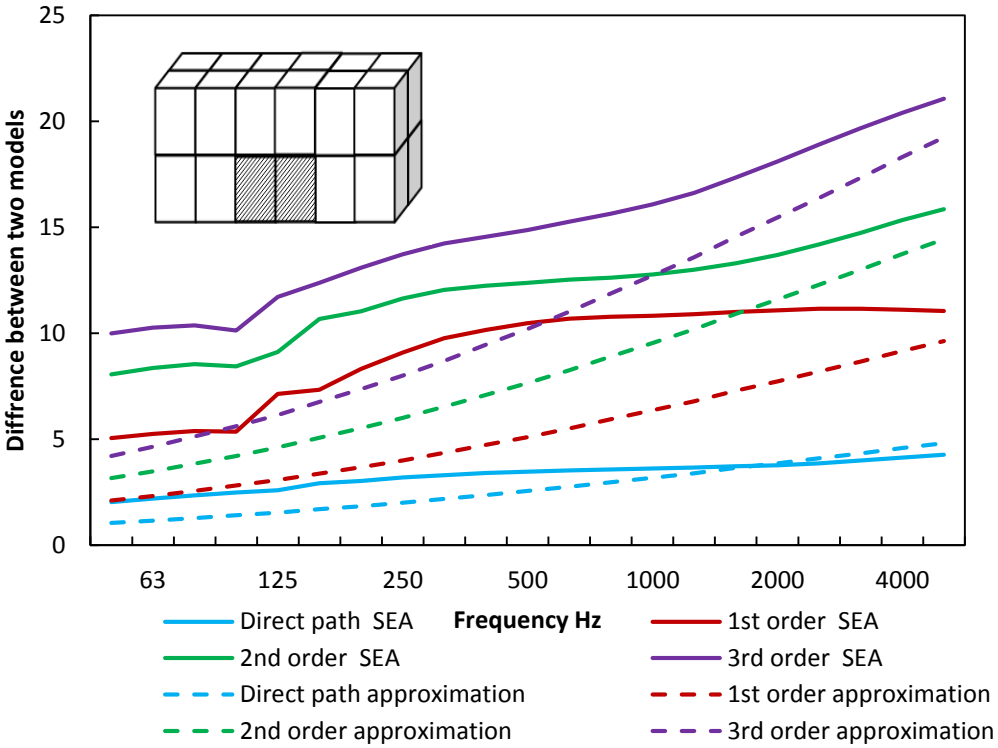

Figure 4-15 Predicted difference in attenuation of path orders for the system where all ILFs equal 0.015 and where all ILFs equal 0.120 – Design 9 (Three wave)

4.7 Conclusion

This section presents simulations of the effect of global damping on reducing the contribution of paths, especially flanking paths, to sound transmission for nine different building designs for both bending only model and three wave model. The results suggest that internal damping can effectively improve sound insulation in buildings if it is applied widely throughout the system. At levels of internal damping typical of masonry materials, in the order of 0.015, the contribution of low order flanking paths is comparable to that of the direct path. If the internal damping of all the structural subsystems in each design is increased from 0.015 to 0.120, the improvement in airborne sound insulation can reach about 14dB for bending only model and around 12dB three-wave model. Initial improvements in performance result from the rapid attenuation of longer flanking paths are more sensitive than shorter paths to changes in damping. Remaining improvements are derived largely from attenuation of the direct transmission path as a result of increasing its damping. As increases in attenuation derived from increasing damping are proportional to the length of a path, the direct path, being the shortest, is the least sensitive. Once flanking paths have been effectively attenuated, the direct paths exhibits improvements of around 3dB each time internal losses are doubled. As there are limits on the extent to which internal damping may be increased, so too are there limits on the degree to which attenuation via the direct path may be effected. The extent to which this strategy may be adopted therefore depends on quantifying the extent to which internal losses may be increased.

The results in this section are purely theoretical and need further experimental evidence to support the findings. Non-resonant transmission from room to room is not included in the treatment presented in this section; however, for the system under study it did not have a significant influence on the findings. A Bending only model is proposed to model the system behaviour in low frequency region and three-wave model is proposed to be used in high frequency region. For most systems, the reduced insulation predicted by the three wave model would be observed in practice at high frequencies where the insulation is typically high and

so may not represent any significant depression in practiced level of sound insulation.

The transmission between proximal subsystems is studied. It is dominant by local damping, i.e. structural subsystems that surrounds the rooms. The energy level difference increases as the system become more complex. There is, however, a threshold when further increasing of the complexity does not have any significant influence on the energy level difference. For transmission between distant subsystems, the number of dominant transmission paths is higher and is less likely to be controlled by local damping. This suggests that a global damping is generally required to have a better insulation between distant subsystems.

Another issue that should to be noticed here is that, as the ILFs get larger, the energy distribution in the structural subsystems becomes less evenly distributed (Craik, 1996). This means successive increases in damping would increasingly violates one of the fundamental assumptions in SEA modelling. This raises a new question: how can one model a heavily damped subsystem within the framework of SEA when it cannot be treated as a normal subsystem? One possible answer is to use the idea of ray tracing, which will be explained in the following chapter.

CHAPTER 5 A REFINED DAMPING MODEL - RAY TRACING

5.1 Introduction

In light of the limitation of modelling heavily damped systems in SEA, an alternative ray tracing modelling method has been proposed in this chapter. In this case, the heavily damped subsystem is treated as an element that couples subsystems. Ray tracing is used to determine the strength of this coupling and use an effective coupling loss factor to quantify this. The basic concept of ray tracing will be introduced first, followed by the details of constructing the ray tracing codes and some numerical studies.

5.2 Optical ray tracing

Ray tracing is a technique first developed to create a 2-D images from a 3-D world in computer graphics (image synthesis) (Glassner, 1989). The basic idea of ray tracing is to trace the path of photons through pixels in an image plane and simulate the visual effect. One may think of a photon as a small light particle that carries energy and can be seen when it lands on our eyes. A light ray is simply the straight travel path of a photon. The term 'pixel' here can be seen as a small, independent window on the image plane (usually the smallest) (Glassner, 1989). The biggest question of 3-D computer graphics is to decide what colour each pixel should be if only one colour can be chosen. The colour of each pixel dependents on photon travel history (what objects the photon hits and what happens when it hits them) and the light source. Figure 5-1 illustrates the basic procedure of how one optical line may arrive at one human eye from the source. In this case, the optical line undergoes three specular reflections and an imaginary image plane is placed between the eye and the third object. The photon goes through a pixel of the image plane and finally lands on the human eye. In reality, a photon may encounter reflection, refraction and diffusion. Certain mathematical expressions may be used to describe each such physical phenomenon. Additional calculation needs to be undertaken when ray combination (different lights go through the same pixel) happens. When the colour of each pixel on the image plane is determined, a vivid

image can be created. This technique is also referred as 'forward ray tracing' and it approximates what happens in real world.

There is also a 'backward ray tracing' where one assumes the eye shoots out light rays. This technique is more commonly adopted although it may seem counterintuitive at first glance. As one conducts a 'forward ray tracing', not all photons land on people's eyes. In other words, not all photons contribute to create the image. It is not computationally beneficial to do a forward ray tracing, although the underlying theory is correct. Reversing the procedure is more computationally efficient.

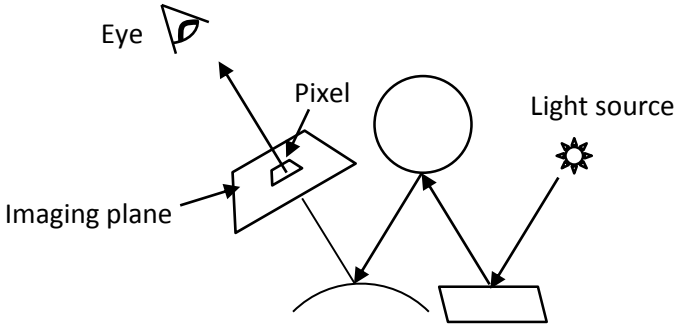

Figure 5-1 Illustration of how one optical line arrives at one human eye from the source

Appel (1968) first proposed the ray tracing algorithm for shadow rendering, which has since been termed 'the ray casting algorithm'. The idea of ray casting is to fire rays from the eye, one ray per pixel, and to find the first surface that blocks that ray. Any surface that faces the ray is defined as 'being illuminated' and the other is in shade. With the knowledge of the material properties and the effect of light source, one may determine the shading of any object.

Whitted (1979) further developed the algorithm by introducing the 'recursive ray tracing algorithm'. The previous algorithm only traces the rays from the eye to the object they first hit. This algorithm keeps tracing the reflected, refracted and shadow rays. The idea of shadow ray is to determine whether the surface is in shadow by testing whether there exists an opaque object between the light and the surface. This algorithm offers a more realistic image.

5.3 Acoustic ray tracing

When many researchers were trying to create algorithms that can produce more realistic images, some acousticians found the extendibility of ray tracing to predict the acoustic response in rooms. Krokstad, Strøm and Sørsdal (1968) first published the paper to use ray tracing algorithm to predict the acoustic impulse response of any given three dimensional model of a room. Later, various ray tracing algorithms have been developed for the research of room acoustics, most of which have been validated to a certain degree (Zeng, Chen and Sun, 2003). The application of ray tracing algorithms later extend to auralization (an analogy with visualization to describe rendering audible sound fields) (Kleiner, Dalenback and Svensson, 1993; Pompei, Sumbatyan and Todorov, 2009; Taylor et al., 2012) and sound visualization (Funkhouser et al., 1998; Bertram et al., 2005). Those algorithms can mainly be classified into two categories, namely path tracing and beam tracing (Funkhouser et al., 1998).

5.3.1 Path tracing

Path tracing methods generally generate rays from the source and emit them into the environment. An appropriate set of rays that finally reach the receiver are chosen to be the reverberation rays. Figure 5-2 shows the reverberation ray that undergoes one reflection. The dashed lines represent rays of the same order that do not reach the receiver.

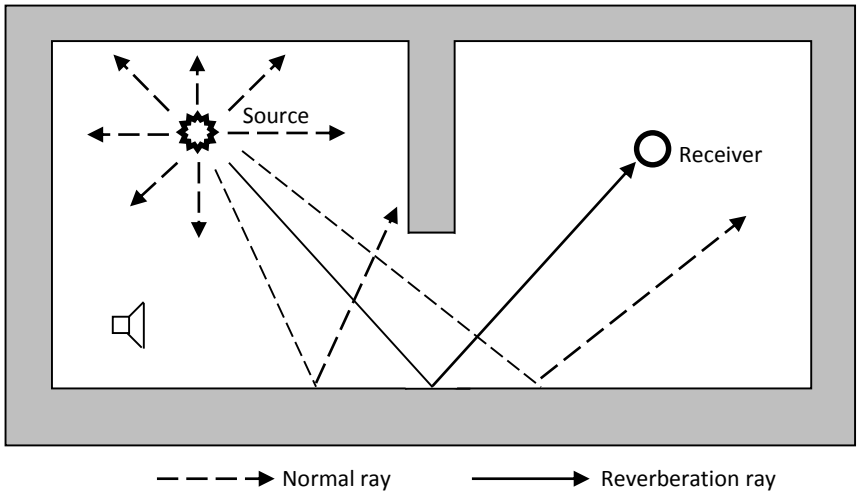

Figure 5-2 Reverberation ray in path tracing (one reflection)

One common way of generating the rays from the source to the receiver is Monte Carlo path tracing method, which was first proposed by Kajiya (1986) building on previous work by Cook, Porter & Carpenter (1984). A typical algorithm is called 'Metropolis Light Transport algorithm' (Veach and Guibas, 1997). It generates the rays by randomly mutating a single current path by adding, deleting or replacing a new vertex to the path. Once the contributing paths are found, the nearby paths can be explored relatively easily. By proper selection of mutation strategies and acceptance probabilities, this algorithm can provide satisfactory results (Funkhouser et al., 1998). Antani et al. (2012) used an energy-based path tracing method for real time auralization considering high order specular and diffuse reflections as well as edge diffractions with moving sound source and receiver.

The primary strength of path tracing is its simplicity and generality. It only requires calculations when the rays interact with surfaces. When each intersection is found, the sampling of specular reflected, diffuse reflected, diffracted and refracted paths can be realized (Cook, Porter and Carpenter, 1984). Another advantage of path tracing is that the growth of computational complexity is sublinear with the number of surfaces included in the model, unlike the image source methods with exponential computational complexity growth (Funkhouser et al., 1998).

The primary disadvantage of path tracing comes from the fact that the number of traceable rays is limited and rays cannot be detected by point-shaped receivers (Lehner, 1993). Errors and aliasing are introduced because the rays are sampled by a set of discrete paths. Moreover, the receiver position and the intersection surface are usually approximated by a small volume rather than an ideal point (in order to find the intersections with infinitely thin rays) (Funkhouser et al., 1998). This may result in paths being counted multiple times and false hits (Lehner, 1993). In order to avoid large errors, path tracing often generates a large number of rays which carries additional computational cost.

5.3.2 Beam tracing

Beam tracing methods define the propagation paths by recursively tracing pyramidal beams (i.e. sets of rays) from a source through the environment (Funkhouser et al., 1998). Normally, a pyramidal beam is designed to cover the whole 2D space from the source direction. The transmission beam will be generated to cover the shadow region and the reflection beam can be obtained by simply mirroring the transmission beam over the intersection plane (see Figure 5-3). Antonacci et al. (2008) proposed a fast beam tracing algorithms for 2D real time auralization taking accounts for diffusion and diffraction. Antonacci, Sarti and Tubaro (2010) further extended this algorithms for propagation phenomena more complex than the specular reflections. Markovic et al. (2010) also presented a beam tracing method for sound field rendering making use of a projective geometry representation.

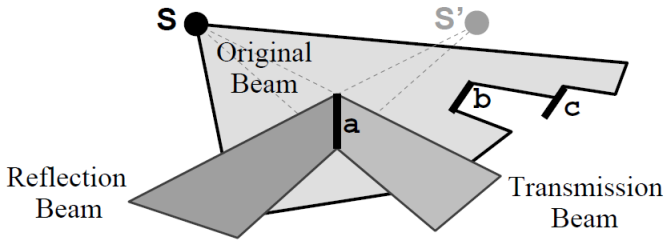

Figure 5-3 Beam tracing method (Funkhouser et al., 1998)

The primary advantage of beam tracing is that it does not suffer from the sampling artifacts of ray tracing by taking advantage of its spacial coherence, i.e. each beam represents an infinate number of rays, and the 'illuminated' 2D space from the source has beem completely covered by the original and reflected beam (Funkhouser et al., 1998).

The primary disadvantage is that it requires a relatively complex model to perform its geometric operation (i.e. intersection and mirroring). Another limitation is that it cannot model the reflection from a curved surface (Funkhouser et al., 1998).

5.4 Difference between acoustic and optical ray tracing

Although acoustic and optical ray tracing share many similarities due to the fact that sound and light can both been described as wave phenomena, there exist two significant differences.

First of all, the magnitude of wave lengths of audible sound are more than five orders longer than visible light (Funkhouser et al., 1998). Acoustic waves may encounter more singificant difractions around the joints of different structural elements than an optical ray does, although the dominant phenomena at the boundaries for both are still specular reflections. One bright side of this is that, for 3D space acoustic field modelling, small objects (Funkhouser et al. uses the example of coffee mugs) can normally be ignored for frequencies below 4,000Hz, expecially when there exist significant reflections and diffractions from other sources (Funkhouser et al., 1998).

Secondly, sound travels around 10^{-6} times slower than light through air, resulting in perceivably different arrival times for different propagation paths (Funkhouser et al., 1998). The human perception of sound depends on both the direct and reverberant sound field, which take time to build up. However, human's eyes can immediately detect light when the source turns on. This leads to considerations for modelling the sound field in its early stage (before its steady state). However, in most cases, it is the steady state response that people are interested in.

5.5 The ray tracing code

5.5.1 Rationale

One primary concern of this research is to determine the energy distribution of heavily damped building elements (i.e. walls, floors, ceilings etc.). Several considerations were made before the development of the ray tracing code.

One may notice that those building elements are usually rectangular plates and the dimensions of their thicknesses in most cases are relatively small compared with the dimensions of their lengths and widths. Moreover, the acoustic bending

wave lengths for audio frequencies are normally more than twice of the magnitude of thickness, i.e. the bending wave length of a 0.2 m thick concrete wall at 4000 Hz is around 0.5 m. Therefore, these subsystems can be treated as 2D systems rather than 3D systems. Path tracing is more suitable than beam tracing for our purpose since the geometry of subsystems is relatively simple, i.e. rectangular.

The ray tracing algorithm proposed in this section only predicts the steady state response in order to model the energy distribution and how the energy is transmitted through a heavily damped 'subsystem' coupling two or more normal subsystems. A forward tracing is used for two reasons. One is for simplicity. It is more intuitively convenient to trace the ray from the source to the receiver. The other reason is due to the fact that the incident energies of rays at the boundaries play significant role in computing the energy transmission coefficients. In other words, there exist a large number of receivers (depending on how we discretize the boundaries). In this case, the backward tracing does not have computational benefit but may induce difficulties when constructing the ray tracing code.

A simpler but more controllable way of ray generation is adopted instead of using Monte Carlo path tracing method. Since the energy distribution of a normal SEA subsystem is assumed to be evenly distributed, it is reasonable to use a large number of evenly distributed point sources at the boundary to simulate the source. Each point source is assumed to contain same amount of energy and radiates several acoustic rays that is also evenly distributed (Figure 5-4). It is very easy to control the number of rays by modifying the number of point sources (i.e. n) and the number of rays each point source radiates (i.e. ang).

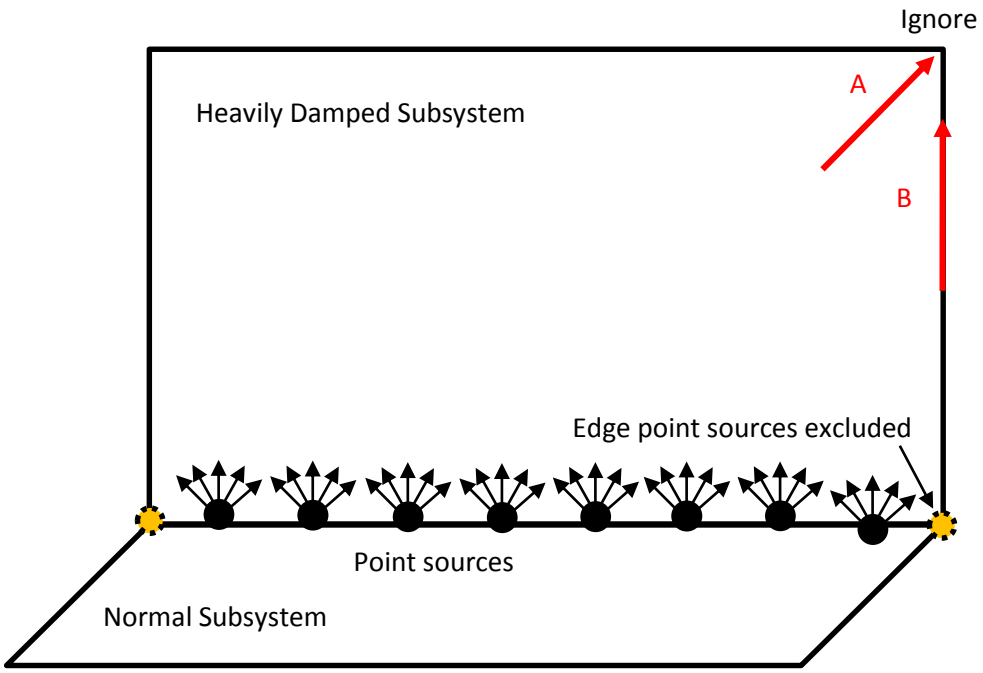

Figure 5-4 Use of several point sources to simulate a linear noise source

Some other assumptions are made for simplicity:

a. The point sources at edges are excluded from the model (see Figure 5-4).
b. Only the rays that enter the heavily damped subsystem are traced.
c. The rays that hit the corners are ignored (Figure 5-4 A).
d. The rays that go along the boundary are ignored (Figure 5-4 B).
e. The number of reflections is used to control how far the code traces the rays rather than travelling time (it is easier to use the number of reflections since all the calculations are carried out based on the position of each reflection).

The influence of these assumptions tends to become neglectable when the total number of rays and the number of reflections become large.

5.5.2 Flow chart

Figure 5-5 shows how the main part of ray tracing code is constructed. Other function codes, which are useful to solve specific tasks, are not listed here. The key part of this code is the generation of three important matrixes, namely the matrix of intersection, the matrix of travel distance and the matrix of incident energy. Knowing the intersections of one specific ray on each boundary helps one to

calculate the distance that ray travels, which is useful in computing the incident energy (see Section 5.5.5). The transmitted energy can then be calculated by rearranging Equation 5-22.

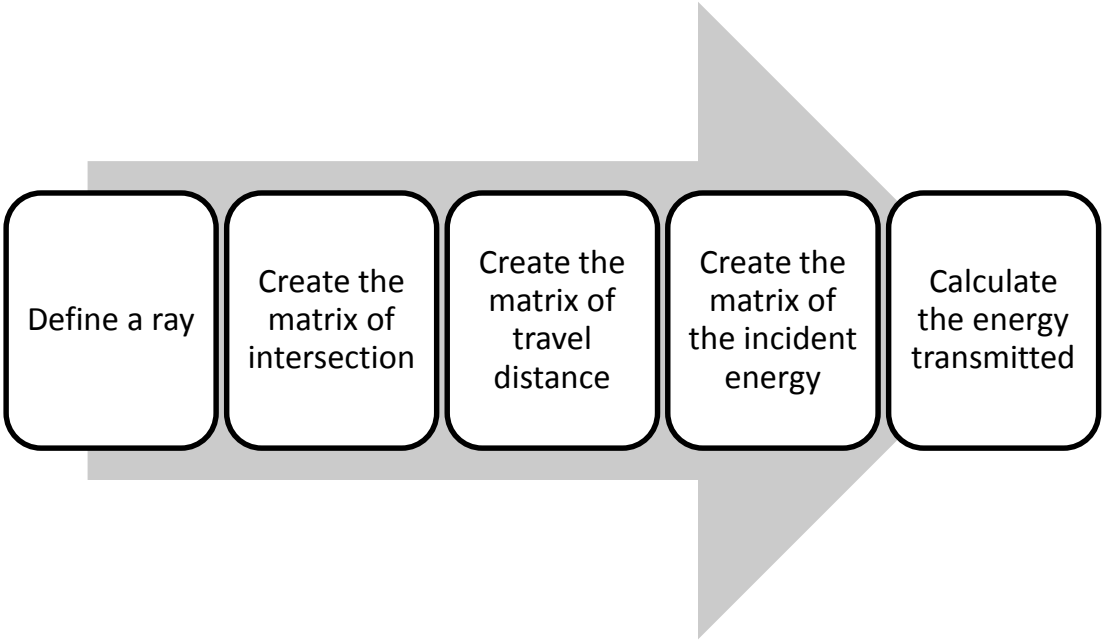

Figure 5-5 Flow chart of the ray tracing procedure

5.5.3 Creation of the matrix of intersection

In the ray tracing code, the length and the width of the plate are denoted by a and b and it is placed in a 2D Cartesian coordinate system as shown in Figure 5-6 (in this case $a = b = 2$).

For a given point source (x_0, y_0), the equation describing a ray generated with start angle θ is given by:

$$tan\theta \cdot x - y = tan\theta \cdot x_0 - y_0 \tag{5-1}$$

where $0 < x_0 < a$, $y_0 = 0$. The start angle θ is always defined in this equation as the angle between the x-axis and the ray measured in an anti-clockwise direction. The number of traceable rays each point source radiates, i.e. ang, determines the angle difference, i.e. $\Delta\theta$ between two neighbouring rays through:

$$\Delta\theta = \frac{180}{ang + 1} \tag{5-2}$$

$\Delta\theta$ is also the smallest starting angle. Rays with starting angles of $0°$ and $180°$ are ignored.

The first intersection is calculated by solving four sets of equations:

$$\begin{cases} tan\theta \cdot x - y = tan\theta \cdot x_0 - y_0 \\ x = a \end{cases} \quad (5\text{-}3)$$

$$\begin{cases} tan\theta \cdot x - y = tan\theta \cdot x_0 - y_0 \\ x = 0 \end{cases} \quad (5\text{-}4)$$

$$\begin{cases} tan\theta \cdot x - y = tan\theta \cdot x_0 - y_0 \\ y = 0 \end{cases} \quad (5\text{-}5)$$

$$\begin{cases} tan\theta \cdot x - y = tan\theta \cdot x_0 - y_0 \\ y = b \end{cases} \quad (5\text{-}6)$$

If the solution (x_1, y_1) satisfies that $\begin{cases} 0 < x_1 < a \\ 0 < y_1 < b \end{cases}$ and $\begin{cases} x_1 \neq x_0 \\ y_1 \neq y_0 \end{cases}$, then solution (x_1, y_1) is accepted as the first intersection.

The second intersection is found by conducting the same procedure, where (x_1, y_1) is used as the new start point and the new start angle is $(180 - \theta)$. The intersections at the four corners of the plate are excluded in this code for simplicity and only specular reflection is considered.

Figure 5-6 illustrates an example of an arbitrary ray that undergoes four reflections (i.e. $N = 4$) where the coordinate of the source is $(1,0)$ with a start angle of $60°$ on a $2m \times 2m$ plate. The information of the start angle and coordinates of each intersection as well as the starting point is stored in the matrix of intersection, i.e. mat_int (see Figure 5-7).

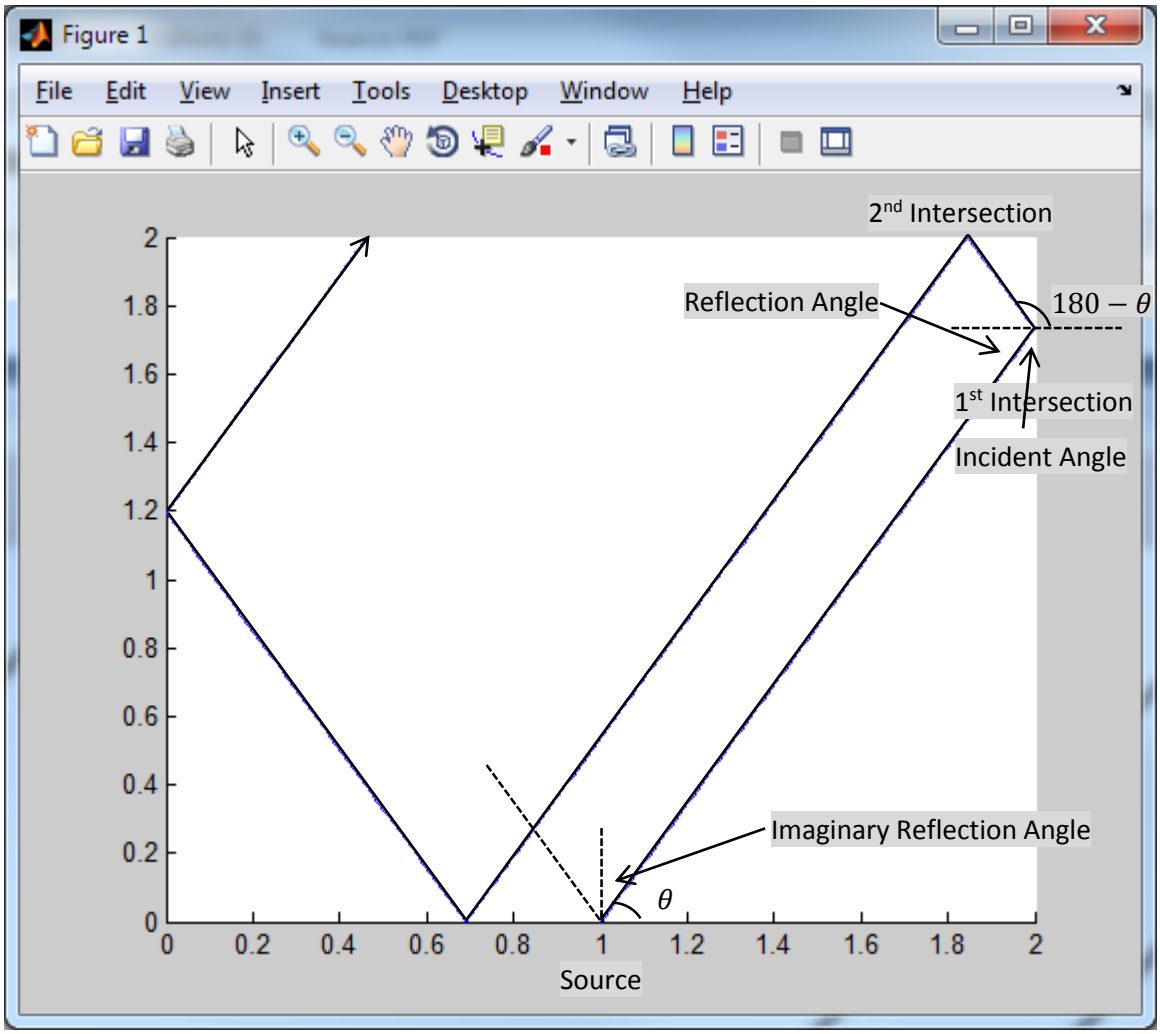

Figure 5-6 An illustration of an arbitrary ray undergoes four reflections where the coordinate of the source is (1,0) with a start angle of 60° on a $2m \times 2m$ plate.

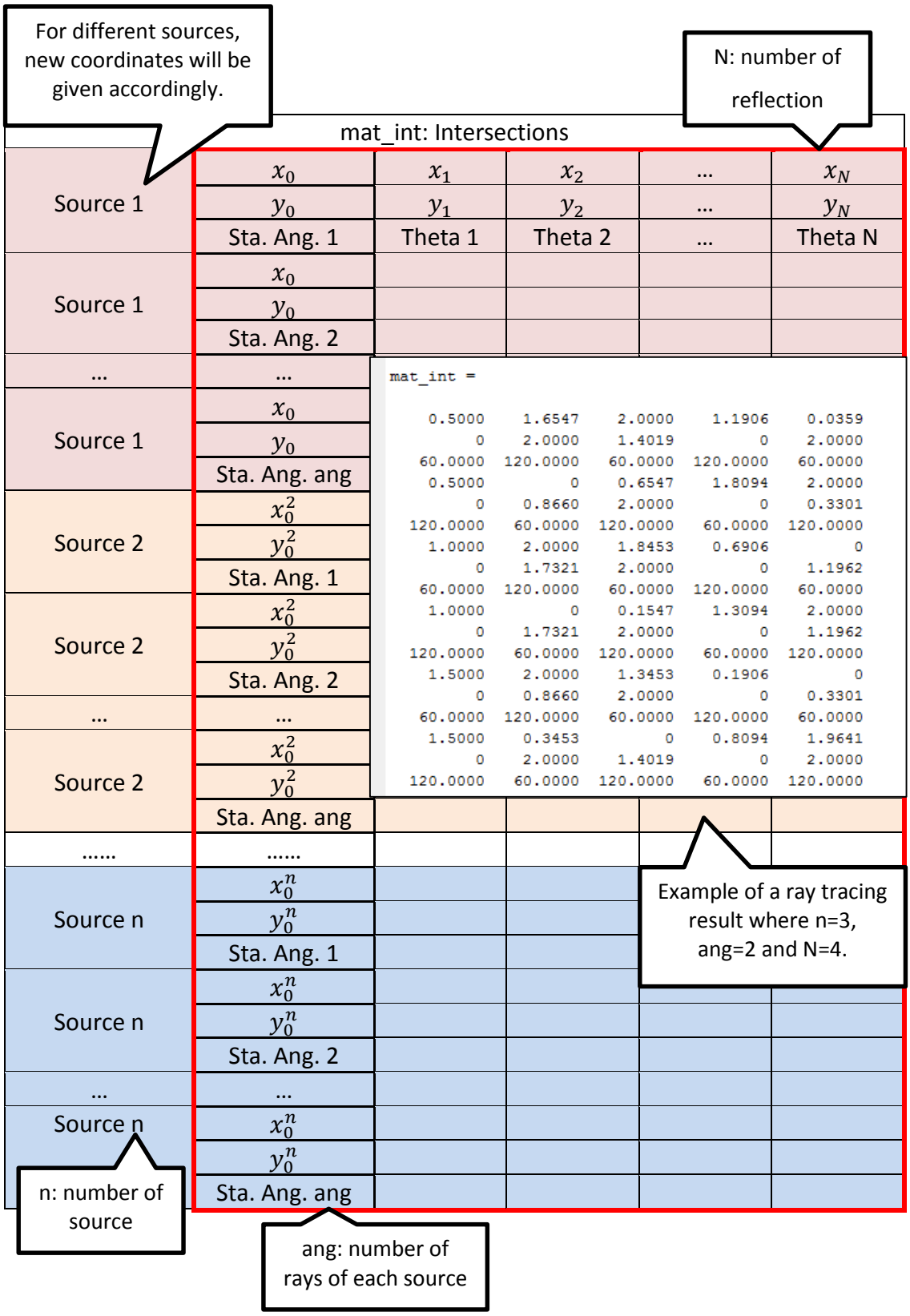

Figure 5-7 Matrix of intersection

5.5.4 Creation of the matrix of travel distance

The distance the ray travelled from the origin (x_0, y_0) to the first intersection (x_1, y_1) can be found through:

$$D_1 = \sqrt{(x_1 - x_0)^2 + (y_1 - y_0)^2} \tag{5-7}$$

The distance travelled by the ray from the first intersection (x_1, y_1) to the second intersection (x_2, y_2) is found by:

$$D_2 = \sqrt{(x_2 - x_1)^2 + (y_2 - y_1)^2} \tag{5-8}$$

The general expression for the distance a ray travels from the $(N-1)^{th}$. intersection to the N^{th} intersection is:

$$D_N = \sqrt{(x_N - x_{N-1})^2 + (y_N - y_{N-1})^2} \tag{5-9}$$

By adding these distances together, one can find the distance the ray travelled from the origin to the N^{th} intersection by:

$$D_{0N} = \sum_{i=1}^{N} D_i \tag{5-10}$$

It is useful to defined a so called the imaginary reflection angle of the origin as:

$$|90 - \theta|$$

The term 'imaginary' is addressed here to show that the origin source does not undergo a reflection. It is defined for the coding simplicity and does not have significant importance in this content.

The reflection angle of the N^{th} intersecion θ_{raN} equals:

$$\begin{cases} \theta_{ra(N-1)}, the\ (N-1)^{th} and\ the\ N^{th} intersection\ are\ on\ two\ parallel\ lines \\ 90 - \theta_{ra(N-1)}, the\ (N-1)^{th} and\ the\ N^{th} intersection\ are\ on\ two\ perpendicular\ lines \end{cases}$$

which is useful when computing the incident energy, i.e. it helps to work out the enery loss due to structural coupling from previous reflection. The incident angle of the the N^{th} intersecion θ_{iaN} is $(180 - the\ start\ angle)$ of the N^{th} intersecion.

The information relating to distances, reflection angles and incident angles is stored in the distance matrix, i.e. mat_dis (see Figure 5-8).

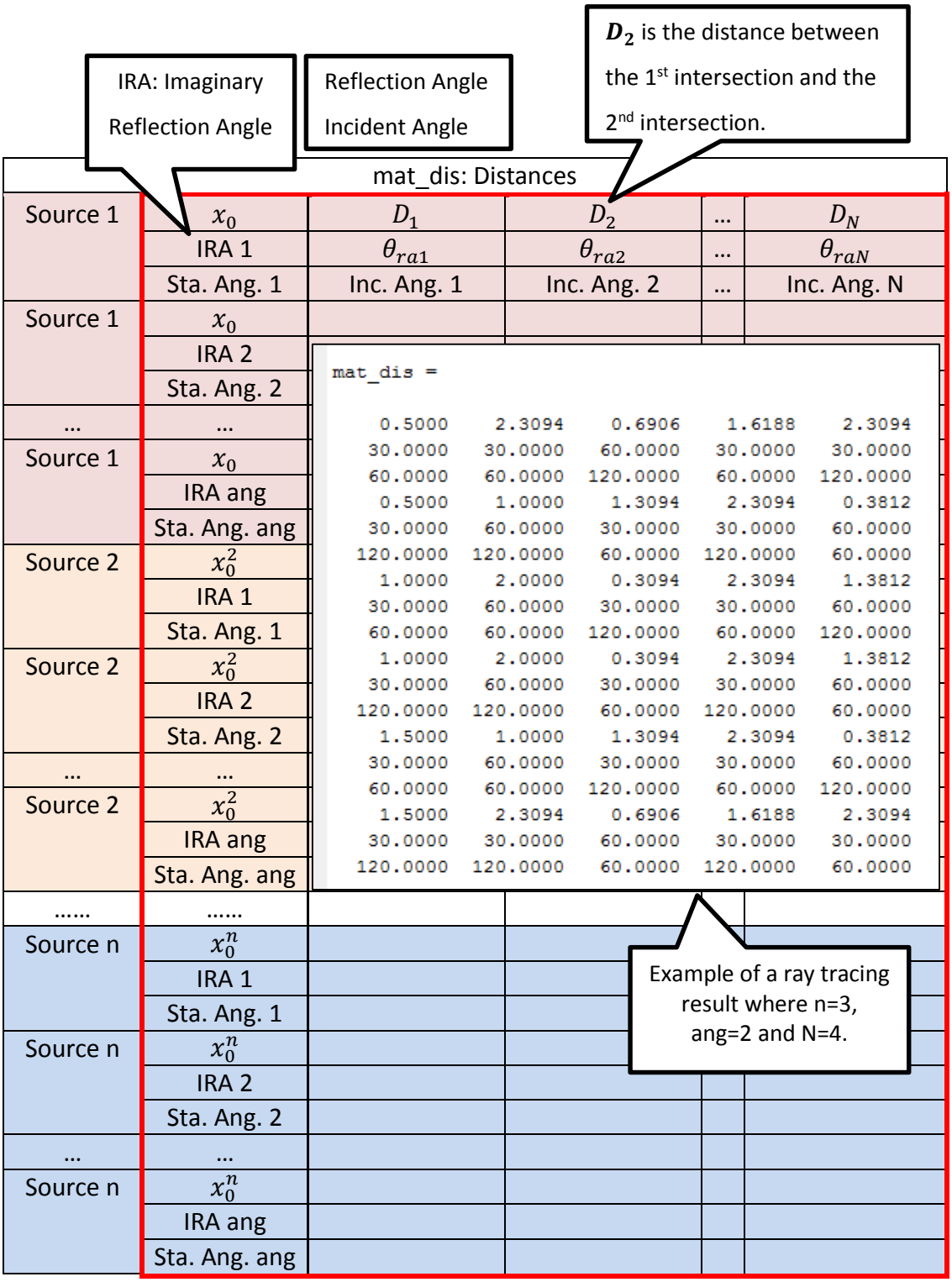

Figure 5-8 Matrix of distance

5.5.5 Creation of the matrix of the incident energy

The complex wavenumber for pure bending waves in a homogeneous isotropic plate is:

$$\underline{k}_B = \underline{k}_B{}^{\perp} - j\underline{k}_B{}^{\shortparallel} \tag{5-11}$$

where $\underline{k}_B{}^{\perp}$ represents the real bending wavenumber and the imaginary bending wavenumber $\underline{k}_B{}^{\shortparallel} = 0.25\eta\underline{k}_B{}^{\perp}$.

For plane waves propagating in the positive x-direction, the velocity can be expressed as (Cremer, Heckl and Ungar, 1988):

$$u(x,t) = Re\{\hat{u}e^{j\omega t - jkx}\} = \hat{u}\cos(\omega t - kx) \tag{5-12}$$

Making use of the complex wave number results in:

$$u(x,t) = Re\left\{\hat{u}e^{j\omega t - j\underline{k}_B{}^{\perp}x - \underline{k}_B{}^{\shortparallel}x}\right\} = \hat{u}e^{-\underline{k}_B{}^{\shortparallel}x}\cos(\omega t - \underline{k}_B{}^{\perp}x) \tag{5-13}$$

This implies exponential decay of propagating plane waves. The amplitude of particle velocity decays by a factor of $e^{-\underline{k}_B{}^{\shortparallel}}$. For bending waves, $\underline{k}_B{}^{\shortparallel} \approx \pi\eta/2\lambda_B$, thus the amplitude decays by a factor of $e^{\frac{-\pi\eta}{2\lambda_B}}$. The bending wave energy can be expressed as $E_B = mu^2(x,t)$. Hence the amplitude of energy decays by a factor of $e^{\frac{-\pi\eta}{\lambda_B}}$. Within a distance Δx there occurs an energy reduction in level by:

$$Energy\ reduction = 10\log\left(e^{\frac{\pi\eta}{\lambda_B}\Delta x}\right) = \frac{4.34\pi\eta\Delta x}{\lambda_B}\,dB = 8.7\underline{k}_B{}^{\shortparallel}\Delta x\ dB \tag{5-14}$$

When the bending wave starts with $u(x_0,t_0)$ and travels with a distance L, the travelling time is $L\frac{\underline{k}_B{}^{\perp}}{\omega}$.

Thus the ratio of the initial bending wave energy, i.e. E_0, to the energy when the wave arrives $x = x_0 + L$, i.e. E_L, is:

$$\frac{E_0}{E_L} = \frac{mu^2(x_0, t_0)}{mu^2\left(x_0 + L, t_0 + L\frac{\underline{k_B}^{\perp}}{\omega}\right)}$$

$$= \left\{ \frac{\hat{u}e^{-\underline{k_B}^{\shortparallel} x_0} \cos(\omega t_0 - \underline{k_B}^{\perp} x_0)}{\hat{u}e^{-\underline{k_B}^{\shortparallel}(x_0+L)} \cos\left[\omega\left(t_0 + L\frac{\underline{k_B}^{\perp}}{\omega}\right) - \underline{k_B}^{\perp}(x_0 + L)\right]} \right\}^2 \qquad (5\text{-}15)$$

$$= e^{2\underline{k_B}^{\shortparallel} L}$$

This gives:

$$E_L = E_0 * e^{-2\underline{k_B}^{\shortparallel} L} \qquad (5\text{-}16)$$

where the real part of bending wave number $\underline{k_B}^{\perp} = \frac{\omega}{c_B}$, the bending wave speed in plates $c_B = \left(\frac{4\pi^2 f^2 B}{\rho_s}\right)^{1/4}$ and the bending stiffness for plates $B = \frac{Eh^3}{12(1-\mu^2)}$ (Craik, 1996).

Each time a ray is incident with the boundary, a certain amount of energy is transmitted if the boundary is connected to another plate. The proportion of the transmitted energy to the incident energy is called the transmission coefficient, i.e. τ. It depends on the incident angle of the ray, the nature of the joint and the material properties of both subsystems.

The transmission coefficient (transmission efficiency) for two perpendicular plates (commonly referred to as a corner joint) is (Cremer, Heckl and Ungar, 1988):

$$\tau = \frac{2\varphi\sqrt{\chi^2 - \sin^2\theta_{raN}}\cos\theta_{raN}}{\varphi^2 + \varphi\left[\sqrt{(\chi^2 + \sin^2\theta_{raN})(1 + \sin^2\theta_{raN})} + \sqrt{(\chi^2 - \sin^2\theta_{raN})}\cos\theta_{raN}\right] + \chi^2}$$

$$\chi = \frac{k_2}{k_1} = \frac{\lambda_1}{\lambda_2} = \sqrt[4]{\frac{m_2' B_1}{m_1' B_2}}$$

$$\varphi = \frac{{k_2}^2 B_2}{{k_1}^2 B_1} = \sqrt{\frac{m_2' B_2}{m_1' B_1}} \qquad (5\text{-}17)$$

where χ and φ are introduced to simplify the expression and $m_1{}'$ and $m_2{}'$ are the surface densities for each plate respectively.

When the two plates share the same properties, $\chi = \varphi = 1$, thus:

$$\tau = 0.5 \cos^2 \theta_{raN} \tag{5-18}$$

The incident energy of the N^{th} intersecion is then calculated by:

$$IE_{0N} = E_0 \cdot e^{-2\underline{k}_B{}^{\shortparallel} D_{0N}} \cdot (1-\tau)^{N-1} \tag{5-19}$$

where E_0 is the original total energy contained in each ray. Here, it is assumed that the damped subsystem is connected to four similar subsystems and they share similar properties except the internal loss factor.

The information of the incident energy, the reflection angles and the incident angles is stored in the matrix of incident energy, i.e. mat_E (see Figure 5-9).

IE_{02} is the incident energy from the origin to the 2nd intersection.

mat_E: Incident Energy					
Source 1	x_0	IE_{01}	IE_{02}	…	IE_{0N}
	IRA 1	θ_{ra1}	θ_{ra2}	…	θ_{raN}
	Sta. Ang. 1	Inc. Ang. 1	Inc. Ang. 2	…	Inc. Ang. N
Source 1	x_0				
	IRA 2				
	Sta. Ang. 2				
…	…				
Source 1	x_0				
	IRA ang				
	Sta. Ang. ang				
Source 2	x_0^2				
	IRA 1				
	Sta. Ang. 1				
Source 2	x_0^2				
	IRA 2				
	Sta. Ang. 2				
…	…				
Source 2	x_0^2				
	IRA ang				
	Sta. Ang. ang				
……	……				
Source n	x_0^n				
	IRA 1				
	Sta. Ang. 1				
Source n	x_0^n				
	IRA 2				
	Sta. Ang. 2				
…	……				
Source n	Sta. Ang. 1				
	IRA 3				
	Sta. Ang. ang				

```
mat_E =

    0.5000    0.6565    0.3618    0.2357    0.0967
   30.0000   30.0000   60.0000   30.0000   30.0000
   60.0000   60.0000  120.0000   60.0000  120.0000
    0.5000    0.8334    0.5744    0.2357    0.1374
   30.0000   60.0000   30.0000   30.0000   60.0000
  120.0000  120.0000   60.0000  120.0000   60.0000
    1.0000    0.6945    0.5744    0.2357    0.1145
   30.0000   60.0000   30.0000   30.0000   60.0000
   60.0000   60.0000  120.0000   60.0000  120.0000
    1.0000    0.6945    0.5744    0.2357    0.1145
   30.0000   60.0000   30.0000   30.0000   60.0000
  120.0000  120.0000   60.0000  120.0000   60.0000
    1.5000    0.8334    0.5744    0.2357    0.1374
   30.0000   60.0000   30.0000   30.0000   60.0000
   60.0000   60.0000  120.0000   60.0000  120.0000
    1.5000    0.6565    0.3618    0.2357    0.0967
   30.0000   30.0000   60.0000   30.0000   30.0000
  120.0000  120.0000   60.0000  120.0000   60.0000
```

Example of a ray tracing result where n=3, ang=2 and N=4.

Figure 5-9 Matrix of incident energy

With these three matrixes, one can easily find the intersection information on certain boundary, i.e. the coordinates of each intersection, the travel distance of each ray and its incident angle. The incident energy and corresponding reflection angle of each ray can be used to compute the energy transmitted through each boundary for that specific ray. This enables one to further study the energy distribution along each edge.

5.6 Study on theoretical model

5.6.1 Introduction to the model

This section seeks to examine the energy transmission across a heavily damped plate. A five-plate system is examined to understand the quantity and distribution of the incident and transmitted energy along different edges of the damped plate. Further numerical study also shows a possible way to quantify the strength of the coupling between subsystems across the damped element using effective coupling loss factors.

The model is assumed to be connected as shown in Figure 5-10. Five identical plates, sharing same geometry and material properties (Table 5-1), are connected perpendicular to each other as shown in the figure. A damping treatment is assumed to be applied on plate 2, which can alter the ILF of the damped plate without changing its other properties.

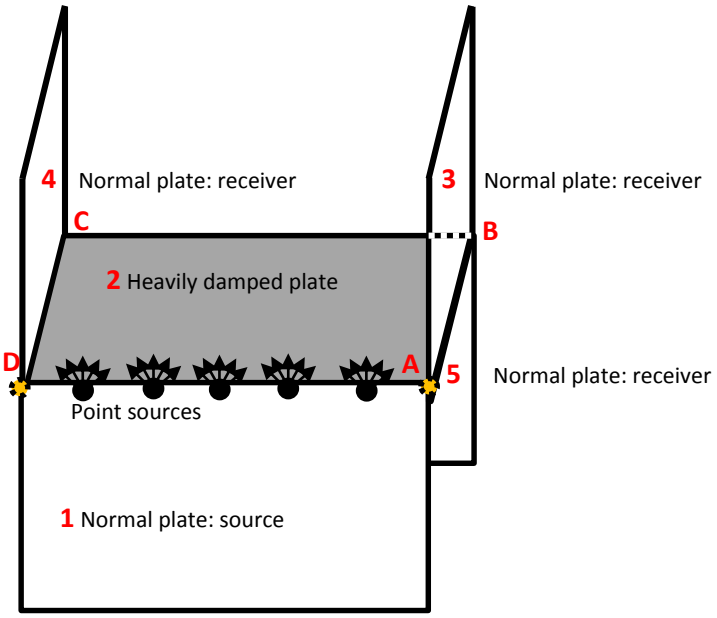

Figure 5-10 Ray tracing model

Table 5-1 Properties of the tray trace model

Material	Density Kg/m^2	Young's modulus N/m^2	Longitudinal wave speed m/s	Dimensions m
Concrete	2300	30×10^9	3686	$2 \times 2 \times 0.005$

5.6.2 Energy distribution along the boundary

The ray tracing algorithm makes it possible to explore both incident and transmitted power at the plate boundaries. Figure 5-11 illustrates the phenomena for the 5 plate model shown in Figure 5-10. It assumes a frequency of 500Hz, an internal loss factor of 0.015 and 100 point sources distributed along edge AD, each radiating 180 rays into plate 2 (this creates sufficient number of rays to simulate the line source at the boundary). The rays are traced through 50 reflections and are assumed to lose energy due to propagation losses in the plate itself and due to transmission to plates coupled to the boundaries. The ratio of incident (or transmitted) power to the total power injected by the point sources is used to describe the angular dependence for each boundary. A sensitivity analysis is done to show that further increasing the number of rays or reflection number does not

have significant influence on the results. The number of sources/rays and reflection used in the rest of the thesis has been informed by this.

It may be seen that the boundaries perpendicular to the source edge (AB and CD) are dominated by energy incident at angles close to the boundary normal. Boundaries parallel to the source edge (AD and BC) are dominated by rays with incident angles close to $90°$. A global reference direction is used for coding simplicity, i.e. $45°$ on AB is the same as $135°$ on CD. In both cases, the rays with these incident directions will tend to have the shortest transmission paths for any given order of reflection.

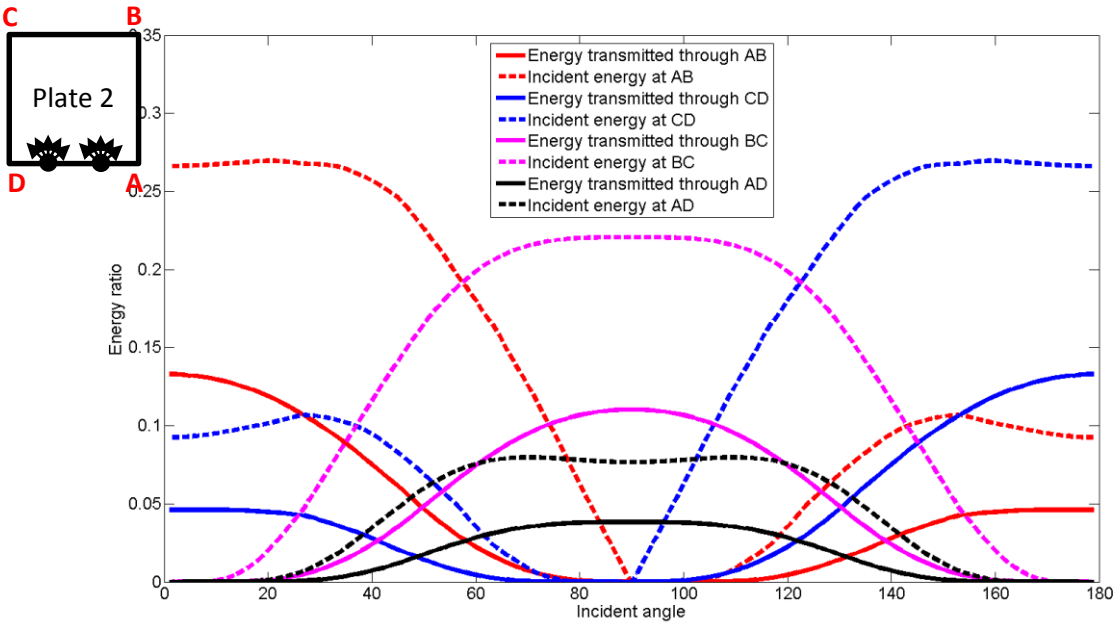

Figure 5-11 Energy ratio at four edges of plate 2 (average across each whole edge) at 500Hz

5.6.3 Effective length ratio

Energy transmitted across different edges of the damped plate from the model shown in Figure 5-10 is examined. It is found that the transmitted energy is not evenly distributed along the length of each boundary. A parameter called 'effective length ratio' is proposed to describe this phenomenon.

5.6.3.1 Edge AB

If one discretises boundary AB into a number of small segments, say 20 in this case (i.e. each segment has a length of 0.1m, which gives sufficient resolution for further analysis without adding too much computational cost), and looks at the incident energy on each segment, one may find that, for edge AB, the incident energy tends to concentrate on the region that is close to the source arriving with very small and very large incident angles (Figure 5-12). This is believed to be a result of direct transmission, i.e. the rays that directly land on edge AB (which have the biggest contribution), and lower order reflection, i.e. the rays that land on edge AB after only a few reflections. The energy losses due to attenuation with distance and at the losses that occur at the boundaries (i.e. transmitted to other subsystems) make the rays with longer travelling distance less important in energy transmission from plate 2 to plate 3. This effect is clearer if one increases the ILF to a value of 0.060 and replots the results (Figure 5-13).

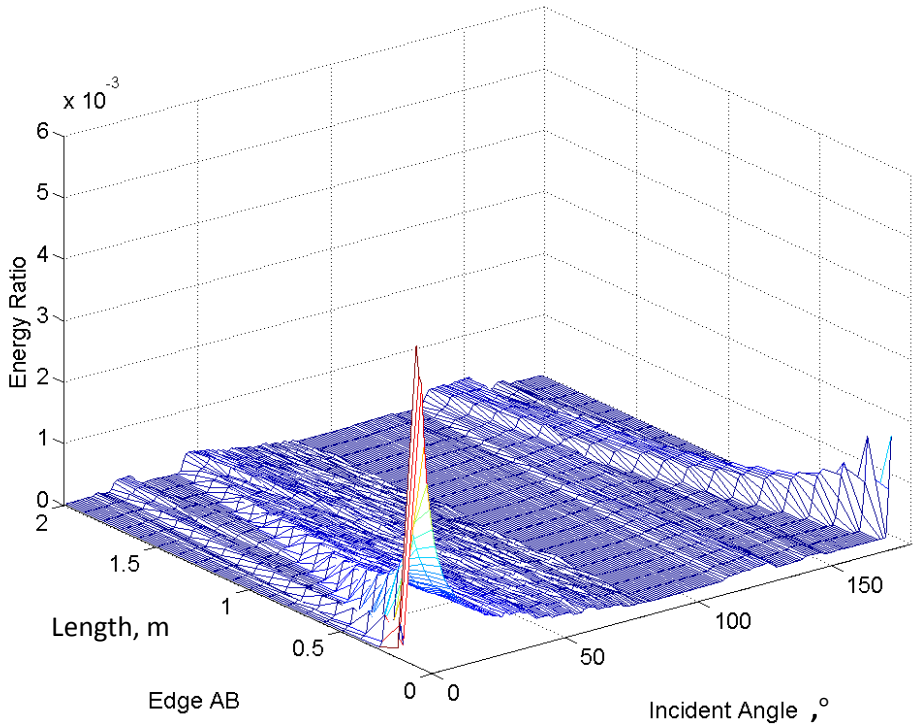

Figure 5-12 3D plot of the energy ratio (incident energy/total initial energy) against length and incident angle with ILF=0.015 at 500Hz (Edge AB)

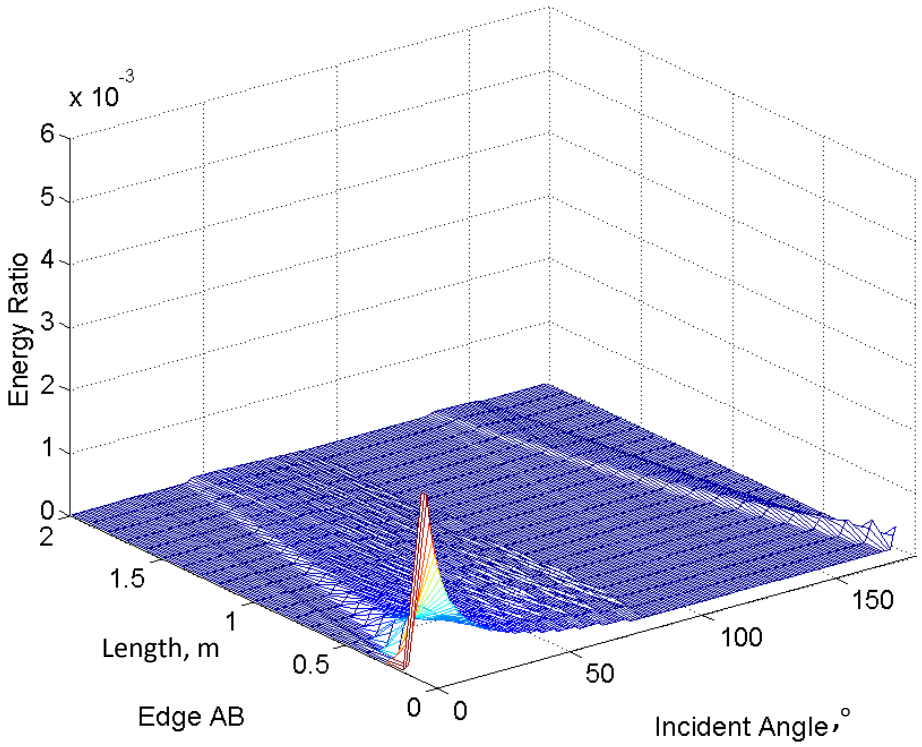

Figure 5-13 3D plot of the energy ratio (incident energy/total initial energy) against length and incident angle with ILF=0.060 at 500Hz (Edge AB)

5.6.3.2 Concept of effective length ratio

If one plots the energy ratio of the energy transmitted through each joint segment to the total energy transmitted, one may find the energy transmitted through each boundary segment appears to have a power decay (Figure 5-14). Majority of the energy transmitted through the segments that are closer to the source and this effect becomes more significant as the ILF increases. This finding effectively suggests that there exists an effective length where the majority of the energy can be transmitted through that joint. It might be more sensible to define an effective length to be the length where certain percent (for example 90%, or greater) of the total energy transmission occurs. If one uses 90% as the threshold to define the effective length, the corresponding effective length for plate 2 with ILF of a value of 0.015 is calculated to be $1.68m$ and the value calculated for the damped system (ILF=0.060) is $1.34m$ (Figure 5-15).

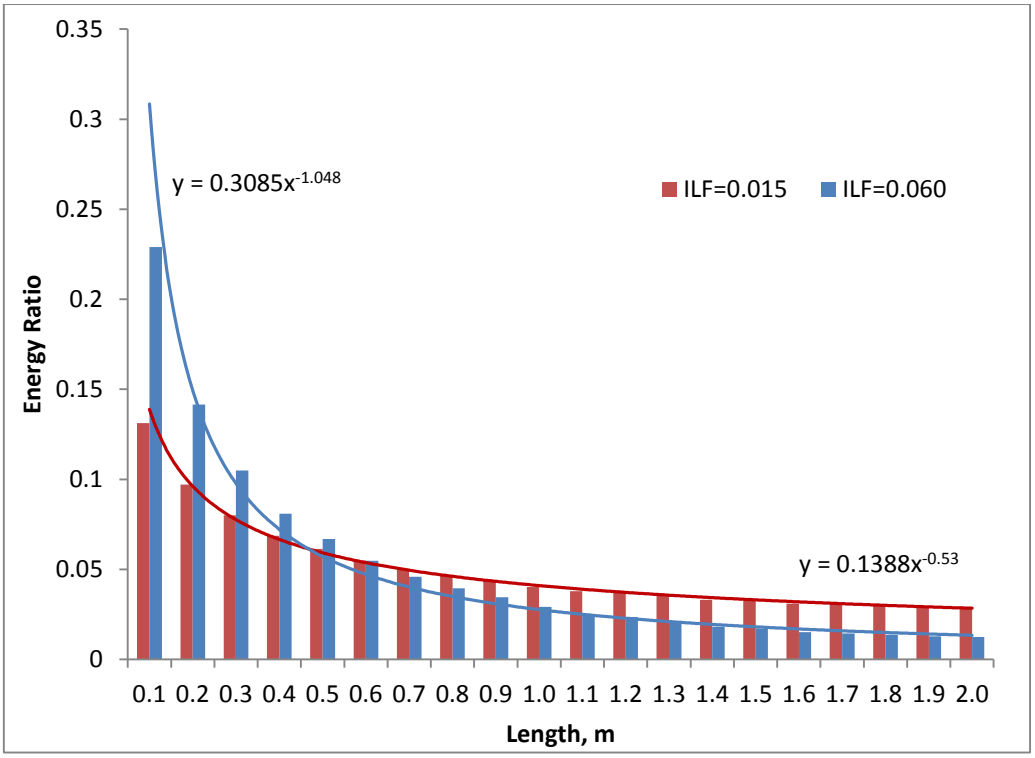

Figure 5-14 Energy ratio at 500Hz (energy transmitted through each segment/total energy transmitted through edge AB) against length with ILF=0.015 and ILF=0.060 at 500Hz (AB=2m)

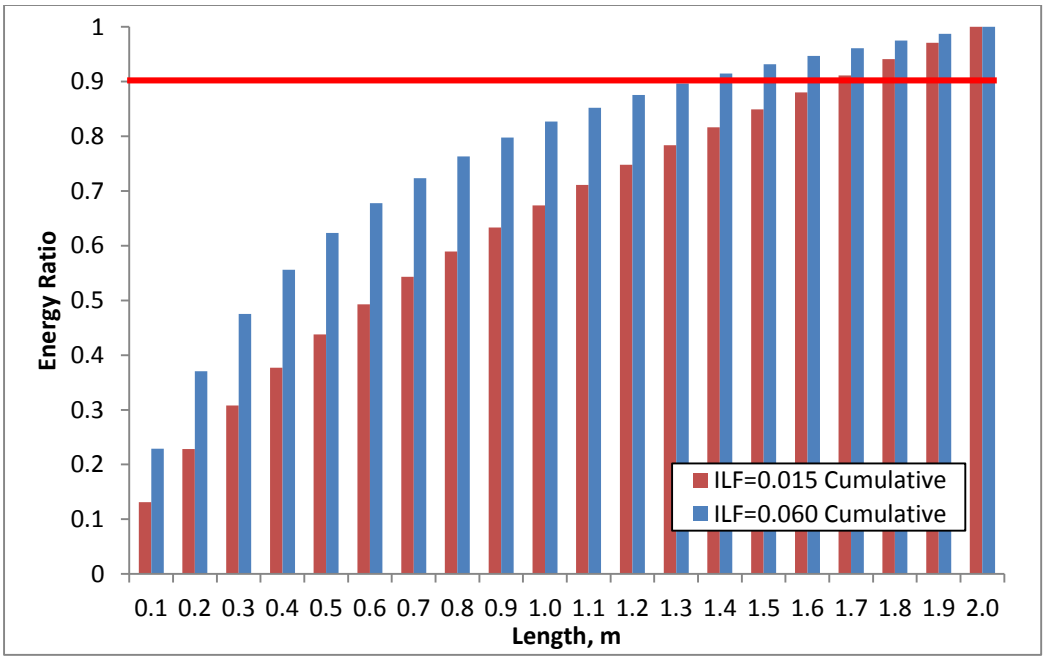

Figure 5-15 Cumulative plot of Figure 5-14

If one doubles the length of AB and does the same analysis, the majority of energy transmission still concentrated on the segments that are close to the source (Figure 5-16). The effective lengths in this case are 3.1m for the undamped plate and 1.8m for the damped plate. Only in this case, the energy concentration is more significant. One may define the 'effective length ratio', denoted as r_e, as:

$$r_e = \frac{\text{effective length}}{\text{total length}} \tag{5-20}$$

This parameter gives a description of the phenomenon of energy transmission concentration at edge AB. A smaller value indicates more significant concentration and it would suggest that it is less likely to be appropriate to consider this damped element as an SEA subsystem.

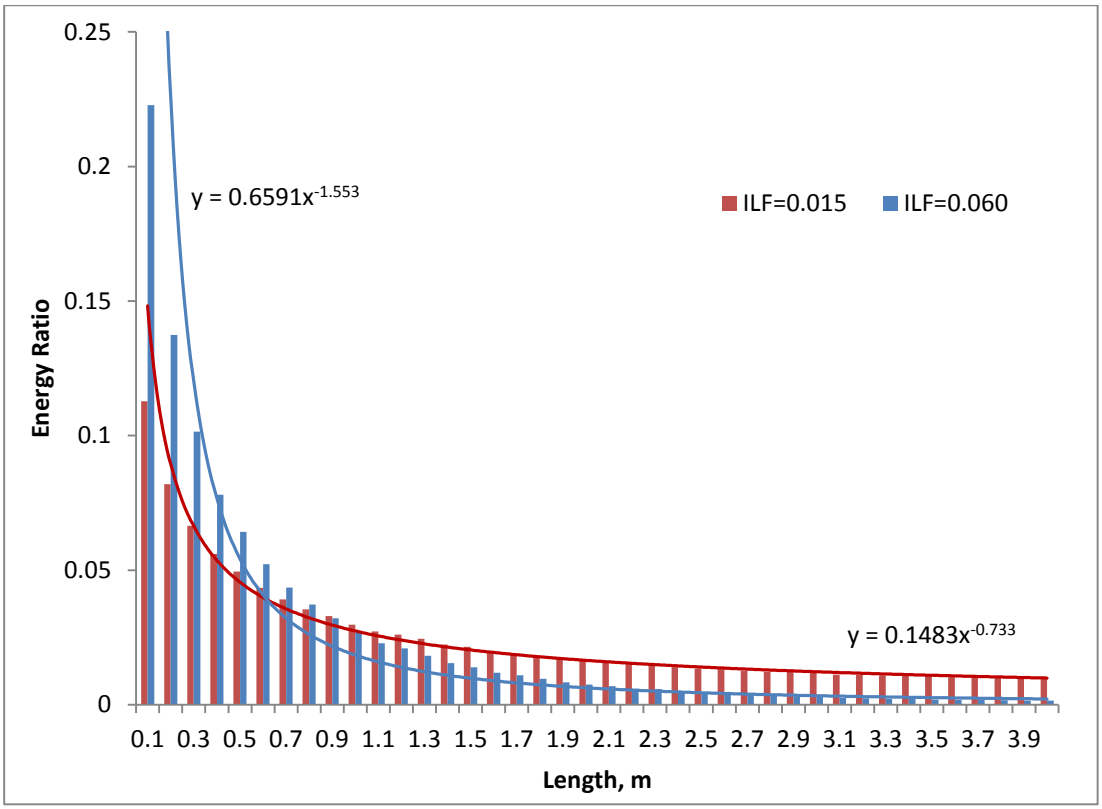

Figure 5-16 Energy ratio at 500Hz (energy transmitted through each segment/total energy transmitted through edge AB) against length with ILF=0.015 and ILF=0.060 at 500Hz (AB=4m)

The effective length ratios for the cases shown in Figure 5-14 and Figure 5-16 are shown in Table 5-2. It suggests that as the ILF or the length of edge AB increases, the energy transmitted tends to concentrate more at edge AB.

Table 5-2 Effective length ratio at 500Hz for different AB lengths and ILFs

Effective length/Total length	ILF=0.015	ILF=0.060
AB=2m	0.85	0.7
AB=4m	0.775	0.45

These predictions relate to 500Hz. It is clear from the definition of complex wavenumber that the excitation frequency plays an important role. A plot of the excitation frequency against the effective length ratio is shown in Figure 5-17. As one increases the excitation frequency, the effective length ratio becomes smaller which indicates that energy concentration near to the source boundary (plate) becomes more obvious. Changing the excitation frequency does not alter the distribution of rays, it however increases the number of cycles the wave will have before it lands on edge AB. This effectively increases the energy loss along the path.

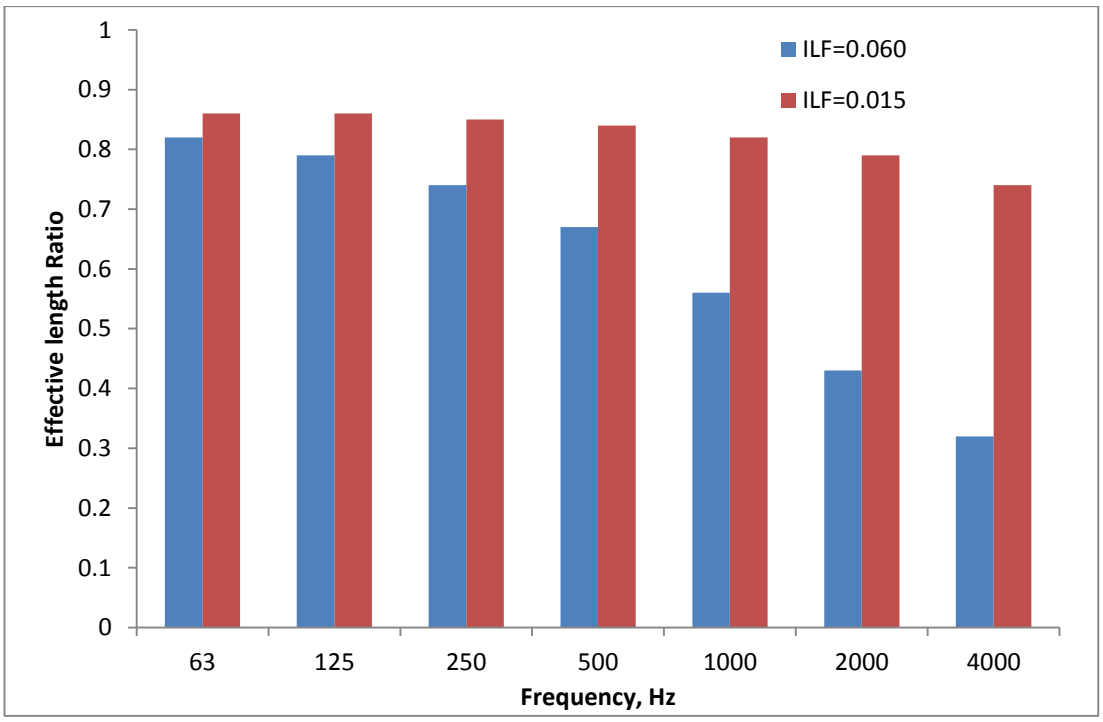

Figure 5-17 Excitation frequency against effective length ratio for ILF=0.015 and ILF=0.060 (AB=2m)

The previous discussion suggests that there are two mechanisms that have a direct relation to the energy concentration phenomenon. One is related to the geometry of the plate. As the size of the plate gets larger, each ray has a longer travel path which results in more energy dissipation. The other is related to the ILF and the excitation frequency. Although the travel distance has not been changed for each ray, either increasing the ILF or the excitation frequency results in more energy loss along the distance.

5.6.3.3 Edge BC and AD

A similar analysis was undertaken for edge BC and AD. As one increases the ILF, the incident energy will decrease as expected (Figure 5-18 and Figure 5-19; Figure 5-20 and Figure 5-21). Edge AD generally receives less energy than edge BC because the rays landing on edge AD generally travel further and undergo more reflections than those landing on edge BC (Figure 5-18 and Figure 5-20; Figure 5-19 and Figure 5-21).

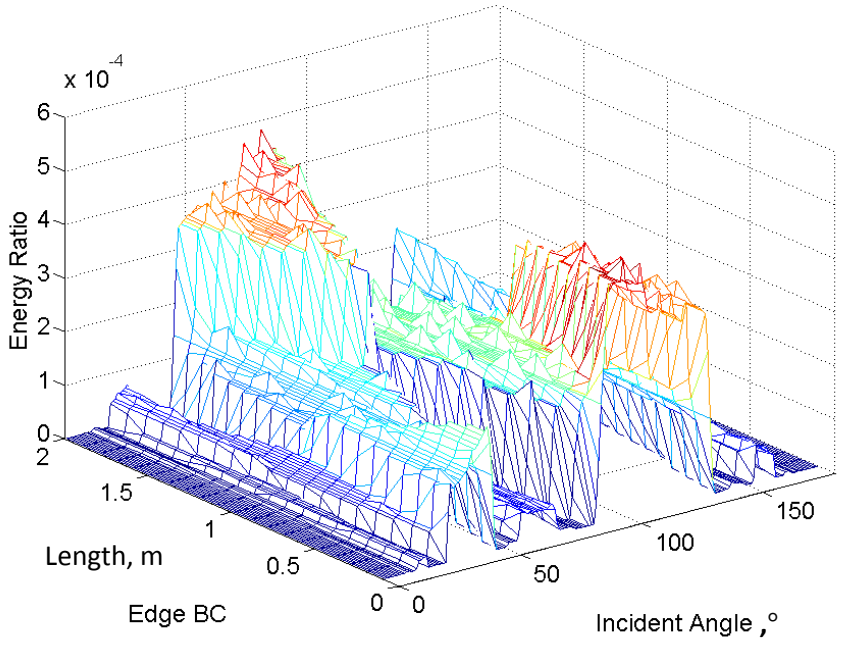

Figure 5-18 3D plot of the energy ratio (incident energy/total initial energy) against length and incident angle with ILF=0.015 at 500Hz (Edge BC)

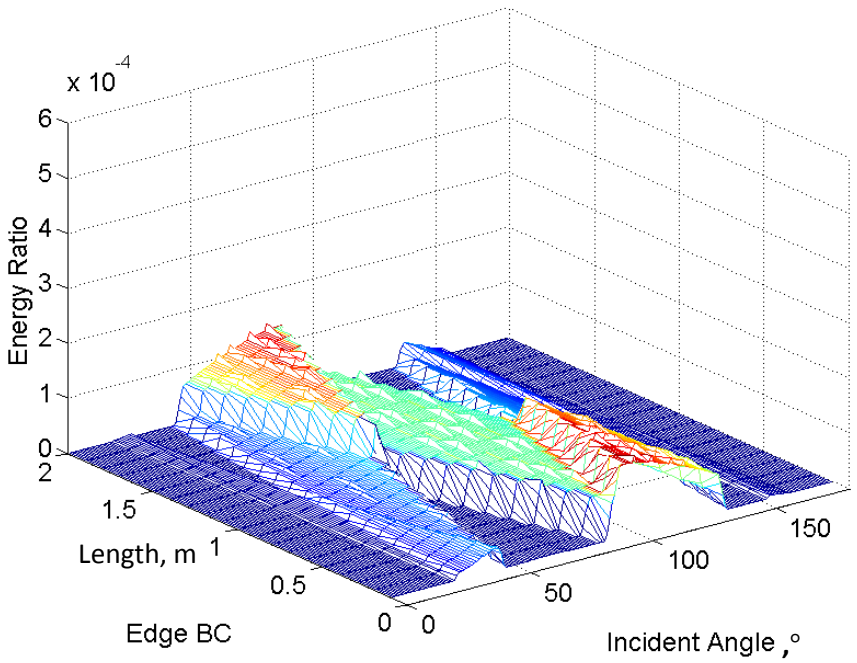

Figure 5-19 3D plot of the energy ratio (incident energy/total initial energy) against length and incident angle with ILF=0.060 at 500Hz (Edge BC)

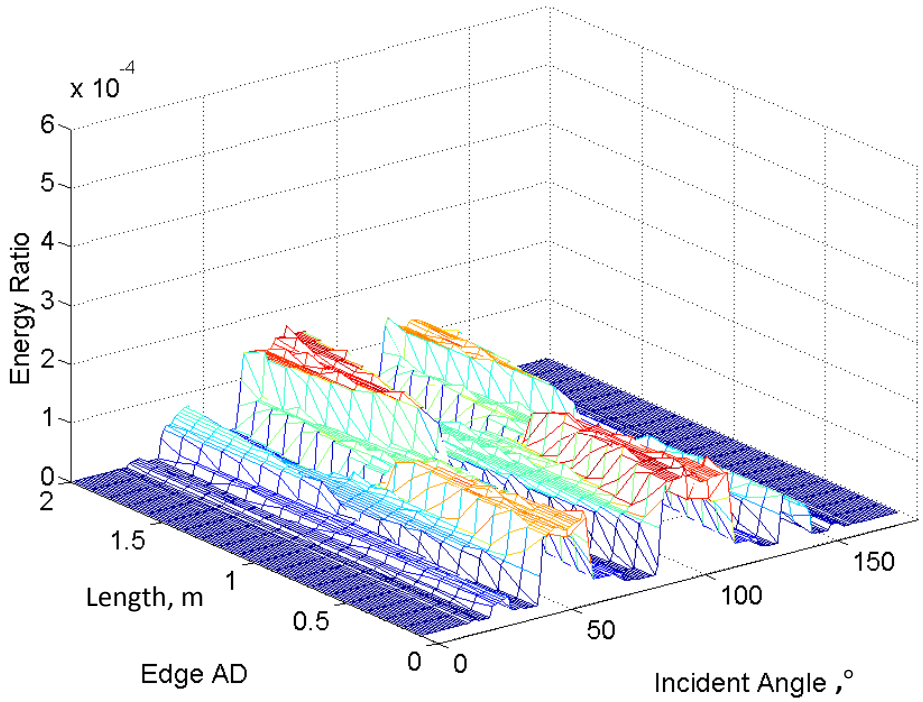

Figure 5-20 3D plot of the energy ratio (incident energy/total initial energy) against length and incident angle with ILF=0.015 at 500Hz (Edge AD)

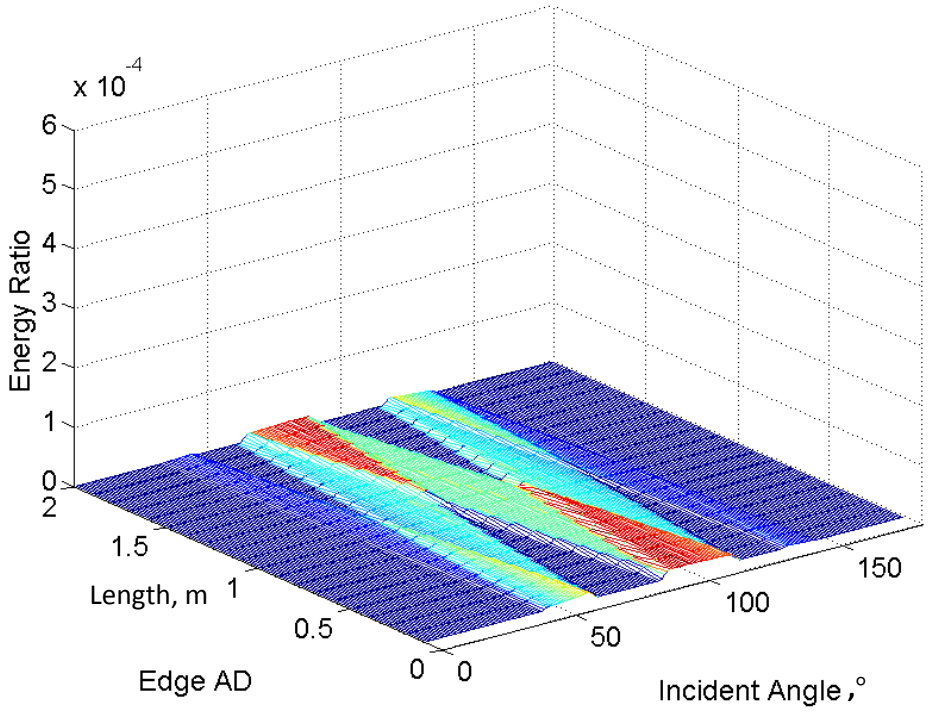

Figure 5-21 3D plot of the energy ratio (incident energy/total initial energy) against length and incident angle with ILF=0.060 at 500Hz (Edge AD)

For edges BC and AD, there is an even energy distribution (Figure 5-22 and Figure 5-23). Therefore no effective length can be obtained for those two edges.

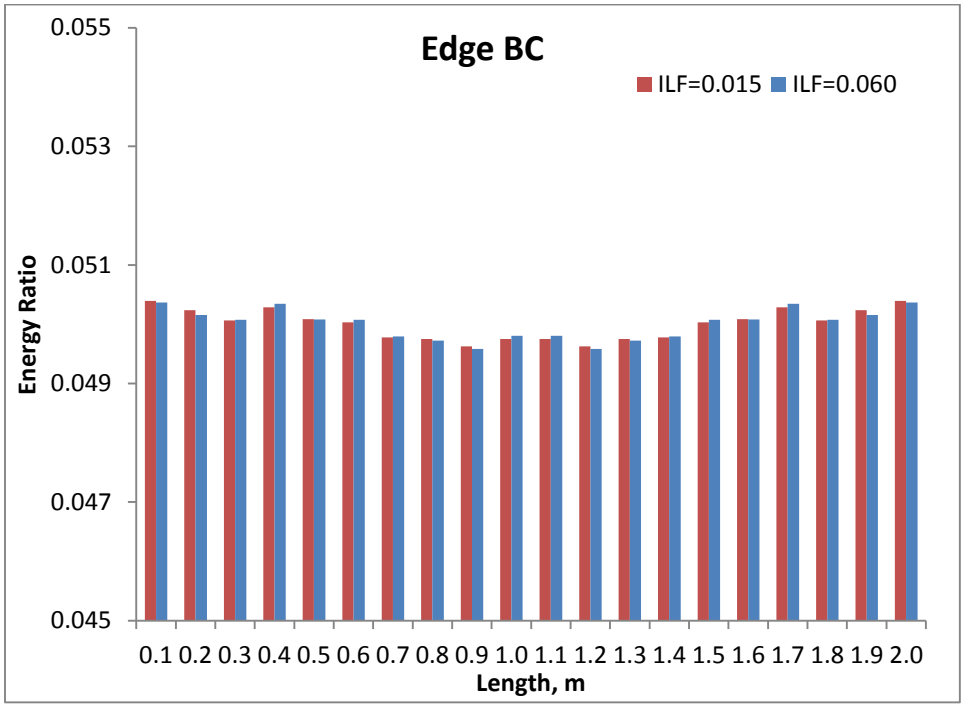

Figure 5-22 Energy ratio at 500Hz (energy transmitted through each segment/total energy transmitted through edge BC) against length with ILF=0.015 and ILF=0.060

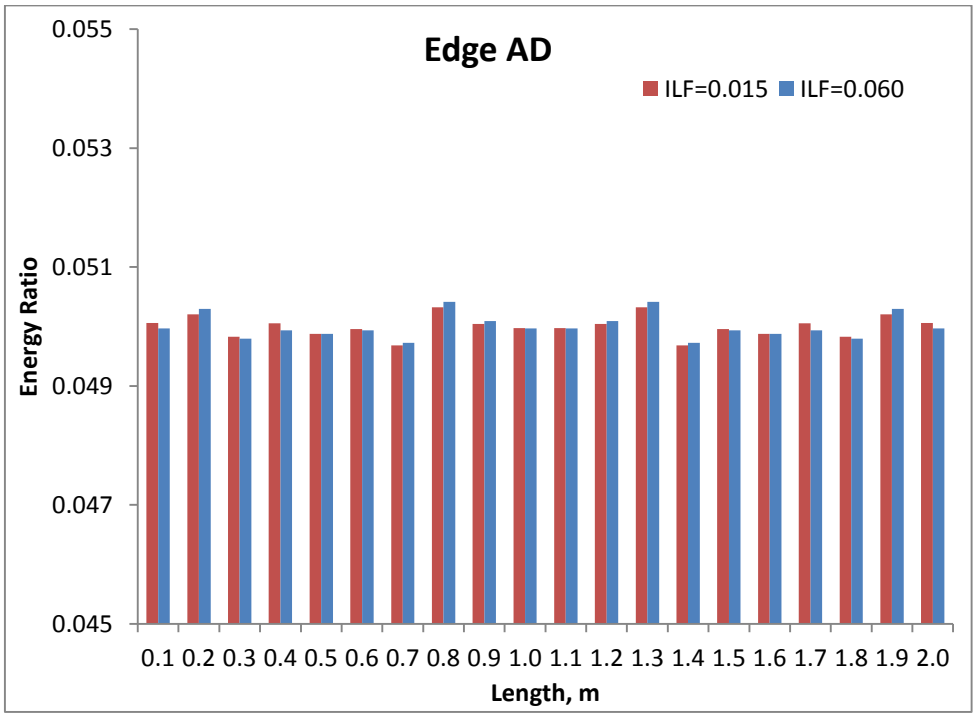

Figure 5-23 Energy ratio at 500Hz (energy transmitted through each segment/total energy transmitted through edge AD) against length with ILF=0.015 and ILF=0.060

5.6.3.4 Generalization

To further understand the contribution from direct field and first order reflection field, an illustration is shown in Figure 5-24. It shows the contribution from direct field and first order reflection field to the total energy transmitted through each segment of edge AB. For both undamped and damped cases, the contribution from direct field tends to be dominant if the segments are closer to the source. When the ILF gets higher, the contribution from direct field becomes even more significant. The first order reflection field tends to play an important role when the segments are far away from the source and becomes as important as the direct field at the far end of edge AB.

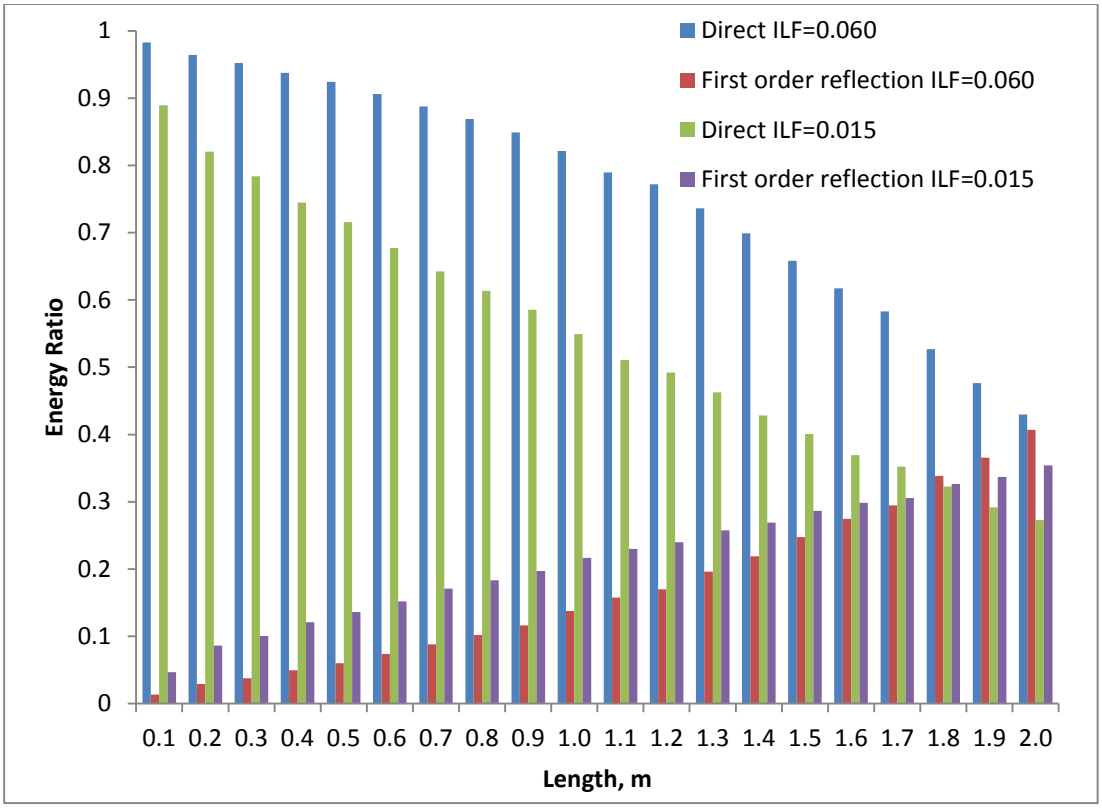

Figure 5-24 Energy ratio (contribution from direct field or first order reflection field to the total energy transmitted through each segment) against length with ILF=0.015 and ILF=0.060 (edge AB)

A simpler way to understand the energy distribution in plate 2 is shown in Figure 5-25. Assuming there is only one point source, the biggest contribution comes from direct field, i.e. triangle SAE, SFD and SBC. Rays with longer travelling distance, i.e. direct transmission in triangle SEB and SCF, or reflected transmission, make less of a contribution to energy transmission at the boundary.

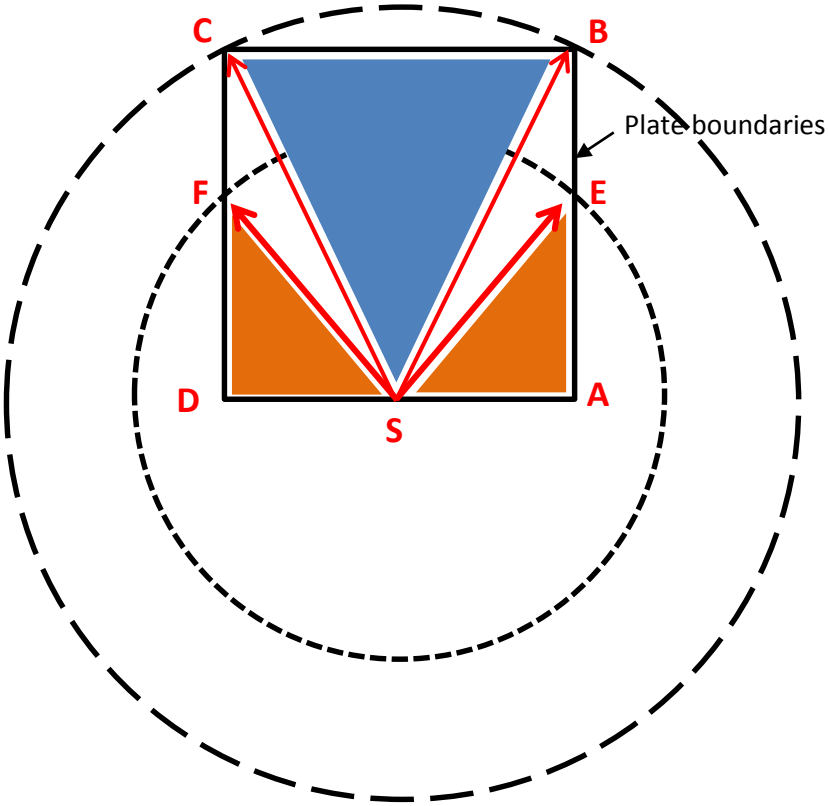

Figure 5-25 Illustration of the ray trace model with single point source

5.6.4 Comparison with SEA modelling

Having developed a model that describes transmission in damped structures, the next step is to explore how this can assist in their inclusion within the SEA framework. The starting point will be modelling the system in Figure 5-10 using standard SEA method.

5.6.4.1 SEA modelling

A pure SEA model (Figure 5-26) can be built for the system shown in Figure 5-10. In this, subsystem 2 represents the element that couples all of the receiving subsystems.

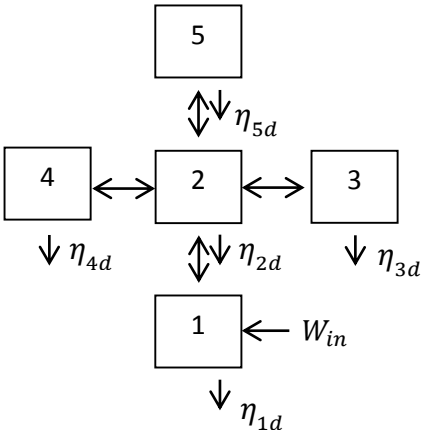

Figure 5-26 SEA model of the 5 plate ray tracing model

The power balance equations can then be written as:

$$E_1\omega(\eta_{1d}+\eta_{12})-E_2\omega\eta_{21}=W_{in}$$

$$E_1\omega\eta_{12}-E_2\omega(\eta_{21}+\eta_{23}+\eta_{24}+\eta_{25}+\eta_{2d})+E_3\omega\eta_{32}+E_4\omega\eta_{42}+E_5\omega\eta_{52}=0$$

$$E_2\omega\eta_{23}-E_3\omega(\eta_{3d}+\eta_{32})=0$$

$$E_2\omega\eta_{24}-E_4\omega(\eta_{4d}+\eta_{42})=0$$

$$E_2\omega\eta_{25}-E_5\omega(\eta_{5d}+\eta_{52})=0$$

(5-21)

This can be solved to give the subsystem energy and hence the energy level difference between the different systems.

5.4.6.2 Hybrid SEA & Ray tracing modelling

One may alternatively use the ray tracing code to work out the averaged transmission coefficients $\overline{\tau}_{ij}$ at four boundaries using its original definition through:

$$\overline{\tau}=\frac{total\ transmitted\ energy}{total\ incident\ energy}=\frac{\sum IE_i*\tau_i}{\sum IE_i} \quad (5\text{-}22)$$

where IE_i is the incident energy at that specific boundary and τ_i is the angle dependent transmission coefficient of that specific ray at the boundary. This can be used to compute the CLFs between each pair of subsystems through (Craik, 1996):

$$\eta_{ij} = \frac{1}{\pi\left(\sqrt{3}\pi\right)^{0.5}}\left[\frac{h_i C_{\mathrm{Li}}}{f}\right]^{0.5}\frac{L_{ij}}{s_i}\overline{\tau}_{ij} \tag{5-23}$$

The obtained CLFs can then be readily used in SEA to find the energy level differences.

If one assumes there is no internal loss in plate 2, the CLFs obtained by using this method for the theoretical model at 500Hz are:

$$\eta_{23} = \eta_{24} = 96.2 \text{ dB re } 10^{-12}$$

$$\eta_{25} = 96.7 \text{ dB re } 10^{-12}$$

$$\eta_{21} = 96.8 \text{ dB re } 10^{-12}$$

The corresponding CLFs calculated by SEA are:

$$\eta_{21} = \eta_{23} = \eta_{24} = \eta_{25} = 96.4 \text{ dB re } 10^{-12}$$

Those two approaches yield very similar answers. Similar comparisons have been undertaken for 1/3 octave bands with centre frequencies from 20Hz to 20,000Hz and have shown same findings, i.e. the difference between those two approaches is not frequency dependent. This comparison also serves as an initial theoretical validation of the proposed ray tracing code.

5.4.6.3 Ray tracing modelling

When subsystem 2 is heavily damped, there is assumed to be weak modal behaviour of subsystem 2. As a result, the transmission from subsystem 1 to other subsystems via subsystem 2 cannot be calculated effectively using normal SEA equations. Under these circumstances, the ray tracing method described in Section 5.6 offers a means of predicting transmission by representing heavily damped components within the SEA framework of analysis.

If it is assumed each ray contains energy E_0, the initial total energy from the rays, i.e. $n * ang * E_0$, equals the energy transmitted from Subsystem 1 to Subsystem 2:

$$n * ang * E_0 = E_1 \omega \eta_{12} \tag{5-24}$$

One can use ray tracing to get the actual energy transmitted from Subsystem 2 to Subsystem i, denoted as W'_{2i}.

For Subsystem 3, one obtains the energy balance equation:

$$W'_{23} = E_3 \omega (\eta_{3d} + \eta_{32}) \tag{5-25}$$

For Subsystem 4, one obtains

$$W'_{24} = E_4 \omega (\eta_{4d} + \eta_{42}) \tag{5-26}$$

For Subsystem 5, one obtains

$$W'_{25} = E_5 \omega (\eta_{5d} + \eta_{52}) \tag{5-27}$$

Hence one can get the energy of each subsystem except Subsystem 2 and eventually get the energy level difference.

In this scenario, subsystem 2 can be removed from the SEA modelling. Instead, the CLFs between the source subsystem to other subsystems occurring via the heavily damped plate can be calculated through:

$$\eta_{13} = \frac{W'_{23}}{E_1 \omega} \tag{5-28}$$

$$\eta_{14} = \frac{W'_{24}}{E_1 \omega} \tag{5-29}$$

$$\eta_{15} = \frac{W'_{25}}{E_1 \omega} \tag{5-30}$$

where $E_1 = n * ang * E_0 / \omega \eta_{12}$ is obtained by rearranging Equation 5-24.

5.4.6.4 Comparison

The energy level differences estimated from a pure SEA model (bending only and three wave) and the proposed inclusion of ray tracing within SEA are shown in Figure 5-27 and Figure 5-28. Predictions from bending only and three wave model do not have significant difference in the examined frequency range as expected.

When adding damping to subsystem 2, larger energy level differences are predicted using both approaches. The discussion in Section 5.6 indicates that for heavily damped subsystem, more energy is transmitted through edges that are perpendicular to the source edge. The prediction from the pure SEA model indicates that the energy transmission along these edges are the same, i.e. ELD13=ELD15. The results in Figure 5-27 and Figure 5-28 show that the energy level difference between subsystem 1 and 3 predicted from ray trace has a smaller value and the energy level difference between subsystem 1 and 5 predicted from ray trace has a larger value. The difference between the prediction from the pure and hybrid SEA predictions tends to increase at higher frequencies in both cases. This is because the energy attenuation with distance becomes more significant at higher frequencies even the ILF stays the same. One may notice that ELD15 predicted from using the hybrid approach is much larger than that from SEA, especially in the high frequency region. For energy transmission from subsystem 1 and 3, even at high frequencies with large ILF, short paths in the direct field are dominant. The direct field transmission from subsystem 1 and 5 generally involves the wave travelling a longer distance, i.e. all rays need to travel at least 2m before they hit edge BC. As a result, more energy has been converted to heat before it enters subsystem 5, which gives very large ELD15. In practice, one may hardly obtain a damping level with ILF=0.3. Thus the difference between the result from SEA and the hybrid method tends to be smaller than the ones showed in Figure 5-27 and Figure 5-28.

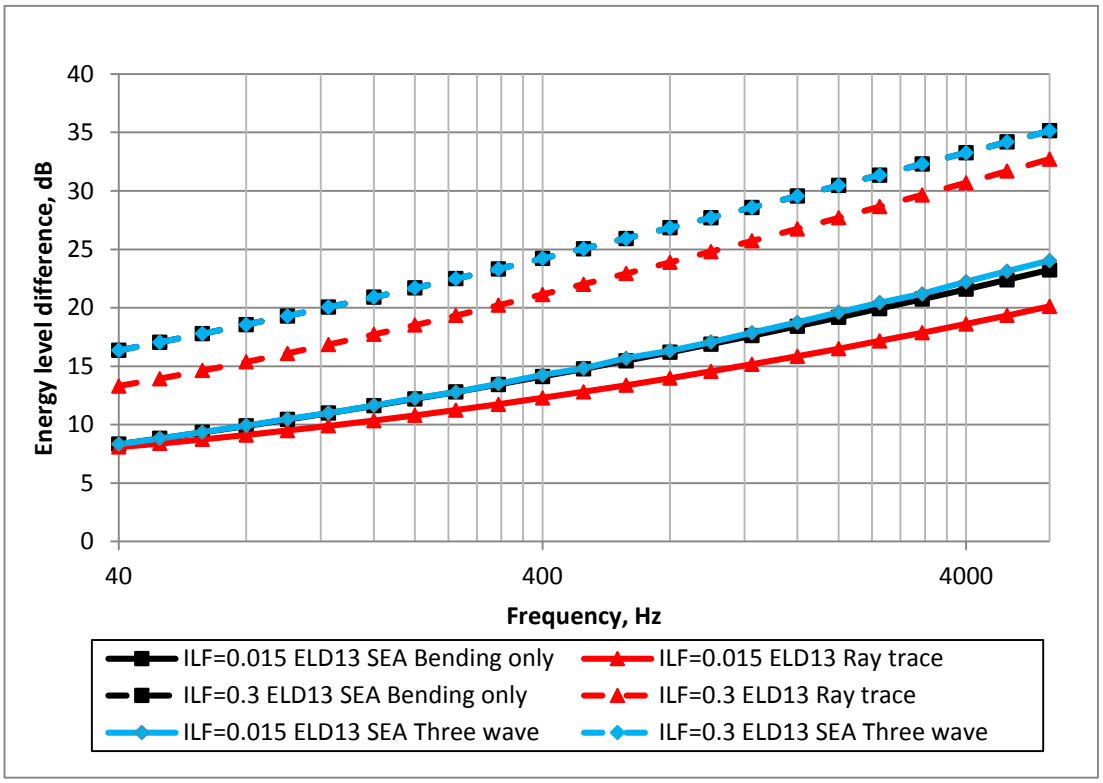

Figure 5-27 Energy level difference between subsystem 1 and 3

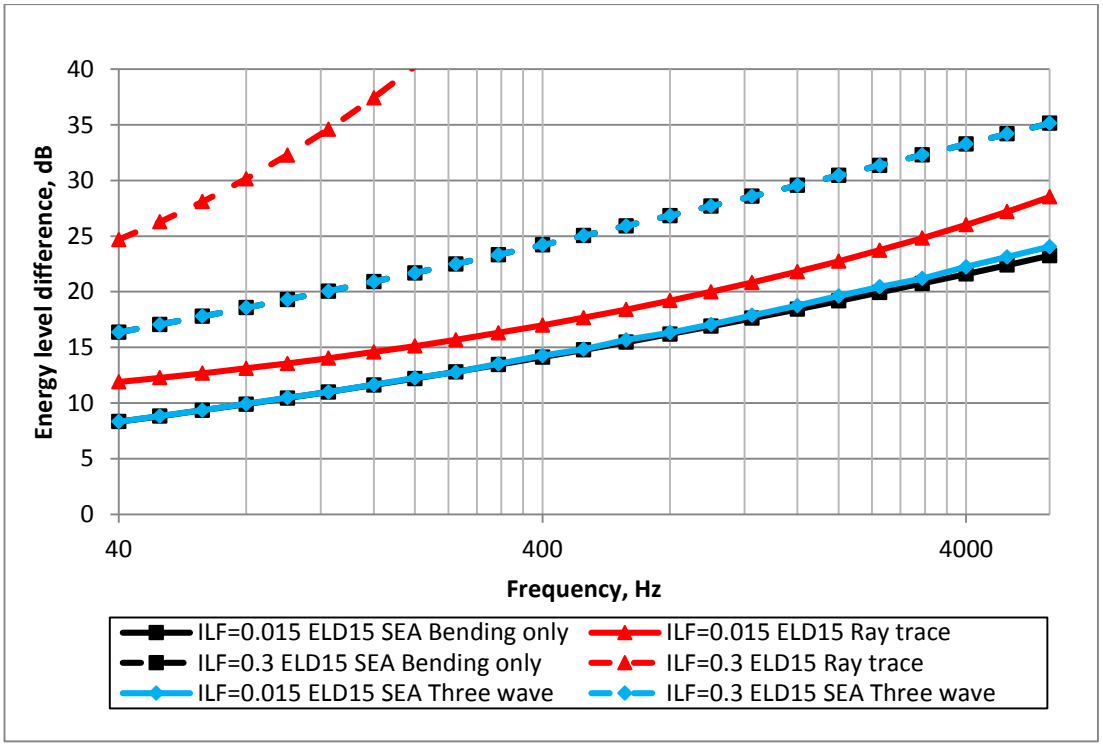

Figure 5-28 Energy level difference between subsystem1 and 5

5.7 Conclusion

This chapter sought to develop a ray tracing code that can be used to predict the energy transmission through a heavily damped building component. Representing such components as damped subsystems in normal SEA is likely to prove unreliable since the assumption of energy equipartition within that subsystem tends to fail as internal damping grows.

A theoretical model has been presented that seeks to overcome this restriction and the results have shown that representing heavily damped component as a subsystem shows different behaviour compared with normal well-behaved SEA subsystem. The main observations are:

For a simple plate, increasing ILF always results in a reduction in energy available for transmission through its four edges. The energy transmission via different edges differs from each other. There are two important mechanisms that influence the energy transmission. One is the energy attenuation with distance, which is controlled by ILF and frequency. The other is the number of reflections, i.e. a certain amount of energy is transmitted to coupled subsystems each time the ray hits an edge.

There exists an effective length where the majority of the energy is transmitted via edges that are perpendicular to an edge receiving energy (represented in the modal as a line source). As the loss factor or the length of a perpendicular edge grows larger, one observes that the energy concentration becomes more significant in the region most immediate to the source. This may be explained if it is noted that the direct field is normally dominant and it will play an important contribution in segments of any receiving boundary that are close to the source. The first order reflection field generally makes much less of a contribution and tends to contribute more in segments of any receiving boundary that are far from the source.

Boundaries that are parallel to a source boundary (edge) tend to exhibit an even transmitted energy distribution along their lengths.

The definition of effective length has been proposed as the length where 90% of the energy transmission occurs within that length. More importantly, a parameter called effective length ratio has been defined as the ratio of the effective length to the total length of that edge. It gives a direct description of the phenomenon of energy concentration along boundaries perpendicular to the source edge. Low values of the effective length ratio suggest a more significant energy concentration close to the source boundary and higher value implies that the transmitted energy is distributed more evenly. This parameter is used in Chapter 8 to describe whether a plate can be seen as heavily damped and should no longer be treated as a normal SEA subsystem.

The discussion so far describes the potential benefit of increasing the damping level and does not explore various ways of passive damping treatments. This will be examined in the next chapter.

CHAPTER 6 DAMPING TREATMENT

6.1 Introduction

Having explored how to represent heavily damped components within the SEA framework, this chapter seeks to explore how high levels of damping may be achieved in practice. The primary focus of this knowledge will be to inform the design of test structures to yield experimental data for comparison with the hybrid SEA model. Different passive damping treatment techniques, i.e. the physical mechanisms behind them, the mathematic models that can be used to predict the damping effects are explored along with rule of thumb techniques to obtain higher damping levels and the theoretical max value of loss factor achievable.

6.2 Categories of damping treatments

An effective damping treatment is to apply damping material in such location where the greatest possible cyclic deformation of the viscoelastic material will occur as the structure vibrates in the modes of interest. This often requires one to have an understanding of the material properties of both the base structure and the damping component (i.e. the complex modulus properties) and the dynamic behaviour of the base structure under excitation. Additionally, in real engineering practice, one may also consider the applicable temperature and frequency range (since the viscoelastic damping properties are temperature-dependent and to a less degree frequency-dependent), bonding techniques and environmental factors (i.e. whether the components are exposed to liquids).

Noise in a dynamic system can be reduced in a number of ways. These can be briefly classified into three categories, namely passive control, active control and semi-active control (Rao, 2003).

Conventional passive control methods use isolators, absorbers, barriers, silencers, mufflers etc. to either isolate or absorb unwanted vibrational energy. Several damping treatments are available for passive damping control, namely free-layer damping, constrained-layer damping, tuned mass damping, granular damping etc. These treatment methods will be reviewed in this chapter.

Active control methods usually generate an out-of-phase signal to the disturbance and use certain active elements (i.e. speakers for air-borne noise and actuators for structural-borne noise) to cancel the unwanted response. Semi-active control (also known as hybrid active-passive) methods normally use both the active (piezoelectric) and passive (viscoelastic) damping treatments to minimize vibration. In building acoustic noise control, one is seeking an easy-to-apply and long-lasting damping treatment. Although the active and semi-active control methods may provide significant damping, the complexity of generating control algorithms, the relatively high initial investment and maintenance cost etc. all limit their application. Therefore, these two methods will not be discussed further in this study. Extensive studies of both methods can been found in the literature, especially in the field of engineering industry. One may refer to the reviews from Stanway, Rongong and Sims (2003) for active control methods and Trindade and Benjeddou (2002) for semi-active control methods.

6.3 Free layer damping

6.3.1 Basic configuration

Free layer damping is the simplest way of introducing lightweight damping into structures (Figure 6-1). It simply applies a viscoelastic layer on top of the base structure (a beam or plate). Because the damping layer has a larger modulus, when the system undergoes deformation, the damping layer generates extra restoring force and resists the deformation. To further understand the property of free layer damping, one may derive the expression of loss factor in the case of longitudinal wave and bending wave.

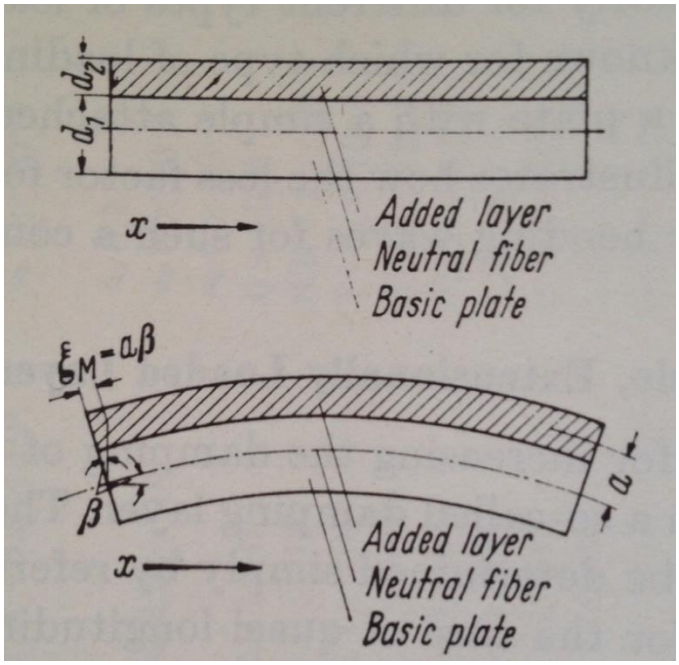

Figure 6-1 Free layer damping (Cremer, Heckl and Ungar, 1988)

6.3.2 One layer treatment

6.3.2.1 Longitudinal load

Recalling the definition of loss factor, it can be expressed as:

$$\eta = \frac{E_l}{2\pi E_m} \tag{6-1}$$

where E_l is the energy loss during one cycle of vibration and E_m is the (reversible) mechanical energy.

For cases involving longitudinal waves, the particle moves in the same direction as the wave propagation. The total mechanical energy can be given by (Cremer, Heckl and Ungar, 1988):

$$E_m = \frac{1}{2}(E_1 d_1 + E_2 d_2)|\varepsilon|^2 A = \frac{1}{2}(E_1 d_1 + E_2 d_2)\left|\frac{d\xi}{dx}\right|^2 A \tag{6-2}$$

where ξ represents the maximum displacement in one cycle, E_1 and d_1 are the real part of the complex modulus and the thickness of the base structure, E_2 and d_2 are the corresponding properties of the damping layer, and A is the surface area.

If one neglects the energy loss of the base structure, the energy lost per cycle of the system only comes from the damping layer and can be expressed as (Cremer, Heckl and Ungar, 1988):

$$E_l = \pi \eta_2 E_2 d_2 \left|\frac{d\xi}{dx}\right|^2 A \tag{6-3}$$

Therefore, the loss factor for longitudinal waves can be given by:

$$\eta_L = \eta_2 \frac{E_2 d_2}{E_1 d_1 + E_2 d_2} \tag{6-4}$$

One may note that the longitudinal loss factor is proportional to the loss modulus $\eta_2 E_2$ of the damping layer.

A simpler analysis can be given if one introduces the concept of complex stiffness. Since the deformation for longitudinal excitation is primarily extensional, the stiffnesses of the combined system are directly added:

$$k^* = k_1 + k_2(1 + i\eta_2) = (k_1 + k_2)(1 + i\frac{k_2 \eta_2}{k_1 + k_2}) \tag{6-5}$$

where $k^* = k(1 + \eta_L)$ is the stiffness of the combined system, k_1 and k_2 are the stiffness of the base structure and the damping layer. Therefore, the effective stiffness k and loss factor η_L can be given as:

$$k = k_1 + k_2 \tag{6-6}$$

$$\eta_L = \frac{k_2 \eta_2}{k_1 + k_2} \tag{6-7}$$

The expression for loss factor is identical to Equation 6-4. However, it is only accurate to predict the loss factor for beam-like members with simple boundary conditions (pinned-pinned or clamped-clamped) (Ross, Kerwin and Ungar, 1959).

6.3.2.2 Bending load

For cases of bending waves, which are more important for noise radiation, the deformation is primarily in extension. If one defines ξ_M as the displacement at the

centre-line of the damping layer, the energy loss can be given by (Cremer, Heckl and Ungar, 1988):

$$E_l = \pi \eta_2 E_2 d_2 \left| \frac{d\,\xi_M}{dx} \right|^2 A \tag{6-8}$$

and the bending mechanical energy can be expressed as (Cremer, Heckl and Ungar, 1988):

$$E_m = \frac{1}{2} B \left| \frac{d^2 \eta}{dx^2} \right|^2 A = \frac{1}{2} B \left| \frac{d\beta}{dx} \right|^2 A \tag{6-9}$$

where B is the bending stiffness of the whole system and β is the angle of flexure. If one defines a as the distance between the centre-line of the damping layer and the neutral axis (the line of zero stress in the cross section), then $\xi_M = a\beta$. Therefore, the loss factor for bending waves is:

$$\eta_B = \eta_2 \frac{E_2 d_2 a^2}{B} \tag{6-10}$$

Here a can be approximated as the distance between the middle of the base layer and damping layer, i.e. $a = (d_1 + d_2)/2$ (Kurtze, 1959), and B can be approximated as (Cremer, Heckl and Ungar, 1988):

$$B \approx \frac{E_1 {d_1}^3}{12} + E_2 d_2 a^2 \tag{6-11}$$

where the second term is only of importance when the damping layer is thicker than the base layer(i.e. $d_2 > d_1$). The analysis above assumes that the force in the damping layer is proportional to the modulus and to the strain and therefore the loss factor is independent of frequency. This assumption becomes vague when the bending wavelength in the base layer is of the same order as longitudinal wavelength in the damping layer. When this matching occurs, the damping layer may be deformed very easily and thus results in smaller losses. Fortunately, this matching only occurs at very high frequencies (around 10 kHz for metal plate with 1 cm thickness) for all good damping materials (Cremer, Heckl and Ungar, 1988).

An alternative analysis can be done by using the legendary Oberst's equation (1952). It assumes the cross-section always remains plane and the amplitude of vibration is relatively small, and has the complex form:

$$\frac{EI}{E_1 I_1}(1+i\eta) = 1 + ed^3(1+i\eta_2) + 3(1+d)^2\left[\frac{ed(1+\eta_2)}{1+ed(1+\eta_2)}\right] \qquad (6\text{-}12)$$

This can be written in real and imaginary part to give:

$$\frac{EI}{E_1 I_1} = \left(\frac{\omega_n}{\omega_{1n}}\right)^2 (1+d\rho) = \frac{1+2ed(2+3d+2d^2)+e^2d^4}{1+ed} \qquad (6\text{-}13)$$

$$\frac{\eta}{\eta_2} = \frac{ed(3+6d+4d^2+2ed^3+e^2d^4)}{(1+ed)(1+4ed+6ed^2+4ed^3+e^2d^4)} \qquad (6\text{-}14)$$

where $e = E_2/E_1$, $d = d_2/d_1$ and $\rho = \rho_2/\rho_1$. The properties of the combined system, i.e. the ratio of the effective flexural rigidity (EI) to the base beam (or plate) flexural rigidity ($E_1 I_1$) and the ratio of the effective loss (η) factor to the damping layer loss factor (η_2), are shown to be affected by three major parameters:

- the ratio of the damping modulus to the base beam (or plate) modulus (e);
- the ratio of the damping thickness to the base thickness (d);
- the loss factor of the damping layer (η).

Although Oberst's equation only works as an accurate approximation for flexural deformation of unstiffened beams or plates with full coverage, it is very useful for making a quick estimation of the effect of free layer treatments due to its relative simplicity (Jones, 1996).

6.3.2.3 Discussion

Cremer, Heckl and Ungar (1988) have shown the value of η_L and η_B for the damping material with loss modulus ($10^9 N/m^2$). Considering the case where the base layer is steel sheet ($E_1 = 2\times10^{11} N/m^2$) and assuming $d_1 = d_2$, one gets $\eta_L \approx 5\times10^{-3}$ and $\eta_B \approx 5.5\times10^{-2}$. The loss factor for bending waves is approximately 10 times larger than the longitudinal case, which indicates that bending waves can be more easily damped than longitudinal waves. The

dependence of the loss factor ratio η_B/η_2 on the thickness ratio d_2/d_1 has also been studied based on the exact analysis of Oberst (1952) and Equation 6-10 has also been validated in Figure 6-2. Clearly, the total damping increases as the loss modulus $\eta_2 E_2$ grows. The system loss factor increases uniformly with respect to h up to 2. It also indicates that when the loss factor and thickness of the damping layer are determined, it is always better to choose the material with higher modulus of elasticity.

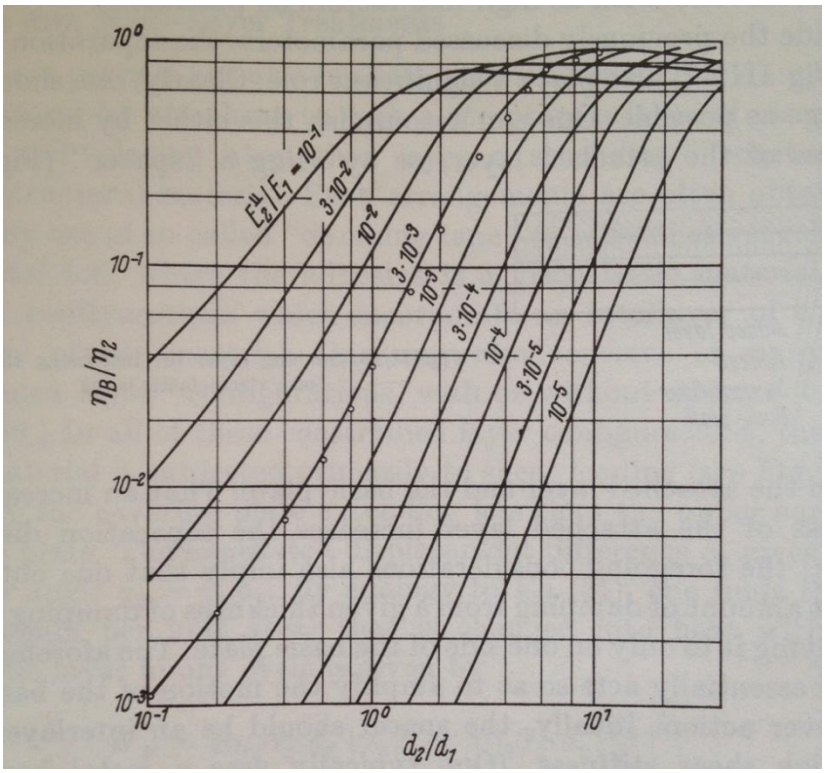

Figure 6-2 Loss factor of beams or plates with single viscoelastic layer for bending waves, after Oberst. Points show values calculated from the approximate relations, Equation 6-10 and Equation 6-11, for $E_2/E_1 = 3 \times 10^{-3}$(Cremer, Heckl and Ungar, 1988).

In reviewing Equation 6-10, one may also find the distance between the neutral axis and the centre-line of the damping layer a is of importance. The action of doubling the value of a results in an increase of loss factor by the factor of 4 (according to Equation 6-10). This is often achieved by adding spacer between the base and damping layer and the spacer is ideally with high shear stiffness (a typical spacer can be a metal honeycomb-like structure).

Therefore, the general rule of thumb of obtaining high loss factor is to apply damping material with high loss factor, high modulus and high thickness, and if necessary to add spacer between those two layers. Although this treatment may sacrifice the useful space and seems inefficient from a weight point of view, it has the lowest costs of materials and application processes compared with other damping treatments (Jones, 2001).

6.3.3 Multiple layer treatment

Since the damping property of viscoelastic materials is temperature-dependent, in order to ensure the damping treatment works properly in a broader temperature range, one may simply add a third layer upon the first damping layer. The third layer has to be softer than the inner layer so that it deforms with it and the plane sections remain plane. Otherwise, it will act like a constrained layer which will be discussed in Section 6.4. Illustration of a two free layer treatment in its undeformed and deformed state is shown in Figure 6-3.

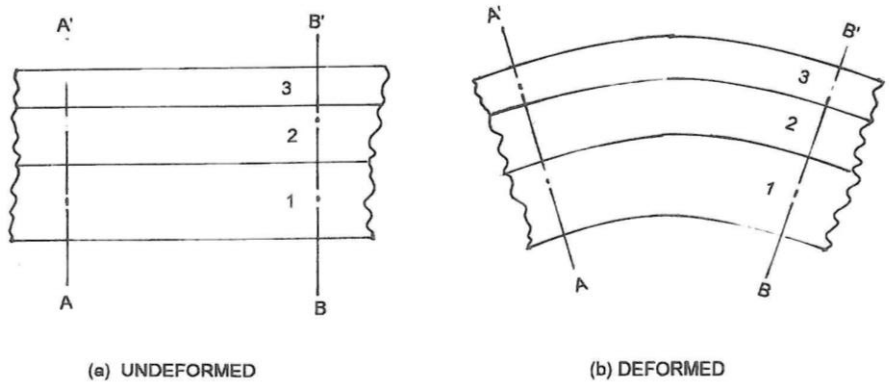

Figure 6-3 Multiple free layer treatments, (a) undeformed, and (b) deformed (Jones, 2001)

It is assumed that the strain distribution across the section of the composite beam or plate is linear with respect to the distance from the neutral axis. The position of the neutral axis is found by applying the condition that the net stress across the combined section is zero. If one defines the distance between the neutral axis to the upper surface of the base beam as md_1, one has the parameter (Jones, 2001):

$$m = \frac{1 - e_2^* {h_2}^2 - e_3^* h_3(2h_2 + h_3)}{2[1 + e_2^* h_2 + e_3^* h_3]} \tag{6-15}$$

where $e_2^* = E_2^*/E_1$, $e_3^* = E_3^*/E_1$, $h_2 = d_2/d_1$ and $h_3 = d_3/d_1$. The superscript '$*$' here means the parameter is complex. The ratio of the effective flexural rigidity to the base flexural rigidity is given by (Jones, 2001):

$$\frac{(EI)^*}{E_1 I_1} = A_1^* + e_2^* B_1^* + e_3^* C_1^* \tag{6-16}$$

where the complex parameter A_1^*, B_1^* and C_1^* are given by (Jones, 2001):

$$A_1^* = 4[m^3 + (1-m)^3] \tag{6-17}$$

$$B_1^* = 4[(m + h_2)^2 - m^3] \tag{6-18}$$

$$C_1^* = 4[(m + h_2 + h_3)^3 - (m + h_2)^3] \tag{6-19}$$

The imaginary part of the complex ratio $(EI)^*/E_1 I_1$ can be readily calculated to give the loss factor of the combined system. One may also verify that these equations reduce to Oberst' equation when e_3^* or d_3 are zero, or when the third layer uses the same material as the inner layer so that $e_2^* = e_3^*$ and $h_2 = h_2 + h_3$. Going to the effort of expressing the complex form in algebraic form is hardly necessary since the results can be easily calculated with commercial software (Jones, 2001).

A numerical study exploring the influence of the ratio $d_3/d_1$and E_3/E_1 has been represented by Jones (2001) for given value of d_2/d_1, E_2^* and E_3^*. The result has been shown in Figure 6-4. The loss factor ratio increases as the ratio of d_3/d_1 and E_3/E_1 gets higher. This indicates that, for multiple layer treatment, a thicker third layer with higher modulus is always favourable. However, compromise needs to make if the strategy is to be practical from a weight point of view.

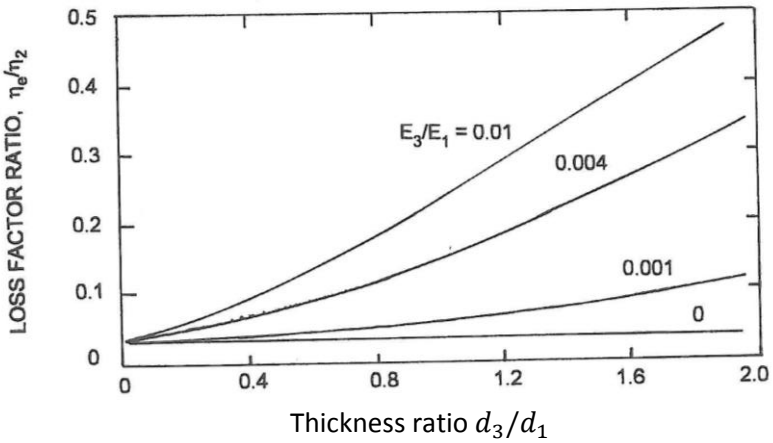

Figure 6-4 Variation of loss factor ratio with given thickness ratio d_2/d_1 for various values of E_3^*/E_1 and d_3/d_1 ($E_2/E_1 = 0.01$, $d_2/d_1 = 0.5$)(Jones, 2001)

The effect of adding a third layer also broadens the applicable temperature range. Jones (2001) shows a numerical study of the modal damping of clamped-clamped beam with two free layers at 200 Hz. The inner layer uses a commercially available damping tile (LD-400), which is has larger lass factor around room temperature. The third layer uses a nitrile rubber (Paracril-BJ with 50 parts per hundred carbon black), which is more effective at lower temperature. A fractional derivative model was used to calculate the complex modulus and the result is shown in Figure 6-5. The use of third layer clearly widens the applicable temperature range of the combined system. However, there exists a 'trough' of loss factor between the two peaks. This drawback might be minimized by choosing the material for the third layer with higher temperature transition region.

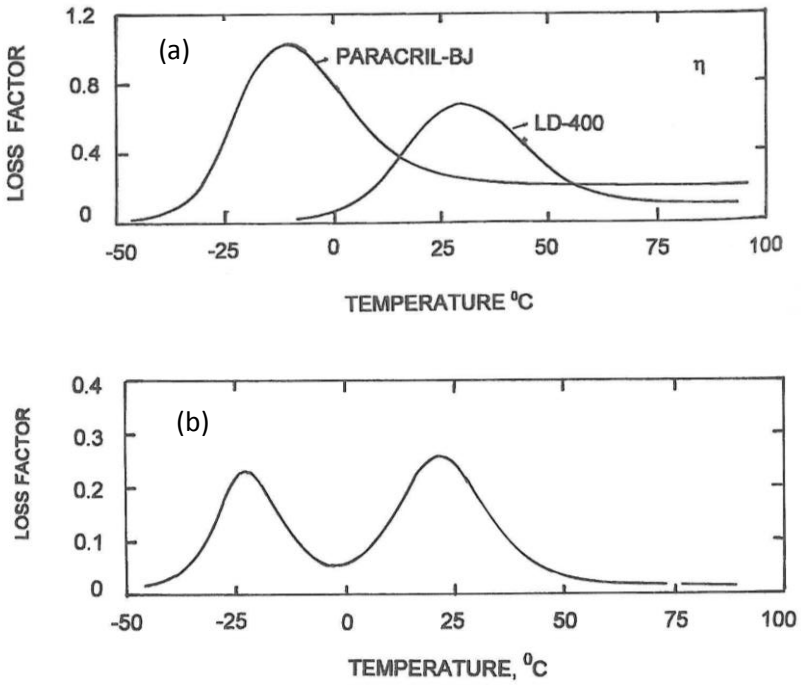

Figure 6-5 Loss factor versus temperature, (a) two free layer materials [LD-400 (layer 2) and Paracril-BJ(layer 3)]; (b) clamped-clamped beam with two free layers added (Jones, 2001).

6.4 Constrained layer damping

6.4.1 Basic configuration

Constrained layer damping is generally more efficient and widely used than free layer damping. However, it adds extra weight and manufacturing complexity in terms of its application as well as presenting greater analytic difficulty. The general configuration of a single constrained layer treatment is shown in Figure 6-6 (a). Unlike free layer damping, where the cross section of the composite remains plane and the deformation mainly occurs in extension, the cross section of the composite of constrained layer treatment no longer remains plan and the damping layer mainly deforms in shear (and to a much lesser degree in extension) as shown in Figure 6-6 (b). This is mainly due to the fact that the deformation of the constrained layer is less than that of the upper surface of the base layer.

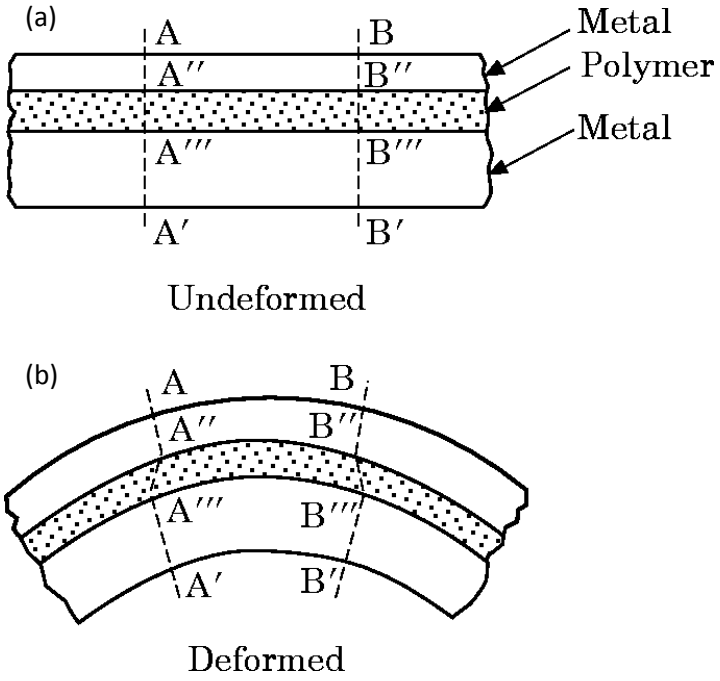

Figure 6-6 Constrained layer damping, (a) undeformed, (b) deformed (Jones, 1996).

6.4.2 RKU equations for a pinned-pined beam

Ross et al. (1959) were the first to publish a study analysing constrained layer damping on a beam or plate. Their contribution is mainly accumulated in the famous 'RKU' equations. The major assumption of these equations is that the flexural deformation of the base layer is spatially sinusoidal in shape and having a semi-wavelength denoted by the symbol λ (Jones, 2001).

The effective flexural rigidity of a single constrained layer damping treatment in RKU equations can be expressed as (Ross et al., 1959):

$$\begin{aligned}(EI)^* = {} & \frac{E_1 {d_1}^3}{12} + \frac{E_2^* {d_2}^3}{12} + \frac{E_3 {d_3}^3}{12} - \frac{E_2^* {d_2}^2}{12}\left(\frac{d_{31} - D}{1 + g^*}\right) \\ & + E_1 d_1 D^2 + E_2^* d_2 (H_{21} - D)^2 + E_3 d_3 (H_{31} - D)^2 \\ & - [0.5 E_2^* d_2 (H_{21} - D) + E_3 d_3 (H_{31} - D)]\left(\frac{H_{31} - D}{1 + g^*}\right)\end{aligned} \tag{6-20}$$

where the various parameters are:

$$D = \frac{E_2^* d_2 (H_{21} - 0.5H_{31}) + g^* (E_2^* d_2 H_{21} + E_3 H_3 H_{31})}{E_1 d_1 + 0.5E_2 d_2 + g^* (E_1 d_1 + E_2 d_2 + E_3 d_3)} \quad (6\text{-}21)$$

$$H_{21} = 0.5(d_1 + d_2) \quad (6\text{-}22)$$

$$H_{31} = d_2 + 0.5(d_1 + d_3) \quad (6\text{-}23)$$

$$g^* = \frac{G_2^* \lambda^2}{E_3 d_2 d_3 \pi^2} \quad (6\text{-}24)$$

The three terms in Equation 6-20 represent the flexural rigidities of the three layers about their own neutral axis. The parameter D defines the neutral axis of the composite system. The most important parameter is the 'shear parameter' g^*, which is a function of the complex shear modulus of the damping layer G_2^*, the Young's modulus of the constrained layer E_3 and the thickness of those two layers. Note the modulus E_3 can also be complex if a damping material is used as the constrained layer. The influence of the shear parameter g^* on the damping performance of the combined system may not appear obvious immediately. By rearranging these RKU equations into a real and imaginary part, one may again derive the flexural rigidity ratio $(EI)^*/E_1 I_1$, and more importantly, the loss factor ratio η/η_2. Figure 6-7 and Figure 6-8 illustrates the effect of the real part of the shear parameter g of those two ratios for given thickness ratio d_2/d_1 (or d_3/d_1) with various value of d_3/d_1 (or d_3/d_1). The best damping performance (peak loss factor ratio η/η_2) occurs when the value of g is near 1. The position of optimum point depends on both the thickness ratios d_2/d_1 and d_3/d_1. Additionally, when other parameters are fixed, greater thickness ratio d_2/d_1 (or d_3/d_1) always results in better performance. Therefore, when designing the constrained layer damping treatment, the rule of thumb is to choose the material properties and layer thicknesses in such a way that the real part of the shear parameter g is near its optimum value. Consideration of the choice of thickness of each layer is also needed to achieve best damping performance in the weight and cost point of view. Note the analysis above is based on a pinned-pinned boundary condition. The semi-wavelength λ equals L/n, where L is the length and n is the mode number.

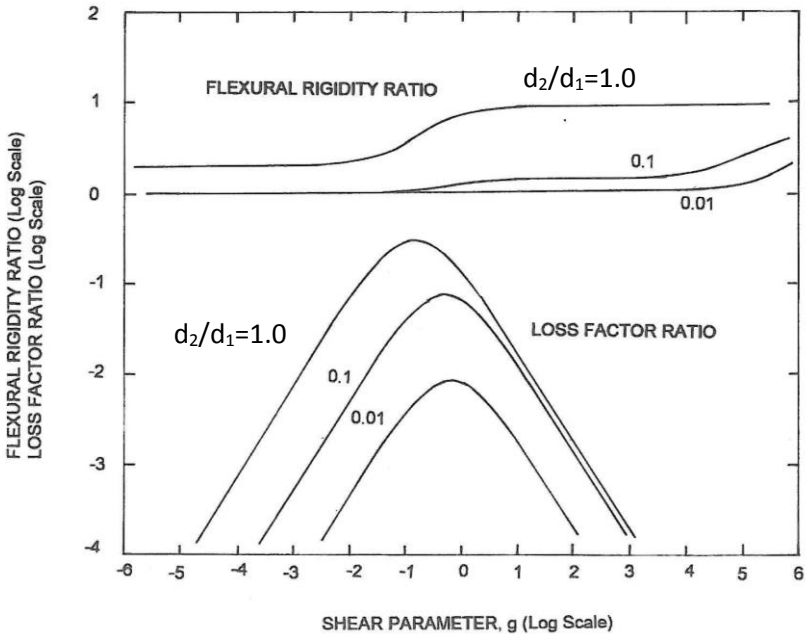

Figure 6-7 Variation of $(EI)^*/E_1I_1$ and η/η_2 with shear parameter g for fixed value of $d_2/d_1 = 0.1$ (Jones, 2001)

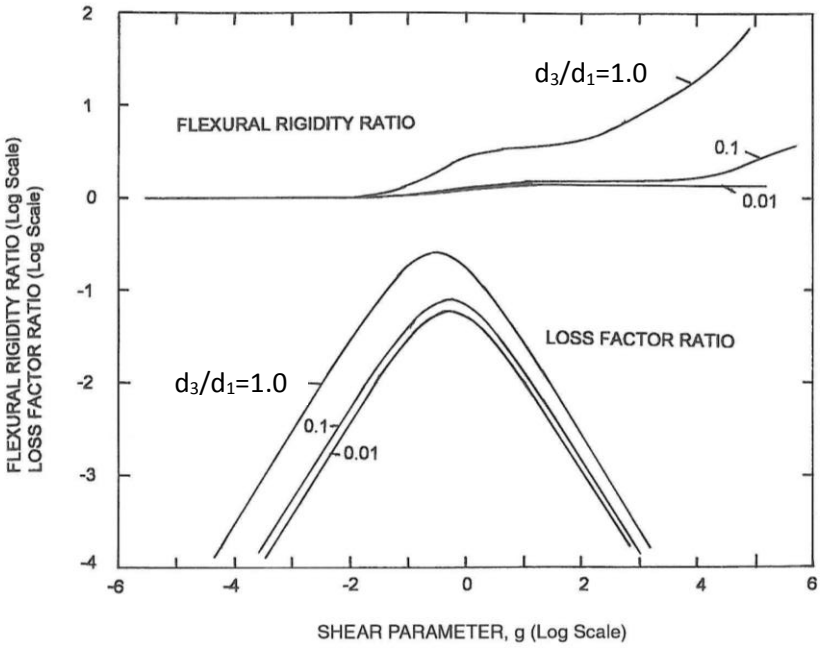

Figure 6-8 Variation of $(EI)^*/E_1I_1$ and η/η_2 with shear parameter g for fixed value of $d_3/d_1 = 0.1$ (Jones, 2001)

Cremer, Heckl and Ungar (1988) also derived the expression of loss factor for constrained layer damping. Furthermore, they discussed the optimum loss factor

obtainable and its corresponding optimum frequency at which maximum damping effect occurs. They concluded that, for stiff base plate with thin constrained layer, the greatest loss factor achievable with $\eta_2 = 2$ (values larger than this are extremely rare) is around $0.9E_3d_3/E_1d_1$; for two equal plates with thin interlayer, the optimum loss factor can never exceed 0.75 and the highest value that is practically available is about 0.4.

6.4.3 Modification for other classic boundary conditions

The original RKU equations dealt with a pinned-pinned boundary condition. For other boundary conditions, Rao (1978) has shown calculations to allow one to correct the value of the shear parameter g^* to correctly predict the damping in the low order mode cases. The results showed that for classic boundary conditions (especially for clamped-clamped and clamped-free cases) only the lowest order modes need correction. No significant errors occur for modes beyond the first mode.

6.4.4 Multiple constrained layer treatment

When multiple constrained layer treatment is applied, the prediction of the composite loss factor is much more tedious. Extensions of the RKU equations for this case are discussed by Ross et al. (1959). Considering the case of multiple constrained layer treatment in Figure 6-9 with 5 layers, two relatively simple analysis can be done.

The first idea is to use the RKU equations to calculate the equivalent modulus and loss factor step-by-step from the outer layer to the base layer. In the case of a 5-layer system in Figure 6-9, one may first calculate the equivalent flexural rigidity $(EI)_e^*$ of System A (i.e. 5-4-3) and hence the relevant equivalent loss factor and modulus. And then one is able to apply the RKU equations to System B (i.e. A-2-1, where System A is treated as an equivalent outer layer) and find the loss factor for the whole system.

Another simpler method combines all the constrained layers as one and only considers the innermost damping layer (ignores all other damping layers). Thus the system is equivalent to a simple three-layer system to which the RKU equations can

readily be applied. The approximation is rather rough and the result becomes less reliable as the number of layers increases and the material property of each layer varies. However, it gives a quick estimation of a multiple constrained layer system.

Verification of both methods has been undertaken by Jones (2001) for clamped-clamped aluminium beam under various conditions. The results have shown that both methods show agreement with the experiment, where the prediction of the first method agrees with the measured data more quantitatively and that from the second method agrees with the measured data more qualitatively. Imperfections, such as non-uniformity, de-bond and bubbles, between different layers are considered as one important factor that influences the fit of measured data and the predictions.

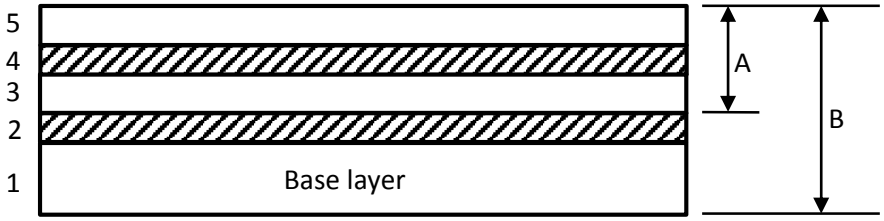

Figure 6-9 Multiple constrained layer damping

6.5 Other passive damping treatments

6.5.1 Tuned mass damping

The passive damping treatments discussed above are effective over a relatively wide range of frequencies, which is desirable for practical noise reduction problems. There is another damping treatment that has a narrowband effect, namely the tuned mass damper. It is specifically designed to achieve a high damping effect by sacrificing the bandwidth. An ideal tuned mass damper consists a simple mass-viscoelastic-spring element that is attached to the surface of the structure where the undesirable vibration occurs (see Figure 6-10). It is best known for reducing the amplitude of the vibration at resonance and in some cases it can also be used to alter the resonant frequency of the combined system. Due to the nature of tuned

mass damping, it is of greater significance in mechanical vibration control rather than a broad band acoustic noise control. Hence no further discussion will be given here. The behaviour of tuned mass damper can be found in standard text books (Cremer, Heckl and Ungar, 1988; Jones, 2001). For practical tuned mass damper design, one may referred to Thompson et al. (2007) for railway track noise reduction and Webster and Vaicaitis (1992) for vibration reduction in composite floor systems.

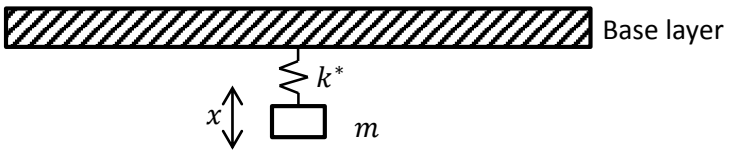

Figure 6-10 Tuned mass damper

6.5.2 Granular damping

Granular materials, such as sands are also used in building constructions to reduce structural vibration mainly for economic reasons (Cremer, Heckl and Ungar, 1988). One simple example of granular damping is to apply ground sand on top of the base structure (beams or plates) to form a sand layer. The energy dissipation is believed to mainly occur within the sand layer after conduction from the base structure to the damping layer (Cremer, Heckl and Ungar, 1988). The effect of granular damping appears to be hard to predict intuitively due to its non-uniformities. However, Cremer, Heckl and Ungar (1988) mentioned that reproducible measurement techniques have been developed by Schimidt (1954) to measure the material properties on 'sand beams', in which sand is contained in a long trough of plastic film. Those measurements gave some average material properties of sand:

Longitudinal wave velocity $c_L \approx 150$ m/s

Transverse wave velocity $c_T \approx 100$ m/s

Loss factor $\eta \approx 0.1$.

Cremer, Heckl and Ungar (1988) suggested that the damping by layers of granular material is not introduced by the friction between sand and the base structure but by conduction of energy into the sand and the subsequent dissipation within it. The mechanism of energy dissipation within sand is related to Coulomb friction discussed in Section 2.4.4.1.

The loss factor of granular material is found to be frequency dependent and the best damping performance occurs at the resonances when the thickness of the sand layer is an odd multiple of a quarter wavelength (Cremer, Heckl and Ungar, 1988). Another interesting finding is that granular materials with the small loss factor appears to have greater performance at resonance but poorer performance in other frequency bands (Cremer, Heckl and Ungar, 1988). Therefore, in order to obtain a broad band damping effect, one should make the sand layers non-uniform (i.e. the thickness should vary across the surface of the damped component).

6.6 Discussion and conclusion

This chapter explains the physical mechanisms behind several common passive damping treatments, especially free-layer damping and constrained-layer damping. These two damping treatments are found to be very applicable in building noise control for several reasons: low cost, ease of application, minimal/no maintenance (compared with active or semi-active dampers), broad frequency effect (compared with tuned mass dampers) and relative ease in predicting behaviour (compared with granular damping).

The general guideline to achieve a better damping effect for free-layer damper is to use thicker damping layers with higher loss factor and higher modulus. For constrained-layer dampers, which generally have much higher loss factors, the damping properties depend on the shear parameter $g^* = \frac{G_2^* \lambda^2}{E_3 d_2 d_3 \pi^2}$. Best performance occurs when the value of g^* approaches unity. The highest value of loss factor that can be achieved (theoretically) is 0.4 for two equal plates with thin damping layer. For a stiff base structure and thin constraining layer, which is more likely to happen in real building structures, the maximum loss factor is $0.9E_3 d_3/$

$E_1 d_1$ for the best damping material ($\eta_2 = 2$). It is found that when the value of shear parameter does not change, thicker damping layer or constraining layer generally result in a better damping performance. One of the most obvious way of manifesting constrained layer damping in building structures would be in the use of viscoelastic materials such as Green Glue as an adhesive for plasterboard (a constraining layer) on masonry (damped layer).

It is clear that bending waves may more readily be damped using applied materials than longitudinal. In terms of its practical application to buildings, this suggests that at high frequency, where longitudinal waves will start to play an increasingly important role in dictating transmission, achieving high levels of damping may not be possible (using constrained layers). However, levels of sound insulation are typically high in the frequency regions where longitudinal waves exhibit modal behaviour in building structures and the need for strategies that improve sound insulation through increasing damping may be unnecessary.

Tuned-mass dampers and granular dampers are also briefly introduced. They are of less importance than the layer damping treatments in indoor noise control but can be useful for some typical cases.

Knowledge of different damping treatment techniques suggest that the proposed value of ILF used in the modelling work in Chapter 4 and Chapter 5 is theoretically achievable. It is also a good preparation for measuring loss factors in the laboratory and validating the findings in theoretical simulation, described in Chapter 7.

CHAPTER 7 EXPERIMENTAL WORK

7.1 Introduction

In this chapter several carefully-selected damping measurement techniques will be introduced to measure the actual loss factor of given systems. The theoretical background and experiment setup of each measurement technique will be given. Analysis and discussion of the data will then follow. Experimental validation of ray tracing code is also included.

7.2 Loss factor measurement

In this study, the damping property is mainly reflected in the theoretical investigation by using the definition of loss factor. Therefore, it is very important to implement a relatively simple and accurate measurement technique that can be applied to a damped system over a wide applicable frequency range. Several approaches were trailed as described in this section and the power injection is argued to be the most appropriate one.

7.2.1 Distance attenuation method

7.2.1.1 Theoretical background

Cremer, Heckl and Ungar (1988) suggested a way to measure the loss factor from a damped beam by measuring the attenuation with distance along the beam. For a very long and highly damped beam, wave propagation is identical to that on an infinitely long beam. For cases where the damping is not extremely high, the loss factor may be expressed as (Cremer, Heckl and Ungar, 1988):

$$\eta = \frac{D^{'}\lambda_B}{13.6} \tag{7-1}$$

This expression can be achieved by rearranging Equation 5-14. The energy level difference per meter between two points x_1 and x_2 can be quantified by:

$$D^{'} = \frac{10\log\left(\frac{v_1}{v_2}\right)^2}{x_2 - x_1} \; or \; \frac{10\log\left(\frac{a_1}{a_2}\right)^2}{x_2 - x_1} \tag{7-2}$$

where v_1, v_2 and a_1 and a_2 are the corresponding velocities and accelerations at x_1 and x_2. The bending wavelength λ_B can either be measured or be estimated by (Craik, 1996):

$$\lambda_B = \frac{c_B}{f} = (\frac{4\pi^2 B}{\rho_s f^2})^{0.25} \tag{7-3}$$

given the bending stiffness $B = Eh^3 b/12$ and the surface density ρ_s.

For a beam that is not heavily damped, one may design an anechoic system to simulate an infinitely long beam where the wave only propagates in one direction when excited at one end. One such system has been built using sponges and ground sand to absorb vibration energy (Figure 7-1). The curvature of the sponges provides non-uniform thickness of the sand layer to achieve a broadband damping effect (Cremer, Heckl and Ungar, 1988). The beam was suspended and the opening was made wide enough to avoid a direct contact with the wooden box. One may also add an acoustic mastic sealant to serve the same purpose.

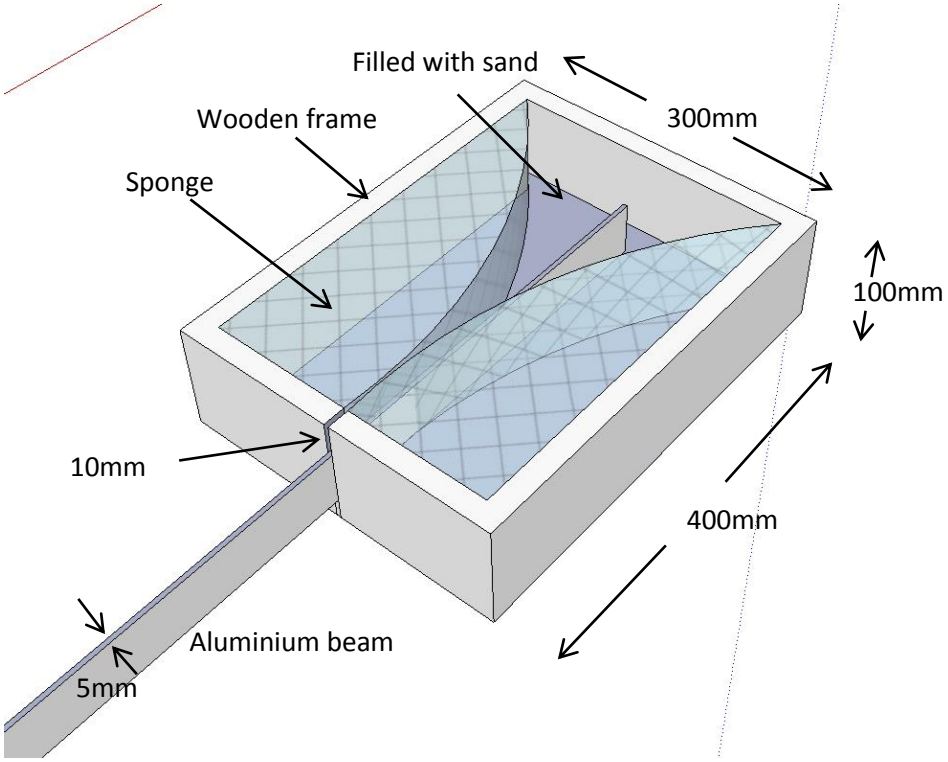

Figure 7-1 Anechoic system design for measuring attenuation along a beam with distance

7.2.1.2 Experiment setup

7.2.1.2.1 Apparatus

The apparatus used in this experiment is described in Table 7-1 and the manner in which the components are connected is shown in Figure 7-2.

Table 7-1 Apparatus for the distance attenuation measurement

Name	**Type**	**Description**
Wood frame	400mm*300mm*100mm wood frame	To hold sand and sponge to form an anechoic system
Sand	Ground sand	To absorb vibrational energy
Sponge		To absorb vibrational energy
Aluminium beam	2000mm*50mm*5mm aluminium beam	The base structure
Shaker	LDS V201 M4-CE	To excite the system
Shaker holder		To hold the shaker horizontally
Accelerometer 1	Brüel & Kjær 4508 B	To measure the acceleration a_1
Accelerometer 2	Brüel & Kjær 4508 B 002	To measure the acceleration a_2
Amplifier	Brüel & Kjær 2706	To amplify the digital excitation signal
B&K frontend analyser	Brüel & Kjær Input/output module: 3109 Power-supply module: 2826 Controller module: 7536	To provide output signal and to acquire input signal
Computer	PULSE LabShop 16.1.0	Signal processing
Cables		To connect different components

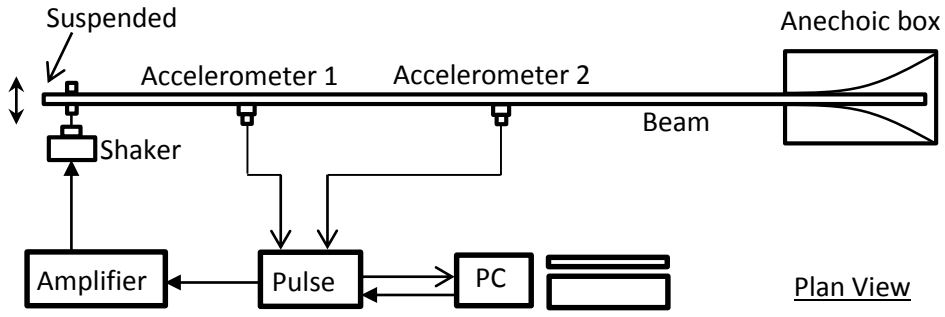

Figure 7-2 Experimental setup for the distance attenuation method

7.2.1.2.2 Procedure

The attenuation of acceleration level difference along distance was measured under three conditions, i.e. the aluminium beam was undamped, lightly damped (5% of the beam is covered with sand) and medium damped (10% of the beam is covered with sand).

a. The beam was excited by the shaker with white noise input (the excitation frequency band was from 100 Hz to 4000 Hz).
b. In each test, the acceleration attenuation was measured with two accelerometers placed 0.25m, 0.5m and 0.75m apart. For each distance, three measurements were taken.
c. Constant Percentage Bandwidth (CPB) analysis was carried out with Brüel & Kjær PULSE LabShop 16.1.0. The average level difference of the each 1/3 Octave band from 100 Hz to 4000 Hz was determined.
d. The wavelength at each 1/3 octave centre frequency in each test was measured and recorded.
e. Recalling Equation 7-2, the attenuation of energy level difference as a function of distance was obtained by dividing the acceleration level difference by the distance between the accelerometers.
f. Recalling Equation 7-1, the loss factor of the beam system was calculated for each measurement. The results were averaged to give the loss factor for each condition (i.e. undamped, lightly damped and medium damped)

All tests were taken under a room temperature ranging from 19.2 to 20.3 ℃ (the room temperature is unlikely to have a significant influence on the test results due to the nature of aluminium and sand).

7.2.1.3 Result and discussion

In developing the experiment, the anechoic system was found to work well for frequency bands ranging from 500Hz to 4000Hz. For frequency bands below 500Hz, the measured data exhibited significant scatter and some data points had negative values suggesting the present of reflected energy and standing waves. Therefore, only the results from 500Hz to 4000Hz were deemed reliable. The loss factor of the

beam system under three different conditions is shown in Figure 7-3. If one excludes the data points below 500Hz, the loss factors for three conditions with different levels of damping do not show significant frequency dependency. The average loss factors for each 1/3 octave centre frequency are 0.0016, 0.11 and 0.24 for three conditions respectively. The published loss factor for aluminium is around 0.0001 (Cremer, Heckl and Ungar, 1988). This method therefore over determines the loss factor for pure aluminium beam, or is not effective at measuring very low loss factors..

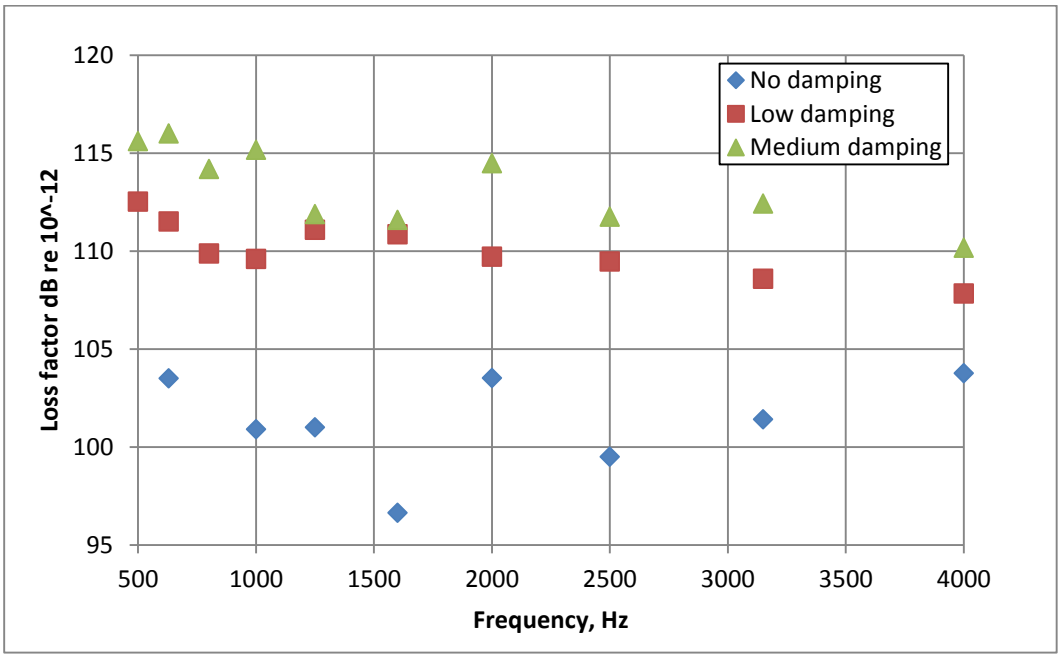

Figure 7-3 Loss factor using distance attenuation method

The advantage of this method is that the measurements and calculations are simple and straight forward. However, the applicable frequency range depends on the design of the anechoic system and the data points in low frequency bands (i.e. below 500Hz in this example) are scattered, which do not provide any useful information. If one wants to use such a method, the general prerequisite is to design an effective anechoic system, which may not always be readily achievable. This method is also limited to one-dimensional system, although it is not unreasonable to assume the loss factor measured from a one-dimensional system would be similar for rays travelling on a similar two-dimensional system.

7.2.2 End-point acceleration method

There are two similar measurement techniques developed to measure the complex modulus of an impacted rod using one-dimensional wave theory, which then gives the loss factor. For predefined boundary conditions, i.e. free-free, only two or three measurements are required to give the results. The formulations of those techniques were proposed by Lundberg and Blanc (1988). They require one to measure the end-point accelerations (or velocities) (Ödeen and Lundberg, 1993) (see Figure 7-4) or the strains along the rod (Lundberg and Ödeen, 1993) and the formulation changes slightly accordingly. Since the technique that measures strains involves inserting strain gauges into the specimen, which in turn causes damage, the end-point acceleration method was chosen for this study.

7.2.2.1 Theoretical background

The basic theory is as follows. For a straight, cylindrical slender rod, made from linearly viscoelastic material with density ρ and complex modulus $E(\omega) = E'(\omega) + E''(\omega)$, by applying the one-dimensional theory, one may express the complex modulus $E(\omega)$ as (Ödeen and Lundberg, 1993):

$$\cosh(\gamma L) + \mu\gamma L \sinh(\gamma L) = \Psi \tag{7-4}$$

where L is the length of the specimen, μ is the mass ratio of the accelerometer to the specimen, and $\Psi = \hat{a}_1/\hat{a}_2 = re^{i\emptyset}$ is the complex acceleration ratio. The expression $\hat{a}$ represents the Fourier Transform of a, i.e. [$\hat{f}(a,\omega) = \int_{-\infty}^{\infty} f(a,t)e^{-i\omega t}dt$]. The square of the wave propagation coefficient is (Ödeen and Lundberg, 1993):

$$\gamma(\omega)^2 = -\rho\omega^2/E(\omega) \tag{7-5}$$

One may also express the wave propagation coefficient as $\gamma(\omega) = \alpha(\omega) + ik(\omega)$, where $\alpha(\omega)$ is the damping coefficient (positive even function) and $k(\omega)$ is the wavenumber (odd function, positive for $\omega > 0$) (Ödeen and Lundberg, 1993). Therefore, one has:

$$\gamma(\omega)^2 = [\alpha(\omega) + ik(\omega)]^2 = -\rho\omega^2/[E'(\omega) + E''(\omega)] \tag{7-6}$$

and, hence:

$$E'(\omega) = \rho\omega^2(k^2 - \alpha^2)/(k^2 + \alpha^2)^2 \tag{7-7}$$

$$E''(\omega) = \rho\omega^2(2k\alpha)/(k^2 + \alpha^2)^2 \tag{7-8}$$

The loss factor can thus be obtained through:

$$\eta = \frac{E''(\omega)}{E'(\omega)} \tag{7-9}$$

Lundberg and Blanc (1988) gave the derivation to solve for $\gamma_0 = \alpha_0 + ik_0$, where:

$$\alpha_0 = (1/L)\sinh^{-1}\left[(C_0 - A_0)^{1/2}\right], \qquad k_0 = (1/L)(s\beta_0 + n\pi) \tag{7-10}$$

and where:

$$C_0 = ({A_0}^2 + {B_0}^2)^{1/2},\ A_0 = \frac{1}{2}[1 - r^2],\ B_0 = r\sin(\emptyset),\ \beta_0 = \sin^{-1}[(C_0 + A_0)^{1/2}],$$

The integers $s = \pm 1$ and $n = 0, 1, 2, \ldots$ can be chosen in such a way that $k(\omega)$ is a continuous and monotonically increasing function with $k(0) = 0$. The dependence of λ, $\emptyset$ and β on ω and the corresponding values to be given to s and n are shown in Table 7-2.

Table 7-2 Wavelength λ, phase $\emptyset$, parameter β and integers s and n vs. radian frequency ω (Lundberg and Blanc, 1988)

ω	0 ↑	↑	↑	↑	↑	↑	↑
λ/4	∞ ↓	a ↓	a/2 ↓	a/3 ↓	a/4 ↓	a/5 ↓	a/6 ↓
sin(ϕ)	0	0	0	0			
cos(ϕ)		0	0	0			
β	0 ↑	π/2 ↓	0 ↑	π/2 ↓	0 ↑	π/2 ↓	0 ↑
s	1	-1	1	-1	1	-1	1
n	0	1		2		3	

7.2.2.2 Experiment setup

7.2.2.2.1 Apparatus

The apparatus used in this experiment are described in Table 7-3 and they are connected in the manner indicated in Figure 7-4.

Table 7-3 Apparatus of end-acceleration method

Name	**Type**	**Description**
Polypropylene rod	1.125m long, density 945kg/m^3, first resonance 917Hz, longitudinal wave speed 2063.25 m/s	The test specimen
Modal hammer	Endevco 2302-10	To excite the system
Accelerometer 1	Brüel & Kjær 4508 B	To measure the acceleration a_1
Accelerometer 2	Brüel & Kjær 4508 B 002	To measure the acceleration a_2
B&K frontend analyser	Brüel & Kjær Input/output module: 3109 Power-supply module: 2826 Controller module: 7536	To acquire input signal
Computer	PULSE LabShop 16.1.0	To analyse the data
Cables		To connect different components

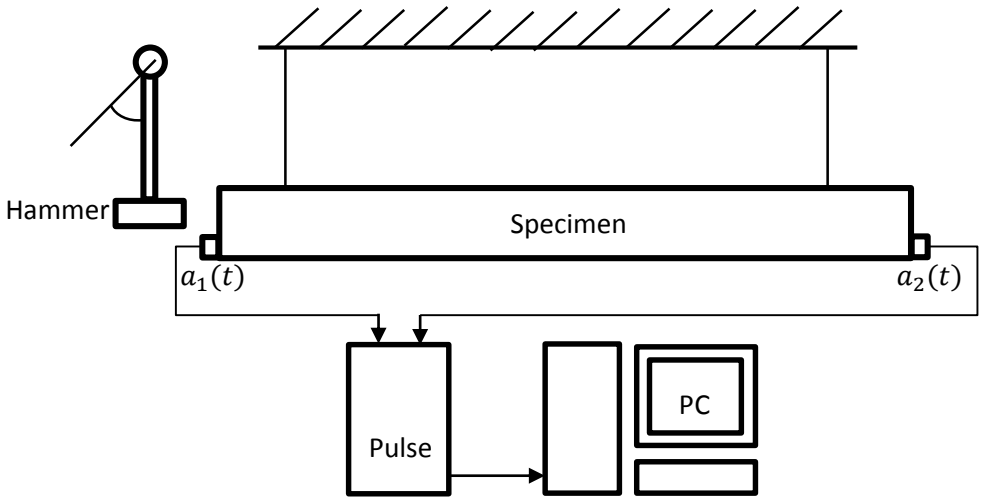

Figure 7-4 Experimental setup for the end-acceleration method

7.2.2.2.2 Procedure

A cylindrical polypropylene rod with circular cross-section and known material properties was used in the first test to gauge its accuracy. The room temperature ranged from 10.1 to 11.4℃ (recall that the damping property of a viscoelastic material is highly temperature-dependent) when taking the test.

By hitting one end of the specimen with a modal hammer, the accelerometers created two signals, i.e. $a_1(t)$ and $a_2(t)$, which were collected by the Pulse front-end analyser. The Brüel & Kjær PULSE LabShop software installed on a PC then took the Fast Fourier Transform (FFT) of those two time-domain signals to give the frequency-domain signals, i.e. $\hat{a}_1(\omega)$ and $\hat{a}_2(\omega)$.

The calculation of $E'(\omega)$ and $E''(\omega)$ can be undertaken readily using Equation 7-7, 7-8 and 7-10. One difficulty encountered was the determination of integer s and n. This could be done by tracing the variation of parameter β_0 and then manually choosing the corresponding values according to Table 7-2. The loss factor was determined using Equation 7-9.

7.2.2.3 Results and discussion

The resulting real and imaginary part of the complex modulus $E(\omega)$ is shown in Figure 7-5. The results from Ödeen and Lundberg's (1993) measurements on polypropylene are shown in Figure 7-6 for comparison. Both the real and imaginary part of the complex modulus in Figure 7-5 have similar order of magnitude as that in Figure 7-6. However, E' is around 2 times larger and E'' around 5 times larger than that indicated in Figure 7-6. This is believed to be influenced by the room temperature at the time when the measurements were taken. The complex modulus measured for polypropylene rod under different temperatures is shown in Figure 7-7. The values of complex modulus are highly temperature-dependent. The general observation is that as the temperature increases, the value of complex modulus drops (this is also reflected in Figure 2-11a).

One may also notice the discontinuities in Figure 7-5, which resulted from changing values of the parameters n and s. The reason for the presence of spikes of E'' in both Figure 7-5 and Figure 7-6 is not clear. One reason may be the influence

introduced by the local disturbance around Accelerometer 1 when the hammer provided an impulse excitation.

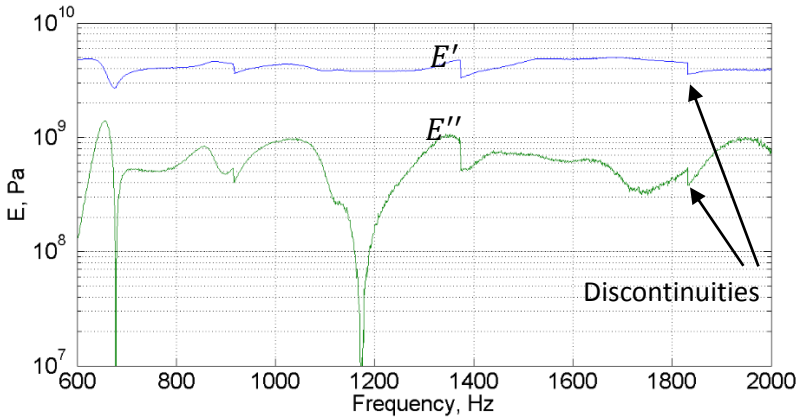

Figure 7-5 Complex modulus measured using End-acceleration method, 1125mm polypropylene rod with room temperature around 10℃

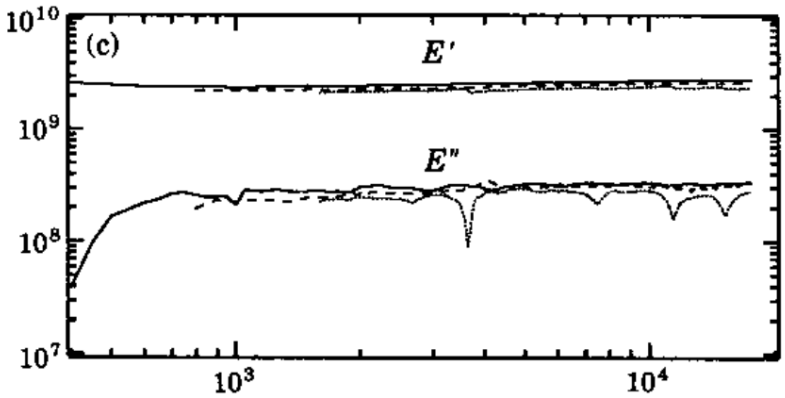

Figure 7-6 Complex modulus measured using End-acceleration method, ……， 200mm；------, 400mm; —, 800mm polypropylene rod with room temperature around 20℃ (Ödeen and Lundberg, 1993)

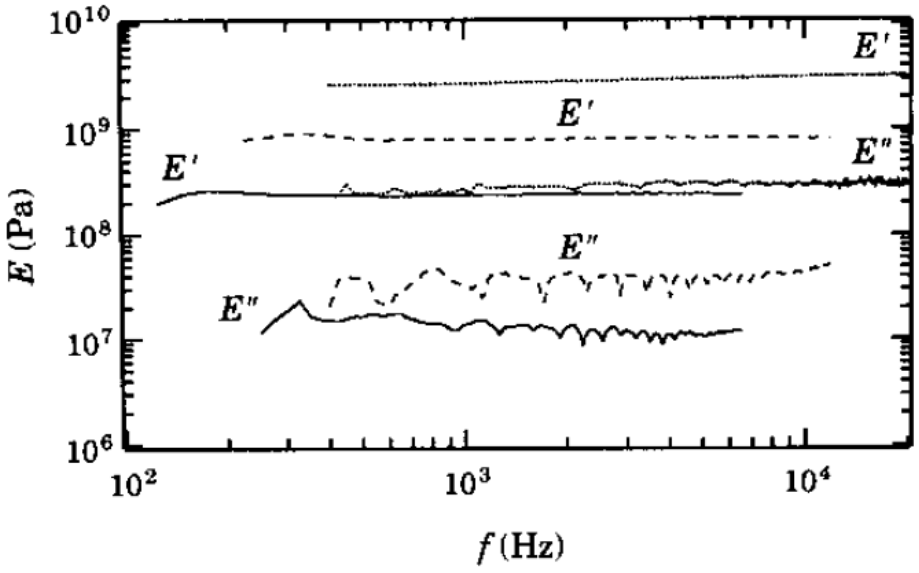

Figure 7-7 Complex modulus for polypropylene at different temperatures: ……, 20℃; --- 80℃; — 140℃ (Ödeen and Lundberg, 1993)

The resulting loss factor is shown in Figure 7-8, where the average is 0.1469. As one may observe in Figure 7-6 and Figure 7-7, the value of E' does not change significantly as the frequency changes while the change of the value of E'' may play an important role in calculating the loss factor.

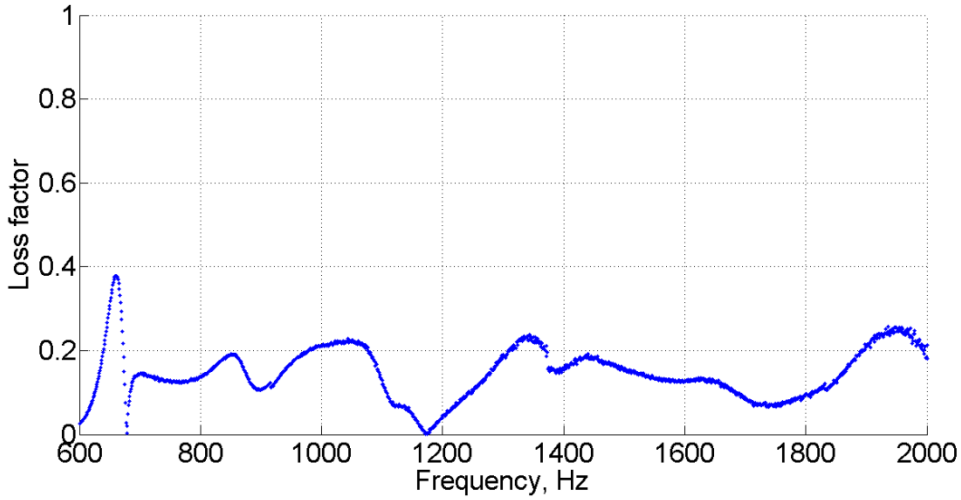

Figure 7-8 Loss factor measured using End-acceleration method

The End-acceleration method requires relatively simple test setup and measurement procedure. However, the mathematics and post-data handling are

tedious, especially for determining the appropriate values of n and s, as one needs to adjust the values by hand every time a new measurement is taken. Theoretically, this technique can be applied for a very wide range of frequency band from 20Hz to 20,000 Hz (Lundberg and Blanc, 1988). However, it is not practical since the data handling is more tedious as the frequency goes higher and the impedance introduced by the accelerometers may affect the results.

Additionally, this method only applies to specimen with homogenous material and the deformation has to be longitudinal. For specimens with certain damping treatments or other excitement types, i.e. transverse or bending, there is no guarantee that it can provide accurate results.

7.2.3 Modified reverberation time method

Reverberation time is very commonly used in building acoustics to determine the damping level of subsystems. Its definition is simple, i.e. the time it takes for the energy of a system to decrease by 60 dB once a steady excitation has been removed (this also holds for impulse excitation). It is a very important parameter in room acoustics and some classic expressions have been given in the literature to predict it, among which the Sabine Equation for rooms is perhaps the most widely used. For complex structures, the reverberation can be related to the total loss factor through Equation 2-98, where the TLF is a sum of all the CLFs and the ILF. The issue in many circumstances is to know what the ILF is or know all CLFs.

The reverberation time method is explored here based on the technique introduced by Schroeder (1965). A band pass digital filter is used to calculate the reverberation at each corresponding 1/3 octave band.

7.2.3.1 Theoretical background

An illustration of how to filter a wide frequency band signal to give the reverberation time of certain frequency band will be given here to illustrate the development of the technique described here. Imagine one has a signal $x(t)$ which is a combination of three different signals, i.e. $x_1(t)$, $x_2(t)$ and $x_3(t)$, where

$$x(t) = x_1(t) + x_2(t) + x_3(t) \tag{7-11}$$

If one uses Equation 2-26 to represent those three different signals (impulse response for damped mass/spring oscilator), thus one has:

$$x_1(t) = \frac{F_1}{m\omega_1\sqrt{1-\zeta_1{}^2}}\sin\left(\omega_1 t\sqrt{1-\zeta_1{}^2}\right)e^{-\zeta_1\omega_1 t} \tag{7-12}$$

$$x_2(t) = \frac{F_2}{m\omega_2\sqrt{1-\zeta_2{}^2}}\sin\left(\omega_2 t\sqrt{1-\zeta_2{}^2}\right)e^{-\zeta_2\omega_2 t} \tag{7-13}$$

$$x_3(t) = \frac{F_3}{m\omega_3\sqrt{1-\zeta_3{}^2}}\sin\left(\omega_3 t\sqrt{1-\zeta_3{}^2}\right)e^{-\zeta_3\omega_3 t} \tag{7-14}$$

An illustration of the three individual signals is shown in Figure 7-9. One may find that it is easy to find the reverberation time for each single signal (because they are expressed in an ideal way in which the decay is exponential). However, it is relatively difficult to find the reverberation for the combined signal $x(t)$.

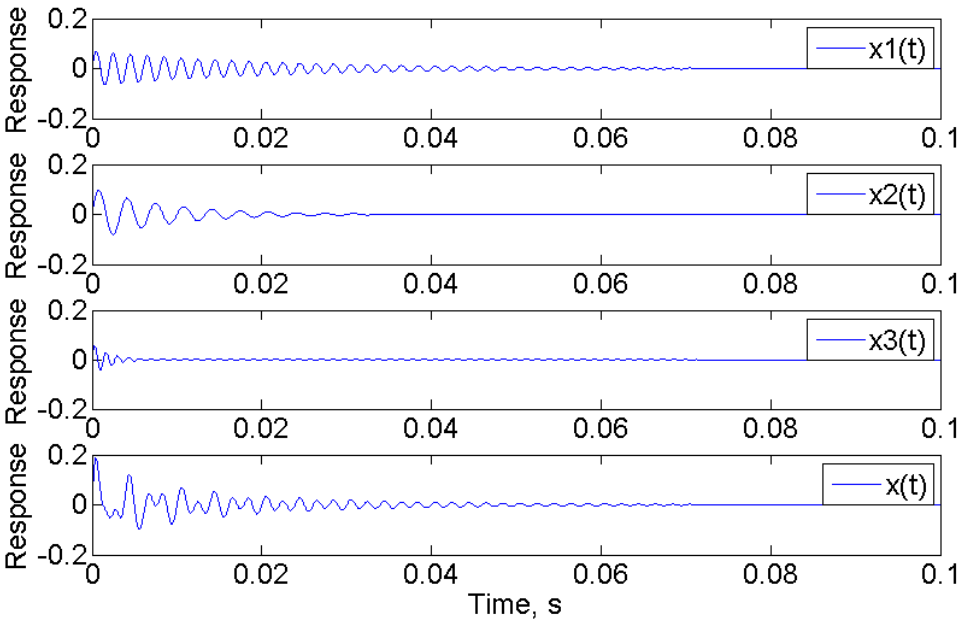

Figure 7-9 Illustration of different signals
($F_1 = 2.2\text{N}, F_2 = 2\text{N}, F_3 = 3\text{N}, m = 0.01\text{kg}, \omega_1 = 2\pi \times 500\text{Hz}, \omega_2 = 2\pi \times 300\text{Hz}, \omega_3 = 2\pi \times 750\text{Hz}, \zeta_1 = 0.015, \zeta_2 = 0.06, \zeta_3 = 0.1,$)

For a given signal $x(t)$, one may use a digital filter to allow certain frequency band to be included in the analysis and to exclude unwanted frequency responses. In this case, a Butterworth band pass filter, which is known for providing a flat frequency response in the pass band, is used to allow signal $x_1(t)$ to pass and to exclude signal $x_2(t)$ and $x_3(t)$. This can be done by using the Filter Design & Analysis toolbox in MATLAB R2013a. The settings used are shown in Figure 7-10, where:

F_s is the sampling frequency;

F_{stop1} is the end of the first stopband;

F_{pass1} is the beginning of the passband;

F_{pass2} is the end of the passband;

F_{stop2} is the beginning of the second stopband;

A_{stop1} is the attenuation in the first stopband;

A_{pass} is the passband ripple;

A_{stop2} is the attenuation in the second stopband

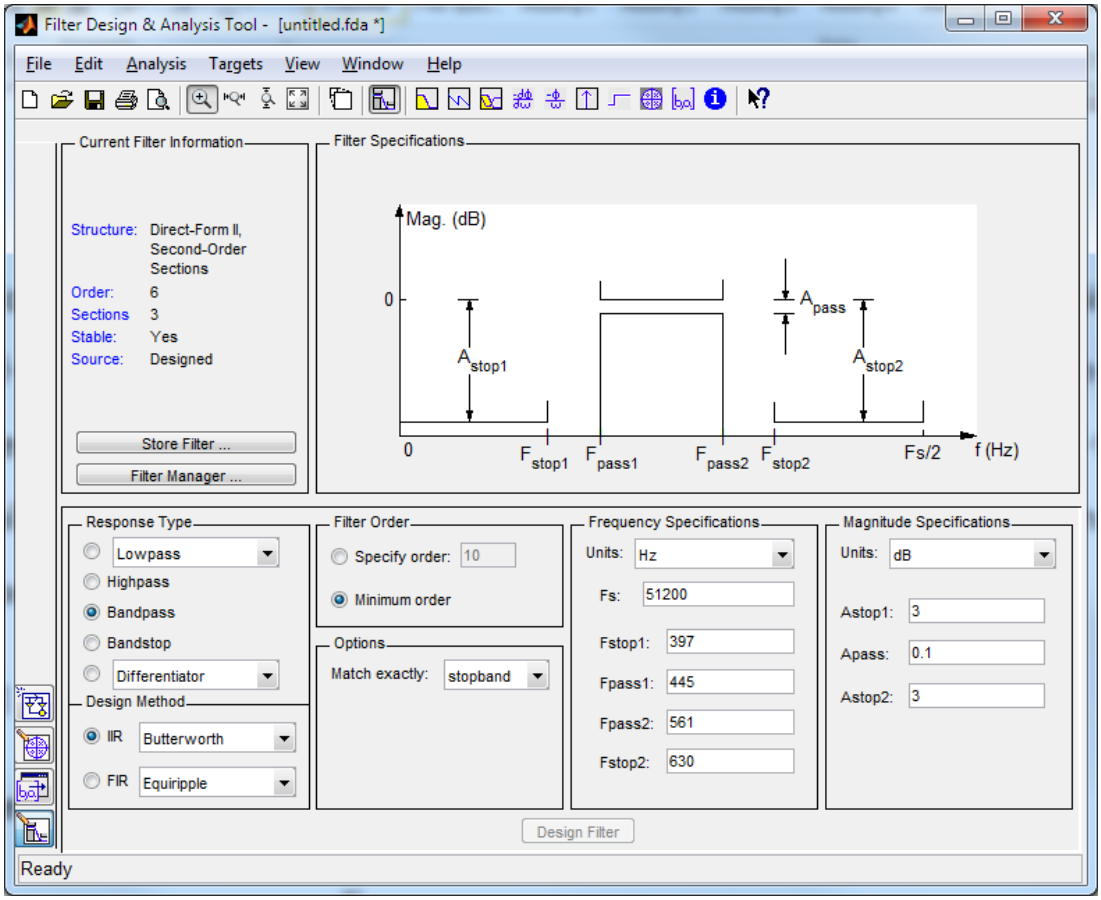

Figure 7-10 Setting for a Butterworth band pass filter in MATLAB R2013a

The resulting magnitude response is shown in Figure 7-11. It retains the response within the frequency band 445-561Hz and attenuates the response outside this frequency band.

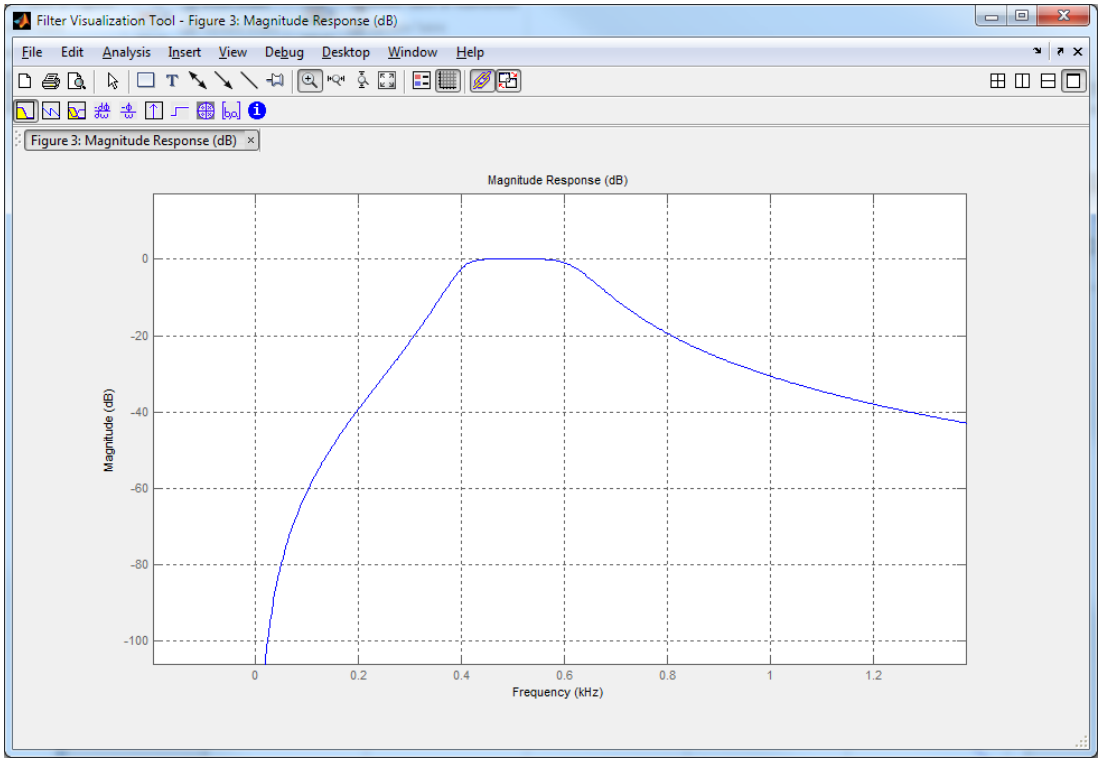

Figure 7-11 Magnitude response of Butterworth band pass filter

A comparison between the wanted signal $x_1(t)$ and the filtered signal $x_{filtered}(t)$ is shown in Figure 7-12. It generally gives good agreement for later part of the decay (i.e. $t > 0.1s$). This might cause problem measuring very heavily damped system where the dominant decay is likely to occur within the earlier part of the time signal.

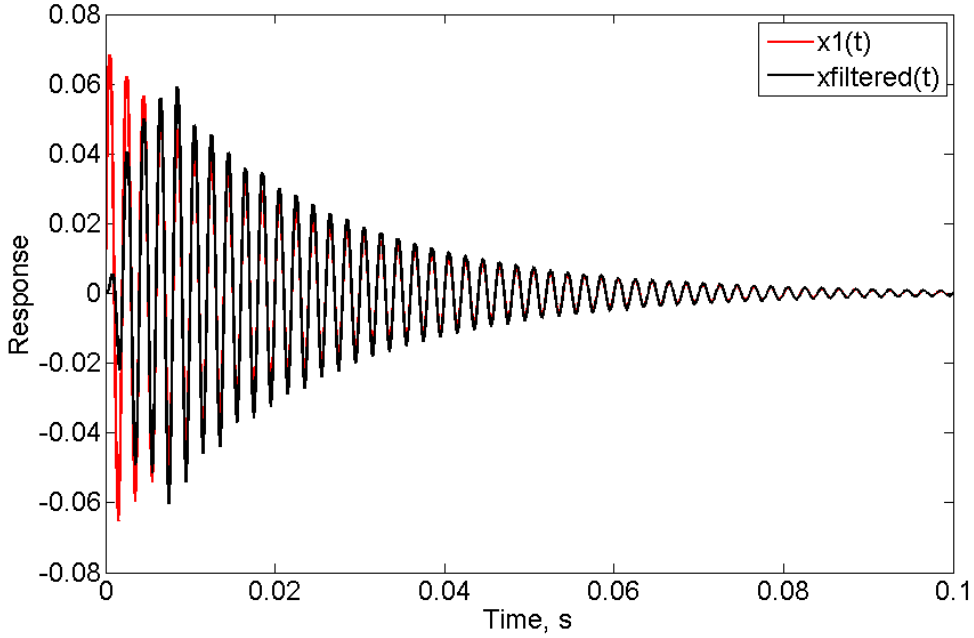

Figure 7-12 Comparison between the wanted signal $x_1(t)$ and the filtered signal $x_{filtered}(t)$ (low damping)

Once the signal has been filtered, one may express the response in dB:

$$Response(dB) = 10\log_{10}\left[\frac{x(t)^2_{filtered}}{10^{-12}}\right] \tag{7-15}$$

where 10^{-12} is the reference value. A trend line can then be found using a least square fit to determine the response (Figure 7-13). The gradient of the trend line can be used to find the reverberation time:

$$\mathrm{T}_{60} = -\frac{60}{\text{gradient}} \tag{7-16}$$

In this case, $\mathrm{T}_{60} = 0.1461\text{s}$. The loss factor can then be determined using:

$$\eta = \frac{2.2}{\mathrm{T}_{60} f} \tag{7-17}$$

One can easily examine whether it agrees with the initial assumption. The loss factor $\eta = 2.2/\mathrm{T}_{60}/f = 2.2/0.1461/500 = 0.0301$ which equals twice the original damping coefficient $\zeta_1 = 0.015$. This satisfies the relation between loss factor and

damping coefficient when $\zeta < 0.1$(see Equation 2-110). In practice, one usually uses a reverse integration (backward integration) to smooth the curve of response as suggested by Schroeder (1965). The reverse integrated response has the same slope as the original response and is easier to identify (Figure 7-13).

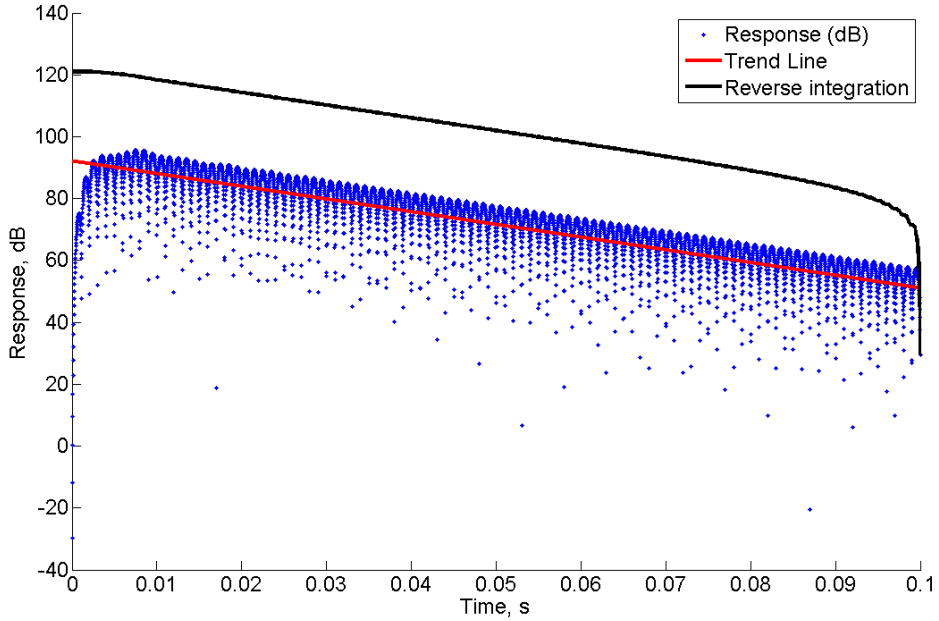

Figure 7-13 Trend line of the filtered signal

7.2.3.2 Experimental setup

7.2.3.2.1 Apparatus

The apparatus used to explore structural reverberation time is shown in Table 7-4 and connected in the manner shown in Figure 7-14.

Table 7-4 Apparatus of modified reverberation time method

Name	**Type**	**Description**
Specimen 1	5mm thick aluminium beam	No damping
Specimen 2	Additional 3mm thick damping layer	Free layer damping
Specimen 2	Sandwich beams with 4mm thick damping layer	Constrained layer damping
Green glue	Green glue noise control compound	Damping material
Hammer	Endevco 2302-10	To excite the system
Accelerometer 1	Brüel & Kjær 4508 B	To measure the acceleration a_1
B&K frontend analyser	Brüel & Kjær Input/output module: 3109 Power-supply module: 2826 Controller module: 7536	To acquire input signal
Computer	PULSE Labshop 16.1.0	To analyse the data
Cables		To connect different components

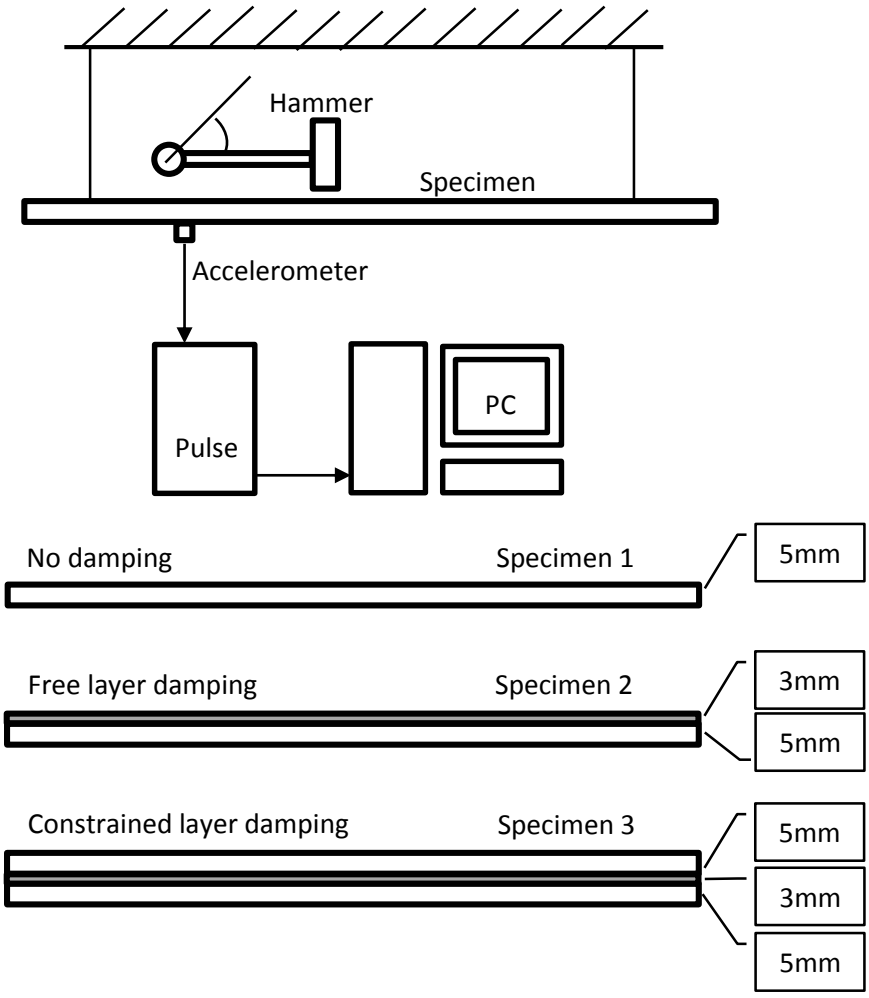

Figure 7-14 Experimental setup for the modified reverberation time method

7.2.3.2.2 Procedure

Three specimens were tested separately (Figure 7-14), namely an aluminium beam with no damping, with free layer damping and with constrained layer damping. In each test, ten measurements were conducted with different pairs of measurement position and impact position. Those positions were chosen randomly. In each measurement, the hammer produced an impulse excitation of the beam and the accelerometer was used to capture the response.

Thirty one Butterworth band path digital filters were generated in MATLAB R2013a to filter the response. They allow one to find the corresponding response of 1/3 octave band with centre frequencies between 20Hz and 20,000Hz. The F_{pass1} and F_{pass2} were chosen to correspond to the upper and lower frequency limits of standard 1/3 octave bands. F_{stop1} and F_{stop2} were chosen to be the previous and next centre frequency of that 1/3 octave band. For example, for a 1/3 octave band with centre frequency 500Hz, one has F_{stop1}=400, F_{pass1}=447, F_{pass2}=562 and F_{stop2}=630. The lower band limits, centre frequencies and upper band limits of 1/3 octave bands are shown in Table 7-5. The centre frequency is determined through $f_{n+1} = 2^{1/3} f_n$ and the lower and upper frequency limit of each band is determined through $f_n^{lower} = f_n/2^{1/6}$ and $f_n^{upper} = f_n * 2^{1/6}$. All the frequencies are calculated by defining $f_{19} = 1000\text{Hz}$.

Table 7-5 One-Third-Octave bands

1/3 Octave Bands		
Lower Band Limit (Hz)	**Centre Frequency (Hz)**	**Upper Band Limit (Hz)**
14.1	16	17.8
17.8	20	22.4
22.4	25	28.2
28.2	31.5	35.5
35.5	40	44.7
44.7	50	56.2
56.2	63	70.8
70.8	80	89.1
89.1	100	112
112	125	141
141	160	178
178	200	224
224	250	282
282	315	355
355	400	447
447	**500**	562
562	630	708
708	800	891
891	1000	1122
1122	1250	1413
1413	1600	1778
1778	2000	2239
2239	2500	2818
2818	3150	3548
3548	4000	4467
4467	5000	5623
5623	6300	7079
7079	8000	8913
8913	10000	11220
11220	12500	14130
14130	16000	17780
17780	20000	22390

The reverberation and hence the loss factor can then be calculated by finding the trend line of the filtered response (dB).

7.2.3.3 Results and discussion

The averaged loss factors for each specimen at the 1/3 octave centre frequency from 50Hz to 5000Hz are shown in Figure 7-15. Reverse integration has been adopted to calculate the loss factor. Specimen 3 with constrained layer damping appears to have the best damping effect. Free layer damping (Specimen 2) appears to be effective at frequencies higher than 500Hz, while constrained layer damping has a broader applicable frequency band and does not work as well at high frequency bands (frequencies above 2000Hz). One may observe that with the increasing of the excitation frequency the damping effect of free layer damper has a transition from no damping to constrained layer damping. One possible explanation is that, as the frequency increases, the constrained layer acts less effectively in constraining the deformation, i.e. the damping layer is more likely to deform in extension rather than in shear which is similar to the case of free layer damping.

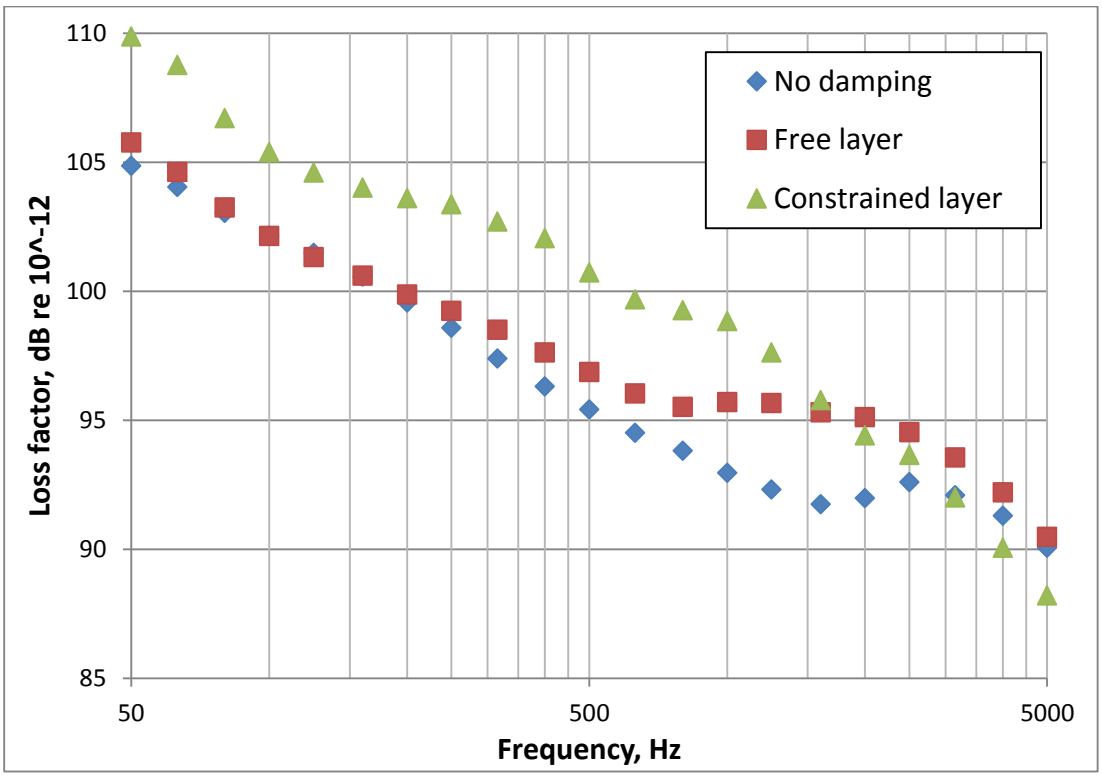

Figure 7-15 Measured loss factor using the modified reverberation time method

The reverberation time for structural elements is usually much lower than rooms (Craik, 1996). For plates with high loss factor, say 0.3 for example, there presents sufficient cycles to get a measure of the decay (around 7 full cycles in this case, refer to the discussion in Section 2.5.1). However, the reverberation time at high frequency is in the order of a few milliseconds, which is relatively hard to measure. Moreover, because energy decays so quickly, it is difficult to find the corresponding decay. Errors in identifying the correct slope may lead to over prediction of the reverberation and hence underestimates in the loss factor. Similar statements have been mentioned by Bloss and Rao (2005). Additionally, the initial part of the filter response is not an accurate representation of the true signal, which introduces another possible error. These may be the reasons why the measured loss factors for both free layer and constrained layer damping have almost the same value as that from the undamped specimen at high frequencies (Figure 7-15).

In order to further understand the errors in measuring heavily damped systems, one may check the synthesised signal $x_1(t)$ with high damping ($\zeta_1 = 0.15$) (Figure 7-16). In this case, the filtered signal differs greatly with the original signal and hence the obtained loss factor is not accurate. Tests on synthesised signal suggest that it only gives accurate result for loss factors smaller than 0.1 (i.e. $\zeta \leq 0.05$).

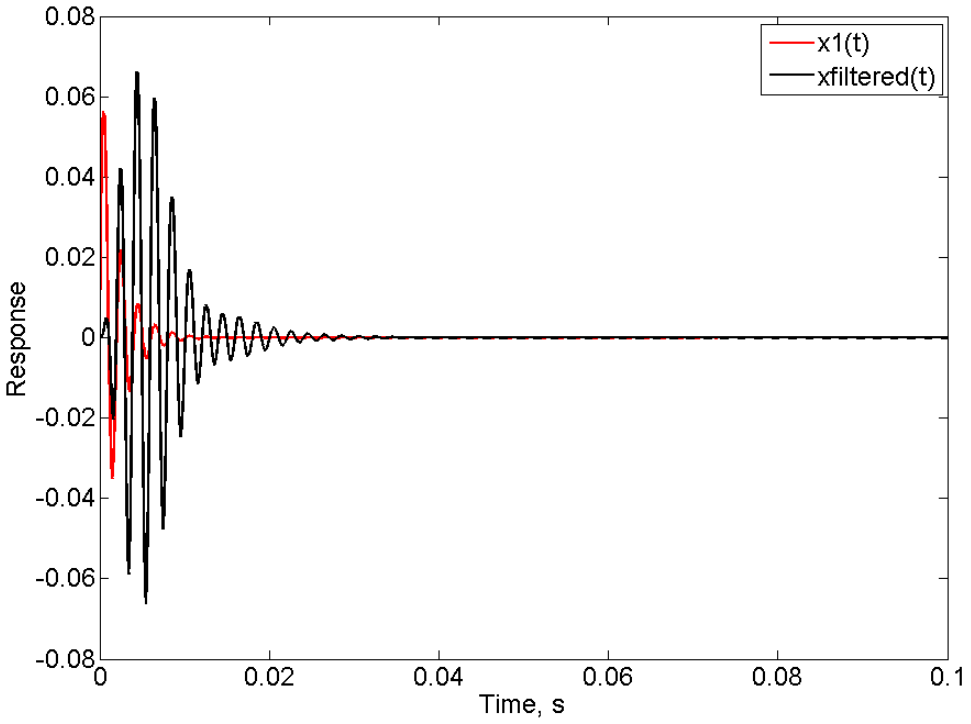

Figure 7-16 Comparison between the wanted signal $x_1(t)$ and the filtered signal $x_{filtered}(t)$ (heavily damped)

Therefore, the application of the modified reverberation time method is limited to structures with relatively low damping such as concrete walls.

7.2.4 Power injection method

Carfagni and Pierini (1999a) introduced the numerical investigation of power injection method to determine structural damping. The idea was to use kinetic energy as an approximation of the strain energy and to evaluate the kinetic energy with a limited number of measurements. Experimental tests have been carried out using impact hammer excitation (Carfagni and Pierini, 1999b) and shaker excitation (Carfagni and Pierini, 1988; Bloss and Rao, 2002) both of which serve as a good guideline for developing loss factor measurements in this study.

7.2.4.1 Theoretical background

Loss factor can be expressed as:

$$\eta(\omega) = \frac{Energy\ dissipated}{Total\ strain\ energy} \tag{7-18}$$

One may compute the loss factor directly if one knows the energy dissipated and the total strain energy in the system. With a stationary force excitation, the energy dissipated equals the energy input and the total strain energy can be approximated by double value of the kinetic energy as suggested by Carfagni and Pierini (1999a). Although it is generally difficult to measure energy directly, the point mobility (velocity/force) can be measured relatively easily.

Carfagni and Pierini (1999a) gave the expression of loss factor as:

$$\eta(\omega) = \frac{Re[h_{FF}(\omega)]}{\sum_{i=1}^{N} m_j \omega |h_{iF}(\omega)^2|} \tag{7-19}$$

where $h_{FF}(\omega)$ is the point mobility spectrum at the excitation point and $h_{iF}(\omega)$ is the transfer mobility spectrum between the excitation point and point i. The idea is to divide a plate into i portions and to sum the kinetic energy of each portion to give the total kinetic energy of the plate. If one substitutes the velocity spectrum and force spectrum into Equation 7-19, one has:

$$\eta(\omega) = \frac{Re[v_0(\omega)/F_0(\omega)]}{\sum_{i=1}^{N} m_j \omega |[v_i(\omega)/F_0(\omega)]^2|} = \frac{Re[v_0(\omega)F_0(\omega)]}{\sum_{i=1}^{N} m_j \omega |v_i(\omega)^2|} \tag{7-20}$$

where $v_0(\omega)$ and $v_i(\omega)$ are the velocity spectra near excitation point and the measurement point respectively, and $F_0(\omega)$ is the input force spectrum. $Re[v_0(\omega)F_0(\omega)]$ is the energy input (it equals the energy dissipated due to damping) and $\sum_{i=1}^{N} m_j \omega |v_i(\omega)^2|$ is the total strain energy, which is identical to Craik's (1996) expression for subsystem energy mv^2 (v is root mean squared velocity averaged over time and space).

7.2.4.2 Experimental setup

7.2.4.2.1 Apparatus

The apparatus for the power injection method is described in Table 7-6 and connected in the manner shown in Figure 7-17.

Table 7-6 Apparatus of power injection method

Name	Type	Description
Test subject	Three coupled aluminium plates	Each plate with a dimension of 900mm*500mm*2mm
Modal hammer	Endevco 2320-10	To excite the system
Accelerometer 1	Brüel & Kjær 4508 B	To measure the acceleration a_1
Accelerometer 2	Brüel & Kjær 4508 B 002	To measure the acceleration a_2
B&K frontend analyser	Brüel & Kjær Input/output module: 3109 Power-supply module: 2826 Controller module: 7536	To acquire input signal
Computer	PULSE Labshop 16.1.0	To analyse the data
Cables		To connect different components

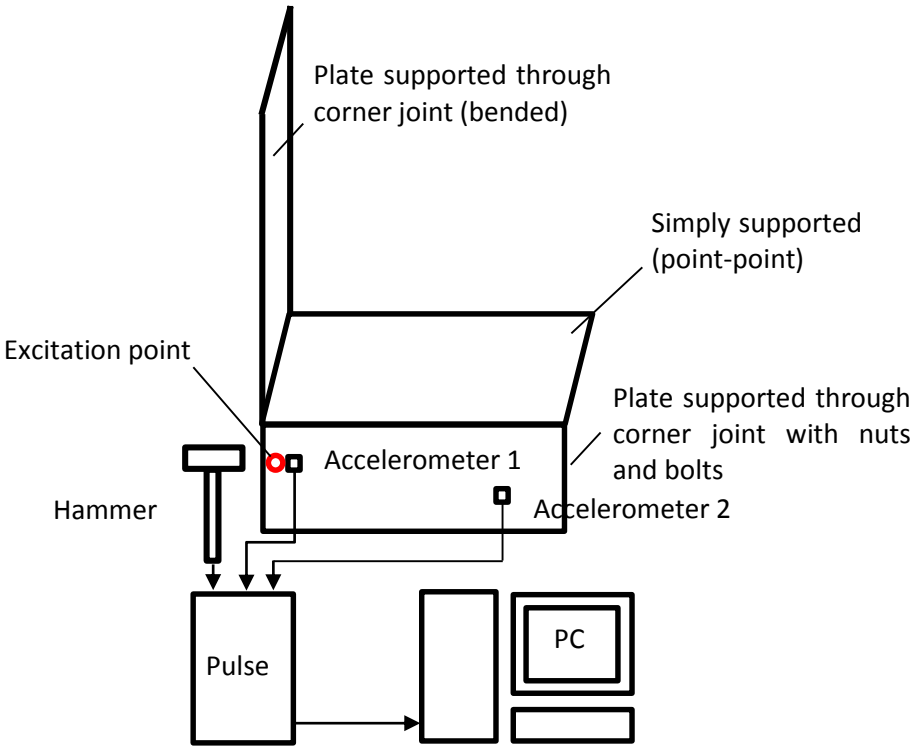

Figure 7-17 Experiment setup for the power injection method

7.2.4.2.2 Procedure

The test plate has dimensions of 900mm*500mm*2mm and a mass of 2.88kg, and is coupled to another two identical aluminium plate (one corner joint is formed with 88 3mm nuts and bolts at 10mm centres and the other is normal corner joint).

Impact hammer excitation was selected to excite the system in the absence of an impedance head that is required by shaker excitation method.

When using a hammer, there are several important tips for the operator to obtain satisfactory results (Carfagni and Pierini, 1999b):

- Hammer taps requires certain amount of force, neither too light nor to heavy.
- One should avoid multiple hammer taps.
- Each hammer tap should be perpendicular to the plate and at the same point on the plate.

Accelerometer 1 was placed near the excitation point. The plate was discretized into 18 portions and accelerometer 2 was placed at the centre of each portion for each tap. The point mobility and transfer mobility spectrum were calculated for each tap. Two excitation points were randomly selected following the suggestion of Carfagni and Pierini (1998), i.e. avoiding positions along the edges and the symmetry axes. The loss factor was then calculated using Equation 7-19.

7.2.4.3 Result and discussion

The measured loss factors as well as the prediction from SEA are shown in Figure 7-18. The loss factor from SEA is calculated by adding the radiation loss, coupling loss to the attached plate and the internal loss. The coupling between the two plates is assumed to be a corner joint with random incidence. One influence of the bolts and nuts is that the coupling is likely to change from a line corner joint to lots of discrete point contacts when half bending wave length is approaching the same magnitude as the dimension of the bolt separation (Craik and Smith, 2000). This does not happen over the frequency band (100Hz to 6300Hz) shown in Figure 7-18. The other influence that the overlap between the two plates and the bolts might make the joint behave as if it contains a beam. These influences are likely at low frequency and are assumed to be negligible. There is also the possibility that mechanisms such as ‘gas pumping’ within this joint may give rise to additional damping effects that are not included in the predicted results.

There is no significant difference when changing the excitation point position. The results have generally agreement with the prediction from SEA especially for frequency band from 250Hz to 1000Hz.

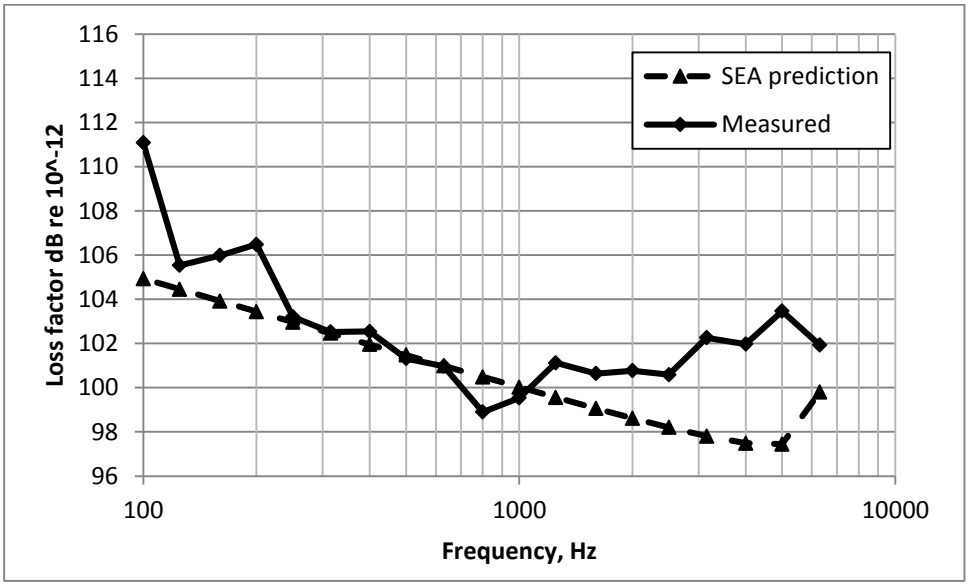

Figure 7-18 Loss factors measured from power injection method

Power injection method has a relatively simple measurement procedure, straight forward calculation, reliable results and the applicability for heavily damped structures (Carfagni and Pierini, 1998). It is thus selected as the loss factor measurement method in the experiment described in Section 7.7.

7.3 Three-plate system

7.3.1 Introduction

A three-plate system (see Figure 7-19) was built to validate the ray tracing algorithm. Energy level differences between plate 1 and 3 were measured when plate 2 is undamped and damped. The findings in Section 5.6 suggest that SEA tends to over predict the energy level difference between plate 1 and 3 when subsystem 2 is heavily damped. Comparison between the measured data and prediction from SEA and the hybrid SEA/ray trace method.

The test subject contains three identical aluminium plates each with a dimension of 900mm*500mm*2mm and a mass of 2.88kg. They are connected in

the manner shown in Figure 7-19. A large plate with a dimensions of 1800mm*500mm*2mm was bent through 90° along the centre line to form plate 1 and plate 2 coupled through a corner joint. Plate 2 and plate 3 were connected with 88 3mm nuts and bolts s as shown in Figure 7-19. It was connected in this way because the equipment available for fabrication the experimental rig cannot bend irregular shaped plates. Partial free layer damping was applied to plate 1 and plate 3 to add damping to the system in an attempt to avoid energy equipartition within the whole system as described in Section 3.2.2. If such treatments are not included, when subsystem 2 is undamped, the energy tends to travel back and forth within the system and attenuates rather slowly. Under such circumstances, it is unlikely that a level difference would be measured between subsystem 1 and 3 (referring to the discussion about weak coupling in Section 3.2.2).

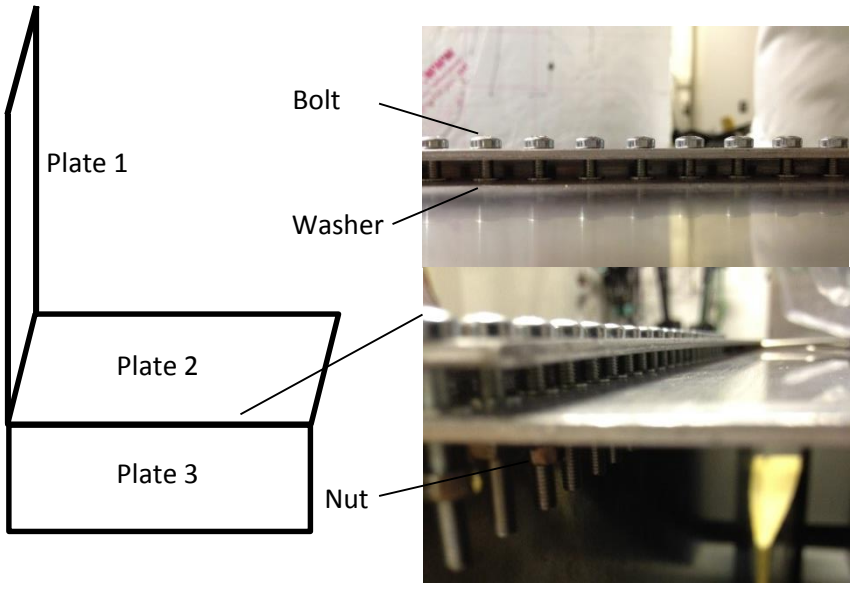

Figure 7-19 Illustration of three-plate system (photograph taken before nots tightened)

7.3.2 Energy level difference

7.3.2.1 Experimental setup

The energy level difference measurement between plate 1 and plate 3 under shaker excitation of plate 1 was conducted for two conditions:

Test 1 no damping on plate 2 (Figure 7-20 a).

Test 2 damping on plate 2 (Figure 7-20 b).

In Test 2, in order to achieve high damping effect, plate 2 was damped with a combination of constrained layer damping and granular damping. A 3mm thick green glue layer was applied on top of the base plate and 0.2mm thick aluminium foil was used as the constrained layer. Additional 3mm thick sand layer was applied on the constrained layer to give an extra damping effect. The mass of plate 2 when damped is 3.93kg. The additional damping adds 36% extra weight on plate 2. It is assumed that this only influences the internal loss within the plate and does not have significant effect on the transmission at the joints.

The test setup is as shown in Figure 7-20. In each test, a white noise excitation (frequency from 40Hz to 6300Hz) was applied with unchanged power input. Two excitation positions were selected (using the same rule described in Section 0). Acceleration levels of plate 1 and plate 3 were measured using the same accelerometer. This avoided the potential error introduced by using two accelerometers with different sensitivities. In each excitation, 20 randomly selected measurement points were used to give the spatial averaged acceleration level for each plate. The rule applied in the selection of the measurement points was to avoid positions near the edges and the excitation point (at least 10cm away). In each test, 40 separate measurements were conducted to give the acceleration level of each plate, i.e. 20 measurements for each excitation position. In order to determine how accurate the mean of a set of measurements is, the standard deviation and 95% confidence intervals were calculated for each test. The standard deviation is given by:

$$sd = \sqrt{\frac{\sum x^2 - \frac{\sum x^2}{n}}{n-1}} \tag{7-21}$$

and the 95% confidence interval is calculated using:

$$95\% confidence\ interval = \frac{sd}{\sqrt{n}} \times t_{v,0.975} \tag{7-22}$$

where n is the number of measurements and $t_{v,0.975}$ is the value taken from the students t-distribution for a 95% confidence interval with v degree of freedom ($v = n - 1$).

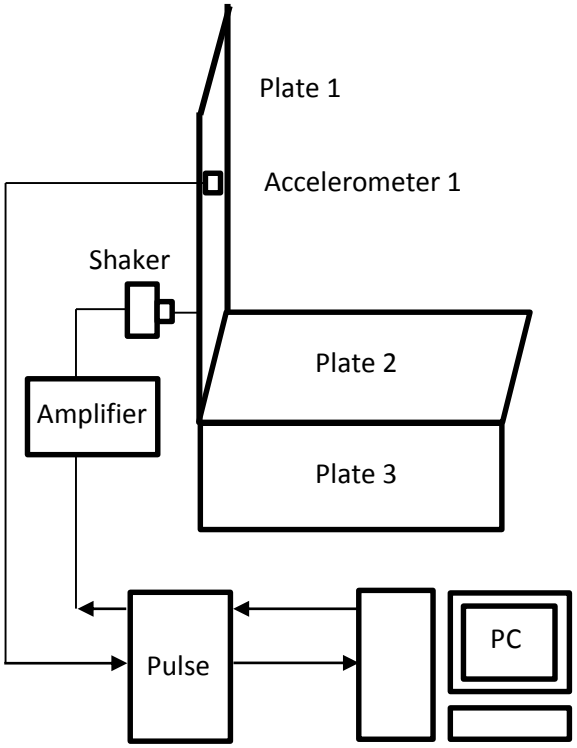

(a) No damping on plate 2 (b) Plate2 with damping

Figure 7-20 Experiment setup for energy level difference measurement

The energy level difference between plate 1 and plate 3 can thus be obtained by:

$$\mathrm{ELD13}(f) = \frac{m_1 \bar{v}_1(f)^2}{m_3 \bar{v}_3(f)^2} = \frac{\bar{a}_1(f)^2}{\bar{a}_3(f)^2} \tag{7-23}$$

where $\bar{v}_1(f)$ and $\bar{v}_3(f)$ are the space averaged velocity spectrum for plate 1 and plate 3, and $\bar{a}_1(f)$ and $\bar{a}_3(f)$ are the space averaged velocity spectrum for plate 1 and plate 3.

7.3.2.2 Results and discussion

The measured energy level differences between plate 1 and plate 3 for the undamped and damped cases are shown in Figure 7-21. The combination of constrained layer damping and granular damping appears to have a very good damping effect. For frequencies above 500Hz, an increase of approximately 15dB in energy level difference can be observed when plate 2 is damped.

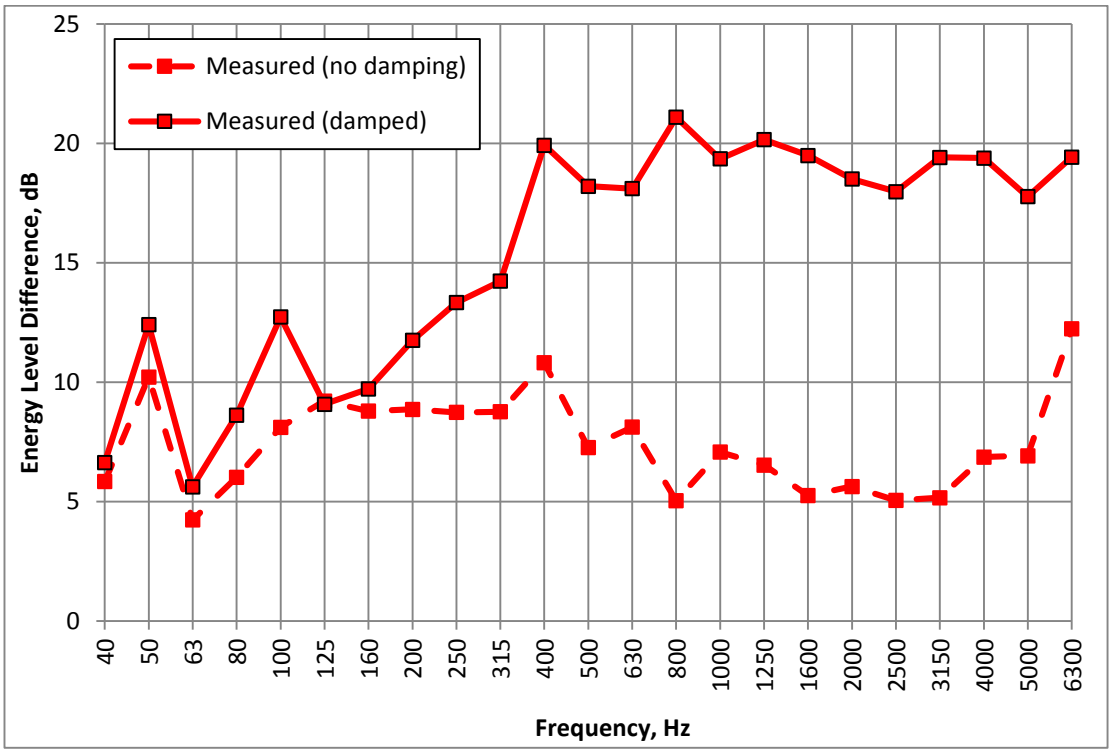

Figure 7-21 Energy level difference between plate 1 and plate 3

The 95% confidence intervals for the third octave energy level measurements for both tests are shown in Figure 7-22. Over most of the frequency range, this was smaller than 1.2dB. Some exceptions occurred at low frequencies but they never

exceeded 2dB. This suggests sufficient accuracy of the measured data to conclude that above 500Hz the damping has had a significant effect.

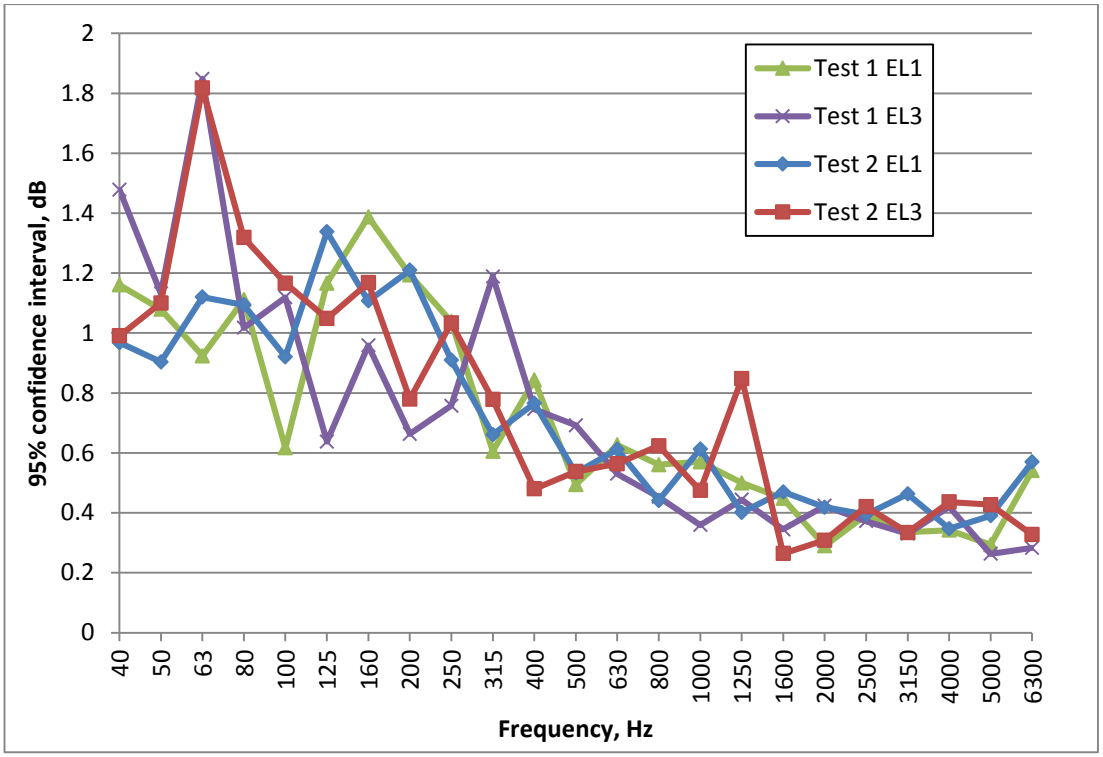

Figure 7-22 95% confidence intervals for energy level (EL) measurements

7.3.3 Validation of ray tracing

Comparison between the measured energy level difference and predictions from SEA and a hybrid SEA/ray tracing model are made to test which modelling method is more accurate in both undamped and damped cases.

7.3.3.1 Loss factor measurement

The power injection method was applied to measure the total loss factor for plate 1, plate 3 and plate 2 (damped and undamped) in the system shown in Figure 7-20. Same technique was used as described in Section 2.4.

7.3.3.2 SEA and hybrid modelling

An SEA model was been built to estimate the energy level difference for the test structure (the analysis was similar to the one shown in Section 5.6.4.1). For the subject studied in this case, a bending only model was used since the mode count for in-plane waves at the highest 1/3 octave frequency centre frequency (6300Hz)

are 2.66 for transverse waves and 0.93 for longitudinal waves. According to Hopkins (2002), SEA works effectively when the mode count exceeds 5. Therefore, in-plane waves are not considered in this SEA modelling.

The second prediction was made using the hybrid SEA/ray tracing method described in Chapter 5.

Plate 2 is connected to two other plates rather than four as discussed in Chapter 5. Therefore, a modified ray trace code was written to reflect the fact that there are only two structural couplings for the damped plate (the analysis was similar to the one shown in Section 5.4.6.3).

In both cases, the total loss factors measured in Section 7.3.3.1 were used.

7.3.3.3 Result and discussion

The measured loss factors of plate 1, plate 2 (damped and undamped) and plate 3 are shown in Figure 7-23. The combination of constrained layer damping and granular damping results in a significant increase in loss factor. In the literature, one usually describes a system is lightly damped when the damping coefficient $\zeta < 0.1$ (Clarence and Silva, 2007). The corresponding loss factor is 0.2 (see Equation 2-97). The measured loss factor of plate 2 when it is damped is greater than 0.2 over the majority of the frequency range. It cannot therefore be described as lightly damped and may be described as underdamped (see Section 2.4.1).

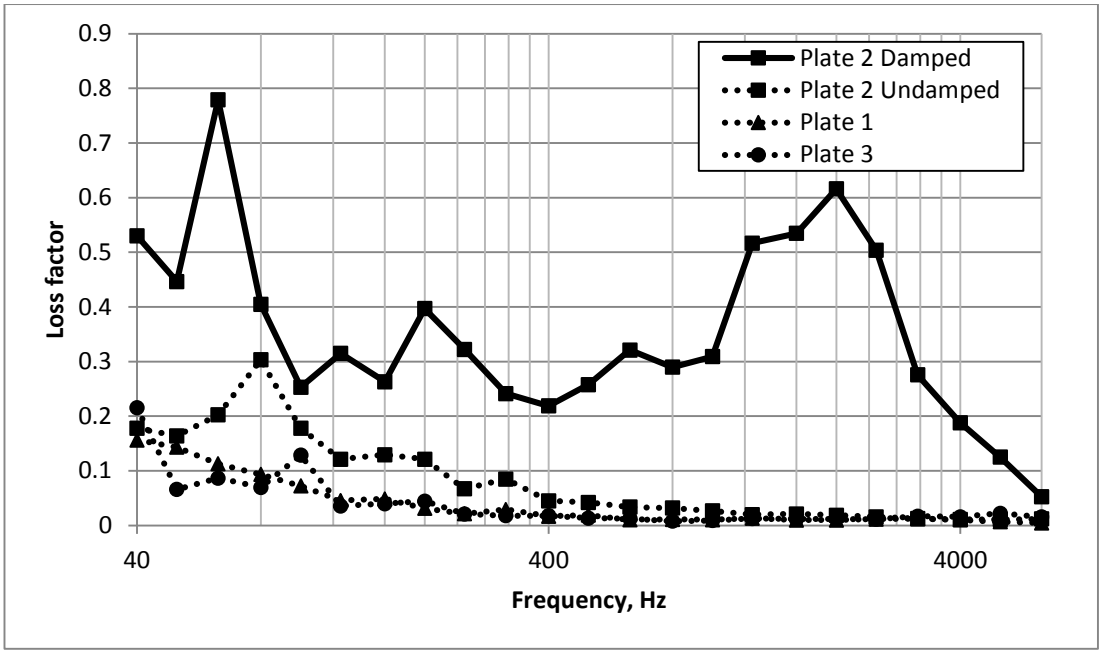

Figure 7-23 Measured loss factors for the components in the three-plate test rig

A comparison between the measured level difference between subsystem 1 and 3 and the results from the SEA and hybrid SEA/ray tracing modelling making use of the measured damping data is shown in Figure 7-24 and Figure 7-25.

Both the SEA and hybrid approaches give satisfactory predictions when subsystem 2 is undamped (see Figure 7-24), which is expected. SEA gives approximately 2dB higher prediction values than the hybrid method. From the results, one may find the hybrid method generally gives better estimation at frequencies above 1600Hz, while SEA works better over frequency range below 1600Hz. At frequencies below 125Hz, neither method shows good agreement with the measured data. The frequency at which the bending mode count exceeds 5 is around 315Hz and as suggested by Hopkins (2002) below this frequencies the mode count is too low for SEA to work effectively. Over the mid and high frequency range, the hybrid method is expected to give better estimation because as the frequency increases the attenuation with distance becomes more significant and the SEA assumption of a diffuse field is less valid. The attenuation with distance is not that significant until the frequency exceeds 1600Hz.

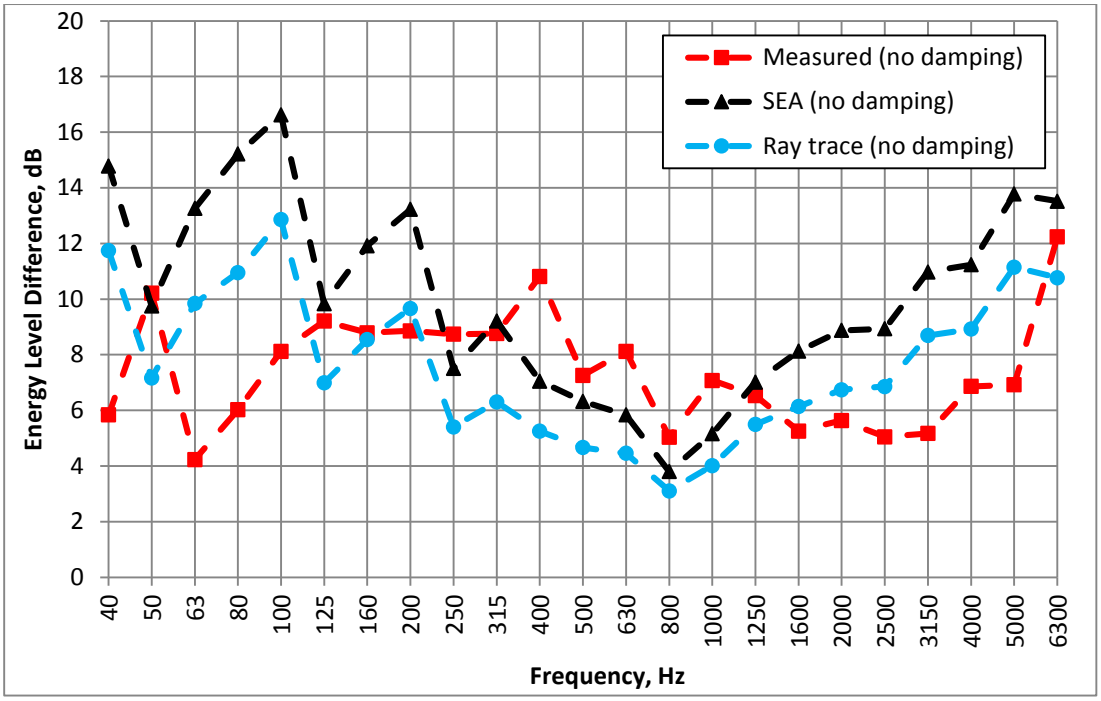

Figure 7-24 Comparison between the measured energy level difference between subsystem 1 and 3 with SEA and hybrid modelling (No added damping)

When subsystem 2 is damped, SEA generally gives approximately 5dB higher estimation than the hybrid SEA/ray tracing method. The hybrid method gives better prediction at frequencies above 1250Hz which is as expected. The unexpected finding is that it gives worse estimation over frequency range between 250Hz and 1250Hz (see Figure 7-25). When subsystem 2 is heavily damped, it becomes less modal and SEA tends to be less reliable. Meanwhile, the energy attenuation with distance tends to be so significant that SEA over predicts the energy level difference between plate 1 and 3. The hybrid method is thus expected to work better over the whole frequency range especially at high frequencies where energy attenuation with distance is more significant. The reason why it is not working properly over frequency range from 250Hz to 1250Hz is unknown. One possible explanation is that the measured loss factor of plate 2 when it is damped is lower than the actual one in mid frequency region (315Hz to 1250Hz). Further modifications of the power injection method, i.e. using a shaker excitation, increasing the number of measurements, using a light weight damping treatment etc., can be performed in the future work.

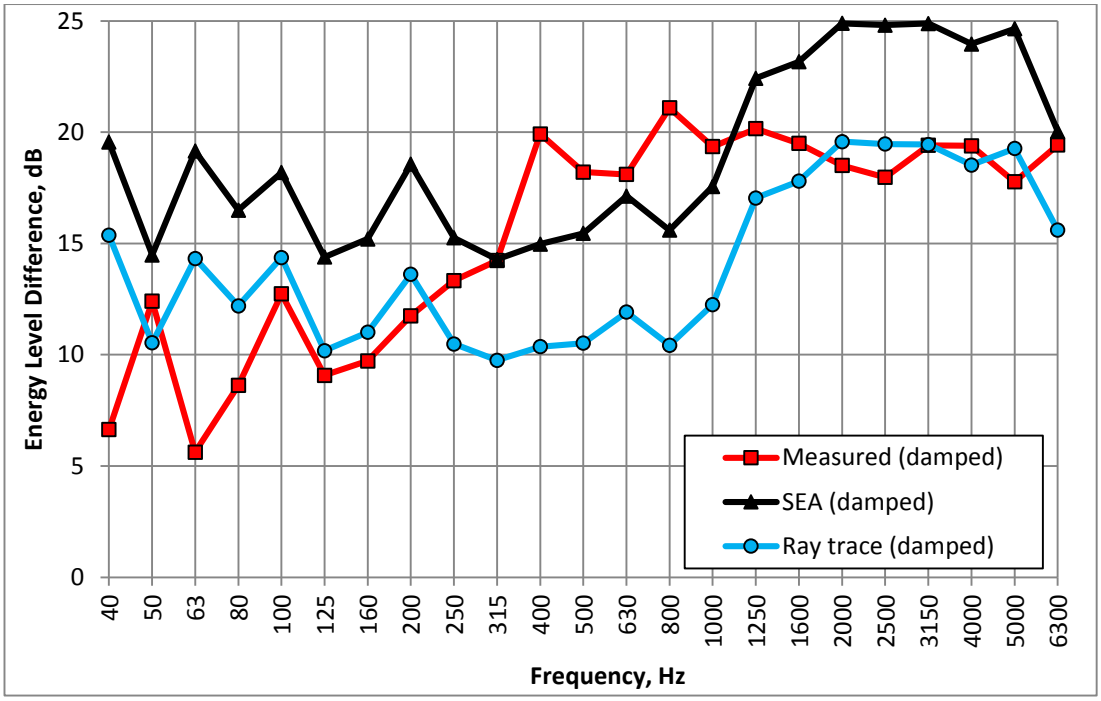

Figure 7-25 Comparison between the measured energy level difference between subsystem 1 and 3 with SEA and hybrid modelling (Damped)

7.4 Conclusion

Several loss factor measurement techniques have been examined in this chapter. The power injection method was suggested as the most appropriate technique for measuring structural loss factor in situations where high level of damping are present.

Experimental validation of the hybrid SEA/ray tracing modelling has been undertaken for a three-plate system. The power injection method was used to measure the loss factors, which were utilised in SEA and hybrid modelling. Both the SEA and hybrid approaches gave satisfactory prediction for an undamped system. For a damped system, the hybrid method was found work well at frequencies above 1250Hz. The experimental results suggest that they hybrid method works well for undamped subsystems and for damped subsystem it gives good approximation in the high frequency range (above 1250Hz).

The next question is how one may use ray tracing in conventional SEA modelling to deal with the transmission problem for systems with heavily damped subsystems, and how it differs from pure SEA modelling. This will be examined in Chapter 8.

CHAPTER 8 APPLICATION OF RAY TRACING IN SEA MODELLING

8.1 Introduction

For lightly damped systems (i.e. common masonry buildings), one may use normal SEA to predict acoustic transmission. For buildings with heavily damped structural elements, one may still use SEA prediction by modifying the ILFs of these elements accordingly. One of the fundamental assumptions in SEA is a diffuse field (Section 3.2.1). As the structural element becomes increasingly heavily damped, the wave fields it supports are less likely to be diffuse and the energy within the subsystem is less likely to be evenly distributed. Thus the reliability of the predictions obtained using SEA are likely to become increasingly doubtful.

An alternative is to use ray trace to account for the behaviour of heavily damped components within the framework of SEA. The energy transmission along these damped elements can be determined using ray trace code. This information can then be substituted back into SEA modelling to work out the energy level difference between the source and receiver. This approach is called the hybrid SEA/ray tracing method.

Comparisons between these two approaches are given for a simple one-room system to understand the implication on performance. This also gives an idea of reliability of the analysis undertaken in Chapter 4. A bending only model for SEA modelling is used for a direct comparison with the hybrid approach because the ray trace code only considers bending transmission. In addition, in-plane waves do not have significant contributions in the transmission in the frequency range considered in this case.

8.2 Definition of heavily damped subsystem

Before starting a discussion about the application of ray tracing in SEA modelling, one needs to understand when a subsystem can be treated as a heavily damped subsystem. There are three important factors that influence the energy transmission through a damped subsystem, i.e. subsystem dimension, internal loss and frequency. One important finding in Chapter 5 (Section 5.6) is the phenomenon

of energy concentration along the edge. One may use the proposed effective length ratio as a parameter to determine whether a subsystem is heavily damped since it is also governed by dimension, internal loss and frequency. The author proposed to define a heavily damped subsystem as the subsystem that has an effective length ratio that is less than 0.5, i.e. 90% of the energy transmission across the edge occurs within the first half of the edge length. By this definition, the transmission through the first half length is about 9.5dB more important than the last half. This criterion is suggested as the resulting error equates to the level of uncertainty present in measured results at high frequencies, e.g. see Figure 7-22.

Recalling the result in Section 7.3.3, the effective length ratio for damped case is 0.525 at 100Hz and 0.125 at 1250Hz. As the frequency increases, the effective length ratio gets smaller. By using the proposed definition, one may say that subsystem 2 is a heavily damped subsystem at frequencies above 100Hz. The ray trace works typically well at frequencies above 1250Hz where the effective length ratio is below 0.125.

For a common concrete wall with dimension of 4m*2.5m*0.15m with ILF=0.3, the effective length ratio drops below 0.5 at frequencies above 100Hz (i.e. if one assumes the shorter edge is the source). Therefore, this concrete wall is treated as a heavily damped subsystem. In light of this, common masonry structures with ILF=0.3 can generally be treated as heavily damped subsystems over the majority of the frequency range (40Hz to 6300Hz). The analysis about the selected one-room system in this chapter used this definition.

8.3 Simple one room system

Assuming there is a room with a dimension of 3m*4m*2.5m as shown in Figure 8-1, it and its enclosing structure may be described using 7 subsystems (6 structural subsystems and 1 room). All structural subsystems are assumed to be made from concrete and share the same thickness and material properties, i.e. $h = 0.15m$, $\rho = 2300kg/m^3$, $c_L = 3686m/s$ and $ILF = 0.015$. The reverberation time for the room is assumed to be $0.5s$. The energy level difference between subsystem 1 and

subsystem 6 can be predicted using SEA if one assumes only subsystem 1 has a power input.

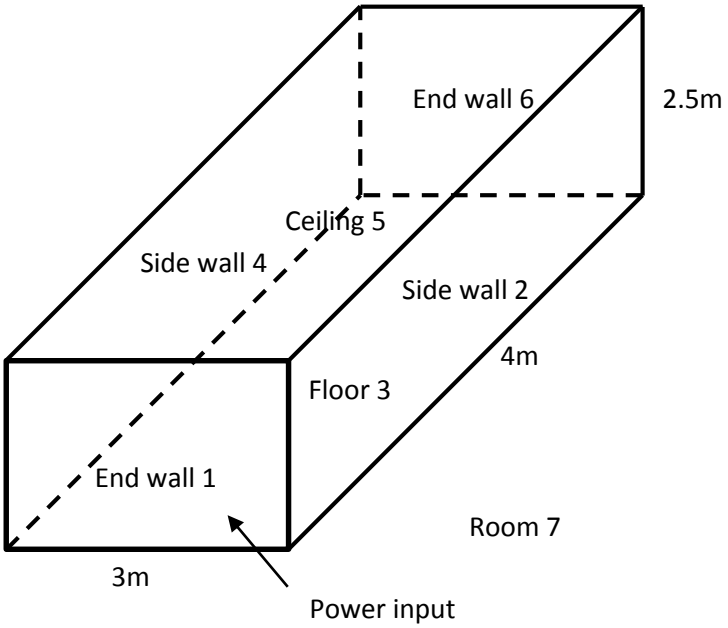

Figure 8-1 Illustration of the one room system

8.3.1 Inherent (Case 1)

The system shown in Figure 8-1 may be described using the SEA model and the classic SEA matrix can be written for the system as:

$$\begin{bmatrix} -\eta_1 & \eta_{21} & \eta_{31} & \eta_{41} & \eta_{51} & \eta_{61} & \eta_{71} \\ \eta_{12} & -\eta_2 & \eta_{32} & \eta_{42} & \eta_{52} & \eta_{62} & \eta_{72} \\ \eta_{13} & \eta_{23} & -\eta_3 & \eta_{43} & \eta_{53} & \eta_{63} & \eta_{73} \\ \eta_{14} & \eta_{24} & \eta_{34} & -\eta_4 & \eta_{54} & \eta_{64} & \eta_{74} \\ \eta_{15} & \eta_{25} & \eta_{35} & \eta_{45} & -\eta_5 & \eta_{65} & \eta_{75} \\ \eta_{16} & \eta_{26} & \eta_{36} & \eta_{46} & \eta_{56} & -\eta_6 & \eta_{76} \\ \eta_{17} & \eta_{27} & \eta_{37} & \eta_{47} & \eta_{57} & \eta_{67} & -\eta_7 \end{bmatrix} \begin{bmatrix} E_1 \\ E_2 \\ E_3 \\ E_4 \\ E_5 \\ E_6 \\ E_7 \end{bmatrix} = \begin{bmatrix} -W_1/\omega \\ 0 \\ 0 \\ 0 \\ 0 \\ 0 \\ 0 \end{bmatrix} \tag{8-1}$$

where $\eta_{61} = \eta_{42} = \eta_{53} = \eta_{24} = \eta_{35} = \eta_{16} = 0$. All the loss factors can be readily calculated using formulas suggested by Craik (1996).

For given power input W_1, one may predict the energy level difference between subsystem 1 and subsystem 6 as:

$$\mathrm{ELD16(dB)} = 10 \log_{10} \frac{E_1}{E_6} \tag{8-2}$$

8.3.2 Damping on subsystem 2 (Case 2)

If one applies damping treatment on subsystem 2, i.e. ILF=0.3, subsystem 2 is no longer modal and needs to be taken out of the SEA model (here it will be referred to as a 'coupling element 2' to distinguish it from a subsystem capable of supporting modes). However, energy transmissions through path 1-2-3, 1-2-5, 1-2-6 still exist (Figure 8-2). One may use ray tracing code to determine the equivalent CLFs (between subsystem 1 and 3 via 2, 1 and 5 via 2, and 1 and 6 via 2), and substitute them into SEA matrix to work out the energy distribution.

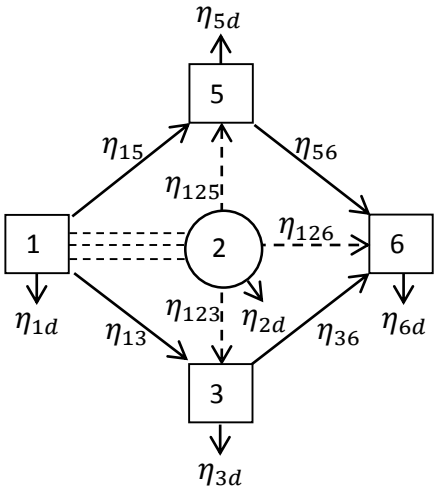

Figure 8-2 SEA model when component 2 is heavily damped (only part of the system is presented)

In the diagram of the systems under investigation, normal SEA subsystems are represented using solid rectangles with numbers. When a subsystem is heavily damped, it is treated as a coupling element, represented by circle with a number. The coupling loss factor between normal SEA subsystems for path 1-2-3 are η_{12} and η_{13}, represented with solid arrow (Figure 8-3 a). When component 2 is heavily damped, it can no longer be represented using a subsystem, and the coupling between subsystem 1 and 3 is denoted as η_{123}, which means the equivalent CLF from subsystem 1 to 3 via coupling element 2. This equivalent CLF is represented with dashed arrow (Figure 8-3 b). If there are two coupling elements in the path, the equivalent CLF is denoted as η_{1234}, which means the transmission occurs from subsystem 1 to 4 via coupling element 2 and 3(Figure 8-3 c). These notations are

intended for use in this chapter only and seek to aid the explanation of how heavily damped elements are accumulated within the SEA framework.

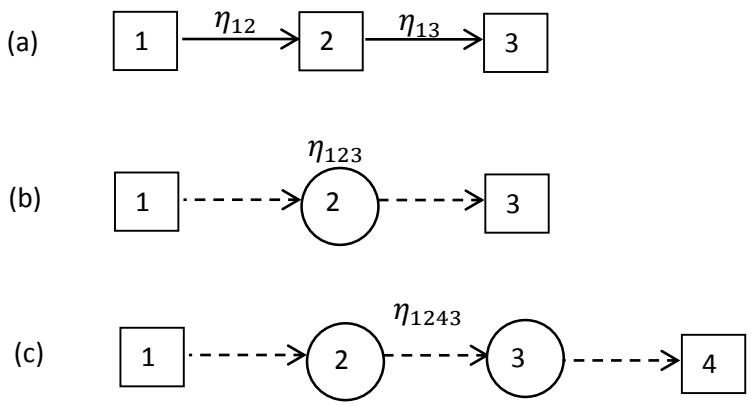

Figure 8-3 Illustration of coupling elements and equivalent CLFs in SEA modelling

In the model presented in Figure 8-1, for path 1-2-i, the energy transmitted from coupling element 2 to subsystem i has the relationship:

$$W_{2i} = E_1 \omega \eta_{12i} \tag{8-3}$$

where η_{12i} is the equivalent CLF from subsystem 1 to subsystem i via coupling element 2.

The energy transmitted from subsystem 1 to coupling element 2 can be written as:

$$W_{12} = E_1 \omega \eta_{12} \tag{8-4}$$

Equation 8-3 and 8-4 gives:

$$\eta_{12i} = \frac{\eta_{12}}{W_{12}/W_{2i}} \tag{8-5}$$

The ratio in the denominator can be readily determined from ray tracing code. One may note that W_{12}/W_{2i} is always greater than unity, which means the equivalent

CLF is always smaller than the CLF between the source subsystem and the heavily damped subsystem.

Therefore, the new CLF from subsystem 1 to subsystem i can be expressed as:

$$\tilde{\eta}_{1i} = \eta_{1i} + \frac{\eta_{12}}{W_{12}/W_{2i}} \tag{8-6}$$

This means the CLF from the source subsystem to the other subsystem contains two parts: one is the direct coupling from the source to the receiver, and the other considers the transmission via the coupling element.

The general form of the new structural CLF from subsystem i to subsystem j, where it is assumed that the coupling element is 2, is thus:

$$\tilde{\eta}_{ij} = \eta_{ij} + \frac{\eta_{i2}}{W_{i2}/W_{2j}} \tag{8-7}$$

The SEA matrix when subsystem 2 is heavily damped is now:

$$\begin{bmatrix} -\eta_1 & \tilde{\eta}_{31} & \eta_{41} & \tilde{\eta}_{51} & \tilde{\eta}_{61} & \eta_{71} \\ \tilde{\eta}_{13} & -\eta_3 & \eta_{43} & \tilde{\eta}_{53} & \tilde{\eta}_{63} & \eta_{73} \\ \eta_{14} & \eta_{34} & -\eta_4 & \eta_{54} & \eta_{64} & \eta_{74} \\ \tilde{\eta}_{15} & \tilde{\eta}_{35} & \eta_{45} & -\eta_5 & \tilde{\eta}_{65} & \eta_{75} \\ \tilde{\eta}_{16} & \tilde{\eta}_{36} & \eta_{46} & \tilde{\eta}_{56} & -\eta_6 & \eta_{76} \\ \eta_{17} & \eta_{37} & \eta_{47} & \eta_{57} & \eta_{67} & -\eta_7 \end{bmatrix} \begin{bmatrix} E_1 \\ E_3 \\ E_4 \\ E_5 \\ E_6 \\ E_7 \end{bmatrix} = \begin{bmatrix} -W_1/\omega \\ 0 \\ 0 \\ 0 \\ 0 \\ 0 \end{bmatrix} \tag{8-8}$$

8.3.3 Damping on subsystem 2 and 4 (Case 3)

When both component 2 and component 4 are damped, i.e. ILF=0.3, they are both considered as coupling elements. Similar analysis can be completed to give the new CLFs.

The new structural coupling between subsystem i to subsystem j, where it is assumed that the coupling elements are 2 and 4, is:

$$\tilde{\eta}_{ij} = \eta_{ij} + \frac{\eta_{i2}}{W_{i2}/W_{2j}} + \frac{\eta_{i4}}{W_{i4}/W_{4j}} \tag{8-9}$$

Therefore, the SEA matrix when both component 2 and 4 are heavily damped is:

$$\begin{bmatrix} -\eta_1 & \tilde{\eta}_{31} & \tilde{\eta}_{51} & \tilde{\eta}_{61} & \eta_{71} \\ \tilde{\eta}_{13} & -\eta_3 & \tilde{\eta}_{53} & \tilde{\eta}_{63} & \eta_{73} \\ \tilde{\eta}_{15} & \tilde{\eta}_{35} & -\eta_5 & \tilde{\eta}_{65} & \eta_{75} \\ \tilde{\eta}_{16} & \tilde{\eta}_{36} & \tilde{\eta}_{56} & -\eta_6 & \eta_{76} \\ \eta_{17} & \eta_{37} & \eta_{57} & \eta_{67} & -\eta_7 \end{bmatrix} \begin{bmatrix} E_1 \\ E_3 \\ E_5 \\ E_6 \\ E_7 \end{bmatrix} = \begin{bmatrix} -W_1/\omega \\ 0 \\ 0 \\ 0 \\ 0 \end{bmatrix} \tag{8-10}$$

8.3.4 Damping on subsystem 2, 3, 4 and 5 (Case 4)

When components 2, 3, 4 and 5 are all damped, i.e. ILF=0.3, they are all considered as coupling elements. In this case, the SEA model only has three subsystems, i.e. subsystem 1, 6 and 7. The couplings between the structural subsystems and the room remain unaltered. The determination of new CLF from subsystem 1 to subsystem 6 is complicated. The equivalent CLFs for paths such as path 1-2-6 can be calculated easily. However, for paths such as path 1-2-5-6, the equivalent CLFs are hard to determine. The ray trace code can predict the transmission and equivalent CLF for path 1-2-5, but the estimation of the equivalent CLF for path 2-5-6 is not that reliable. This is because, when component 2 is no longer modal, the energy transmission from component 2 to 5 is less likely to be a line source and hence the approximation using discrete acoustic rays with same initial energy tends to fail. This happens every time two coupling elements are physically connected.

If one assumes that ray trace still works properly under this circumstance (i.e. the energy along the source edge is evenly distributed), the new CLF from subsystem 1 to subsystem 6 is thus:

$$\tilde{\eta}_{16} = \eta_{16} + \frac{\eta_{12}}{W_{12}/W_{26}} + \frac{\eta_{14}}{W_{14}/W_{46}} + \frac{\eta_{13}}{W_{13}/W_{36}} + \frac{\eta_{15}}{W_{15}/W_{56}}$$
$$+ \frac{\eta_{125}}{W_{25}/W_{56}} + \frac{\eta_{123}}{W_{23}/W_{36}} + \frac{\eta_{132}}{W_{32}/W_{26}} + \frac{\eta_{134}}{W_{34}/W_{46}} + \frac{\eta_{143}}{W_{43}/W_{36}} + \frac{\eta_{145}}{W_{45}/W_{56}} \tag{8-11}$$
$$+ \frac{\eta_{152}}{W_{52}/W_{56}} + \frac{\eta_{154}}{W_{54}/W_{46}}$$

where η_{16} is the airborne CLF, $\frac{\eta_{12}}{W_{12}/W_{26}} + \frac{\eta_{14}}{W_{14}/W_{46}} + \frac{\eta_{13}}{W_{13}/W_{36}} + \frac{\eta_{15}}{W_{15}/W_{56}} = \eta_{126} + \eta_{146} + \eta_{136} + \eta_{156}$ is the sum of the equivalent direct CLFs (path 1-2-6, 1-4-6, 1-3-6 and 1-5-6), and the rest is the sum of the equivalent first order flanking CLFs (path

1-2-5-6, 1-2-3-6, 1-3-2-6, 1-3-4-6, 1-4-3-6, 1-4-5-6, 1-5-2-6 and 1-5-4-6). When the ILFs are high, longer paths do not have significant contribution to the transmission (referring to Section 4.5 and 4.6). Therefore, longer paths such as path 1-2-3-5-6 are not included (i.e. only direct paths and 1st order flanking paths are considered).

Similarly, one has:

$$\tilde{\eta}_{61} = \eta_{61} + \frac{\eta_{62}}{W_{62}/W_{21}} + \frac{\eta_{64}}{W_{64}/W_{41}} + \frac{\eta_{63}}{W_{63}/W_{31}} + \frac{\eta_{65}}{W_{65}/W_{51}}$$
$$+ \frac{\eta_{625}}{W_{25}/W_{51}} + \frac{\eta_{623}}{W_{23}/W_{31}} + \frac{\eta_{632}}{W_{32}/W_{21}} + \frac{\eta_{634}}{W_{34}/W_{41}} + \frac{\eta_{643}}{W_{43}/W_{31}} + \frac{\eta_{645}}{W_{45}/W_{51}} \quad (8\text{-}12)$$
$$+ \frac{\eta_{652}}{W_{52}/W_{51}} + \frac{\eta_{654}}{W_{54}/W_{41}}$$

The SEA matrix for damped subsystem 2, 3, 4 and 5 is thus:

$$\begin{bmatrix} -\eta_1 & \tilde{\eta}_{61} & \eta_{71} \\ \tilde{\eta}_{16} & -\eta_6 & \eta_{76} \\ \eta_{17} & \eta_{67} & -\eta_7 \end{bmatrix} \begin{bmatrix} E_1 \\ E_6 \\ E_7 \end{bmatrix} = \begin{bmatrix} -W_1/\omega \\ 0 \\ 0 \end{bmatrix} \quad (8\text{-}13)$$

8.4 Results and discussion

Predictions for the energy level difference between subsystem 1 and 6 for different damping arrangements are shown in Figure 8-4. Higher energy level difference can generally be observed when adding damping treatment to the system. The results from SEA and hybrid SEA/ray tracing predictions have similar results for Case 2 where only component 2 is damped and Case 3 where both components 2 and 4 are damped. When components 2, 3, 4 and 5 are all damped (Case 4), the hybrid method tends to give higher level difference, especially at high frequencies. One may also find first order flanking transmission in Case 4 makes a big contribution in the transmission. Considering direct paths only results in over prediction of the energy level difference.

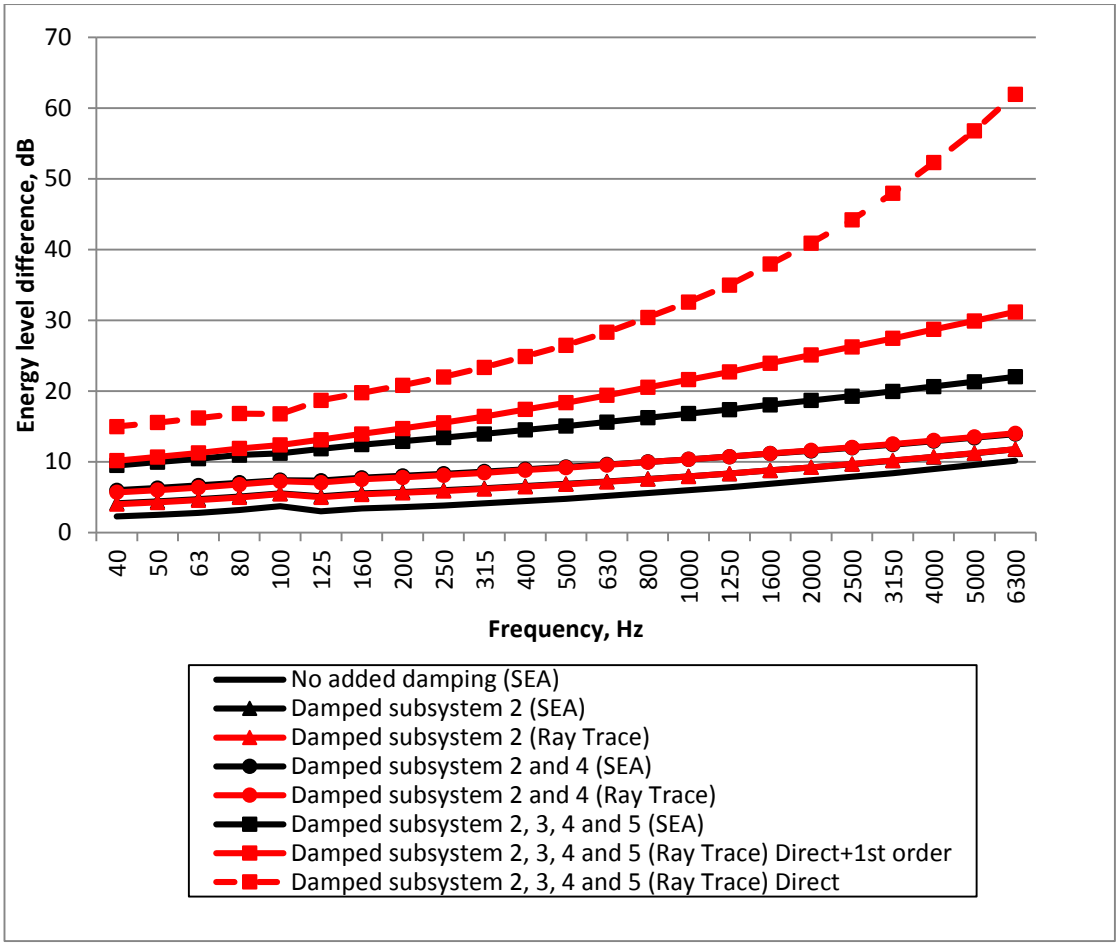

Figure 8-4 Energy level difference between subsystem 1 and 6 for one-room system

In order to further understand the reason why SEA and the hybrid approach give similar results in Case 2 and Case 3, the contribution of specific paths have been analysed. The discussion in Section 5.6.4 indicates that SEA under predicts the transmission across the perpendicular edges and over predicts the transmission across the parallel edge. These errors may cancel with each other in a one-room system.

If one assumes subsystem 1 is the source, the energy in subsystem n due to transmission along path 1-2-3-4…n can be given as (Craik, 1996):

$$\hat{E}_n = E_1 \frac{\eta_{12}\eta_{23}\eta_{34}\cdots\eta_{(n-1)n}}{\eta_2\eta_3\eta_4\cdots\eta_n} \tag{8-14}$$

In Case 2, the same analysis can be performed for path 1-2-3, 1-2-4, 1-2-6 and path 1-2-1. In pure SEA modelling, one has:

$$\hat{E}_3 = E_1 \frac{\eta_{12}\eta_{23}}{\eta_2\eta_3} \tag{8-15}$$

$$\hat{E}_4 = E_1 \frac{\eta_{12}\eta_{24}}{\eta_2\eta_4} \tag{8-16}$$

$$\hat{E}_6 = E_1 \frac{\eta_{12}\eta_{26}}{\eta_2\eta_6} \tag{8-17}$$

$$\hat{E}_1 = E_1 \frac{\eta_{12}\eta_{21}}{\eta_2\eta_1} \tag{8-18}$$

The total energy contribution from subsystem 1 via subsystem 2 to other structural subsystems is thus:

$$E_{SEA} = E_1 \frac{\eta_{12}\eta_{23}}{\eta_2\eta_3} + E_1 \frac{\eta_{12}\eta_{24}}{\eta_2\eta_4} + E_1 \frac{\eta_{12}\eta_{26}}{\eta_2\eta_6} + E_1 \frac{\eta_{12}\eta_{21}}{\eta_2\eta_1} \tag{8-19}$$

If one excludes subsystem 2 from the SEA model and uses equivalent CLF, one has:

$$\hat{E}_3 = E_1 \frac{\eta_{123}}{\eta_3} \tag{8-20}$$

$$\hat{E}_4 = E_1 \frac{\eta_{124}}{\eta_4} \tag{8-21}$$

$$\hat{E}_6 = E_1 \frac{\eta_{126}}{\eta_6} \tag{8-22}$$

$$\hat{E}_1 = E_1 \frac{\eta_{121}}{\eta_1} \tag{8-23}$$

Similarly, the total energy contribution is:

$$E_{Ray\ Trace} = E_1 \frac{\eta_{123}}{\eta_3} + E_1 \frac{\eta_{124}}{\eta_4} + E_1 \frac{\eta_{126}}{\eta_6} + E_1 \frac{\eta_{121}}{\eta_1} \tag{8-24}$$

The difference between $E_{Ray\ Trace}$ and E_{SEA} is thus:

$$10\log_{10}\frac{E_{Ray\ Trace}}{E_{SEA}} = 10\log_{10}\frac{\frac{\eta_{123}}{\eta_3}+\frac{\eta_{124}}{\eta_4}+\frac{\eta_{126}}{\eta_6}+\frac{\eta_{121}}{\eta_1}}{\frac{\eta_{12}\eta_{23}}{\eta_2\eta_3}+\frac{\eta_{12}\eta_{24}}{\eta_2\eta_4}+\frac{\eta_{12}\eta_{26}}{\eta_2\eta_6}+\frac{\eta_{12}\eta_{21}}{\eta_2\eta_1}} \quad (8\text{-}25)$$

The same analysis can be performed for path 3-2-1, 3-2-6, 3-2-5 and 3-2-3. The result is shown in Figure 8-5. If the energy enters subsystem 2 through the coupling between subsystem 1 and 2, SEA under predicts the overall energy that leaves subsystem 2. If the energy enters subsystem 2 through the coupling between subsystem 3 and 2, SEA over predicts the total energy that leaves subsystem 2. Those two errors have similar values and tend to cancel with each other. As a result, SEA gives similar prediction result as ray trace. Same curve can be obtained for Case 3 because of geometry similarity.

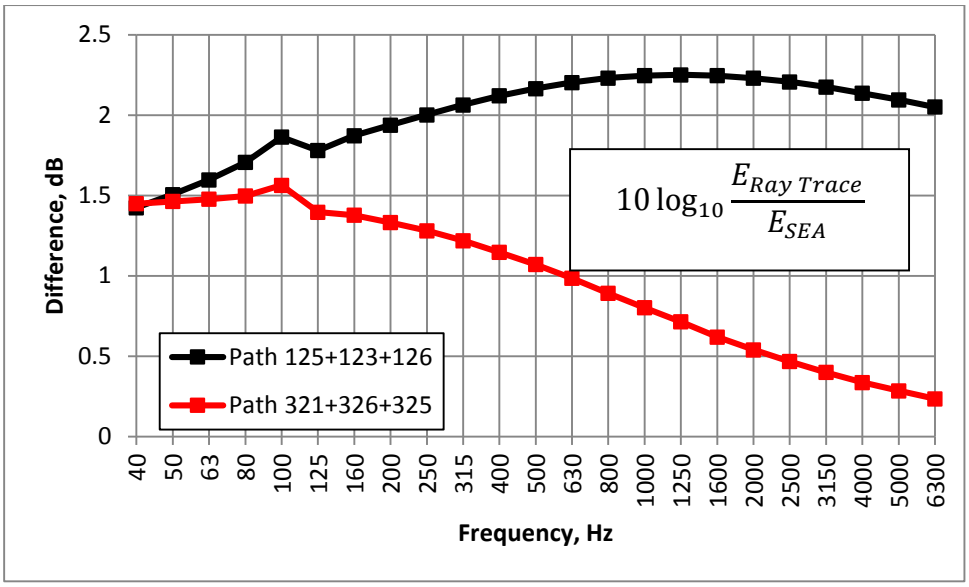

Figure 8-5 Difference between the total energy contribution from subsystem 1 (subsystem 3) via subsystem 2 predicted by Ray trace and SEA (Case 2 and 3)

Recalling the analysis in Section 5.6.4, SEA under predicts the transmission through the edges that are perpendicular to the source edge and over predicts the transmission through the edges that are parallel to the source edge. One can conclude that if the energy enters through the shorter edge, SEA over predicts the energy loss within that component, and if the energy enters through the longer edge, SEA under predicts the energy loss within that component.

For Case 4, since none of components 2, 3, 4 and 5 is modal, Equation 8-14 can only be used to describe the transmission between subsystem 1 and 6. Hence, one has:

$$E_{Ray\ Trace} = E_1 \frac{\tilde{\eta}_{16}}{\eta_6} \tag{8-26}$$

$$\begin{aligned} E_{SEA} = E_1 \Bigg(& \frac{\eta_{12}\eta_{26}}{\eta_2\eta_6} + \frac{\eta_{13}\eta_{36}}{\eta_3\eta_6} + \frac{\eta_{14}\eta_{46}}{\eta_4\eta_6} + \frac{\eta_{15}\eta_{56}}{\eta_5\eta_6} + \frac{\eta_{12}\eta_{23}\eta_{36}}{\eta_2\eta_3\eta_6} + \frac{\eta_{12}\eta_{25}\eta_{56}}{\eta_2\eta_5\eta_6} \\ & + \frac{\eta_{13}\eta_{32}\eta_{26}}{\eta_3\eta_2\eta_6} + \frac{\eta_{13}\eta_{34}\eta_{46}}{\eta_3\eta_4\eta_6} + \frac{\eta_{14}\eta_{43}\eta_{36}}{\eta_4\eta_3\eta_6} + \frac{\eta_{14}\eta_{45}\eta_{56}}{\eta_4\eta_5\eta_6} \\ & + \frac{\eta_{15}\eta_{52}\eta_{26}}{\eta_5\eta_2\eta_6} + \frac{\eta_{15}\eta_{54}\eta_{46}}{\eta_5\eta_4\eta_6} \Bigg) \end{aligned} \tag{8-27}$$

where direct paths (i.e. path 1-2-6, 1-3-6, 1-4-6 and1-5-6) and first order flanking paths (i.e. path 1-2-3-6, 1-2-5-6, 1-3-2-6, 1-3-4-6, 1-4-3-6, 1-4-5-6, 1-5-2-6 and 1-5-4-6) are considered.

The result for Case 4 is shown in Figure 8-6. SEA tends to predict higher transmission from subsystem 1 to subsystem 6. In this case, over prediction of the transmission via the parallel edge dominates the influence of underestimating the transmission via the perpendicular edges and results in an over prediction of the total transmission. This is the reason why SEA shows a smaller energy level difference to the hybrid method in Figure 8-4 and the divergence between two modelling methods tends to increase at higher frequencies.

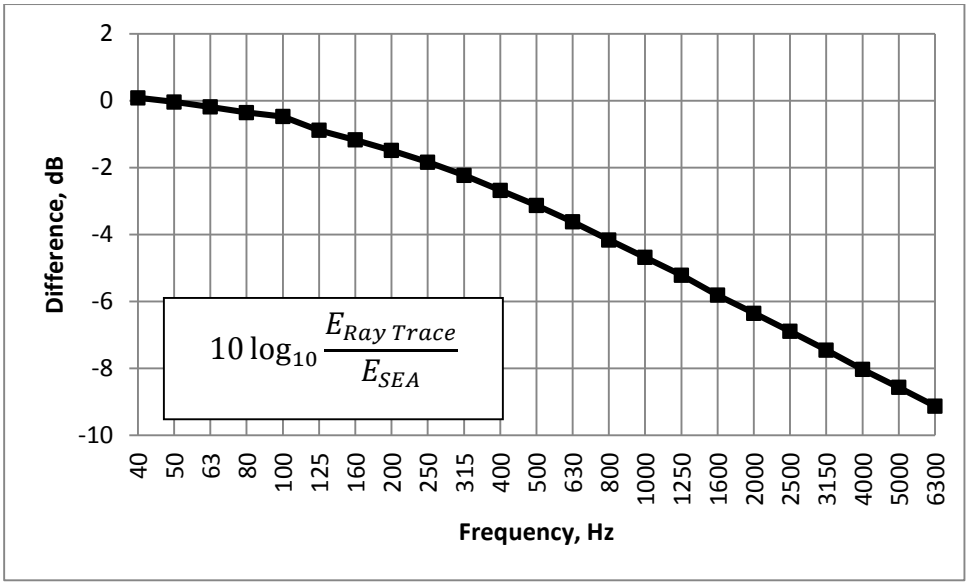

Figure 8-6 Difference between the total energy contribution from subsystem 1 to subsystem 6 predicted by Ray trace and SEA (Case 4)

To further understand the prediction difference when the coupling elements are physically connected, the same analysis is done assuming the case where components 2 and 3 are damped, and another case where components 2, 3 and 4 are damped. Again, only direct paths and first order flanking paths are considered. The result is shown in Figure 8-7. One may find the difference between SEA and the hybrid prediction is small when only some of the flanking structures are heavily damped. The difference becomes more significant if one increases the frequency or the number of damped components. Significant difference occurs when all of the flanking structures (i.e. subsystem 2, 3, 4 and 5) are heavily damped, i.e. all the paths except the air-borne path 1-7-6 have been damped. This finding suggests that when all of the structural paths are damped, SEA tends to over predict the transmission. Referring back to the discussion in Chapter 4, a greater benefit of applying damping treatment can be expected.

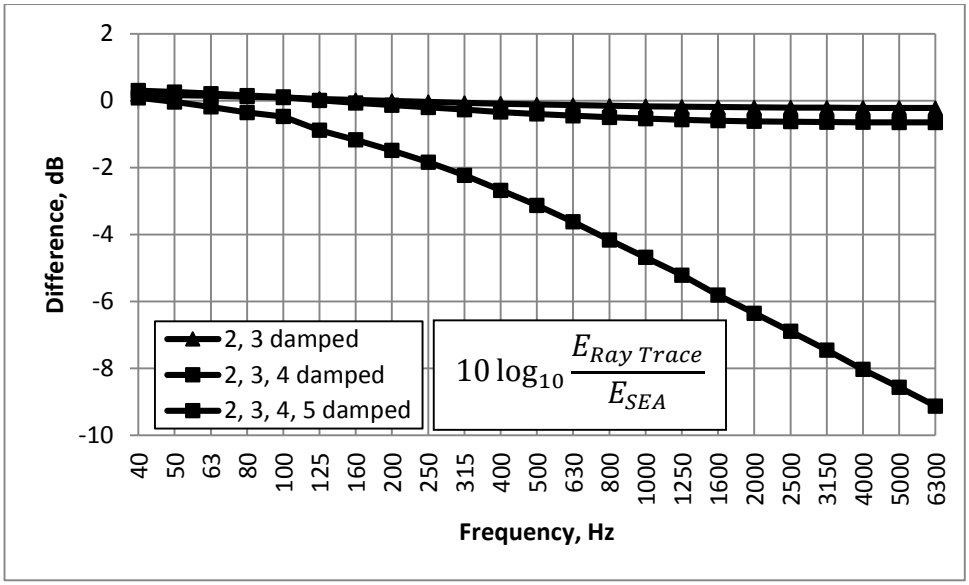

Figure 8-7 Difference between the total energy contribution from subsystem 1 to subsystem 6 predicted by Ray trace and SEA for different numbers of coupling elements

A plot of the energy level difference between subsystem 1 and 3 when subsystem 5 is damped and undamped due to specific path 1-5-6 is shown in Figure 8-8 to help explain the result in Figure 8-7. There exists significant difference between SEA and ray trace prediction for specific path when subsystem 5 is damped. When not all of the structural paths are damped, the transmission between subsystem 1 and 6 is dominant by the undamped paths so the difference between SEA and ray trace prediction is not obvious. This is another reason why SEA and ray trace show no significant difference in case 1 and 2 as shown in Figure 8-4. When all of the structural paths are damped, the estimation difference becomes much more obvious.

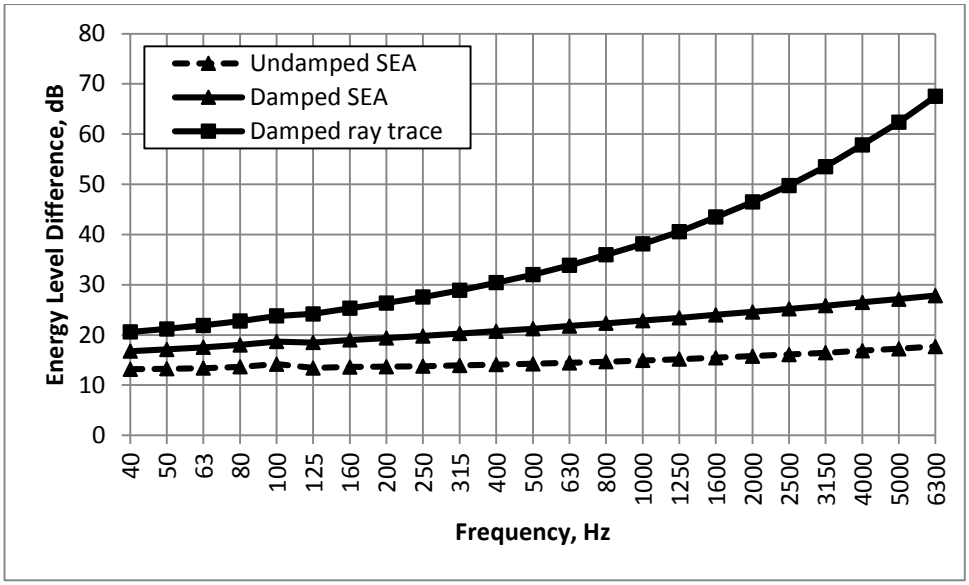

Figure 8-8 Energy level difference between subsystem 1 and 6 when subsystem 5 is damped and undamped due to specific path 1-5-6

8.5 Conclusion

A definition of heavily damped subsystem is proposed as the subsystem with effective length ratio smaller than 0.5.

Implication of ray trace in SEA frame work has been done for a one-room system. The result shows that the prediction from pure SEA for damped system is relatively reliable when a small number of the structural components are heavily damped because the prediction errors tends to cancel with each other and the transmission is dominated by paths that are not damped. When all of the structural paths are damped, SEA tends to underestimate the energy level difference, which implies a greater benefit may be observed when applying damping treatments globally such as in he case studied in Chapter 4.

The above findings are valid for simple one-room system and are believed to reflect the system behaviour for more complicated systems since the underlying principle does not change. Further validation of these findings for more complicated systems is far more complicated and would require further investigation.

CHAPTER 9 SUMMARY AND RECOMMENDATIONS FOR FUTURE WORK

9.1 Summary

This study aims to examine the potential benefit of applying passive damping technique to increase sound insulation in complex large buildings. Different mathematical models have been reviewed in order to understand the underlying principle of damping mechanisms. Statistical Energy Analysis has been chosen as the theoretical modelling framework due to its reliability and relatively simplicity in modelling complex vibrational problems. Both the advantages and limitations of SEA have been studied, which allows one to determine the applicability of SEA modelling.

Nine different theoretical models have been examined using both bending only and three wave SEA models. These models are constructed from simple two-room system to complex 24-room system. Common masonry material properties are used to represent real buildings. The general findings suggest that the effect of global damping application result in a better acoustic insulation and the initial application has better benefit. Damping treatment is found to be more effective for longer paths and as internal damping is increased, short paths, i.e. the direct path, tends to dominate transmission.

A forward path tracing algorithm has been developed to simulate the energy transmission through a heavily damped subsystem where SEA modelling tends to fail. A theoretical study of a 5-subsystem system is given and the direct field is found to dominate the transmission when the plate is heavily damped. Energy attenuation with distance (which is influenced by the internal damping and frequency), and transmission through edges (which occurs each time the rays are reflected from a boundary connected to other structural elements) are the two governing mechanisms. The phenomenon of energy concentration is observed along edges that are perpendicular to the source edge. A parameter named ‘effective length ratio’ is proposed to quantify this phenomena. Comparison between pure SEA and hybrid SEA/ray tracing modelling suggests that SEA tends to

over predict the transmission through an edge that is parallel to the source edge and under predict the transmission through edges that are perpendicular to the source edge.

Different passive damping treatment techniques including free layer damping, constrained layer damping, tuned mass damping and granular damping were reviewed. Constrained layer damping was found to be able to give a better loss factor and is suitable for building noise control.

Several loss factor measurement techniques were examined. A power injection method was selected for further validation of the ray trace code (hybrid method) due to its simplicity and reliability. Ray trace modelling has been validated by measuring the energy level difference within a three-plate system. It has been proven to work properly over all frequency bands above 1,600Hz for undamped case and gave good prediction for heavily damped case at frequencies above 1250Hz. It is proposed that a structural element with an effective length ratio below 0.5 can be defined as heavily damped.

Comparison between pure SEA and hybrid SEA/ray tracing modelling is given for one-room system. SEA generally gives similar result when part of flanking subsystems are damped as the prediction errors tend to cancel with each other and the undamped paths tend to dominate the transmission. When all of the structural paths are damped, SEA tends to over predict the transmission and results in underestimation of the energy level difference. The predictions of the energy level difference in Chapter 4 should have larger values and it suggests better sound insulation. The application of damping treatments can offer improvement in sound insulation in complex/large building structures

9.2 Recommendations for future work

The analyses in Chapter 4 and Chapter 8 are purely theoretical. Further experimental work is needed to validate predictions. One may study the damping effect in either real buildings or scale models to see the accuracy of the estimations.

The effect of global application of damping treatments on sound insulation improvement has been examined. Further study can be undertaken to explore the effect of damping application on parts of the system.

The current ray trace code only deals with transmission across a corner. Further development can be carried out to explore transmission across other types of joint. Wave conversion at the boundary could also be taken into consideration.

Using a combination of constrained layer damping and granular damping results in a very good damping effect on aluminium plate. The effectiveness of applying such technique on concrete walls or floors needs further validation. The effect of additional weight (introduced by damping treatment) on the wave propagation within the plate also needs to be studied.

Modifications can be done in using power injection method to measure the loss factor. Shaker excitation can provide constant power input and hence will provide more stable results. Using laser vibrometer instead of accelerometers may reduce the errors introduced by accelerometer mass.

Further comparison between pure SEA and hybrid SEA/ray tracing methods is needed for more complex systems.

REFERENCES

ADHIKARI, S. & PHANI, A. S. No date. Rayleigh's Classical Damping Revisited.

ANTANI, L., CHANDAK, A., SAVIOJA, L. & MANOCHA, D. 2012. Interactive sound propagation using compact acoustic transfer operators. *ACM Transactions on Graphics (TOG)*, 31(1), 7.

ANTONACCI, F., FOCO, M., SARTI, A. & TUBARO, S. 2008. Fast tracing of acoustic beams and paths through visibility lookup. *Audio, Speech, and Language Processing*, IEEE Transactions on, 16(4), 812-824.

ANTONACCI, F., SARTI, A. & TUBARO, S. 2010. Two-dimensional beam tracing from visibility diagrams for real-time acoustic rendering. *EURASIP Journal on Advances in Signal Processing*, 2010(1), 1-18.

ARGYRIS, J. & P., M. H. 1991. Dynamics of structures. *Text on computational mechanics* The Netherlands: Elsevier Science Publishers.

ARIKOGLU, A., 2014. A new fractional derivative model for linearly viscoelastic materials and parameter identification via genetic algorithms. *Rheologica Acta*, 53(3), 219-233.

BAGLEY, R. L. & TORVIK, P. 1983. A theoretical basis for the application of fractional calculus to viscoelasticity. *Journal of Rheology (1978-present),* 27**,** 201-210.

BAGLEY, R. L. & TORVIK, P. J. 1986. On the fractional calculus model of viscoelastic behavior. *Journal of Rheology (1978-present),* 30**,** 133-155.

BALDANZINI, N., NIEROP, G., PIERINI, M. & SCIPPA, A. 2003. Hybrid numerical-experimental characterisation of non conservative joints for SEA applications. In *Tenth International Congress on Sound and Vibration*.

BERT, C. W. 1973. Material damping: An introductory review of mathematic measures and experimental technique. *Journal of Sound and Vibration,* 29**,** 129-153.

BERTRAM, M., DEINES, E., MOHRING, J., JEGOROVS, J. & HAGEN, H. Phonon tracing for auralization and visualization of sound. Visualization, 2005. VIS 05. IEEE, 2005. IEEE, 151-158.

BESHARA, M. & KEANE, A. J. 1996. Statistical energy analysis of multiple, non-conservatively coupled systems. *Journal of Sound and Vibration,* 198**,** 95-122.

BIOT, M. A. Linear thermodynamics and the mechanics of solids. Proceedings of the Third US National Congress of Applied Mechanics, American Society of Mechanical Engineers, 1958. Citeseer.

BISHOP, R. E. D. & JOHNSON, D. C. 2011. *The mechanics of vibration*, Cambridge University Press.

BLOSS, B. & RAO, M. D. 2002. Measurement of damping in structures by the power input method. *Experimental Techniques,* 26**,** 30-32.

BLOSS, B. C. & RAO, M. D. 2005. Estimation of frequency-averaged loss factors by the power injection and the impulse response decay methods. *The Journal of the Acoustical Society of America,* 117**,**240-249.

REGULATION, B. 2010. Approved document E: resistance to the passage of sound.

BURROUGHS, C. B., FISCHER, R. W. & KERN, F. R. 1997. An introduction to statistical energy analysis. *Journal of the Acoustical Society of America,* 101**,** 1779-1789.

BÜSSOW, R. & PETERSSON, B.A.T. 2007. Path sensitivity and uncertainty propagation in SEA. *Journal of Sound and Vibration*, 300(3), 479-489.

CAPPS, R. N. 1983. Dynamic Young's moduli of some commercially available polyurethanes. *The Journal of the Acoustical Society of America,* 73**,** 2000-2005.

CARFAGNI, M., CITTI, P. & PIERINI, M. Determining loss factors using the power input method with shaker excitation. SPIE proceedings series, 1998. Society of Photo-Optical Instrumentation Engineers, 585-590.

CARFAGNI, M. & PIERINI, M. 1999a. Determining the loss factor by the power input method (PIM), Part 1: numerical investigation. *Journal of vibration and acoustics,* 121**,** 417-421.

CARFAGNI, M. & PIERINI, M. 1999b. Determining the loss factor by the power input method (PIM), Part 2: experimental investigation with impact hammer excitation. *Journal of vibration and acoustics,*121**,** 422-428.

CAUGHEY, T. Vibration of dynamic systems with linear hysteretic damping (linear theory). Proceedings of the 4th US National Congress of Applied Mechanics, 1962. 87-97.

CAUGHEY, T. & VIJAYARAGHAVAN, A. 1970. Free and forced oscillations of a dynamic system with "linear hysteretic damping"(non-linear theory). *International Journal of Non-Linear Mechanics,* 5**,** 533-555.

CHEN, G. & SOONG, T. T. 1991. POWER FLOW AND ENERGY-BALANCE BETWEEN NONCONSERVATIVELY COUPLED OSCILLATORS. *Journal of Vibration and Acoustics-Transactions of the Asme,* 113**,** 448-460.

CHOWDHURY, I. & DASGUPTA, S. P. 2003. Computation of Rayleigh damping coefficients for large systems. *The Electronic Journal of Geotechnical Engineering,* 8.

CLARKSON, B. L. & RANKY, M. F. 1984. ON THE MEASUREMENT OF THE COUPLING LOSS FACTOR OF STRUCTURAL CONNECTIONS. *Journal of Sound and Vibration,* 94**,** 249-261.

COOK, R. L., PORTER, T. & CARPENTER, L. Distributed ray tracing. ACM SIGGRAPH Computer Graphics, 1984. ACM, 137-145.

CORSARO, R. D. & SPERLING, L. H. 1990. Sound and vibration damping with polymers.

COTONI, V., SHORTER, P. & LANGLEY, R. 2007. Numerical and experimental validation of a hybrid finite element-statistical energy analysis method. *The Journal of the Acoustical Society of America,* 122**,**259-270.

COX, T.J. & D'ANTONIO, P., 2009. *Acoustic absorbers and diffusers: theory, design and application*, CRC Press.

CRAIK, R. J. 1996. *Sound transmission through buildings: using statistical energy analysis*, Gower Aldershot, England.

CRAIK, R. J. M. 2001. The contribution of long flanking paths to sound transmission in buildings. *Applied Acoustics,* 62**,** 29-46.

CRAIK, R. J. M. 2003. Non-resonant sound transmission through double walls using statistical energy analysis. *Applied Acoustics,* 64**,** 325-341.

CRAIK, R. J. M. 2011. Parallel Programmable Calculator (PPC). Version 13.320 [computer software] ed. Edinburgh.

CRAIK, R. J. M. & EVANS, D. I. 1989. THE EFFECT OF WORKMANSHIP ON SOUND-TRANSMISSION THROUGH BUILDINGS .2. STRUCTURE-BORNE SOUND. *Applied Acoustics,* 27**,** 137-145.

CRAIK, R. J. M. & SMITH, R. S. 2000. SOUND TRANSMISSION THROUGH LIGHTWEIGHT PARALLEL PLATES. PART II: STRUCTURE-BORNE SOUND. *Applied Acoustics,* 2000, 61**,** 247-269.

CRAIK, R. J. M. & STEEL, J. A. 1989. THE EFFECT OF WORKMANSHIP ON SOUND-TRANSMISSION THROUGH BUILDINGS .1. AIRBORNE SOUND. *Applied Acoustics,* 27**,** 57-63.

CREMER, L., HECKL, M. & UNGAR, E. Structure-Borne Sound, 1988. Springer-Verlag, NY.

DAVIES, H. G. & WAHAB, M. A. 1981. ENSEMBLE AVERAGES OF POWER FLOW IN RANDOMLY EXCITED COUPLED BEAMS. *Journal of Sound and Vibration,* 77**,** 311-321.

DE SILVA, C. W. 2007. *Vibration damping, control, and design*, CRC Press.

DOBSON, S., NOORI, M., HOU, Z., DIMENTBERG, M. & BABER, T. 1997. Modeling and random vibration analysis of SDOF systems with asymmetric hysteresis. *International Journal of Non-Linear Mechanics,* 32**,** 669-680.

EN 12354-1, 2000 (ISO 15712-1 since 2005). *Building acoustics–Estimation of acoustic performance of buildings from the performance of elements–Part 1 : airborne sound insulation between rooms.*

FAHY, F. Sound and structural vibration, 1985. Academic Press, London.

FAHY, F. & MOHAMMED, A. 1992. A study of uncertainty in applications of SEA to coupled beam and plate systems, part I: computational experiments. *Journal of Sound and Vibration,* 158**,** 45-67.

FAHY, F. J. 1994. STATISTICAL ENERGY ANALYSIS - A CRITICAL OVERVIEW. *Philosophical Transactions of the Royal Society a-Mathematical Physical and Engineering Sciences,* 346**,** 431-447.

FAHY, F. J. & DEYUAN, Y. 1987. POWER FLOW BETWEEN NON-CONSERVATIVELY COUPLED OSCILLATORS. *Journal of Sound and Vibration,* 114**,** 1-11.

FREDO, C. R. 1997. A SEA-like approach for the derivation of energy flow coefficients with a finite element model. *Journal of Sound and Vibration,* 199**,** 645-666.

FRIEDRICH, C. & BRAUN, H. 1992. Generalized Cole-Cole behavior and its rheological relevance. *Rheologica Acta,* 31**,** 309-322.

FUNKHOUSER, T., CARLBOM, I., ELKO, G., PINGALI, G., SONDHI, M. & WEST, J. A beam tracing approach to acoustic modeling for interactive virtual environments. Proceedings of the 25th annual conference on Computer graphics and interactive techniques, 1998. ACM, 21-32.

GAUL, L. 1983. WAVE TRANSMISSION AND ENERGY-DISSIPATION AT STRUCTURAL AND MACHINE JOINTS. *Journal of Vibration Acoustics Stress and Reliability in Design-Transactions of the Asme,* 105**,**489-496.

GAUL, L., KLEIN, P. & KEMPLE, S. 1991a. Damping description involving fractional operators. *Mechanical Systems and Signal Processing,* 5**,** 81-88.

GAUL, L., KLEIN, P. & KEMPLE, S. 1991b. Damping description involving fractional operators. *Mechanical Systems and Signal Processing,* 5**,** 81-88.

GLASSNER, A. S. 1989. *An introduction to ray tracing*, Morgan Kaufmann.

GUASCH, O. & ARAGONÈS, À. 2011. Finding the dominant energy transmission paths in statistical energy analysis. *Journal of Sound and Vibration*, 330(10), 2325-2338.

HALL, J. F. 2006. Problems encountered from the use (or misuse) of Rayleigh damping. *Earthquake engineering & structural dynamics,* 35**,** 525-545.

HOPKINS, C. 2002. Statistical energy analysis of coupled plate systems with low modal density and low modal overlap. *Journal of Sound and Vibration,* 251**,** 193-214.

HOPKINS, C., 2012. *Sound insulation*, Routledge.

INAUDI, J. A. & KELLY, J. M. 1995. Linear hysteretic damping and the Hilbert transform. *Journal of Engineering Mechanics,* 121**,** 626-632.

JONES, D. 1996. Reflections on damping technology at the end of the twentieth century. *Journal of sound and vibration,* 190**,** 449-462.

JONES, D. I. G. 2001. *Handbook of Viscoelastic Vibration Damping*, John Wiley & Sons.

KINSLER, L. E., FREY, A. R., COPPENS, A. B. & SANDERS, J. V. 1999. Fundamentals of acoustics. *Fundamentals of Acoustics, 4th Edition, by Lawrence E. Kinsler, Austin R. Frey, Alan B. Coppens, James V. Sanders, pp. 560. ISBN 0-471-84789-5. Wiley-VCH, December 1999.,* 1.

KLEINER, M., DALENBACK, B. I. & SVENSSON, P. 1993. AURALIZATION - AN OVERVIEW. *Journal of the Audio Engineering Society,* 41**,** 861-875.

KRAMERS, H. Estratto dagli Atti del Congresso Intemazionale di Fisica. *Como (Nicolo Zanichelli, Bologna 1927)*.

KROKSTAD, A., STROM, S. & SØRSDAL, S. 1968. Calculating the acoustical room response by the use of a ray tracing technique. *Journal of Sound and Vibration,* 8**,** 118-125.

KURTZE, G. 1959. Bending wave propagation in multilayer plates. *The Journal of the Acoustical Society of America,* 31**,** 1183-1201.

LABONNOTE, N., RØNNQUIST, A. & MALO, K.A. 2013. Modified hysteretic damping model applied to Timoshenko timber beams. *Computers & Structures*, 121, 22-31.

LAFONT, T., TOTARO, N. & LE BOT, A. 2014. Review of statistical energy analysis hypotheses in vibroacoustics. *Proceedings of the Royal Society a-Mathematical Physical and Engineering Sciences,* 470**,** 20.

LAZAN, B. J. 1968. *Damping of materials and members in structural mechanics*, Pergamon Press.

LEHNERT, H. 1993. Systematic errors of the ray-tracing algorithm. *Applied Acoustics,* 38**,** 207-221.

LEPPINGTON, F. G., HERON, K. H., BROADBENT, E. G. & MEAD, S. M. 1987. RESONANT AND NONRESONANT ACOUSTIC PROPERTIES OF ELASTIC PANELS .2. THE TRANSMISSION PROBLEM. *Proceedings of the Royal Society of London Series a-Mathematical Physical and Engineering Sciences,* 412**,** 309-337.

LUNDBERG, B. & BLANC, R. 1988a. Determination of mechanical material properties from the two-point response of an impacted linearly viscoelastic rod specimen. *Journal of Sound and Vibration,* 126**,** 97-108.

LUNDBERG, B. & BLANC, R. 1988b. Determination of mechanical material properties from the two-point response of an impacted linearly viscoelastic rod specimen. *Journal of Sound and Vibration,* 126**,** 97-108.

LYON, R. H. 1974. Needed: a new definition of diffusion. *The Journal of the Acoustical Society of America,* 56**,** 1300-1302.

LYON, R. H. & EICHLER, E. 1964. RANDOM VIBRATION OF CONNECTED STRUCTURES. *Journal of the Acoustical Society of America,* 36**,** 1344-&.

LYON, R. H. & MAIDANIK, G. 1962. POWER FLOW BETWEEN LINEARLY COUPLED OSCILLATORS. *Journal of the Acoustical Society of America,* 34**,** 623-&.

MACE, B. R. 1994. ON THE STATISTICAL ENERGY ANALYSIS HYPOTHESIS OF COUPLING POWER PROPORTIONALITY AND SOME IMPLICATIONS OF ITS FAILURE. *Journal of Sound and Vibration,* 178**,** 95-112.

MACE, B. R. & SHORTER, P. J. 2000. Energy flow models from finite element analysis. *Journal of Sound and Vibration,* 233**,** 369-389.

MADIGOSKY, W. M. & LEE, G. F. 1983. Improved resonance technique for materials characterization. *The Journal of the Acoustical Society of America,* 73**,** 1374-1377.

MAGRANS, F.X. 1993. Definition and calculation of transmission paths within an SEA framework. *Journal of sound and vibration*, 165(2), 277-283.

MARKOVIĆ, D., CANCLINI, A., ANTONACCI, F., SARTI, A. & TUBARO, S. 2010, October. Visibility-based beam tracing for soundfield rendering. In *Multimedia Signal Processing (MMSP)*, 2010 IEEE International Workshop on (40-45). IEEE.

MAXIT, L., EGE, K., TOTARO, N. & GUYADER, J.L. 2014. Non resonant transmission modelling with statistical modal energy distribution analysis. *Journal of Sound and Vibration*, 333(2), 499-519.

MONTALVÃO, D., CLÁUDIO, R.A.L.D., RIBEIRO, A.M. & DUARTE-SILVA, J. 2013. Experimental Measurement of the complex Young's modulus on a CFRP laminate considering the constant hysteretic damping model. *Composite Structures*, 97, 91-98.

MORIN, A. 1833. New friction experiments carried out at Metz in 1831–1833. *Proceedings of the French Royal Academy of Sciences,* 4**,** 128.

NASHIF, A. D., JONES, D. I. G. & HENDERSON, J. P. 1985. *Vibration Damping*, Wiley.

OBERST, H. & FRANKENFELD, K. 1952. On the damping of bending vibrations on thin sheet metal by firmly bonded coatings. *Acustica,* 2**,** 181-194.

OLMOS, B. A. & ROESSET, J. M. 2010. Evaluation of the half-power bandwidth method to estimate damping in systems without real modes. *Earthquake Engineering & Structural Dynamics,* 39**,** 1671-1686.

PRITZ, T. 1996. Analysis of four-parameter fractional derivative model of real solid materials. *Journal of Sound and Vibration,* 195**,** 103-115.

RAO, D. 1978. Frequency and loss factors of sandwich beams under various boundary conditions. *Journal of Mechanical Engineering Science,* 20**,** 271-282.

RAO, M. D. 2003. Recent applications of viscoelastic damping for noise control in automobiles and commercial airplanes. *Journal of Sound and Vibration,* 262**,** 457-474.

RAYLEIGH, L. 1945. The theory of sound (1877). *Mac Millan London*.

RENJI, K., NAIR, P. S. & NARAYANAN, S. 2001. Non-resonant response using statistical energy analysis. *Journal of Sound and Vibration,* 241**,** 253-270.

REYNOLDS, O. 1886. On the Theory of Lubrication and Its Application to Mr. Beauchamp Tower's Experiments, Including an Experimental Determination of the Viscosity of Olive Oil. *Proceedings of the Royal Society of London,* 40**,** 191-203.

ROGERS, L. 1983. Operators and fractional derivatives for viscoelastic constitutive equations. *Journal of Rheology (1978-present),* 27**,** 351-372.

ROOZEN, N. B. 1992. Quiet by design: numerical acousto-elastic analysis of aircraft structures.

ROSS, D., UNGAR, E. E. & KERWIN, E. 1959. Damping of plate flexural vibrations by means of viscoelastic laminae. *Structural damping,* 3**,** 44-87.

SCHARTON, T. D. & LYON, R. H. 1968. POWER FLOW AND ENERGY SHARING IN RANDOM VIBRATION. *Journal of the Acoustical Society of America,* 43**,** 1332-&.

SCHROEDER, M. R. 1965. New method of measuring reverberation time. *The Journal of the Acoustical Society of America,* 37**,** 409-412.

SHENG, M. P., WANG, M. Q. & SUN, J. C. 1998. Effective internal loss factors and coupling loss factors for non-conservatively coupled systems. *Journal of Sound and Vibration,* 209**,** 685-694.

SIMMONS, C. 1991. STRUCTURE-BORNE SOUND-TRANSMISSION THROUGH PLATE JUNCTIONS AND ESTIMATES OF SEA COUPLING LOSS FACTORS USING THE FINITE-ELEMENT METHOD. *Journal of Sound and Vibration,* 144**,** 215-227.

SMITH, P. W. 1979. STATISTICAL-MODELS OF COUPLED DYNAMICAL-SYSTEMS AND THE TRANSITION FROM WEAK TO STRONG COUPLING. *Journal of the Acoustical Society of America,* 65**,** 695-698.

SONG, J. & DER KIUREGHIAN, A. 2006. Generalized Bouc–Wen model for highly asymmetric hysteresis. *Journal of engineering mechanics,* 132**,** 610-618.

STANWAY, R., RONGONG, J. & SIMS, N. 2003. Active constrained-layer damping: a state-of-the-art review. *Proceedings of the Institution of Mechanical Engineers, Part I: Journal of Systems and Control Engineering,* 217**,** 437-456.

STEEL, J. A. & CRAIK, R. J. M. 1994. STATISTICAL ENERGY ANALYSIS OF STRUCTURE-BORNE SOUND-TRANSMISSION BY FINITE-ELEMENT METHODS. *Journal of Sound and Vibration,* 178**,** 553-561.

SUN, J. C., LALOR, N. & RICHARDS, E. J. 1987. POWER FLOW AND ENERGY-BALANCE OF NON-CONSERVATIVELY COUPLED STRUCTURES .1. THEORY. *Journal of Sound and Vibration,* 112**,** 321-330.

TAYLOR, M., CHANDAK, A., MO, Q., LAUTERBACH, C., SCHISSLER, C. & MANOCHA, D. 2012. Guided multiview ray tracing for fast auralization. *Visualization and Computer Graphics*, IEEE Transactions on, 18(11), 1797-1810.

TORVIK, P. J. & BAGLEY, D. 1987. Fractional derivatives in the description of damping materials and phenomena. *The role of damping in vibration and noise control***,** 125-135.

TORVIK, P. J. & BAGLEY, R. L. 1984. On the appearance of the fractional derivative in the behavior of real materials. *Journal of Applied Mechanics,* 51**,** 294-298.

TRINDADE, M. A. & BENJEDDOU, A. 2002. Hybrid active-passive damping treatments using viscoelastic and piezoelectric materials: review and assessment. *Journal of Vibration and Control,* 8**,** 699-745.

UNGAR, E. E. & ZAPFE, J. A. 2007. Structural damping. *Noise and Vibration Control Engineering: Principles and Applications, Second Edition***,** 579-609.

VEACH, E. & GUIBAS, L. J. Metropolis light transport. Proceedings of the 24th annual conference on Computer graphics and interactive techniques, 1997. ACM Press/Addison-Wesley Publishing Co., 65-76.

WANG, I. 2011. An analysis of higher order effects in the half power method for calculating damping. *Journal of Applied Mechanics,* 78**,** 014501.

WANG, J.-T., JIN, F. & ZHANG, C.-H. 2012. Estimation error of the half-power bandwidth method in identifying damping for multi-DOF systems. *Soil Dynamics and Earthquake Engineering,* 39**,** 138-142.

WANG, M. Q., SHENG, M. P. & SUN, J. C. 1998. The direct and indirect power flows of three non-conservatively series coupled oscillators. *Journal of Sound and Vibration,* 212**,** 231-251.

WEAVER, R. L. 2001. Equipartition and mean-square responses in large undamped structures. *Journal of the Acoustical Society of America,* 110**,** 894-903.

WEBSTER, A. C. & VAICAITIS, R. 1992. Application of tuned mass dampers to control vibrations of composite floor systems. *Engineering Journal of the American Institute of Steel Construction,* 29**,** 116-124.

WEN, Y.-K. 1976. Method for random vibration of hysteretic systems. *Journal of the engineering mechanics division,* 102**,** 249-263.

WHITTED, T. An improved illumination model for shaded display. ACM SIGGRAPH Computer Graphics, 1979. ACM, 14.

ZENER, C. 1948. *Elasticity and anelasticity of metals*, University of Chicago press.

ÖDEEN, S. & LUNDBERG, B. 1993. Determination of complex modulus from measured end-point accelerations of an impacted rod specimen. *Journal of Sound and Vibration,* 165**,** 1-8.

APPENDICES

Appendix 1: Script for generating SEA models

This script is based on the program language used in Parallel Programmable Calculator. Specific numbering systems are applied to create rooms, end walls, front walls, floors and joints. The script to create a 2*2*2 system is:

```
zap * * *
isystem  3 9 4 2
         4 2 2
         0 10 1 0 10000

$a=2 $b=2 $c=2 $l=4 $w=3 $h=2.5 $i=0.015 $r=0.5 for $x 1 1 $a for $y
1 1 $b for $z 1 1 $c isubsystem      [100 $x * 10 $y * + $z +]    1
$l      $w    $h    $r  /* room */

for $x 1 1 $a for $y 1 1 $b for $z 1 1 $c isubsystem   [1000 100 $y
* + 10 $z * + 1 +]    2       $w    $h    0.1    2   2000     0.2
2    324   $i  /* Plate */
for $x 2 1 $a for $y 1 1 $b for $z 1 1 $c isubsystem   [1000 $x *
100 $y * + 10 $z * + 1 +]    2       $w    $h    0.2    2   2000
0.2    2    162   $i  /* Plate */
for $x 1 1 $a  for $y 1 1 $b for $z 1 1 $c isubsystem   [$a 1 + 1000
* 100 $y * + 10 $z * + 1 +]    2       $w    $h    0.1    2   2000
0.2    2    324   $i  /* Plate */

for $x 1 1 $a for $y 1 1 $b for $z 1 1 $c isubsystem    [1000 $x *
100 + 10 $z * + 2 +]       2       $l    $h    0.1    2   2000
0.2    2    324   $i  /* Plate */
for $x 1 1 $a for $y 2 1 $b for $z 1 1 $c isubsystem    [1000 $x *
100 $y * + 10 $z * + 2 +]      2       $l    $h    0.1    2   2000
0.2    2    324   $i  /* Plate */
for $x 1 1 $a for $y 1 1 $b for $z 1 1 $c isubsystem    [$b 1 + 100
* 1000 $x * + 10 $z * + 2 +]       2       $l    $h    0.1    2
2000    0.2    2    324   $i  /* Plate */

for $x 1 1 $a for $y 1 1 $b for $z 1 1 $c isubsystem    [1000 $x *
100 $y * + 10  + 3 +]       2       $l      $w   0.15    2   2300
0.2    2    127   $i  /* Plate */
for $x 1 1 $a for $y 1 1 $b for $z 2 1 $c isubsystem    [1000 $x *
100 $y * + 10 $z * + 3 +]       2       $l      $w   0.15    2
2300    0.2    2    127   $i  /* Plate */
for $x 1 1 $a for $y 1 1 $b for $z 1 1 $c isubsystem    [$c 1 + 10 *
1000 $x * + 100 $y * + 3 +]       2       $l      $w   0.15    2
2300    0.2    2    127   $i  /* Plate */

/* Input joint details */
for $x 1 1 $a for $y 1 1 $b for $z 1 1 $c $R=(1000 $x *) ijoint [$R
10110 +]  [$R 112 +] [$R 113 +] 0 0    $l     1    /* Normal joint
*/
for $x 1 1 $a for $y 1 1 $b for $z 2 1 $c $R=(1000 $x * 10 $z * +)
ijoint [$R 10100 +] [$R 102 +] [$R 103 +] [$R 92 +] 0    $l     1
/* Normal joint */
for $x 1 1 $a for $y 1 1 $b for $z 1 1 $c $R=(1000 $x * 10 $c * +)
ijoint [$R 10110 +] [$R 113 +] [$R 102 +] 0 0    $l     1    /*
Normal joint */
```

```
for $x 1 1 $a for $y 2 1 $b for $z 1 1 $c $R=(1000 $x * 100 $y * +)
ijoint [$R 10010 +] [$R 87 -] [$R 12 +] [$R 13 +] 0     $l      1
/* Normal joint */
for $x 1 1 $a for $y 2 1 $b for $z 2 1 $c $R=(1000 $x * 100 $y * +
10 $z * +) ijoint [$R 10000 +] [$R 2 +] [$R 3 +] [$R 8 -] [$R 97 -]
$l     1    /* Normal joint */
for $x 1 1 $a for $y 2 1 $b for $z 1 1 $c $R=(1000 $x * 100 $y * +
10 $c * +) ijoint [$R 10010 +] [$R 13 +] [$R 2 +] [$R 87 -] 0    $l
1    /* Normal joint */

for $x 1 1 $a for $y 1 1 $b for $z 1 1 $c $R=(1000 $x * 100 $b * +)
ijoint [$R 10110 +] [$R 13 +] [$R 112 +] 0 0     $l      1     /*
Normal joint */
for $x 1 1 $a for $y 1 1 $b for $z 2 1 $c $R=(1000 $x * 100 $b * +
10 $z * +) ijoint [$R 10100 +] [$R 92 +] [$R 3 +] [$R 102 +] 0    $l
1    /* Normal joint */
for $x 1 1 $a for $y 1 1 $b for $z 1 1 $c $R=(1000 $x * 100 $b * +
10 $c * +) ijoint [$R 10110 +] [$R 102 +] [$R 13 +] 0 0    $l     1
/* Normal joint */

for $x 1 1 $a for $y 1 1 $b for $z 1 1 $c $R=(10 $z *) ijoint [$R
21110 +] [$R 1101 +] [$R 1102 +] 0 0    $h     1    /* Normal joint
*/
for $x 2 1 $a for $y 1 1 $b for $z 1 1 $c $R=(1000 $x * 10 $z * +)
ijoint [$R 20110 +] [$R 898 -] [$R 101 +] [$R 102 +] 0     $h     1
/* Normal joint */
for $x 1 1 $a for $y 1 1 $b for $z 1 1 $c $R=(1000 $a * 10 $z * +)
ijoint [$R 21100 +] [$R 102 +] [$R 1101 +] 0 0     $h      1     /*
Normal joint */

for $x 1 1 $a for $y 2 1 $b for $z 1 1 $c $R=(100 $y * 10 $z * +)
ijoint [$R 21000 +] [$R 1001 +] [$R 1002 +] [$R 901 +] 0    $h     1
/* Normal joint */
for $x 2 1 $a for $y 2 1 $b for $z 1 1 $c $R=(1000 $x * 100 $y * +
10 $z * +) ijoint [$R 20000 +] [$R 1 +] [$R 2 +] [$R 99 -] [$R 998 -]
$h     1    /* Normal joint */
for $x 1 1 $a for $y 2 1 $b for $z 1 1 $c $R=(1000 $a * 100 $y * +
10 $z * +) ijoint [$R 21000 +] [$R 901 +] [$R 2 +] [$R 1001 +] 0
$h     1    /* Normal joint */

for $x 1 1 $a for $y 1 1 $b for $z 1 1 $c $R=(100 $b * 10 $z * +)
ijoint [$R 21100 +] [$R 1102 +] [$R 1001 +] 0 0     $h      1     /*
Normal joint */
for $x 2 1 $a for $y 1 1 $b for $z 1 1 $c $R=(1000 $x * 100 $b * +
10 $z * +) ijoint [$R 20100 +] [$R 102 +] [$R 1 +] [$R 898 -] 0
$h     1    /* Normal joint */
for $x 1 1 $a for $y 1 1 $b for $z 1 1 $c $R=(1000 $a * 100 $b * +
10 $z * +) ijoint [$R 21100 +] [$R 1001 +] [$R 102 +] 0 0     $h
1    /* Normal joint */

for $x 1 1 $a for $y 1 1 $b for $z 1 1 $c $R=(100 $y *) ijoint [$R
31010 +] [$R 1011 +] [$R 1013 +] 0 0    $w     1    /* Normal joint
*/
for $x 1 1 $a for $y 1 1 $b for $z 2 1 $c $R=(100 $y * 10 $z * +)
ijoint [$R 31000 +] [$R 1001 +] [$R 1003 +] [$R 991 +] 0    $w     1
/* Normal joint */
for $x 1 1 $a for $y 1 1 $b for $z 1 1 $c $R=(100 $y * 10 $c * +)
ijoint [$R 31010 +] [$R 1013 +] [$R 1001 +] 0 0     $w      1     /*
Normal joint */
```

```
for $x 2 1 $a for $y 1 1 $b for $z 1 1 $c $R=(1000 $x * 100 $y * +)
ijoint [$R 30010 +] [$R 987 -] [$R 11 +] [$R 13 +] 0     $w      1
/* Normal joint */
for $x 2 1 $a for $y 1 1 $b for $z 2 1 $c $R=(1000 $x * 100 $y * +
10 $z * +) ijoint [$R 30000 +] [$R 1 +] [$R 3 +] [$R 9 -] [$R 997 -]
$w     1    /* Normal joint */
for $x 2 1 $a for $y 1 1 $b for $z 1 1 $c $R=(1000 $x * 100 $y * +
10 $c * +) ijoint [$R 30010 +] [$R 13 +] [$R 1 +] [$R 987 -] 0    $w
1    /* Normal joint */

for $x 1 1 $a for $y 1 1 $b for $z 1 1 $c $R=(1000 $a * 100 $y * +)
ijoint [$R 31010 +] [$R 13 +] [$R 1011 +] 0 0     $w      1     /*
Normal joint */
for $x 1 1 $a for $y 1 1 $b for $z 2 1 $c $R=(1000 $a * 100 $y * +
10 $z * +) ijoint [$R 31000 +] [$R 991 +] [$R 3 +] [$R 1001 +] 0
$w     1    /* Normal joint */
for $x 1 1 $a for $y 1 1 $b for $z 1 1 $c $R=(1000 $a * 100 $y * +
10 $c * +) ijoint [$R 31010 +] [$R 1001 +] [$R 13 +] 0 0    $w     1
/* Normal joint */

/* Calculate CLFs */
for $x 1 1 $a for $y 1 1 $b for $z 1 1 $c clf [1000 100 $y * + 10 $z
* + 1 +] [100 10 $y * + $z +] [$w $h *] [$w $h + 2 *] /* CLF room to
wall */
for $x 2 1 $a for $y 1 1 $b for $z 1 1 $c clf [1000 $x * 100 $y * +
10 $z * + 1 +] [100 $x * 10 $y * + $z +] [$w $h *] [$w $h + 2 *] /*
CLF room to wall */
for $x 2 1 $a for $y 1 1 $b for $z 1 1 $c clf [1000 $x * 100 $y * +
10 $z * + 1 +] [100 $x * 10 $y * + $z + 100 -] [$w $h *] [$w $h + 2
*] /* CLF room to wall */
for $x 1 1 $a for $y 1 1 $b for $z 1 1 $c clf [1000 $a * 100 $y * +
10 $z * + 1001 +] [100 $a * 10 $y * + $z +] [$w $h *] [$w $h + 2 *]
/* CLF room to wall */

for $x 1 1 $a for $y 1 1 $b for $z 1 1 $c clf [1000 $x * 100 + 10 $z
* + 2 +] [100 $x * 10 + $z +] [$l $h *] [$l $h + 2 *] /* CLF room to
wall */
for $x 1 1 $a for $y 2 1 $b for $z 1 1 $c clf [1000 $x * 100 $y * +
10 $z * + 2 +] [100 $x * 10 $y * + $z +] [$l $h *] [$l $h + 2 *] /*
CLF room to wall */
for $x 1 1 $a for $y 2 1 $b for $z 1 1 $c clf [1000 $x * 100 $y * +
10 $z * + 2 +] [100 $x * 10 $y * + $z + 10 -] [$l $h *] [$l $h + 2 *]
/* CLF room to wall */
for $x 1 1 $a for $y 1 1 $b for $z 1 1 $c clf [1000 $x * 100 $b * +
10 $z * + 102 +] [100 $x * 10 $b * + $z +] [$l $h *] [$l $h + 2 *]
/* CLF room to wall */

for $x 1 1 $a for $y 1 1 $b for $z 1 1 $c clf [1000 $x * 100 $y * +
10 + 3 +] [100 $x * 10 $y * + 1 +] [$l $w *] [$l $w + 2 *] /* CLF
room to wall */
for $x 1 1 $a for $y 1 1 $b for $z 2 1 $c clf [1000 $x * 100 $y * +
10 $z * + 3 +] [100 $x * 10 $y * + $z +] [$l $w *] [$l $w + 2 *] /*
CLF room to wall */
for $x 1 1 $a for $y 1 1 $b for $z 2 1 $c clf [1000 $x * 100 $y * +
10 $z * + 3 +] [100 $x * 10 $y * + $z + 1 -] [$l $w *] [$l $w + 2 *]
/* CLF room to wall */
for $x 1 1 $a for $y 1 1 $b for $z 1 1 $c clf [1000 $x * 100 $y * +
10 $c * + 13 +] [100 $x * 10 $y * + $c +] [$l $w *] [$l $w + 2 *] /*
CLF room to wall */
```

```
joint *
dwin 211 100
ftlf
HEALTH
solve
```

Appendix 2: Ray tracing code

```
%% Ray tracer for 5 connected concrete plates

clc
f=[40 50 63 80 100 125 160 200 250 315 400 500 630 800 1000 1250
1600 2000 2500 3150 4000 5000 6300];
mat_EL_xa=zeros(length(f),1);
N=50;%the times of reflection
a=2;%the length of the plate
b=2;%the width of the plate
n=100;%number of point sources (excluding (0,0) and (a,0))
m=20;%discritize the boundary into m part
ang=180;%number of rays for each point source(ang rays, excluding 0
and 180)
mat_int=zeros(3*ang*(n-1)+3*ang,N+1);%the matrix that store all the
intersection data
mat_xa=zeros(3*ang*(n-1)+3*ang,N+1);%the matrix that store
information of intersectins on x=a
ET_all_x0=0;
ET_all_xa=0;
ET_all_yb=0;
ET_all=[0];

%% Create a ray
for num_f=1:length(f)
for num_n=1:n
    for num_ang=1:ang
        for num=1:N
            num1=3*ang*(num_n-1)+3*num_ang-2;
            num2=3*ang*(num_n-1)+3*num_ang-1;
            num3=3*ang*(num_n-1)+3*num_ang;
            mat_int(num1,1)=a/(n+1)*num_n;
            mat_int(num3,1)=180/(ang+1)*num_ang;

            %initilization
            x0=mat_int(num1,num);
            y0=mat_int(num2,num);
            theta=mat_int(num3,num)/180*pi;
            %create matrix
            A_x0=[tan(theta),-1;1,0];
            B_x0=[tan(theta)*x0-y0;0];

            A_xa=[tan(theta),-1;1,0];
            B_xa=[tan(theta)*x0-y0;a];

            A_y0=[tan(theta),-1;0,1];
            B_y0=[tan(theta)*x0-y0;0];

            A_yb=[tan(theta),-1;0,1];
            B_yb=[tan(theta)*x0-y0;b];
            if mat_int(num3,1)==90

                mat_int(num1,num+1)=mat_int(num1,1);
                mat_int(num2,num+1)=(1-rem(num+1,2))*b;
                mat_int(num3,num+1)=90;

            else
                %solve the matrix
```

```
                C_x0=A_x0\B_x0;
                C_xa=A_xa\B_xa;
                C_y0=A_y0\B_y0;
                C_yb=A_yb\B_yb;

                %Reflections=(num)% show reflection times

                %check wheather the ray hits the line x=0
                if C_x0(1,1)~=x0 && C_x0(2,1)~=y0 && C_x0(2,1)>0 &&
C_x0(2,1)<b;
                    mat_int(num1,num+1)=C_x0(1,1);
                    mat_int(num2,num+1)=C_x0(2,1);
                    mat_int(num3,num+1)=180-mat_int(num3,num);%store
new data in vec_int
                    %'The ray hits x=0'
                    %C_x0
                else
                    %check wheather the ray hits the line x=a
                    if C_xa(1,1)~=x0 && C_xa(2,1)~=y0 && C_xa(2,1)>0
&& C_xa(2,1)<b;
                        mat_int(num1,num+1)=C_xa(1,1);
                        mat_int(num2,num+1)=C_xa(2,1);
                        mat_int(num3,num+1)=180-
mat_int(num3,num);%store new data in vec_int
                        %'The ray hits x=a'
                        %C_xa
                    else
                        %check wheather the ray hits the line y=0
                        if C_y0(1,1)~=x0 && C_y0(2,1)~=y0 &&
C_y0(1,1)>0 && C_y0(1,1)<a;
                            mat_int(num1,num+1)=C_y0(1,1);
                            mat_int(num2,num+1)=C_y0(2,1);
                            mat_int(num3,num+1)=180-
mat_int(num3,num);%store new data in vec_int
                            %'The ray hits y=0'
                            %C_y0
                        else
                            %check wheather the ray hits the line
y=b
                            if C_yb(1,1)~=x0 && C_yb(2,1)~=y0 &&
C_yb(1,1)>0 && C_yb(1,1)<a;
                                mat_int(num1,num+1)=C_yb(1,1);
                                mat_int(num2,num+1)=C_yb(2,1);
                                mat_int(num3,num+1)=180-
mat_int(num3,num);%store new data in vec_int
                                %'The ray hits y=b'
                                %C_yb
                            else
                                %'The ray hits nothing'
                            end
                        end
                    end
                end
            %mat_all(num1:num3,:)=mat_int; %show all the data of
intersection
           % mat_all
            end
        end
    end
end
```

```
mat_int

%% Creat the distance matrix
%The first column is the initial condition [x0;Imaginary reflection
angle;start angle]
%Other columns follow [Distance between the intersection to the
previous intersection; Reflection angle; Incident angle]
mat_dis=zeros(3*ang*(n-1)+3*ang,N+1);
for num_n=1:n
    for num_ang=1:ang
         for num=1:N
            num1=3*ang*(num_n-1)+3*num_ang-2;
            num2=3*ang*(num_n-1)+3*num_ang-1;
            num3=3*ang*(num_n-1)+3*num_ang;
            mat_dis(num1,1)=mat_int(num1,1);
            mat_dis(num2,1)=abs(90-mat_int(num3,1));
            mat_dis(num3,1)=mat_int(num3,1);
            mat_dis(num3,num+1)=mat_int(num3,num);
            mat_dis(num1,num+1)=((mat_int(num1,num+1)-
mat_int(num1,num))^2+(mat_int(num2,num+1)-mat_int(num2,num))^2)^0.5;
            if (mat_int(num2,num)==b && mat_int(num2,num+1)==0) ||
(mat_int(num2,num+1)==b && mat_int(num2,num)==0) ||
(mat_int(num1,num)==0 && mat_int(num1,num+1)==a) ||
(mat_int(num1,num)==a && mat_int(num1,num+1)==0)
                mat_dis(num2,num+1)=mat_dis(num2,num);
            else
                mat_dis(num2,num+1)=90-mat_dis(num2,num);
            end

         end
    end
end

mat_dis

%% Create incident energy matrix
% [Incident energy, Reflection angle, Incident angle]
mat_E=zeros(3*ang*(n-1)+3*ang,N+1);
PR=0.2;
h=0.15;
E=30*10^9;
m_surface=2300*h;
B_real=E*h^3/12/(1-PR^2);
LF=0.3;
cB=(4*pi^2*B_real.*f(num_f)^2/m_surface).^0.25;
kB_rea=2*pi*f(num_f)/cB;
kB_ima=kB_rea*LF/4;
wavelength=cB./f;

for num_n=1:n
    for num_ang=1:ang
         for num=1:N+1
            num1=3*ang*(num_n-1)+3*num_ang-2;
            num2=3*ang*(num_n-1)+3*num_ang-1;
            num3=3*ang*(num_n-1)+3*num_ang;
            mat_E(num2,num)=mat_dis(num2,num);
            mat_E(num3,num)=mat_dis(num3,num);
            mat_E(num1,1)=mat_dis(num1,1);
```

```
            mat_E(num1,2)=exp(-2*kB_ima*mat_dis(num1,2));
            if num>2
                mat_E(num1,num)=mat_E(num1,num-1)*exp(-
2*kB_ima*mat_dis(num1,num))*(1-0.5*(cos(mat_dis(num2,num-
1)*pi/180))^2);
            else
            end
         end
    end
end

mat_E;

%% Discretization
% Discretize each boundary into m parts.

dis=zeros(3*ang*n,N+1);
IE_xa=zeros(m+1,ang+1);%Incident energy on x=a
IE_x0=zeros(m+1,ang+1);%Incident energy on x=0
IE_yb=zeros(m+1,ang+1);%Incident energy on y=b
IE_y0=zeros(m+1,ang+1);%Incident energy on y=0

for num_m=1:m
    for num_ang=1:ang
        for  num_n=1:n
             for num=1:N+1
                 for num_ang2=1:ang
                    num1=3*ang*(num_n-1)+3*num_ang-2;
                    num2=3*ang*(num_n-1)+3*num_ang-1;
                    num3=3*ang*(num_n-1)+3*num_ang;
                    IE_xa(1,num_ang2+1)=180/(ang+1)*num_ang2;
                    IE_xa(num_m+1,1)=b/m*num_m;
                    IE_x0(1,num_ang2+1)=180/(ang+1)*num_ang2;
                    IE_x0(num_m+1,1)=b/m*num_m;
                    IE_yb(1,num_ang2+1)=180/(ang+1)*num_ang2;
                    IE_yb(num_m+1,1)=a/m*num_m;
                    IE_y0(1,num_ang2+1)=180/(ang+1)*num_ang2;
                    IE_y0(num_m+1,1)=a/m*num_m;
                    if num>1 && mat_int(num1,num)==a &&
mat_E(num3,num)== IE_xa(1,num_ang2+1) &&
mat_int(num2,num)>b/m*(num_m-1) && mat_int(num2,num)<= b/m*num_m


IE_xa(num_m+1,num_ang+1)=IE_xa(num_m+1,num_ang+1)+mat_E(num1,num);
                    else
                    end
                    if num>1 && mat_int(num1,num)==0 &&
mat_E(num3,num)== IE_x0(1,num_ang2+1) &&
mat_int(num2,num)>b/m*(num_m-1) && mat_int(num2,num)<= b/m*num_m


IE_x0(num_m+1,num_ang+1)=IE_x0(num_m+1,num_ang+1)+mat_E(num1,num);


                    else
                    end
                    if num>1 && mat_int(num2,num)==b &&
mat_E(num3,num)== IE_yb(1,num_ang2+1) &&
mat_int(num1,num)>a/m*(num_m-1) && mat_int(num1,num)<= a/m*num_m
```

```
IE_yb(num_m+1,num_ang+1)=IE_yb(num_m+1,num_ang+1)+mat_E(num1,num);


                    else
                    end
                    if num>1 && mat_int(num2,num)==0 &&
mat_E(num3,num)== IE_y0(1,num_ang2+1) &&
mat_int(num1,num)>a/m*(num_m-1) && mat_int(num1,num)<= a/m*num_m


IE_y0(num_m+1,num_ang+1)=IE_y0(num_m+1,num_ang+1)+mat_E(num1,num);


                    else
                    end
                end
            end
        end
    end
end

%% Energy transmitted
ET_xa=zeros(m+1,ang+1);%energy transmited through xa

ET_xa(:,1)=IE_xa(:,1);
ET_xa(1,:)=IE_xa(1,:);
for num_m=2:m+1
    for num_ang=2:ang+1
        if IE_xa(1,num_ang)<90

ET_xa(num_m,num_ang)=IE_xa(num_m,num_ang)*(cos(IE_xa(1,num_ang)*pi/1
80))^2;
        else
            ET_xa(num_m,num_ang)=IE_xa(num_m,num_ang)*(cos(pi-
IE_xa(1,num_ang)*pi/180))^2;
        end
    end
end
ET_all_xa(num_f)=sum(ET_xa(2,2:end));

ET_x0=zeros(m+1,ang+1);%energy transmited through x0

ET_x0(:,1)=IE_xa(:,1);
ET_x0(1,:)=IE_xa(1,:);
for num_m=2:m+1
    for num_ang=2:ang+1
        if IE_x0(1,num_ang)<90

ET_x0(num_m,num_ang)=IE_x0(num_m,num_ang)*(cos(IE_x0(1,num_ang)*pi/1
80))^2;
        else
            ET_x0(num_m,num_ang)=IE_x0(num_m,num_ang)*(cos(pi-
IE_x0(1,num_ang)*pi/180))^2;
        end
    end
end
```

```
ET_all_x0(num_f)=sum(ET_x0(2,2:end));

ET_yb=zeros(m+1,ang+1);%energy transmited through yb

ET_yb(:,1)=IE_yb(:,1);
ET_yb(1,:)=IE_yb(1,:);
for num_m=2:m+1
    for num_ang=2:ang+1
        if IE_yb(1,num_ang)<90

ET_yb(num_m,num_ang)=IE_yb(num_m,num_ang)*(cos(IE_yb(1,num_ang)*pi/1
80))^2;
        else
            ET_yb(num_m,num_ang)=IE_yb(num_m,num_ang)*(cos(pi-
IE_yb(1,num_ang)*pi/180))^2;
        end
    end
end
ET_all_yb(num_f)=sum(ET_yb(2,2:end));

ET_y0=zeros(m+1,ang+1);%energy transmited through y0

ET_y0(:,1)=IE_y0(:,1);
ET_y0(1,:)=IE_y0(1,:);
for num_m=2:m+1
    for num_ang=2:ang+1
        if IE_y0(1,num_ang)<90

ET_y0(num_m,num_ang)=IE_y0(num_m,num_ang)*(cos(IE_y0(1,num_ang)*pi/1
80))^2;
        else
            ET_y0(num_m,num_ang)=IE_y0(num_m,num_ang)*(cos(pi-
IE_y0(1,num_ang)*pi/180))^2;
        end
    end
end
ET_all_y0(num_f)=sum(ET_y0(2,2:end));

end
ET_all_xa=ET_all_xa'
ET_all_yb=ET_all_yb'
ET_all_x0=ET_all_x0'
ET_all_y0=ET_all_y0'
```